Detection of Superparamagnetic Beads with TMR Sensors

written by
Sascha Walkenhorst

Department of Physics
Bielefeld University
Germany

January 2007

Declaration

I wrote this thesis by myself and used none but the indicated resources.

Bielefeld, February 8, 2007

(Sascha Walkenhorst)

Contents

Introduction

Magnetic particles have been used in medical applications for several years in various ways[LPLK06], such as in integrated microfluidic systems, where they were used as "docking stations" which are moved with an electromagnet[COT$^+$02]. They can also be used to influence a magnetic sensor with their magnetic stray field. Among many advantages, it is the usual absence of a magnetic background in biological environment, the varying material composition and the varying size down to a few nanometers in diameter, which opens up a wide field of applications for magnetic particles. Using the smallest nanoparticles with a diameter of less than $10\,nm$ it should also be possible to label tiny biomolecules without hindering them to behave natural and this should make it possible e.g. to track reactions inside cells. It is also important to reach the size of proteins and small DNA fragments in order to label such a biomolecule with exact one marker, which reduces the consumption of material[Wan05].

Other detection systems, using electrical, electrochemical or optical methods, are already used for many applications. Very popular is e.g. fluorescence in combination with laser, which needs large space and also much material[LJW$^+$03], i.e. "approximately 10^4 molecules to achieve an useful signal-to-noise ratio" [Wan05]. Furthermore goals like low-cost, high miniaturization, immediate detection combined with a low threshold down to measurements of single beads[1] are said to be achievable or are already reached and makes it interesting for research on detection systems, which are using magnetic beads[MP05].

Detection of magnetic markers is essential for magnetic detection systems in biological applications in general, such as the bio-chip for detection of diseases. Therefore biomolecules like proteins and DNA are labeled with magnetic particles, which can be coated e.g. with proteins or SH-groups to bind on biomolecules. Due to a microfluidic system, labeled biomolecules can be carried near magnetic sensors, which use magneto-resistive effects to detect the presence of a magnetic particle.[2] Research concentrates on different kinds of sensors: *Hall sensors* (deploying the Hall-effect), *spin valve sensors* (SV sensors) and GMR sensors (based on the *giant-magnetoresistance* (GMR) as well as TMR sensors which use the *tunnel-magnetoresistance* (TMR). A detailed overview on biosensors etc. is given by SCHOTTER in his PhD thesis[Sch04, chapter 1] and MEGENS

---

[1]Particles which consist of magnetic material are called "beads", and with respect to the application "marker" or "label".

[2]Another sensing scheme uses the change in the Brownian relaxation time if magnetic markers bind to target molecules in a liquid, confer [MXvM$^+$05].

and PRINS[MP05] gave an overview of SV and GMR sensors.

For Hall-, spin valve and GMR sensors the principle was proofed working even for the detection of single beads (see [LJW+03] for SV, [ETS+00] for GMR and [BBD+02, JLMB06] for Hall sensors) and several research groups in institutes and companies are working on that task (see references [MP05, MXvM+05, Pan05, Sch04, SLMX05, vDC05, ZYYJ05] in section 1.4, as well as [CTMH05, COT+02, dBKJ+06, FGFC03, FFGF05, GFB+02, KJO+04, SSBR06, TPL00, Wan05]). In principle[SSBR04a, SSBR04b] also TMR sensors should work and furthermore be the leading choice concerning sensitivity due to higher effects and possible minimization, which means better integration into (Si-) chips. SCHOTTER gave a proof of basic concept in 2004[Sch04] and in 2005 SHEN *et al.*[SLMX05] were able to measure single magnetic beads using *magnetic tunnel junctions* (MTJs) with realtime measurements in a fluidic system. It was necessary to use an AC bridge configuration combined with lock-in technique, which is an universal disadvantage for the integration and built up of a lab-on-a-chip. Therefore such signal enhancement should not be necessary to get a low-cost and low-power consuming machine every general practitioner can place in his own surgery.

The main goal of this thesis was the detection of magnetic beads without a special signal enhancement (e.g. like a Wheatstone bridge[ETS+00, JLMB06]) so that higher integration is possible. In the beginning relative big beads should be applied, i.e. microbeads which were already used successfully with GMR/TMR sensors[Sch04, Pan05]. Further research should lead to the detection of small amounts of beads, or even single beads. Furthermore the dimensions of self fabricated sensors should be minimized coming along with using smaller beads. In the last step magnetic nanoparticles could be applied to biomolecules so that a single biomolecule should be detectable.

The basics of this work are presented in the first two chapters: Beginning with the theoretical background and basic concepts in chapter 1, where all keywords are introduced and formulas are given which are related to the topic of this thesis. Machines are introduced in chapter 2, followed by an exemplary process, where a sample is prepared and characterized. This chapter includes the used materials and further information on the handling of the introduced machines. Several approaches for measuring the influence of a magnetic marker on sensors are presented in chapter 4. The setup was changed due to improvements based on the discussion of former results applying double coils or permanent magnets. In the second experimental part of this thesis MgO magnetic tunnel junctions were used in combination with shape anisotropy. General aspects and the utilization of shape anisotropy, which is encouraged by the results of the first experimental part, are discussed in the fifth chapter. At the end first results of new sensors for the detection of superparamagnetic beads are presented.

Chapter 1

Theory and Basics

This chapter contains the theoretical background, beginning with magnetism in general, especially the superparamagnetism of the used beads. Afterwards the fields of coils and properties of permanent magnets and beads in general are discussed. Furthermore the characteristics of the used beads are presented and their field and its influence on a sensor[3] are calculated. Section 1.3 deals with the TMR effect used in the sensors, followed by the actual state of biosensors which are based on magnetoresistive effects. The last part in this chapter gives a deeper insight to thin films which is needed as background information for chapter 5.

1.1 Magnetism

If a material is inserted into a magnetic field the magnetic induction[4] $\vec{B}$ looks in simple cases, e.g. for paramagnetic material which is discussed in detail later in this section, (in SI-system) like[Tip99]:

$$
\begin{aligned}
\vec{B} &= \mu \cdot \vec{H} \\
&= \mu_0 \mu_r \cdot \vec{H} \\
&= \mu_0 \left(1 + \chi\right) \cdot \vec{H} \\
&= \mu_0 \cdot \left(\vec{H} + \vec{M}\right)
\end{aligned}
\tag{1.1}
$$

with "permeability of vacuum" $\mu_0 = 4\pi \cdot 10^{-7} \frac{Vs}{Am}$[NIS04], "relative permeability" μ_r, "(magnetic) permeability" μ and "(magnetic) susceptibility" χ. With cgs-units the equation can be written as $\vec{B} = (\vec{H} + 4\pi\vec{M})$ $(\mu_0 = 1)$. In general χ is fix for "linear" materials which have no hysteresis (see below). $\vec{M}$ is the material's magnetization which is induced from the outer magnetic field $\vec{H}$ by alignment of the direction of already existing magnetizations, i.e. alignments of magnetic moments, or producing new magnetizations.

---

[3]The term "sensor" is normally only used for structured pillars, called "elements", which have a lower and upper contact.

[4]$\vec{B}$ is also called "magnetic-flux density", or sometimes also "magnetic field" in confusion with $\vec{H}$

μ_r and therefore μ depends on the material, its sign and total value indicating the kind of magnetism as seen in the following sections.

For magnetic fields SI-units, i.e. "A/m", are the national standard, although in research the old unit "Oerstedt" Oe[5] is still in use; $1\,Oe = 79.577\,A/m$. Therefore in this thesis normally the unit Oe is used. Formulas and conversion of units between cgs and SI-system can be found e.g. in [Uni, section "Magnetic Units & Terminology"] or [Enn03, table 1.1].

1.1.1   Para- and Ferromagnetism

The susceptibility is positive in the case of *para-* and *ferromagnetism*, so that the "inner" magnetization increases the outer applied field. The direction of already existing magnetic moments begin to follow the outer field direction until (almost) all match to the outer field. In the latter case of ferromagnetism the magnetic moments are strongly coupled which leads to a permanent magnetization and intrinsic areas where all magnetic moments are aligned, the so called "(magnetic) domains"[6], which is the reason for high susceptibilities, e.g. $\mu_r = 5500$ for iron[Tip99, p.912, table 29-2]. Those domains are stable below the *Curie temperature* (T_C), afterwards the thermal energy overcomes the coupling of the magnetic moments and their directions begin to vary, ending with a steady distribution and a decreasing net magnetic moment down to zero, see figure 1.1. The basic equations are the Curie law (equation (1.2)) and the (Curie-)Weiss law (equation (1.3)), confer [Kit86, p. 402 et seq., 424] or [Vog97, p. 391f]:

$$\chi = \frac{C}{T} \quad \text{Curie law} \tag{1.2}$$

$$\chi = \frac{C}{T - T_C} \quad (T < T_C) \quad \text{(Curie-)Weiss law} \tag{1.3}$$

where C is the "Curie constant". In case of paramagnetism the interaction between the magnetic moments is not as high as required to build stable domains so that only values of 10^{-5} for the susceptibility are achieved [Tip99, p, 905].

An important difference is that ferromagnetic materials can have a hysteresis, i.e. they remember in which way they are magnetized see figure 1.2. Starting with a "virgin curve" the inner field increases up to saturation magnetization M_S, but with decreasing outer field it still exhibits the remanence-field M_R at vanishing outer field. It goes down, reaching zero at outer "coercivity field" H_C, down to negative saturation and on its way back to positive saturation experience also remanence and coercivity fields. The total recall can only be circumvented when the material is heated above the Curie temperature.

---

[5]Hans Christian Øerstedt, 1777–1851, Danish chemist and physicist, first observed the deviation of a magnetic needle caused by electric current. According to a collection of formulas [FD96] it is officially forbidden to use the unit Oe any longer.

[6]Domains are also called "Weißsche Bezirke"
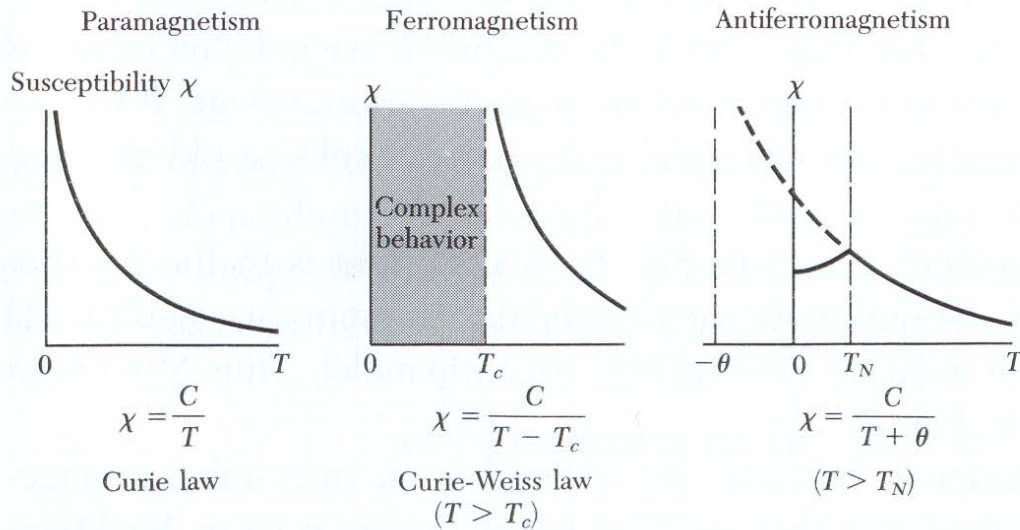
Figure 1.1: Magnetic susceptibility of paramagnetic (a), ferromagnetic (b) and antiferromagnetic (c) material [Kit86, p. 444, figure 15.23].

1.1.2 Superparamagnetism

If the thermal energy below Curie temperature is high enough to change the orientation of magnetic moments in small volumes one speaks of *superparamagnetism*. This is true for crystallites in the range of several nanometers, e.g. SUDFELD calculated that the superparamagnetic limit of miscellaneous nanoparticles with Co, Fe and/or Pt lays between approx. $\varnothing 3$–$31\,nm$[Sud05, section 3.2], in contrast to paramagnetism where atomic magnetic moments are changed.

The theoretical basics are the uniaxial anisotropy energy[BL59]

$$E \sim K_u \cdot V \tag{1.4}$$

which is given by the thermal energy $k_B T$, with anisotropy constant K_u, a crystalline volume V and Boltzmann-constant $k_B \approx 1.38 \cdot 10^{-23}\,J/K$[FD96], The Langevin equation describes the decreasing magnetization for (super)paramagnetic material, see e.g. [KPF$^+$02]:

$$M(x) = M_S \cdot \left(\coth(x) - \frac{1}{x} \right), \quad x = \frac{\mu_0 m H}{k_B T} \tag{1.5}$$

(formula for SI-units; set μ_0=1 for cgs-system).

DENNIS *et al.*[DBB$^+$02] gives an example calculation for Co particles which have an uniaxial anisotropy energy $K_u \approx 1.5 \cdot 10^6\,erg/cm^3$ leading to a formula for the *blocking temperature* T_B which is the threshold to measure ferromagnetic behavior if it is cooler,
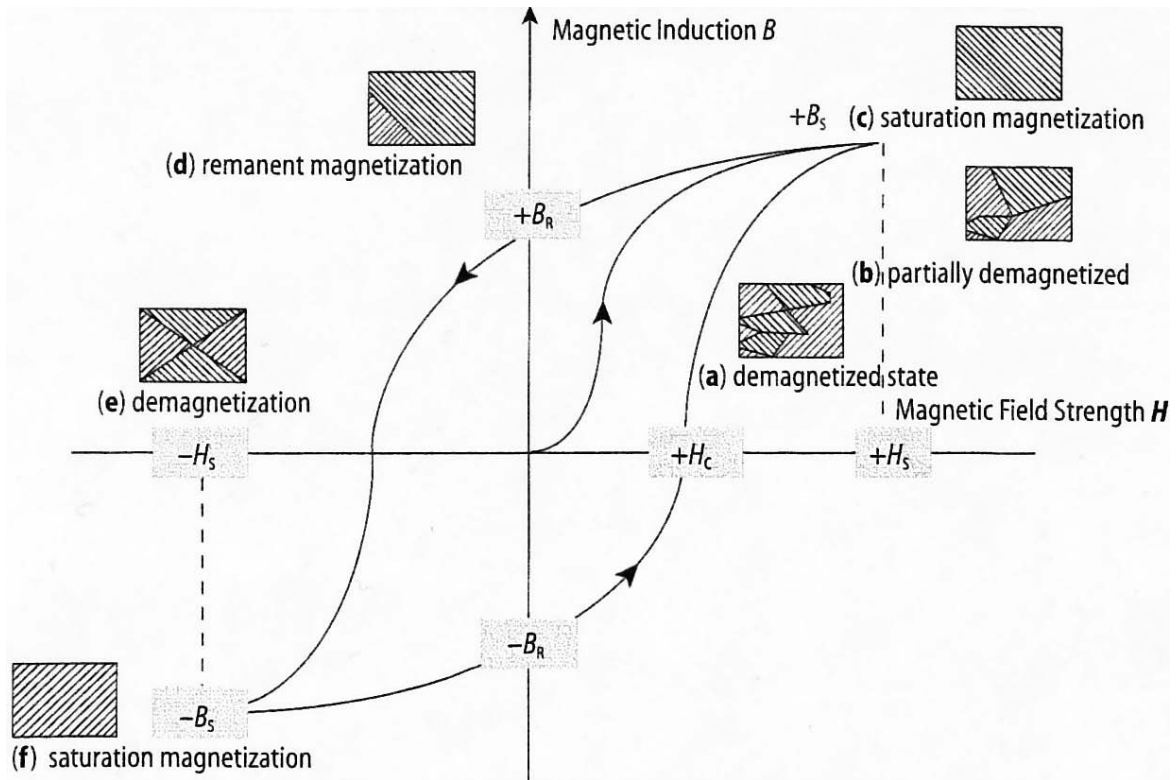
Figure 1.2: Sketch of hysteresis for a ferromagnetic material (after [Car00, p. 283]).

i.e. having hysteresis and remanence in the magnetization curve:

$$T_B = \frac{K_u V}{25 k_B} \tag{1.6}$$

where V denotes the particle volume. K_u can be calculated via the saturation magnetization M_S and the "anisotropy field" H_{anis}, that is the field where M_S is reached, [Enn03, p. 54]:

$$K_u = M_S \cdot H_{anis}/2. \tag{1.7}$$

1.1.3 Ferri- and Antiferromagnetism

Furthermore exists phenomena like *ferri-* and *antiferromagnetism*: In ferrimagnetic materials spins of adjacent atoms are antiparallel aligned but not equal which results in a net magnetic moment similar to the behavior of ferromagnets with less amplitude, i.e. saturation magnetization M_S is much lower. Equal spins of next atoms are antiparallel in antiferromagnetic materials compensating each other up to the *Néel temperature* (T_N) when they are disordered. The susceptibility increases until T_N and follows then paramagnetic behavior.

According to KITTEL [Kit86, p. 438 et seq.] magnetite is naturally ferrimagnetic: FeO·Fe$_2$O$_3$ consists of two Fe^{3+}-ions which spins are antiparallel, compensating each

other out, leaving the spins of Fe^{2+}. Consequently such materials with 2+-ions such as Zn, Cd, Fe, Ni, Cu, Co, Mg etc. were called "ferrites"; today all materials with partly vanishing spins are called ferrimagnetic.

1.1.4 Diamagnetism

Negative susceptibility also must be mentioned: In diamagnetism magnetic dipoles are induced by the outer magnetic field which diminish this field. That is quite normal for all materials, but in ferro- and paramagnetic materials it is dominated by these much higher effects. Total compensation of the applied field, i.e. $\vec{B} = 0$, is gained by superconductors.

1.2 Magnetic Fields

The applied magnetic fields during measurements are the measurement field itself H_{meas} to see an influence of the field from the bead H_b (see section 1.2.3), induced by H_{meas} or an additional field H_{oop} originated by a permanent magnet or (Helmholtz-) coils. H_{oop} is oriented *out-of-plane* (OOP) towards the sensing plane of the sensors, consequently H_{meas} will be called H_{ip} because it is orientated *in-plane* (IP).

1.2.1 Coils

The field of a simple coil (one turn) can be calculated starting with Biot-Savart's law [Tip99, p. 885]:

$$d\vec{B} = \frac{\mu_0}{4\pi} \cdot I \cdot \frac{\vec{dl} \times \vec{r}/r}{r^2} \tag{1.8}$$

for an infinitesimal long element $\vec{dl}$ of a wire with the current I. In figure 1.3 the vector $\vec{r}$ is shown, which points from the coil-element to a point on the x-axis, where the direction of the total magnetic field $\vec{B}$ is given by the cross-product $\vec{dl} \times \vec{r}$.
The x-component of the magnetic field of an entire coil is

$$d\vec{B}_x = \frac{\mu_0}{2} \cdot I \cdot R^2 \cdot \left(x^2 + R^2\right)^{-\frac{3}{2}} \tag{1.9}$$

using Biot-Savart's law (1.8) and $|\vec{dl} \times \vec{r}| = dl \cdot r$ with $r = \sqrt{x^2 + R^2}$ as well as $\oint dl = 2\pi R$. Furthermore the field components non-parallel to the x-axis are symmetric, so $B_{i \nparallel x}$ compensate each other.

Helmholtz-coils are two identical coils with radius R and n turns, laying on the same axis with a distance d. With the origin placed in the middle of one coil as in figure 1.4 one get from equation (1.9) for the component of the magnetic field at the coil's axis:

$$d\vec{B}_x = \frac{\mu_0}{2} \cdot I \cdot n \cdot R^2 \cdot \left[\left(x^2 + R^2\right)^{-\frac{3}{2}} + \left((x-d)^2 + R^2\right)^{-\frac{3}{2}}\right]. \tag{1.10}$$

For $R = d$ one get the largest homogenous field possible over a relative big length between the two coils[Mes04, p. 452, figure 8.13].
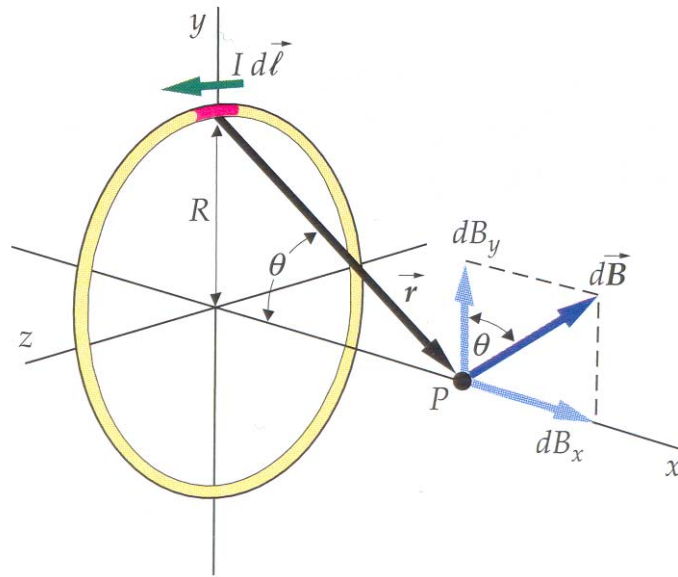
Figure 1.3: Sketch of coil with single turn for field calculation using Biot-Savart's law. [Tip99, p. 886, figure 29-5]

Compared to permanent magnets, see next section 1.2.2, coils exhibit the advantage to choose the field strength via varying I to ones requirements with respect to the thickness of the wires used which limits the maximum current due to overheating[7].

1.2.2   Permanent Magnets

In this thesis NdFeB-magnets are used which exhibit a high magnetization so that relative tiny magnets have high magnetic fields. In general magnets based on rare-earth-metals are a good choice showing high fields with less volume than older permanent magnets, and the strength can even easily be increased by using several magnets in a

---

[7]Therefore e.g. thermal fuses are installed.

Figure 1.4: Sketch of Helmholtz-coils. The line between the coils indicate that for a distance which is equal to the radius, see the left part, one gets the strongest and most homogenous field (after [Mes04, p. 452]).

stack. Different types are available, such as SmCo, AlNiCo, and NdFeB, separated into classes of strength, e.g. from N30 ($11\,kOe$) to N45 ($13.3\,kOe$) as in a product list from XIANGYING MAGNETIC MATERIALS CO.[Xia06]. The strength depends on the production procedure and further materials combined in those alloys. Maximum working temperature for the older SmCo-magnets is $250\,°C$[Xia06]–$300\,°C$[Ree04] whereas $Nd_2Fe_{14}B$ already looses magnetization over $80\,°C$–$180\,°C$[Xia06], having the opportunity of higher field. But on the other hand they are susceptible to corrosion, see [Gut00] where several combinations of materials are discussed. The material is therefore covered with a thin protecting film of e.g. nickel, which must be treated carefully to avoid damage.

The disadvantage of such permanent magnets is the great variation in field strength depending on the position and distance towards the surface (see section 4.5.1).

References for reviews and further articles on permanent magnets are given in [HS98, section 6.3], as well in [Uni] where also the historical development and increasing field strength is visible.

1.2.3 Magnetic Beads

Basic requirements for magnetic markers are:

- small size,

- uniform shape and size,

- good binding properties, i.e. strong and specific,

- high magnetic moment.

General Composition

The beads which are used in this thesis have a core and a surrounding matrix which can be coated with functionalized groups, e.g. SH-groups, or proteins, e.g. biotin, avidin, streptavidin etc.[8] With such a biological coating it is possible to bind biomolecules which have a corresponding biomolecule on their surface, which is essential for the use in biochips. For connections to non-organic materials other linker can be used, e.g. the SH-groups for Au. If connections are not needed or useful one can get also "plain" beads without a special coating (please read ahead for information on properties of used beads in this thesis). Figure 1.5 shows that in the core, which is in real a matrix of e.g. silicate, crystallites are enclosed which are magnetic or can be made magnetic, such as magnetite Fe_3O_4. Although magnetite is ferromagnetic, its crystallites can show superparamagnetic behavior if the dimensions are small enough, so that the thermal energy below Curie temperature is high enough to change the orientation of magnetic moments of a whole crystallite, as mentioned in section 1.1.2 on page 5.

---

[8]Information on proteins and view of structures can be found at the "Protein Data Bank" at www.pdb.org.
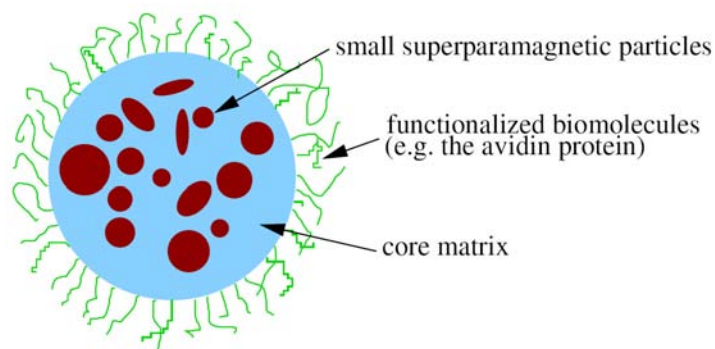
Figure 1.5: Sketch of a functionalized bead. [Pan05, figure 1.7]

Magnetite Fe_3O_4 is the common used magnetic material although it does not provide the best magnetic characteristics. Further experiments will use nanoparticles in the range of a few nanometers up to several hundred of nanometers, depending on the fabrication process and the material, e.g. Au or CoFe, and are also commercial available[9] in many variations. $Co_{50}Fe_{50}$ (at %) is for example a good candidate for a new generation of real nanoparticles with a saturation magnetization five times higher than for magnetite, leading to a reduced number of needed particles for transportation (factor 20–25) and smaller particles in the nanometer regime. Therefore the danger of tissue irritation and conflicts with the immune system is less, but contrary to Fe_3O_4 the Co is sometimes thought to be poisonous so that a bio-compatible coating is needed, a serious task for researchers. Confer e.g. [Enn03, section 4.2.2], [Sho05, p. 22], [Pan05, p. 19] and [HSE$^+$04] for mentioned aspects. Nevertheless such relative big superparamagnetic beads were already successfully used in other (single) bead detection experiments (see section 1.4.2), although they are too big for some biological application.

Magnetic Properties of Micromod Beads

Micromod beads had already been used by Michael Panhorst during his PhD thesis [Pan05], so it is reasonable to use these beads, whose behavior was well known. All beads consist of magnetite Fe_3O_4 as the magnetic material in a silicate core with different coatings, which are listed in table 1.1. The magnetic particles are called "sicastar® -M" being "extremely stable in organic solvents" and having a "hydrophobic surface with terminal Si-OH-bonds" (called "plain" as visible in table 1.1) according to the company's online catalog[Mic, 1. 6. 2006].

The "plain" beads are used for measurements according to dropping tests, described in the "Exemplary Preparation and Characterization", see section 3.3. Micromod's technical datasheet (39-00-153 sicastar®-M plain) gives following information: size = $1.5\,\mu m$, spherical shape, density = $2.5\,g/ccm$, specific magnetization = $4\,emu/g$ at $1\,kOe$

---

[9]Companies which offer beads are e.g. Micromod[Mic], Seradyn[Ser], Bangs[Ban], Chemagen[Che], Sigma Chemical Coompany[Ald] or Dynal[Dyn].

coating	product no.	concentration	diameter
plain	39-00-153	$25\,mg/ml$	$1.5\,\mu m$
avidin	39-18-153	$10\,mg/ml$	$1.5\,\mu m$
biotin	39-26-153	$50\,mg/ml$	$1.5\,\mu m$
SH	39-93-153	$50\,mg/ml$	$1.5\,\mu m$
SH	39-93-252	$25\,mg/ml$	$0.25\,\mu m$

Table 1.1: Available MICROMOD beads, confer product catalog at www.micromod.de for further information.
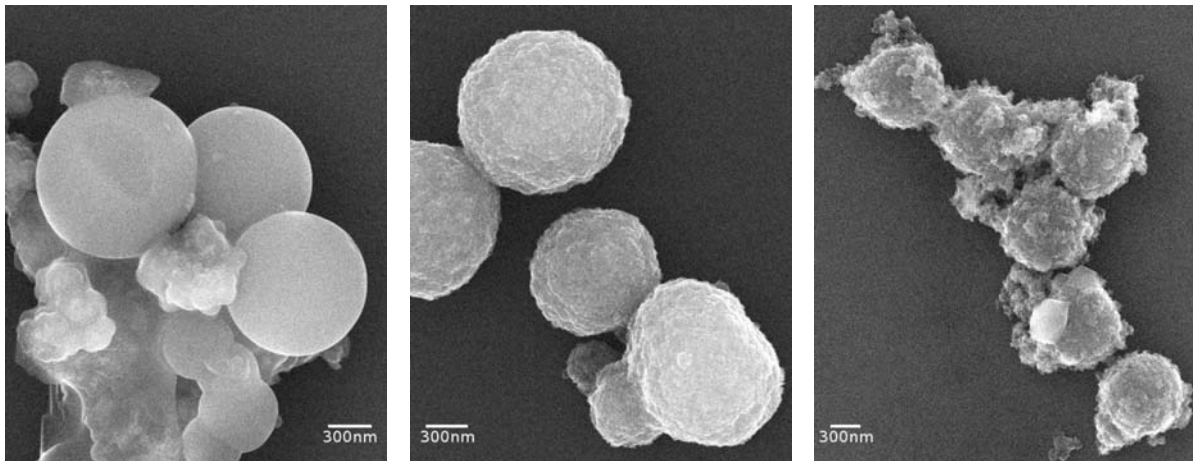
(a) Micromod   (b) Chemagen   (c) Seradyn

Figure 1.6: SEM images of beads by MICHAEL PANHORST – these examples show representative variation in size, surface and intermixed substances (from [Pan05, section 1.2]).

($\approx 80\,kA/m$). They were delivered in an "aqueous suspension" with a concentration of $25\,mg/ml$ according to the packaging. In general the beads are stable in "aqueous buffers pH > 3, organic solvents", but the share of magnetic material was not specified. Therefore MICROMOD told in an email [Tel06] that the matrix consists of approx. $25\,\%$ (m/m) magnetite as statistical distributed crystallites of 7–$15\,nm$ and their aggregates. The saturation magnetization is for dry particles $>6\,emu/g$ at $>10\,kOe$ ($\approx >800\,kA/m$) and $5\,emu/g$ at $2\,kOe$ ($\approx 160\,kA/m$). Out of the given magnetite amount by mass of $25\,\%$ the amount by volume is calculated, with a mean density of magnetite of $5.15\,g/ccm$[10] and the density of beads $2.5\,g/ccm$, to $12.14\,\%$(v/v).

PANHORST[Pan05] got for product no. 39-18-153 (i.e. surface avidin, density $4\,g/ccm$) a magnetic moment $m = 0.4\,fAm^2$ at $100\,Oe$ ($\approx 8\,kA/m$) (AGM measurements). The size distribution is relative large and there were "other substances intermixed in between the beads"[Pan05, p. 18], visible at SEM picture 1.6(a). Own SEM observations show a range of the bead diameter in between 342 and $1300\,nm$, see section 3.3.2.

---

[10]http://webmineral.com/data/Magnetite.shtml
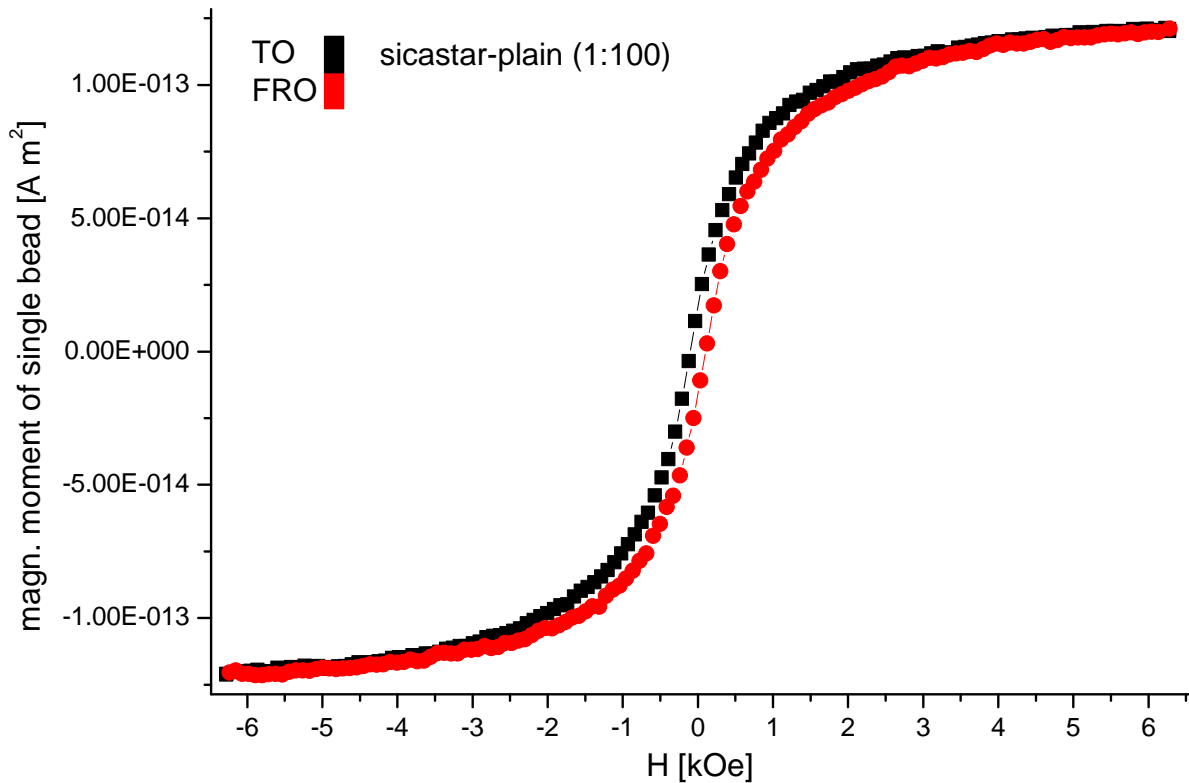
Figure 1.7: Mean magnetic moment of single beads, calculated from AGM measurement of dilution 1:100 (approx. 113200 beads), done by MICHAEL SCHILLING. (unpublished data [Scha])

Superparamagnetic Behavior of Micromod Beads

Superparamagnetic beads should only have a magnetization if an external field is applied so that they can act without influencing other magneto-sensitive materials or devices as far as no external magnetic field is applied which "switches them on". Then the beads try to concatenate to minimize field energy by aligning in one direction.

  Measurements done by MICHAEL PANHORST with the AGM, see figure 1.7 and confer [Pan05, section 2.6], show indeed a remanence field, i.e. they show partly ferromagnetic behavior. The hysteresis is not as large as it can be expected for the ferromagnetic iron, see e.g. measurements of Fe nanoparticles by WEI *et al.*[WSP+06] or by GONG *et al.*[GLZC91], so only a few beads are ferromagnetic[Scha]. These beads attract the normal ones and lead to small agglomerations within the radius of their field. In videos[11] made by PANHORST[Pan05, chapter 5] during experiments for the positioning of beads this behavior is visible: Small groups of particles come together if a field is applied, but if the field is turned off, they leave each other (due to brownian motion). The average of hysteresis-free beads and ferromagnetic beads results in a hysteresis of about $16 \, kA/m$.

---

[11]http://www.panhorst.com/PhD/manipulation/Star.html

Reasons of the ferromagnetic behavior can be (confer [Pan05, p. 35]):

⋆ Bigger crystallites – so big that they are really ferromagnetic (confer section 1.1.2 for size dependence).

⋆ Due to incomplete oxidation there is Fe instead of Fe_3O_4, which is ferromagnetic.

⋆ Clustering can make the alignment of crystallites easier due to higher interaction.

The clustering can be avoided due to pipette spotting the dilution on a heated sample (e.g. hot-plate), but this made no improvement[Pan05, p. 36]. Nevertheless there can be an influence and somewhat interaction between the beads, because tests with six different concentrations in the former mentioned thesis [Pan05, p. 36] showed different magnetic moments. One should keep in mind that the calculation of the magnetic moment cannot be very exact; the AGM measurements have an accuracy of 98 %, see section 2.6 in [Pan05] for details on AGM setup, and although the sensitivity ranges down to $10\,pAm^2$ one has to measure a vast quantity of beads to get a signal, in fact almost millions were used which cannot be counted but is calculated due to the dilution. This way has the uncertainty of the density in the delivered tube and possible loss of liquid using the pipet.

Remembering the behavior of superparamagnetism one should check whether it is possible in general to measure paramagnetic behavior if a magnetic field is applied, i.e.: is the blocking temperature T_B low enough? If T_B is too high, i.e. higher than RT, which is in this case the temperature during measurement, the beads would behave ferromagnetic (see the context of equation (1.6) in section 1.1.2).

If $H_a = 6.3\,kOe$ ($\approx 500\,kA/m$) is chosen, as the saturating field, see figure 1.7, this leads with equation (1.7) to $K_u = 1.2{\cdot}10^6\,erg/cm^3$, or more general $K_u = 3150\,erg/cm^3 \times M_S[emu/cm^3]$. The volume is simply $V = 4/3\pi \times r[m]^3 \approx 4.2 \cdot 10^{-27}m^3 \times r[nm]^3 = 4.2 \cdot 10^{-28}Jcm^3/erg \times r[nm]^3$, so that with equation (1.6) the dependency of T_B on the saturation magnetization and on the radius of the magnetic crystallites can be written as

$$T_B(M_S, r)\,[K] = \frac{168\pi}{1.38} \cdot 10^{-5}\,K \times M_S[emu/cm^3] \cdot r[nm]^3 \qquad (1.11)$$

The different radii are chosen for calculations: $r = 3.5\,nm,\ 5.5\,nm\ and\ 7.5\,nm$ according to the data given by Micromod, confer page 11, speaking of statistical dispersed magnetite crystallites ranging from 7 to $15\,nm$ in diameter. So a mean diameter of $11\,nm$ is assumed and this value is chosen to have an additional value among the maximal values. This shows how calculated values are developing.

Three different values are taken for the saturation magnetization: 380, 477 and $560\,emu/cm^3$. The saturation magnetization of magnetite is given in [Enn03, table 4.3] to $380\,emu/cm^3$ at $300\,K$. In a "materials handbook" from 2000 [Car00] one can find a value of approx. $477\,emu/cm^3$ at a not specified temperature. This higher value fits also with $480\,G$ @RT and $510\,G$ @0K, respectively, found in [Kit86, table 15.2] and [Ash76, table 33.3].

A third value of M_S is given by the AGM measurement done by Schilling, see figure 1.7: At $6.3\,kOe$ ($\approx 500\,kA/m$) the curve does not change any longer, which means that the saturation is reached, with a magnetic moment per bead $m_{s,b} \approx 1.2{\cdot}10^{-13}\,Am^2 =$

$1.2 \cdot 10^{-10} \, emu$. In the calculation of M_S the magnetic volume is given due to the amount of magnetite in one bead which is according to the afore done calculations on page 11 $12.14\,\%(\mathrm{v/v})$: $M_S = m_{s,b}/0.1214 \cdot V_{bead} \approx 2.37 \cdot 10^{11} \, emu/cm^3 \times r[nm]^{-3}$. With a mean bead radius of $750\,nm$ the third magnetization saturation is $560\,emu/cm^3$.

The calculated blocking temperatures with respect to the radius and saturation magnetization are given in table 1.2 with the result, that the biggest crystallites will show at room temperature ferromagnetic behavior for sure. Although the tiny crystallites below the mean diameter of $11\,nm$ should give a signal without hysteresis, confer table 1.2, the ferromagnetic crystallites can lead to a hysteresis as already discussed for the beads.

crystallites		$M_S \, [emu/cm^3]$	
radius	380	477	560
min.: $3.5\,nm$	-211 °C	-195 °C	-181 °C
mean: $5.5\,nm$	-31 °C	30 °C	83 °C
max.: $7.5\,nm$	340 °C	496 °C	630 °C

Table 1.2: T_B of Micromod sicastar®-M plain beads, calculated with equation (1.11).

Field Calculations

The magnetic moment of uniformly magnetized sphere with radius a can be calculated to $\vec{m} = \frac{4\pi a^3}{3}\vec{M}$ ([Jac75, p. 195] and [ZYYJ05] using cgs-system or [TPL00] using SI-system), where $\vec{M}$ is the uniform permanent magnetization, correlated to the applied field $\vec{H}_a$ via $\vec{M} = \chi\vec{H}_a$, see formula (1.1). Using the "vector potential" $\vec{A} = \frac{\vec{m}\times\vec{r}}{|\vec{r}|^3}$[Jac75, p. 182] the magnetic dipole field $\vec{H}$ can be calculated by evaluating the curl, assuming a homogeneous magnetization, i.e. $\vec{m}$ only depends on the applied field at any place in the bead.

$$\vec{H}(\vec{r}) = \frac{3\vec{r}(\vec{r}\cdot\vec{m})}{|\vec{r}|^5} - \frac{\vec{m}}{|\vec{r}|^3} \tag{1.12}$$

This is of course an idealization to simplify the calculations, assuming perfect oxidized iron crystallites (magnetite) with a narrow range in dimension which are distributed homogeneously. Even more critical is taken a theoretical approach for an uniformly magnetized (compact) sphere, but a bead has a matrix containing the magnetic material in a more or less good distribution and the shape is in general not that of a round ball, see figure 1.6. In [Sch04, section 3.2.1] SCHOTTER points out that it is not a matter of course[12] to use an uniformly magnetized sphere for a bead, but the calculations were indeed successful in that thesis using this formula for the beads saturation magnetization:

$$M_{s,bead} = M_{s,mat} \cdot V_{mat}/V_{bead} \tag{1.13}$$

---

[12]Many, maybe all other calculations are done in this way, see e.g. [ZYYJ05, LWSL+05, TPL00]. For (micromagnetic) simulations of GMR and TMR sensors and their response to a beads field see also [SSBR04a, SSBR04b, SSBR06].

with V_{mat} and V_{bead} as the volume of magnetic material and of the bead, respectively, and $M_{s,mat}$ the materials saturation magnetization. An additional error could come along with the use of $\vec{m} = \frac{4\pi a^3}{3}\vec{M}$, because OMMERING at PHILIPS[vONP06] found that m_b is not proportional to the volume.

Based on equation (1.13) one can deduce the field components of the bead $\vec{H}_b$, with respect to the measurement field $\vec{H}_{meas}$ and/or the field for saturating the beads, called $\vec{H}_{sat}$. In an "in-plane setup" the measurement field is oriented in the (x-y-)plane of the sample, without loss of generality in x-direction: $(H_i, 0, 0)$. In this case $\vec{H}_{meas} = \vec{H}_{ip}$ acts also as the saturating field. If the saturating field is applied perpendicular to the plane of the sample $(\vec{H}_{oop})$ the setup accordingly is called "out-of-plane" (OOP), nevertheless is the measurement field oriented in-plane, so the total applied field can be written as $(H_m, 0, H_{oop})$. With these notations one get the following formulas for the dipole field using formula (1.12):

$$H_{b,x}^{ip} = \frac{3}{r^5} \cdot m_x \cdot \left(x^2 - \frac{r^2}{3} \right) \tag{1.14}$$

$$H_{b,y}^{ip} = \frac{3}{r^5} \cdot m_x \cdot xy \tag{1.15}$$

$$H_{b,z}^{ip} = \frac{3}{r^5} \cdot m_x \cdot xz \tag{1.16}$$

$$H_{b,x}^{oop+ip} = \frac{3}{r^5} \cdot \left(m_z^{oop} \cdot xz + m_x' \cdot x^2 - \frac{r^2}{3} \cdot m_x' \right) \tag{1.17}$$

$$H_{b,y}^{oop+ip} = \frac{3}{r^5} \cdot (m_z^{oop} \cdot yz + m_x' \cdot xy) \tag{1.18}$$

$$H_{b,z}^{oop+ip} = \frac{3}{r^5} \cdot \left(m_z^{oop} \cdot z^2 + m_x' \cdot xz - \frac{r^2}{3} \cdot m_z^{oop} \right) \tag{1.19}$$

$$H_{b,x}^{oop} = \frac{3}{r^5} \cdot m_z^{oop} \cdot xz \tag{1.20}$$

$$H_{b,y}^{oop} = \frac{3}{r^5} \cdot m_z^{oop} \cdot yz \tag{1.21}$$

$$H_{b,z}^{oop} = \frac{3}{r^5} \cdot m_z^{oop} \cdot \left(z^2 - \frac{r^2}{3} \right) \tag{1.22}$$

where $\vec{r}$ denotes the distance from the beads center, and because the values of the measurement and the saturating field will generally differ, so the magnetic moments are differing too: $m_z^{oop}(\vec{H}_{oop}) \neq m_x'(\vec{H}_{meas})$. The latter three formulas (1.20) to (1.22) give the stray field if there is only the out-of-plane field magnetizing the beads, whereas formulas (1.17) to (1.19) give the situation during measurements with an additional applied in-plane field.
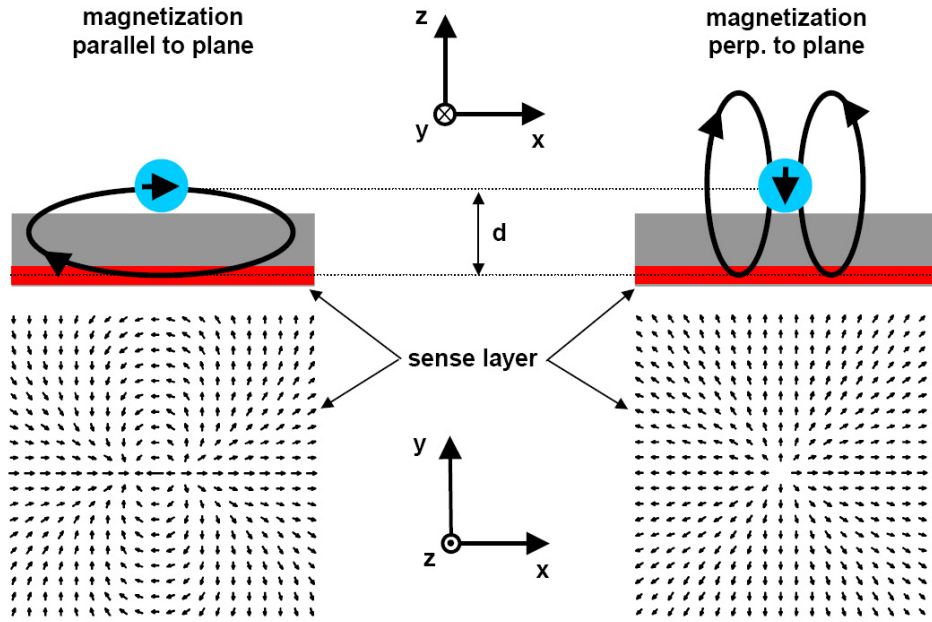
Figure 1.8: In-plane components of the stray field of a bead, from [Sch04, figure 18].

Calculations for Magnetic Beads on TMR Sensors

For OOP magnetization of beads sometimes the question comes up, whether the opposite parts of the magnetic stray field of a bead would cancel each other out due to their symmetry as visible in figure 1.8. Another question is whether in the same way the fields of several beads would cancel each other out, so that the influence on the sensor could vanish. In a perfect symmetric arrangement, i.e. e.g. one bead with symmetric field is placed on the middle of a symmetric shaped sensor the signal can indeed vanish, but that is more a philosophical aspect. In real almost never such a symmetry is reached.

To answer the question, whether the stray fields are big enough and which influence could be expected, micromagnetic calculations/simulations have been published by several groups [BBB+04, LJW+03, SSBR04a, SSBR04b, SSBR06, TPL00, ZYYJ05]. Therefore generally special simulation software like OOMMF is used, taking domains and their interaction, as well as energy aspects (see section 1.5.3) into consideration.

For TMR sensors Brückl *et al.*[BBB+04] showed in 2004 that "single molecule detection with a single "bead" marker is possible due to the high sensitivity of MTJs". In this article also fields in bead agglomerations was simulated, which indeed does not cancel out, consistent with experiments. An array of beads unfortunately favors the appearing of 360° walls, contrary to single markers, which is therefore an advantage. Furthermore the success in the detection of magnetic markers show that the principle is working (see section 1.4.2).

The success of an special setup depends among other things on the design and geometry, such as Jiang[JLMB06] is pointing out: "Detection of the resulting field change is
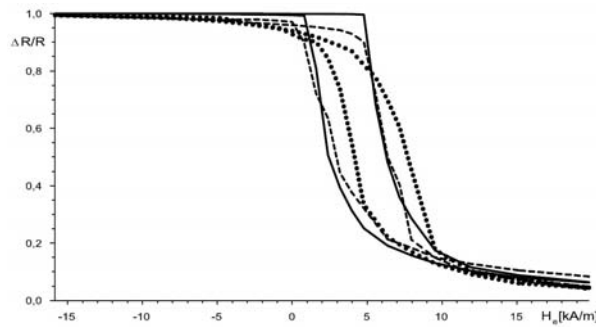
Figure 1.9: Calculation of the influence on a sensor (solid: without beads) by arrays with 8×8 beads (short dash) or 8×6 beads (dotted) [SSBR04a, figure 8].

optimized by designing a sensor that has similar dimensions to the beads being detected, by minimizing the sensor-bead distance, and by positioning the bead directly on top of the sensor." (See e.g. also [TPJ⁺05].)

The question whether an IP or OOP field should be used is according to simulations by SCHEPPER[SSBR04a] negligible, where IP calculations are compared to OOP experiments, because "TMR calculations for the out of plane case certainly are possible, they look quite similar". The calculated influence is a smoothed curve and a shift of the hysteresis in the direction of the applied field, as visible in figure 1.9.

In a publication from our group[BJS⁺04], as well as in [Sch04, section 3.2.1], reasons pro and contra TMR in combination with the question of the magnetizing field orientation, i.e. of the field which magnetizes the beads, are balanced. An important role plays the "demagnetizing field" which originates out of the small thickness of the ferromagnetic layers and hinders the magnetic moments from out-of-plane orientation. Due to this only high perpendicular fields can disturb the sensing layer which has two effects: On the one hand the in-plane components of the beads stray field are essential and in this category an in-plane magnetizing field leads to both higher maximal total stray field components (factor 1.2). More important is an unidirectional alignment instead of a radially symmetric one which is visible in figure 1.8. This round concerning field geometry and strength goes to in-plane fields. On the other hand an in-plane field makes it necessary to have a high sensitive sensor at relative high field regions, which is opposed by the normal design. It brings the disadvantage that the stray field is always "on", which makes an additional reference sensor necessary. Here comes out the advantage of an OOP magnetizing field which does not hinder sensing and makes it possible to switch the stray field on and off. (Maybe perpendicular fields help avoiding 360° Néel walls[PPL90] as an additional positive effect.) This reason counts much more with respect to the magnetoresistive sensor design[BJS⁺04], which is for TMR in general also used in this thesis. In summary there is no question that the magnetizing field should be oriented out-of-plane.

Although the perpendicular field can be varied independent from the measuring field,
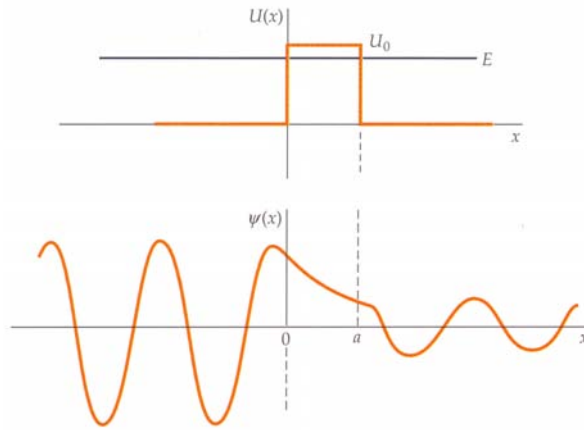
Figure 1.10: Exponential decay of wave function.[Tip99, figure 36-12, p. 1153]

the stray-field is also influenced by H_a. That encourages measurements with a small applied field.

1.3   Tunnel Magnetoresistance

1.3.1   Tunnel Effect

1928 Gamow[GM01] explained the tunneling of electrons based on *quantum mechanics* (QM) (see figure of wave function with exponential decay 1.10). Two conducting areas are separated by a thin insulating barrier so that in the classical view an electron cannot pass the potential wall. When applying a (positive) voltage V on the right side, as visible in the right part of figure 1.11 the fermi energy E_F is shifted on that side, yielding to varying *density of states* (DOS) which influences the tunneling of electrons through the barrier. Characterization is done via I/V measurements (IV-curves) which are fitted
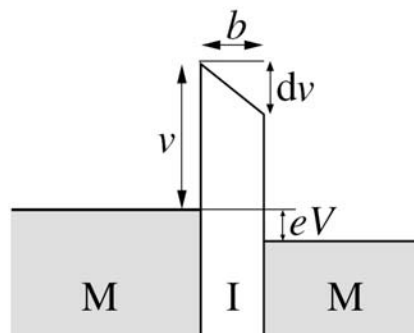
Figure 1.11: Sketch of potential wall; M means metal and I isolator, see text for other parameters which are given by Brinkman fit, taken from [Pan05].

with a Brinkman-fit, giving barrier parameters like thickness b, asymmetry $d\nu$ and the total barrier height ν as depicted in figure 1.11. For more details and references have a look at [Pan05, section 1.5].

The evolving current, so called "tunneling current" from the left side to the right is given by

$$I_{l \to r} = \int_{-\infty}^{\infty} \rho_l(E) \cdot \rho_r(E + eV) \cdot \left| T(E)^2 \right| \cdot f(E) \cdot (1 - f(E + eV))dE \qquad (1.23)$$

Here is ρ the DOS and f is the "Fermi function", both depending on the energy E of the electrons, and T is the transmission probability, see [Har61]. Summing up both directions gives the total current $I_{total} = I_{l \to r} - I_{r \to l}$, which can be solved[Sim63] using the WKB approximation ("Wenzel-Kramers-Brillouin"), confer [Wie06] for a short summary.

The tunnel effect is applied e.g. in "tunnel diode" (also called "Esaki-Diode"[Har61]) or *scanning tunnel microscope* (STM), and is also the basis for the TMR effect.

1.3.2 Magnetic Tunnel Junctions

The general stack layout of a magnetic tunnel junction is a trilayer with layers of ferromagnetic material (FM) and isolator (I), often enlarged by antiferromagnetic layers (AFM) for exchange bias: AFM / FM / I / FM / AFM. Based on the tunnel effect (see above) electrons can overcome the thin isolating barrier, which has generally a thickness of about $1\,nm$. The current, and therefore the resistance, depends on the alignment of the FMs relative to each other: In the parallel state, i.e. parallel alignment of the magnetization in FMs, a higher current can flow than in the antiparallel state (see figure 1.13). A typical measurement curve is also called a loop, because the field is usually applied from a negative(positive) value a up(down) to a maximal positive(negative) value c and backwards down(up) to a. In figure 1.12 on the left is the measured current vs. field and on the right side the resulting *resistance R*, calculated via $R = U_b \cdot I$, where U_b is the bias voltage and I is the measured current. A stack is also characterized by its *area resistance AR*, i.e. the product of the area of the sensing layer, which is given by the dimensions of the barrier in a structured element, and the resistance at zero applied field.

If only the soft layer switches one speaks of a *minor loop*, if both layers switch it is called a *major loop*, as sketched in figure 1.13. The magnetoresistive effect for tunneling is calculated with TMR (effect) $\equiv \frac{\Delta R}{R} \equiv \frac{R_{ap} - R_p}{R_p}$, where R_p is the resistance in the parallel state and R_{ap} is the resistance in the antiparallel state (see also equation 1.28 in the "Historical Development").

In the last years a race for higher effects took place, starting in 2004 with $220\,\%$ @RT[PKP$^+$04][13] using MgO as isolator (sandwiched by Fe). One year later it was raised by IKEDA *et al.*[IHL$^+$05] to $355\,\%$ @RT with a CoFeB/MgO/CoFeB stack. Therefore MgO is superior to barriers with AlO$_x$ which exhibit $70\,\%$ according to [SMZ$^+$06] and

---

[13]RT stands for room temperature.
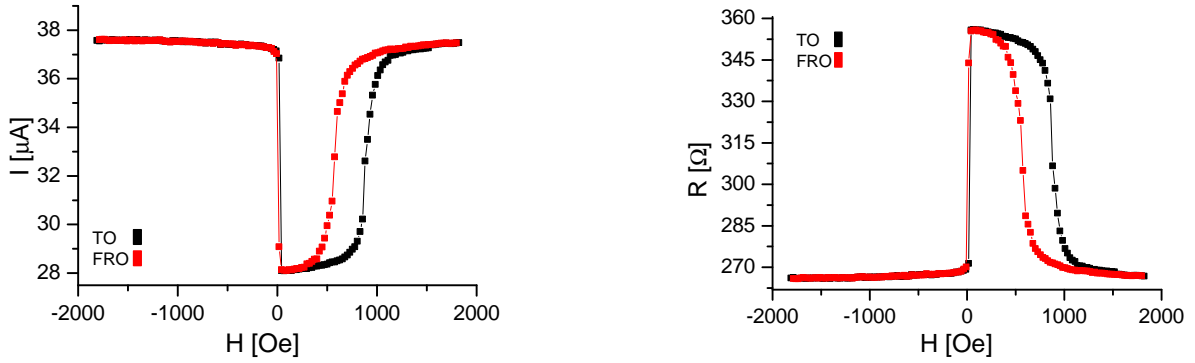
Figure 1.12: Example loop: Left measured current at bias voltage of $10\,mV$, on right side resulting resistance.

[NHT$^+$05]. In 2006 YUASA *et al.*[YFK$^+$06] reported $410\,\%$ @RT switching the FM to [metastable] bcc Co(001). Calculations showed for "coherent tunneling" several $1000\,\%$ TMR effect, so there is still space for improvements. A short overview towards improved TMR ratios with varying materials is given in the introduction of [SMZ$^+$06] and [NHT$^+$05].

The research on TMR resulted in the non-volatile MRAM[SLMX05], and MTJs can be used for sensing of magnetic fields, e.g. in read heads and micro compasses[JNK$^+$06]. Latest research was done on the application in "FPGAs" (Field Programmable Gate Arrays)[Mey06] with the goal of combined memory and processors which are programmable during work, as well as on biosensors, see section 1.4.

1.3.3   Historical Development

The historical development starts with JULLIERE in 1975[Jul75] who gave a first formula of the relative conductance change for a special case – he studied Fe-Ge-Co junctions at low temperature ($\leq 4.2\,K$) which magnetizations are parallel or antiparallel oriented. Applying a "spin conservation hypothesis" he got for the conductance G:

$$TMR \quad \equiv \quad \frac{\Delta G}{G} = \frac{2PP'}{1+PP'} \tag{1.24}$$

$$(\quad = \quad \frac{\Delta R}{R} = \frac{R_{AP} - R_P}{R_{AP}}) \tag{1.25}$$

(according to DE TERESA[TBF$^+$99]) with the spin polarizations of conduction electrons (in FM) $P = 2\,a - 1, P' = 2\,a' - 1$, where a gives the fraction of tunneling electrons in borders between NM and FMs with magnetic moments parallel to magnetization. (If FMs are parallel aligned it is $G \sim aa' + (1-a)(1-a')$, in antiparallel alignment it is $G \sim a(1-a') + a'(1-a)$.) The basis for the connection between the "declaration" of the
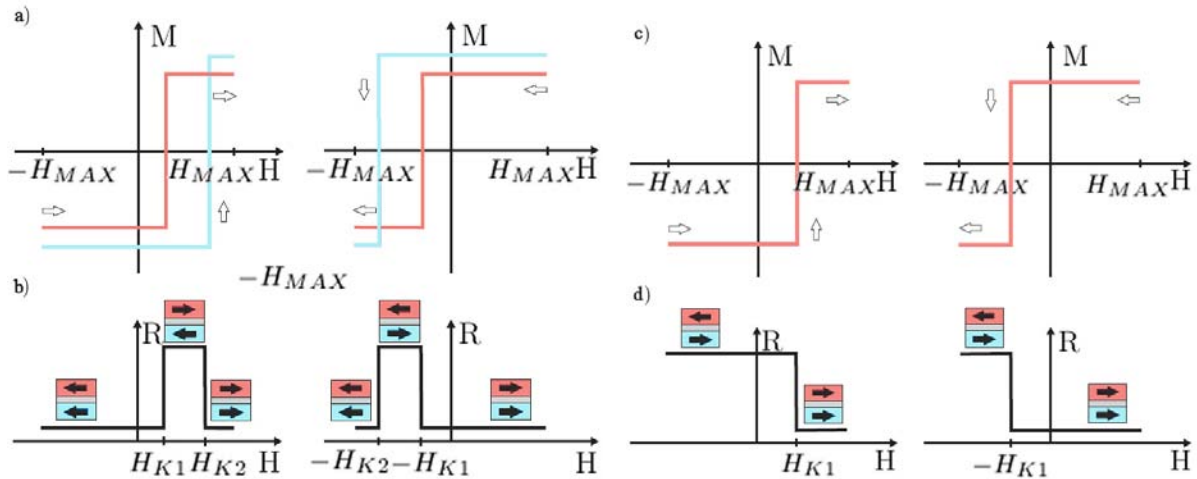
Figure 1.13: Sketch of major (a/b) and minor loop (c/d) of magnetizations of soft (red) and hard (blue) magnetic layer (a & c), with related magnetic orientations of FMs and resulting tunnel magnetoresistance in lower parts b) and d) (after [Mey01, figures 1.2 and 1.3]).

TMR[14] itself and the polarization of spins was the former model of spin polarization by TEDROW and MESERVEY[TM71], and so one speaks of *spin-dependent tunneling* (SDT).

STEARNS[Ste77] pointed out that the transfer probability of electrons depends on the effective electron mass, confer [Mey06, p. 9] (and discussed the role of d-like electrons and the relation to the three-dimensional density of states (DOS)).

In 1989 SLONCZEWSKI[Slo89] introduced the influence of barrier characteristics, which led to an improved formula for the *tunneling magnetoresistance ratio* (TMR):

$$\frac{\Delta R}{R} = \frac{2P_1 P_2}{1 - P_1 P_2} \tag{1.26}$$

with the spin polarization coefficient of electrode $\sigma = 1, 2$[SWN99] and

$$P_\sigma = \frac{k_{\sigma\uparrow} - k_{\sigma\downarrow}}{k_{\sigma\uparrow} + k_{\sigma\downarrow}} \tag{1.27}$$

with $k_{\uparrow\downarrow}$ being the free electron wave vector, identical with the density of states at given energy level (e.g. E_F) and special spin orientation, see [Ash76, p. 44].

Still free electrons were assumed instead of band structure[15], based on Schrödinger equation according to MEYNERS[Mey06, p. 8] and BRATKOVSKY[Bra97].

Improvements were driven by unexpected results, e.g. the negative TMR investigated by SHARMA *et al.*[SWN99], connecting to change of polarization. A last model by

---

[14]According to THOMAS[TBS+03, section 1.1] the original formula by Julliere denotes the "junction magnetoresistance" JMR whereas the TMR is given as TMR $\equiv \frac{R_{AP} - R_P}{R_P}$ instead of JMR $\equiv \frac{R_{AP} - R_P}{R_{AP}}$, see also [Krä04, p. 4]. Because R_P is normally lower than R_{AP} one talks of TMR as the "optimistic value".

[15]See e.g. [Ash76] for basics on band structure.

BRATKOVSKY in 1997, considering "impurity scattering" and "reduced effective mass of carriers inside barrier", looks like this[Bra97]:

$$MR = \frac{G^P - G^{AP}}{G^{AP}} = \frac{2PP'}{1 - PP'} = \frac{R^{AP} - R^P}{R^P} \tag{1.28}$$

Now with the "effective polarization" P:

$$P = \frac{k_\uparrow - k_\downarrow}{k_\uparrow + k_\downarrow} \cdot \frac{\kappa_0^2 - m_{eff}^2 k_\uparrow k_\downarrow}{\kappa_0^2 + m_{eff}^2 k_\uparrow k_\downarrow} \tag{1.29}$$

$$\kappa_0 = \sqrt{\frac{2m_{eff}}{\hbar}(U_0 - E)}. \tag{1.30}$$

M_{eff}, U_0 and E is, respectively, the effective carrier (electron) mass, energy of the barrier, and the energy of carriers, $\hbar = h/2\pi = 1.05459 \cdot 10^{-34} J\,s$ is Planck's constant[Kit86].

Actual models must include several aspects like polarization change[SWN99], influence of defects[Mey06, p. 10 et. seq.], i.e. impurity scattering[Bra97], interface characteristics[Mey06, p. 8 et. seq.] in combination with different materials (in [TBF⁺99] they spoke of dependency of amplitude and sign of the spin polarization), and related band structure which influences the effective electron mass (see [Mey06, p. 9] and [Ste77]). There are still many influences on the TMR ratio, e.g. deals latest research with the Ar-pressure during sputtering, see [SMZ⁺06], so there are "still gaps in understanding"[TBF⁺99].

A short overview of the historical development, used for this section, can be found in [Mey06, section 1.1], and a more detailed introduction gave LECLAIR[LeC02, chapter 2], as well as THOMAS[TBS⁺03, chapter 1], who analyzed in his PhD thesis the influence of exchange bias, oxidation parameters, orange peel coupling, annealing temperature dependence, etc.

1.3.4 Exchange Bias

Exchange bias (EB) appears if an *antiferromagnetic* (AFM) and a *ferromagnetic* (FM) layer, i.e. layers that consist of antiferromagnetic- and ferromagnetic materials, are in contact so that electron spins are aligning antiparallel and parallel respectively. This hinders a free spin-orientation in the FM, so one speaks of that the FM is "pinned" by the AFM. Two prominent methods are used to achieve an EB: In the *field cooling* (FC) the sample is at first heated up in a vacuum-furnace to $T_{N,(AFM)} < T < T_{C,(FM)}$, where temperature must be chosen not too high, which increases intermixing, and afterwards it is important to wait until room-temperature, because the surface could be too reactive. Then it is cooled down in a magnetic field ("cooling field" H_{FC}) which aligns the FM. Due to ferromagnetic coupling at the interface the AFM is also aligned if temperature sinks below T_N, starting at the interface, introducing unidirectional anisotropy, see sketch in figure 1.14. The other way to establish EB is to sputter in the presence of magnets, i.e. applying a magnetic mask, see also section 2.2, so that the magnetization of a layer is aligned during sputtering.

The general result is a shift of the loop in opposite direction to the cooling field, the so called "exchange bias" or H_{EB}, discovered by MEIKLEJOHN and BEAN [MB56, MB57] in 1956, as shown in the right part of figure 1.14. If $T < T_N$ the FMs magnetization is less stable than that of the AFM for certain fields, but due to the ferromagnetic interaction at the interface the FM is stabilized.
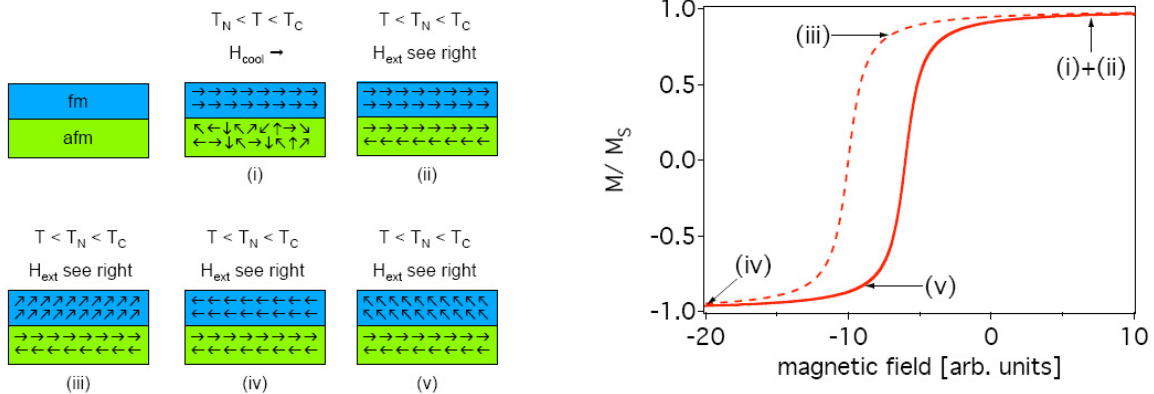
Figure 1.14: Establishing and result of exchange bias via field cooling (here the AFM is ordered in the so called "uncompensated" way, according to the net magnetization at the interface, cf. [Sch04, section 6.1.4]). Taken from [TBS$^+$03, figure 1.5].

By using different thicknesses of FM and AFM one can influence the strength of pinning, resulting in a (relative) hard magnetic or soft magnetic FM layers, i.e. with high or low intrinsic magnetization. The interested reader is encouraged to confer the PhD thesis of ANDY THOMAS[TBS$^+$03, section 3.2] who made calibrations.

Although the principle of exchange bias is used very often there were a few years ago many unsolved aspects[NS99, section 6]. Among other things[16] e.g. the "blocking temperature"[17] $T_B < T_N$ instead of $T_B \approx T_N$[18]. See review from NOGUES and SCHULLER[NS99] for information how to analyze and information on materials and their properties. For a deeper overview of principle and uncertain aspects see the PhD thesis by DIRK MEYNERS[Mey06, section 1.3.2].

---

[16]Unsolved aspects were (a general law for) dependence on thicknesses, spin alignments (perpendicular to surface, compensated or uncompensated AFM, etc.), interface characteristics (roughness, crystallinity, grain size, inter-layers), anisotropy, "training effect", field strength during cooling, and the analysis of coercivity, see [NS99, section 6].

[17]Below the blocking temperature the exchange bias effect vanishes, so normally this should be at the Néel temperature where magnetization disappears due to fluctuating spins, see section 1.1. (This temperature is something different than the former used T_B of paramagnetic material in section 1.2.3; well, in both cases the effect is blocked if the temperature decreases under this threshold.)

[18]The values for MnIr here used are according to NOGUES[NS99]: Ir_xMn_{1-x}, "AFM layer with (1 1 1) texture (a range of compositions have been studied)", T_B=127–247℃, T_N=417℃. In [BG03] for $Ir_{18}Mn_{82}$ these values can be found: T_B=265℃, T_N=417℃.
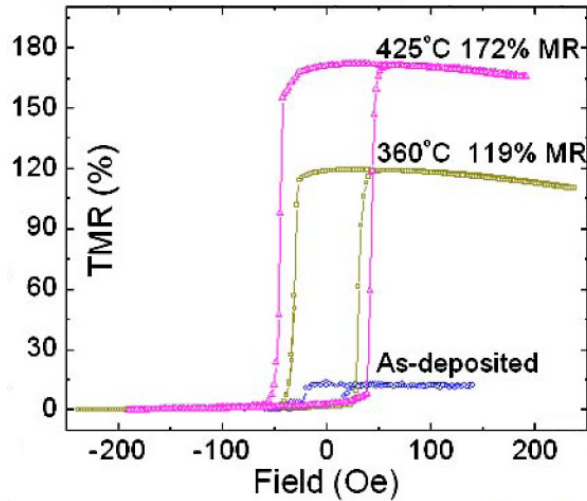
Figure 1.15: Example of MgO which exhibits high TMR only after annealing, taken from [SMZ$^+$06].

1.3.5 Annealing[19] & Field Cooling

The high TMR effects are only possible after special treatment of the sputtered stack: On the one hand the stack must be *annealed* due to heating so that defects can heal and/or a crystalline structure is established. On the other hand an EB is necessary, which can be done by field cooling, as mentioned in the last section. Both processes can be combined and done in a vacuum furnace: A sample is heated for a specific time and then cooled down in the presence of a magnetic field.

An annealing temperature around 300 °C is good for MTJs with AlO$_x$ barrier, because healing of defects in barrier appear up to this temperature[Sch01, section 7 E] and also the distribution of oxygen, which diffusion takes place at grain borders[Sch01, section 6.3.3 A] gets more homogenous. On the other hand diffusion processes start in this regime, e.g. diffusion of Mn, which has an affinity for oxygen, starts at 275 °C according to [TBS$^+$03, section 3.4] and so TMR decreases beyond 275 °C, see figure 1.16. A *ultra high vacuum* (UHV) chamber is needed for annealing to prevent oxidation during annealing.

The applicability of higher temperatures on MTJs can be important for the mass production, which is also a goal for biosensor-applications. Especially it is interesting for the MRAM production, where it is necessary for the backend process[LHI$^+$06].

Relatively high annealing temperatures for stacks with MgO-barriers above the aforementioned threshold of about 300 °C were successfully applied in the first publications by PARKIN (higher resistance and almost the same high TMR with increased annealing temperature up to 400 °C) and also YUASA (annealing at 350 °C at $2 \cdot 10^{-10} \, mbar$!) in 2004 reporting TMR ratios over 200 %[PKP$^+$04, YNF$^+$04].

The use of CoFeB as FM leads also to higher ratios, along with enlarged coercitive

---

[19]also called "tempern"
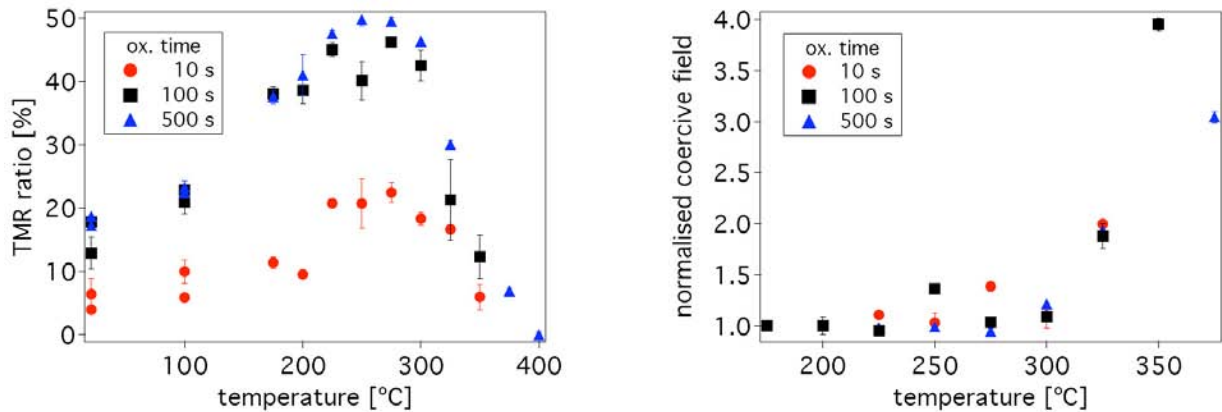
Figure 1.16: SiOx/Cu 30(nm)/Mn-Ir 15/Co-Fe 3/Al 1.4/Py 4/Ta 5 (+Cu 55/Au 20), from [TBS$^+$03, figure 3.13 and 3.15].

fields, compared with CoFe[DTN$^+$05], due to its amorphous structure (CoFe is polycrystalline) after sputtering. For AlO$_x$ barriers this cannot be due to the hampered diffusion of Mn, because the grain boundaries are absent[DGW$^+$04], but maybe because the interface CoFeB/MgO is very sharp, which is visible in figure 1.17, corresponding to little roughness[DTN$^+$05] of the amorphous FM. The result could be that MgO can grow in good order, i.e. texture; another hypothesis is according to DIRK BRINKMANN[Bri], that the amorphous CoFeB leads to an amorphous barrier which is more easily ordered in single crystalline phase, because no domains or predefined structures hinder this process.

IKEDA *et al.*[IHL$^+$05] also made the crystallization of CoFeB, promoted by MgO, responsible for their TMR of 355 % @RT in 2005. For GMR sensor-stacks investigations of annealing temperature on CoFeB layers were published in 1997 byJIMBO *et al.*[JKS$^+$97]: Amorphous as-deposited CoFeB begins to crystallize after annealing at 250 °C, increasing the GMR effect and enlarging coercive field. Above 360 °C the crystallization of CoFeB, with MgO as template, leads to larger coercive fields and the maximal TMR ratios were found for 375 to 425 °C annealing temperature[SMZ$^+$06].

These temperatures fit to the demands for the field cooling: As mentioned in section 1.3.4 the maximum temperature of field cooling is in the range between $T_{B,(AFM)}$ and $T_{C,(FM)}$. For the materials used in this thesis, i.e. MnIr as AFM and CoFe(B) as FM, it is $T_{B,(MnIr)} \approx$ 230–260 °C[SHR$^+$03, FSK$^+$97, BT99] and $T_{C,(CoFeB)} \approx$ 900–980 °C[Car00, Sho05, DJM$^+$04].

1.4 Magnetoresistive Biosensors

In this thesis TMR sensors are used for the detection of magnetic markers with the possible further application as biosensors for the detection of biomolecules. When applying TMR sensors for detection of magnetic beads one should know how successful other approaches are and how they function. So at first an overview on applied magnetore-
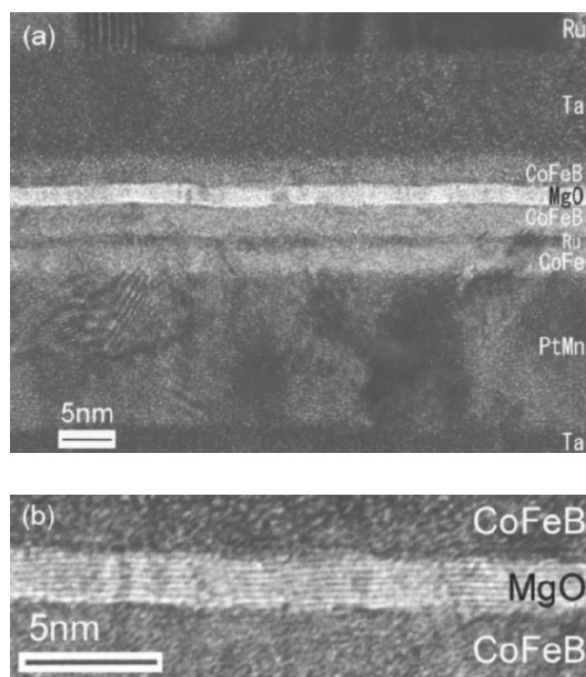
Figure 1.17: high-resolution transmission electron microscopy (HRTEM) of amorphous CoFeB at sharp interface to MgO, which has "surprisingly" good crystalline structure, from [DTN+05].

sistive effects is given, followed by a short discussion of the advantages and necessary characteristics of a biosensor. In the end of this section the actual state of research is mentioned.

1.4.1   Application of MR Effects

Among other things[20] mentioned in the introduction, magnetoresistance is applied in biosensors, which is based on the change of resistance due to magnetic fields. Out of several kinds of MR effects, such as the *ballistic magnetoresistance* (BMR) [GnQ+01, WTN+88], *colossal magnetoresistance* (CMR) [Ram97] or *extraordinary magnetoresistance* (EMR), see [MRMRS03] for recent publications, it is the *anisotropic magnetoresistance* (AMR), *giant magnetoresistance* (GMR) and *tunnel magnetoresistance* (TMR) that are used in biosensors.

Hall sensors In "planar hall sensors" the Hall-effect produces a variation in voltage due to varying angles of effective magnetization M onto a current in the sensor. See

---

[20]Only the "prominent" and convincing approaches are presented. Furthermore the *giant magnetoimpedance* (GMI) and first results from 2005[CTMH05] showed successful response giving rise for an estimated limit of concentrations down to 25 markers/μl, but the sensor is with size of $25 \times 1000 \, \mu m^2$ and a sensitivity of $200 \, \%/Oe$ @2.5 Oe in other regimes than SV, GMR or TMR sensors are. According to SCHOTTER[Sch04, section 1.3] up to 2004 there had been no convincing results.

e.g. [ZYYJ05], where ZHANG *et al.* simulate the influence of a bead, describing also the general principle. This MR effect is called anisotropic magnetoresistance, which is according to BÜRGLER[BG03, section 4.1] "the dependence of the electric resistivity on the angle between the current and the magnetization direction. AMR is a volume effect discovered in 1857 and applied in read heads since the 1970's."

Giant Magnetoresistance Many applications use the GMR, such as sensors and hard disks, where the giant[21] magnetoresistance effect can be observed in a "sandwich system" consisting of FM/NM (non metallic)/FM, when a voltage is applied perpendicular (*current perpendicular plane* CPP) towards the stack, as in TMR stacks, or also current applied in-plane (*current in plane* CIP). The amplitude of this effect is defined with respect to the resistance as in equation 1.28. An overview on GMR theory and its historical development is given in e.g. [Sch04, section 5.1][22].

Spin Valves Several approaches use almost the same layer stack as in "normal" GMR sensors, but one pinned FM via EB (AFM/FM/NM/FM) so that there is one hard and one soft magnetic layer (see [BG03, section 4]). The result is an antiparallel alignment of the FMs after passing zero field in one direction due to the hysteresis effect by the harder to switch pinned layer. In GMR stacks the antiparallel alignment at zero field is contrary achieved by appropriate FM thicknesses, i.e. by IEC as mentioned above. A short review can be found in [Coe99].

1.4.2 Detection of (Single) Beads

A detailed overview on biosensors etc. is given by SCHOTTER in his PhD thesis[Sch04, chapter 1] and MEGENS and PRINS[MP05] gave an overview of SV and GMR sensors. Here are some examples, with the focus especially on the detection of single beads.

AMR/Hall sensors:
JIANG *et al.*[JLMB06] reported in 2006 of an integrated microfluidic cell (IMC) consisting of AMR sensors of $18 \times 4.5 \, \mu m^2$ or $\varnothing 10 \, \mu m$ ring arranged in Wheatstone bridge configuration combined with microfluidic channel. Sensors show $0.5 \, \%$, linear between 22 and $77 \, Oe$, expecting that it should be possible to detect $9 \, \mu m$ ferromagnetic beads (from Spherotech™).

Already in 2002 BESSE *et al.*[BBD+02] were able to detect a single bead ($\varnothing = 2.8 \, \mu m$) using a silicon Hall sensor ($2.4 \times 2.4 \, \mu m^2$). In 2005 MIHAJLOVIĆ *et al.*[MXvM+05] reported for an "InAs quantum-well micro-Hall sensor" the successful detection of single

---

[21]The name derives by comparison with the AMR, see e.g. [BGSZ89].

[22]First papers were published in the late 80's by BAIBICH[BBF+88] and BINASCH[BGSZ89]. The simplified basics are spin-dependent scattering of electrons, where spins oriented parallel to the magnetization in FM experience less scattering contributing to lower resistance. Magnetization of FMs itself is described with the *interlayer exchange coupling* (IEC), also called "oscillatory interlayer coupling", discovered in 1986 by GRÜNBERG [GSP+86]. It is based on the RKKY-coupling ("Ruderman-Kittel-Kasuya-Yosida", after early publications in the mid 1950's in three publications [RK54, Kas56, Yos57]) transmitted by spin polarized electrons in the non metallic interlayer, which is oscillating between ferromagnetic and antiferromagnetic coupling of adjacent FM layers.

beads using lock-in amplification and assessed the employment of such Hall sensors for detection of $10\,nm$-nanoparticles if the senors are minimized. They point out characteristics like wide ranges of linearity and no saturation at relative low fields, with equal sensitivity compared to magnetoresistive approaches.

GMR sensors:
Also for GMR biosensors exist several publications of successful setups, e.g. the so called "BARC biosensor" in 2000 by EDELSTEIN[ETS$^+$00] or in 2004 by SCHOTTER[Sch04].

SV sensors:
In 2003 LI *et al.*[LJW$^+$03] published the detection of $2.8\,\mu m$ beads with a sensor of 2.5–$3\,\mu m$, and suggested achievable detection of 1–$10 \sim 11\,nm$ Co nanoparticles with miniaturization ($200\,nm$ sensor), encouraged by micromagnetic simulations (see page 40). One year earlier GRAHAM[GFB$^+$02] also reported the detection of single beads.

TMR sensors:
SHEN[SLMX05] was able in 2005 to measure single magnetic beads (superparamagnetic γ-Fe$_2$O$_3$, $2.8\,\mu m$ in diameter) using $2{\times}6\,\mu m^2$ elliptical MTJs with Al$_2$O$_3$ barriers with realtime measurements in a fluidic system.

A new task comes up with the miniaturization: (single) beads must find the tiny sensors. Therefore exists the solution of using on the one hand a whole array of TMR sensors[SLMX05] (maybe with a logical output) or on the other hand the usage of small amounts of sensors and guide the beads in a fluidic system (successful applied by SHEN[SLMX05] and also a research topic in our group[Scha]).

One can also use single sensors and catch single/a few beads with conducting lines, as presented by PANHORST[Pan05, chapter 5 and 6]. The beads are collected in the edges of those lines visible in figure 1.18[23]. This method has the advantage, that only magnetic material is collected for sure.

Another way can use sinks in the surface in order to position single beads, like it has been done by GORDON and PEYRADE, see [GP06]; they structured squares, triangles and rectangles with e-beam lithography in resist (200–$400\,nm$) and due to capillary force assembly and different stickiness they achieved exact positioning of one to four nanoparticles (Au $\varnothing 50$ and $100\,nm$) due to a specific evaporation rate, see figure 1.19.

1.4.3 Characteristics

A good sensor must be sensitive and has a reproducible signal. With respect to the MR effect these important necessities favor a signal curve which has a high and constant slope $[\%/Oe]$. Furthermore is no hysteresis desirable, so that a certain point of resistance can be used for measurements. As a third aspect the *signal-to-noise ratio* (SNR) must of course as good as possible, but this is in all approaches so far only achieved with signal enhancement, which is an universal disadvantage for the integration and built up of a lab-on-a-chip.

---

[23]A video is available online at www.panhorst.com/PhD/TMR/Optical.html.

(a)   (b)
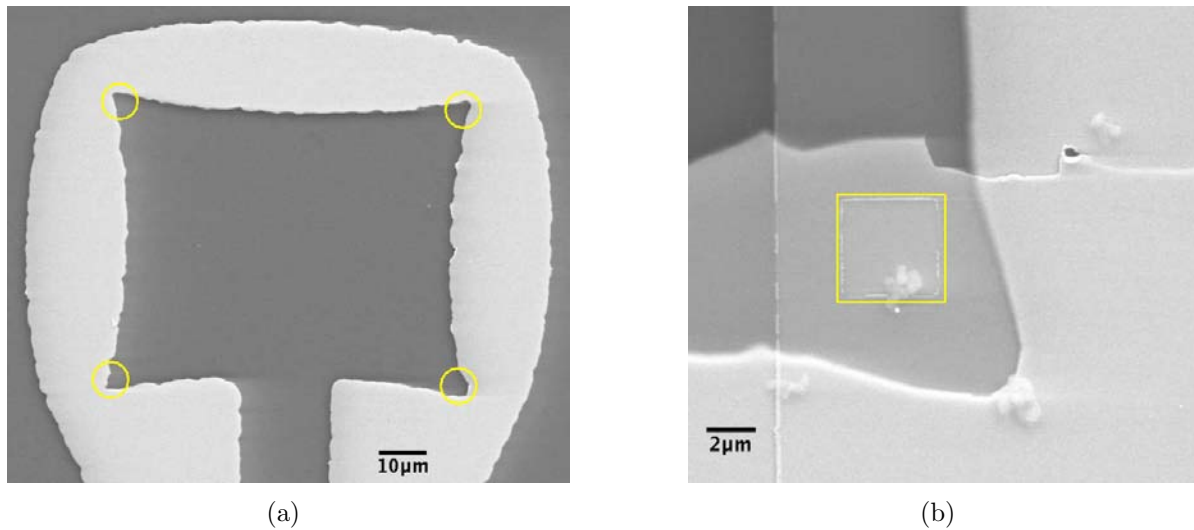
Figure 1.18: (a) Design of a conducting line for collecting beads at the four inner corners. (b) Example of a single $\varnothing 1.5\,\mu m$ MICROMOD bead on a $4\times4\,\mu m^2$ TMR sensor. (SEM images after [Pan05, figure 5.2 and 6.10b].)

Exemplary the characteristics of the successful applied sensors of SHEN[SLMX05] are given to see which range of sensitivity works. The sensors show typical 15.3 % TMR, with sensitivity of 0.4 %/Oe @"0-15 Oe" applied in-plane, which is at least as good as other approaches. It was necessary to use an AC bridge configuration combined with lock-in technique to enhanced the signal. That leads to a SNR of 16 (i.e. $24\,dB$[24]). This SNR is a little bit better compared with the referred work of LI[LJW+03] who gained up to a factor of 12 ($22.1\,dB$) for SV sensors, but was not able to already measure single beads. Those factors are not that important, e.g. SHEN's value was topped by the Hall sensor from MIHAJLOVIC[MXvM+05] with SNR of 19 ($25.6\,dB$), but it was not able to detect single particles.

The total values of sensitivity have to be mentioned with the field range they can used with, i.e. a low slope in a wide field range is in general as good as a high constant slope at small fields. For the application in a lab-on-a-chip the former case should be favorable, because with integrated conducting lines or small coils it is possible to apply a small local field for measurements. For SV sensors VAN DIJKEN mentioned in 2005[vDC05] a value of 0.0018 %/Oe @$\leq$500 Oe. Latest TMR stacks by JANG[JNK+06] showed in 2006: 0.0047 %/Oe @$\pm$150 Oe (0.7 nm CoFeB), but 0.433 %/Oe @$\pm$30 Oe (1 nm CoFeB). For the detection of single beads by SHEN[SLMX05] in 2005 a sensitivity of 0.4 %/Oe @"0–15 Oe" was enough.

The important role of the specific curve characteristics can be seen in [Sch04, p. 112-114]: SCHOTTER had 0.136 %/Oe with spiral shaped GMR sensors and maximum 24 %/Oe or 0.24 %/Oe with circular shaped TMR sensors for parallel and perpendicular

---

[24]Calculation of decibel: $V_{dB} = 20 \cdot \log\left(V_{\mathrm{signal}}/V_{\mathrm{noise}}\right)$.

(a)   (b)
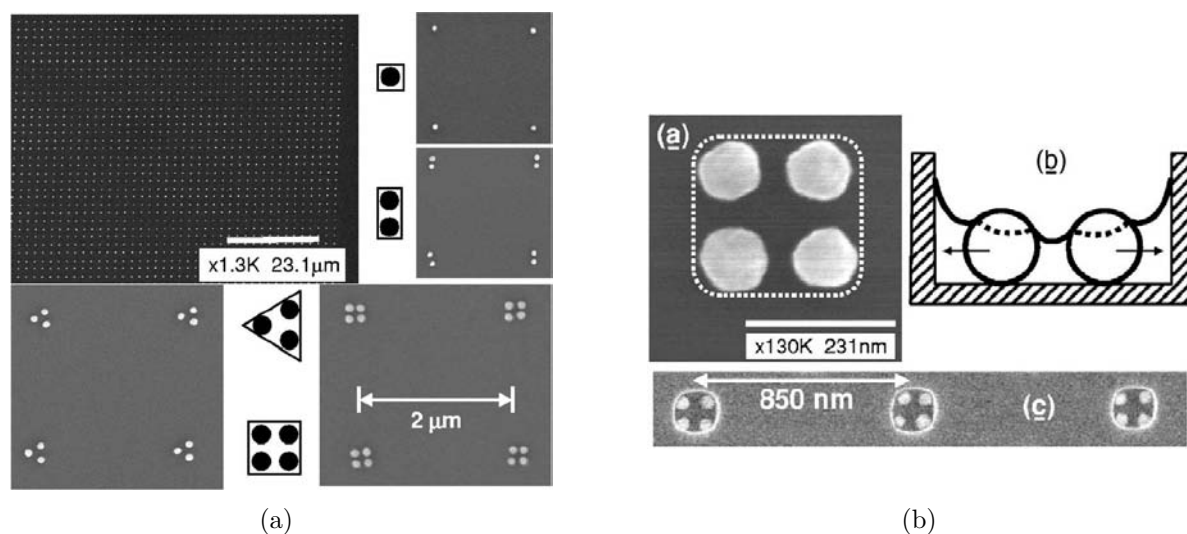
Figure 1.19: Positioning by using sinks in PMMA:
(a) "Highly controlled pattern filling can be achieved over very large areas of $100 \times 100 \, \mu m^2$ and different hole geometries [...] allow one-, two-, three-, and four-particle groupings to be created." (Taken from [GP06, figure 1c].)
(b) "(a) Isolated Au NPs [nanoparticles] ($100 \, nm$) after template removal (dashed square). (b) Probable free surface of the liquid in the pattern which leads to particle separation. The overall tilt of the particle contact line results in a net lateral force toward the wall and corners. (c) $50 \, nm$ Au NPs in the resist template, demonstrating particle preference for the pattern corners." (Taken from [GP06, figure 2].)

fields towards pinning direction, respectively. So at the first glance the TMR sensors with the former saturation alignment (parallel to pinning) are much better than for the latter case, but they can not be used for detection because the maximum sensitivity is only a sharp peak besides zero applied field (see [Sch04, p. 111 and figure 91b]).

Perpendicular Pinning

A separate pinning of upper and lower FM twisted by 90° in-plane to each other should be good for linearity and reversibility, without hysteresis, confer [Sch04, section 6.6] and [JNK⁺06]. In the latter article different approaches are mentioned, like "specific circuitry, shape anisotropy in the sensing layer and combining the use of step bunched substrates with exchange biasing of the sensing layer"[JNK⁺06] to get perpendicular pinning. Each approach has a "complicated sensor design" as a drawback which hinders the integration in Si-chips and the usage in a low power consuming setup. But according to van Dijken[vDC05], who used perpendicular magnetization out-of-plane towards the sensing layer in SV sensors, in general SV and MTJ approaches with *perpendicular pinning* should be good to get the required hysteresis-free signal.
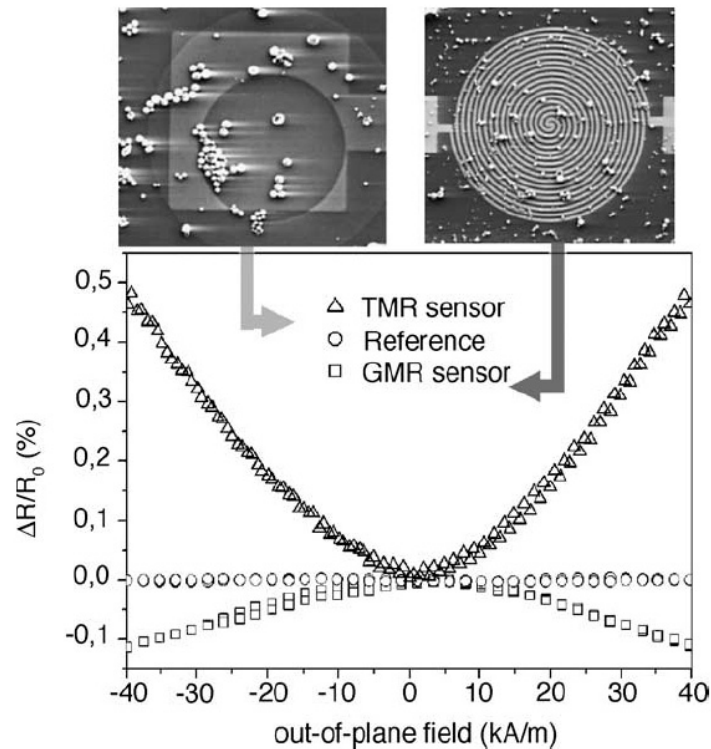
Figure 1.20: Comparison between GMR and TMR signal of sensors, showing the intrinsic higher sensitivity of the latter ones (from [BJS$^+$04]).

Comparing GMR and TMR sensors

Although GMR sensors were already successful used for detection of biomolecules, see 1.4.2, research is done on TMR sensors and therefore exists good reasons. Sensors based on the TMR effect should yield in general a higher effect (see section 1.3.2) which means steeper curve which (can) result in higher sensitivity, but one has to consider also the measurement regime, i.e. whether compared with other approaches the same magnitudes of fields can be applied to measure in the most sensitive field range.

SCHOTTER [Sch04, chapter 7] made a "Comparison of GMR- and TMR-type magnetic biosensors", with the result, that GMR sensors are a good choice "for gene expression type experiments, which require the simultaneous large scale detection of different DNA sequences at relatively high concentrations well beyond the single molecule regime." Their relative big size fits to such tasks, which leads furthermore to the advantage of easier fabrication and handling (high currents, robustness) than TMR sensors had. With sensitivity in view SCHOTTER finds that TMR sensors are not much better than GMR sensors, although they have a higher net sensitivity with respect to noise level and magnitude of response (see also figure 1.20). The latter aspect is true also of TMR sensors in comparison with SV sensors: WANG *et al.*[Wan05] simulated the response of a MTJ ($1 \times 0.3 \, \mu m^2$) to a single magnetic marker (10-100 nm), see article for

more details, and found that the "level of output is about ten times larger than a SV sensor with the similar specifications" has. The measurement regime is unfortunately limited to avoid "irreversible and hysteretic processes"[Sch04, p. 104]. For the detection of single molecules TMR sensors should be the leading choice, with respect to the needed miniaturization of the sensors down to the size of markers (calculated for GMR sensors in [TPL00]) and the minimum detectable number of beads (in [Sch04, sections 5.5, 6.6] it is 100 for GMR and 20 beads for TMR sensors). Also the aspect of resistance favors TMR because for these sensors the resistance increases naturally with miniaturization which makes measurements easier, see also [BJS+04]. Furthermore the CPP geometry of MTJs makes the integration into high-density sensor arrays possible[SLMX05]. Such arrays can be used for examination of position and movement of particles with a good accuracy, probably in combination with gradiometry methods.

Comparing AlO_x and MgO Tunnel Junctions

The already achieved TMR values using MgO as barrier material ($>400\,\%$[YFK+06]) are superior to those using AlO_x ($70\,\%$ according to [SMZ+06] and [NHT+05]), and theoretical calculations encourage hope to get even more, see section 1.3.2. The latter sensors were already successfully employed for detection of single beads[SLMX05], so MgO sensors can provide even better characteristics with respect to the TMR ratio. If one can use the high TMR ratios of MgO barriers in sensors which have a smooth curve without hysteresis, the sensitivity should be higher than for AlO_x sensors.

The superiority of MgO is nevertheless not given automatically, because as mentioned above, the higher slope of the signal must coincident with linearity and no hysteresis. On the way to higher TMR ratios these aspects are not important. So the preparation of a MgO stack with extraordinary high TMR ratio maybe has to be modified in order to get a signal with good characteristics for the application as a sensor. This can result in a less steep signal which reduces the advantage or even makes it worse than a good AlO_x stack.

1.5   Thin Films

There are many aspects concerning thin films, based on energies and forces between electrons and other elementary particles, based on the spin and wave-functions, which are in combination with the lattice and deduced band structure responsible for their behavior giving materials characteristics. An introduction with respect to mathematical background of spins and wave-functions is given by ASHCROFT and MERMIN [Ash76]. The behavior of thin films[25] can differ very much from bulk material giving rise to many

---

[25]There is no special/official threshold for speaking of "thin layers" and there is no big border to "normal life", so as mentioned in the historical section in [Ohr02] even the Egyptians were able to produce leafs of $300\,nm$ in thickness and today gold can be beaten by hand down to $50\,nm$ (by machines $100\,nm$), which is used e.g. to cover statues in churches with smallest amounts of gold (e.g. in the "Marktkirche" in Paderborn the whole statues of the altar with an area of $22\,m$ in height and a width of $12\,m$ excluding pictures are covered with $>375\,g$ gold, plated into sheets of $8 \times 8\,cm^2$ with an alleged
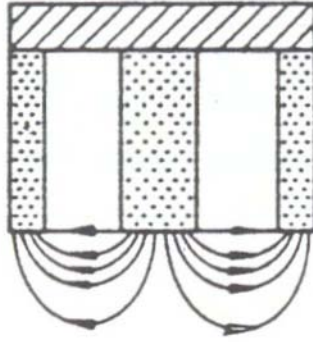
Figure 1.21: Principle of the used magnetron setup. [Ohr02, p. 228, figure 5-10]

new aspects so that only a few are mentioned here which belong to the presented topic. The following sections begin with the used deposition technique, the way thin films are growing and adhere to each other, as well as the role of magnetic domains of little structures, related to their size and shape, and energy related aspects.

1.5.1 Magnetron Sputtering

Plasma sputtering with Ar has advantages like the usability of alloy-targets, e.g. used for MgO, relative low temperature, good adjustable deposition rate and deposition of fine target material. Reactive sputtering in presence of a working gas, confer [Ohr02, section 5.2.5], makes it possible to deposit oxides, nitrides etc., e.g. with oxygen one gets Al_2O_3 out of pure Al. In [Ohr02, chapter 4] details and advantages of plasma sputtering are described and section 5.3 in OHRING[Ohr02] deals with the commonly used "magnetron sputtering".

In magnetron sputtering magnets are placed under the target to form a magnetic field which on the one hand catch nearby electrons aside the target, guiding them above the target, and on the other hand force the electrons on a spiral trajectory. So they remain longer near the target where many of the Ar-ions are located which results in a drastically increased number of ions. Therefore further more target material is ablated by the Ar-ions and deposited on the sample.

1.5.2 Adhesion

In the stack layout used in this thesis, see section 3.2.4 and 5.1, the adhesion plays an important role when glass (SiOx) is the next or former layer to a metal layer, such as Cu or Au. According to OHRING[Ohr02, section 12.7(.4.1)] the experience indicates that an

thickness of $>125\,nm$[Nüb04]);

"Thin films" means in the relation with domains a thickness of e.g. $<80\,nm$ as a typical value for polycrystalline Permalloy [HS98, p. 450]; the layers which are used in this thesis are in the range of 1 to $100\,nm$, see chapters 4 and 5.

oxide layer between glass and metal "glues" them together with the help of oxide bonds, so that highly oxidizing metals like Cr, Ti, Mo and Ta are sputtered in between. A thin "glue layer" of approx. $5\,nm$ of the latter metal has proven good results in our group. For adhesion in general see e.g. [Cha74] who gave a review in 1974 and discussed problems when speaking about adhesion and enhancement of it: The difficulty (in the past) was first of all that it depends on the viewpoint, i.e. academic or technological background, whether an aspect is a problem at all, and the lack of an exact definition what "adhesion" is, which could make different measurements techniques comparable.

Among those glue layers the adhesion can be also increased due to cleaning of substrate surface, heating of substrate, thin intermediate layers , especially with the aforementioned fast oxidizing metals, so called "bias sputtering", where a negative potential is applied to the substrate, or ion bombardment during deposition of material, the so called "ion plating". References for those methods and the role of energy of ions at the surface are given in [Cha74, section 7], see also [Ohr02, section 12.7.4.2].

1.5.3   Domains

Domains are areas with the same direction of magnetization inside, but differing to their neighbors. They are separated by domain walls, the most popular called *Néel walls* and *Bloch walls*, where the orientation of the magnetization changes using different ways.
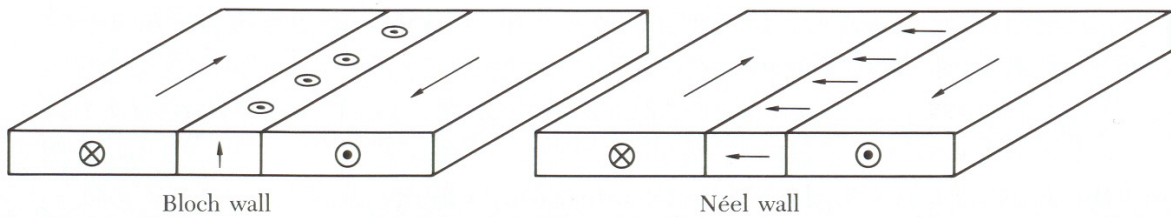
Figure 1.22: Sketch of Bloch versus Néel wall, with more or less smooth transition in real. From [Kit86, p. 460, figure 15.37].

In Néel walls magnetization is twisted in the layer, i.e. in-plane, therefore avoiding stray fields by perpendicular orientation, and so in thin films they are preferred. Conversely in Bloch walls the change is going on perpendicular to plane of magnetizations as seen in figure 1.22. These two kinds are the famous walls out of a large family of walls: Several kinds of "Néel walls" are distinguished, e.g. 90°, 180°, 360° walls, in addition to the normal symmetric one, and in Bloch walls exist substructures like "Bloch lines", not always based on energy minimization [HS98, section 3.6.5]. Other wall-types are e.g. *zigzag wall* or *cross-tie wall*[HS98, p. 236 & 240], visible in figure 1.23.

Néel walls will appear instead of Bloch walls if thickness of film is similar to width of possible Bloch wall, see equation (1.31) according to [HS98, p. 239]. It is

$$\text{Bloch wall width} \sim \sqrt{A/K} \qquad (1.31)$$
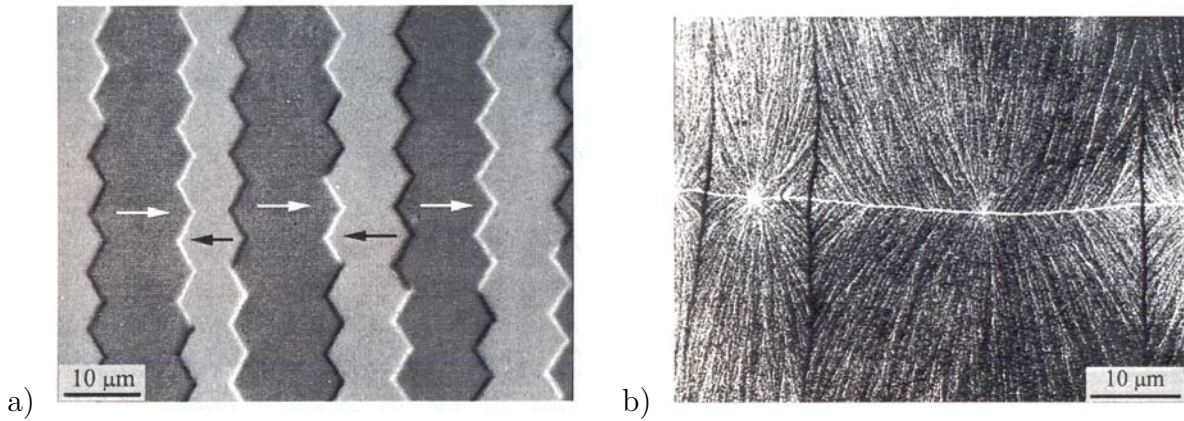
Figure 1.23: Examples for walls: a) zigzag [HS98, p. 236, figure 3.69] and b) cross-tie wall [HS98, p. 240, figure 3.74].

where A is the "exchange energy" and K is the anisotropy-constant, see [HS98, p. 153], but the width of the Bloch walls is not uniformly set, according to [HS98, p. 219] there are four definitions of the width.

Examples for different arrangements of domains are visible in figure 1.24: "stripe domains" (figure 1.24a), "bubble domains" (figure 1.24b), "closure domains" (figure 1.24c), "Néel blocks" (figure 1.24d) or "(fir-)tree pattern" (figure 1.24e).
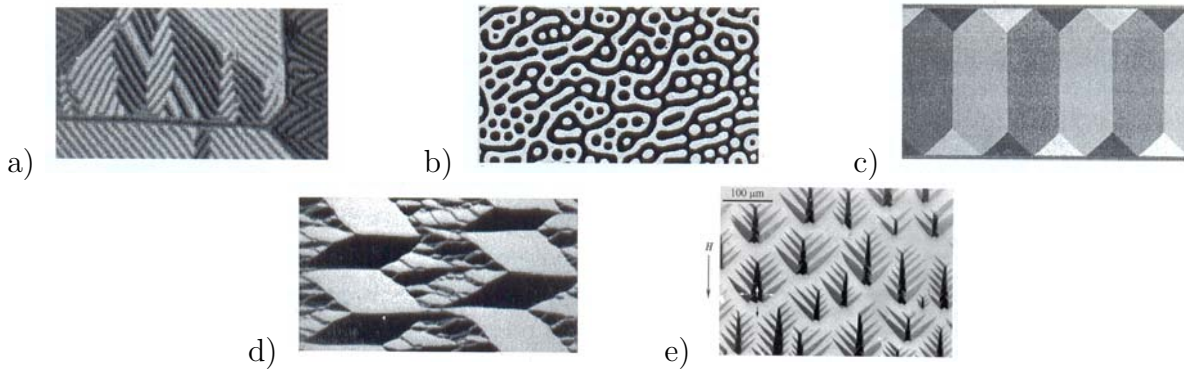
Figure 1.24: Examples for domains: a) stripe, b) bubble and c) closure domains, d) Néel blocks [HS98, p. 291] and e) (fir-)tree pattern [HS98, p. 297, figure 3.107].

Mobility of Domains and Walls

The higher the applied magnetic field H_a, the higher is the magnetization inside various areas of a material, but the basic events can be different[Kit86, p. 448 et seqq.], see figure 1.25. If H_a is small the better aligned domains grow even if their direction is not parallel to H_a, whereas for high H_a the magnetization changes its direction to get
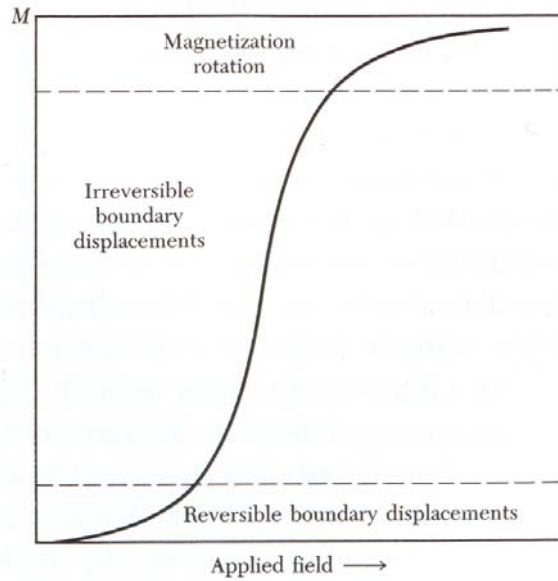
Figure 1.25: Movement of domains depends on applied field strength. [Kit86, p. 449, figure 15.28]

parallel to the outer field. The change of magnetization is possible via moving walls (easy way), typical for soft magnetic materials like NiFe, or changing direction/rotation of whole domains, e.g. in hard magnetic NdFeB, see [HS98, sections 3.6.6–3.6.8] for more information on wall motion.

In this context should also be mentioned the phenomenon of *magnetostriction*, i.e. change of volume of macro-structures with changing domain configuration which is sometimes even audible.

Those aspects are important e.g. in the case of transformers, where the core should have no domains to prevent energy loss during the magnetization cycle, or in permanent magnets, confer section 1.2.2, where a high anisotropy is useful, which is served especially by the rare earth metals in combination with Mn, Fe, Co and Ni, e.g. $SmCo_5$ or PrFeN [Kit86, p. 455 et seq.]. In "Magnetic Domains"[HS98, chapter 6] a whole chapter deals with the "Relevance of Domains" in sensors, memory media and heads, etc.

The size and shape of the domains are important, see e.g. a long Fe particle: Higher coercivity H_c is gained due to hindered rotation by shape-anisotropy[Kit86, p. 456]. According to MEYNERS *et al.* [MBR03] and BRYAN[BAC04], boundary roughness is important, because walls are pinned at clefts, so that a loop/switching field is less symmetric due to jerky moving walls and maybe increased number of domains, and steps in loop due to annihilation of edge domains.
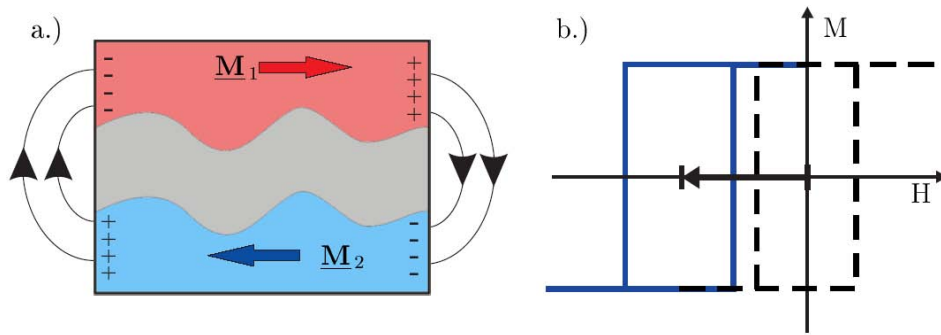
Figure 1.26: Sketch of stray field coupling, by MEYNERS[Mey01].

Single domains

Especially for sensor elements and the application in logic gates, confer [Mey06, p.29], structures with only one domain are important, because they should show a reproducible switching behavior, without the just mentioned steps in measurement curves, and serve maximal TMR amplitudes. "Stoner-Wolfarth-asteroids" characterize single domain particles[26]: The asteroid appears more symmetric and with sharp borders, the better the domain configuration is, i.e. single domain state, confer [LTA+99].
With respect to the energy minimization, an overview follows at once, only in tiny structures single domains can appear, but it is not easy to give a limiting size, e.g. for NiFe the theoretical threshold is about $1\,\mu$, but separate calculations for Fe and Co gave different results from various groups, going down to the range of $30\,nm$[Mey06, p. 29].

1.5.4 Stray Fields and Néel Coupling

These two aspects are important contributions towards energies and play an important role for energy minimization; more aspects are mentioned in the next section. Stray fields occur at the surfaces of magnetic materials. Minimization of the stray field energy leads to antiparallel aligned adjacent layers as seen in figure 1.26, due to *stray field coupling*. *Néel coupling*, also called *orange-peel coupling* (referring to [BG03]), is an interface effect at magnetic layers separated by a thin nonmagnetic interlayer. Depending on the interface roughness which shrinks the gap between the layers, the magnetization in the magnetic layers aligns parallel, i.e. ferromagnetic, as depicted in figure 1.27. For a deeper view the reader is encouraged to look in [Mey06, section 1.3.1].

Both effects lead to a shift in the measurement loop, but due to the different alignment they are working against each other: Néel coupling has positive $H_{\text{Néel}}$, but stray field coupling has negative H_S as seen in figure 1.28.

---

[26]A Stoner-Wolfarth-particle is indeed introduced as a particle with one domain.
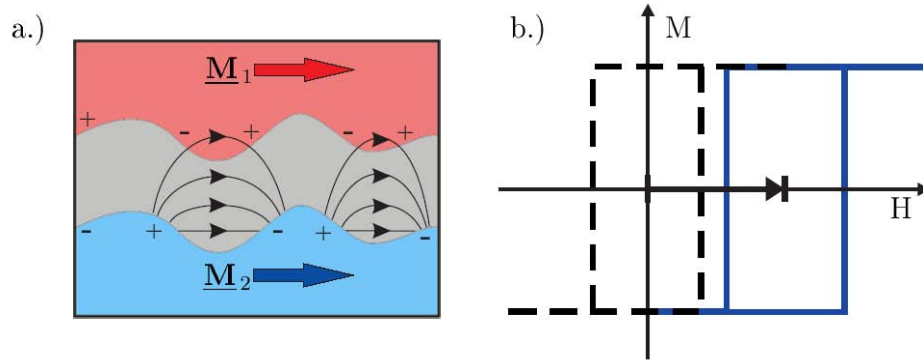
Figure 1.27: Sketch of Néel (or orange peel) coupling, by MEYNERS[Mey01].
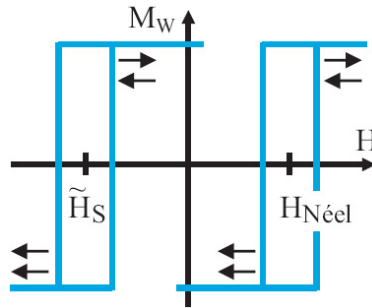
Figure 1.28: Shift of Néel coupling $H_{\text{Néel}}$ versus stray field coupling H_S, by MEYNERS[Mey06].

Energy Aspects

The building of domains and the selection of separating walls and their dimensions is (often) driven by "minimization of energy", especially decreasing stray fields. LANDAU and LIFSHITZ realized in 1935 that this general principle is a leading factor[HS98]. A handful of energies are important for the formation of domains and the appearing domain walls, see [HS98, section 3.2] or [Mey06, section 1.2]:

Zeeman energy $(\equiv \sigma_{zee})$ Origin is the tendency to align parallel to the outer field, also called "applied field energy"[HS98]

anisotropy energy / magnetic crystal energy $(\equiv \sigma_{anis})$ Magnetization tends to align with easy magnetization direction, also called *easy axis* (EA).

exchange energy $(\equiv \sigma_{exch}$ On the basis of spin-orbit interaction less variation of spins is favored.

(non-local) stray field or dipole energy $(\equiv \sigma_{stray}$ or $\sigma_{dip})$ In figure 1.26 is shown how a dipole region leads to a stray field on the surface which helps to form a second antiparallel aligned dipole to get a closed magnetic cycle. So this is contrary

to the aforementioned Néel coupling, and it is stronger for smaller structures, see [Mey06, p. 26]

According to [HS98] several other contributions exist, e.g. the "magneto-elastic (interaction) energy", a "stress field of non magnetic origin", and the "(non-local) magnetostrictive energy" based on "elastic interactions of regions".
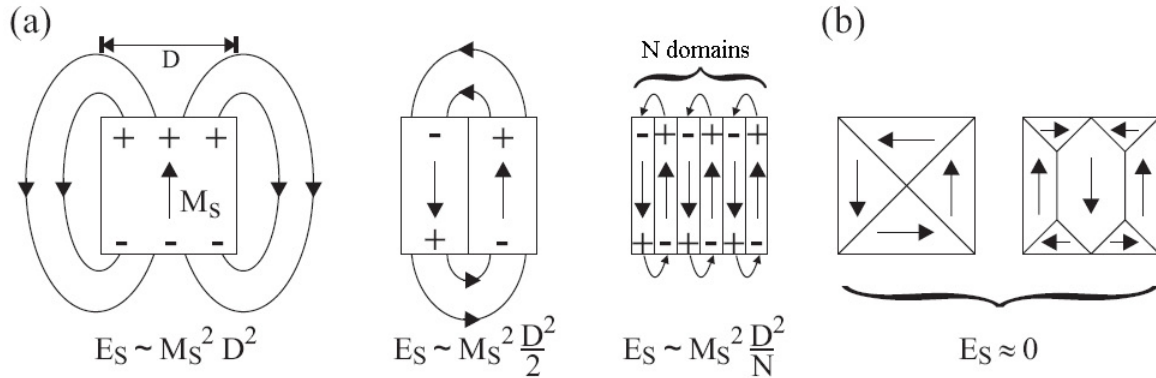
Figure 1.29: Splitting into domains due to energy reasons: a) stray field energy $E_S \sim 1/N$, b) closure domains lead to energy minimization (sketch by MEYNERS [Mey06], translated).

Energy minimization of total energy $\sigma_{tot} = \sigma_{zee} + \sigma_{anis} + \sigma_{exch} + \sigma_{stray}$ is the goal and therefore the formation of domains can be influenced as following:

- The size of walls is limited by the anisotropy energy, otherwise the exchange energy would try to broaden walls as much as possible.

- Splitting into N domains reduces magnetic stray field energy with factor $1/N$, figure 1.29a [Kit86, p. 455] ,but walls cost also energy, which limits the number.

- Aligning parallel to border[27] as shown in part b of figure 1.29 leads to closed circuits which reduces the magnetic energy almost to zero, called "Landau-Lifschitz configuration" [Mey06, section 1.4.3].

- Tiny particles of about $<$10-100 nm square have single domains, because a closed circuit is not applicable; the change of magnetization is not possible via wall-movement, but due to whole change, see Kittel [Kit86, p. 455 et seq.].

- For thin films with thickness $<$10 nm only Néel walls are favored due to their in-plane change of magnetization, avoiding out-of-plane stray fields (see also next section).

It is hard to analyze all those energy contributions, and the approach to use quantum physics is not applicable because too much "ingredients" play a role. The way out are

---

[27]Such domains are also called *closure domains* in [HS98, p. 315], a special kind of surface domains.

"micromagnetic simulations": The probe is divided into small cells, so that it is possible to average over enough magnetic vectors to get rid of quantization. Classical calculations are applied for each cell's magnetization (vector), starting with a magnetization configuration, followed by iterations until a certain minimum of energy is reached. Confer [Mey06, section 1.4.4] for a short overview of the principle and [Mey01, section 2] for applying simulation software and discussion of several contributions to micromagnetic equations. Additional historical information can be found in [SSBR04a, section 2], and last but not least see [HS98, section 3.2.7] for further details.

1.5.5   Shape Anisotropy

In small long structures the magnetization can align parallel to the long dimension, i.e. the EA, although no external field is applied. This *shape anisotropy* effect is based on the prevention of stray fields. In literature normally a threshold ratio of 1:3 is used to be sure that shape anisotropy is working[Rot]. In experiments a lower limit down to 1:2 was successful working[Rot], so a reduced ratio below 1:3 could also be working[Mey].

According to simulations by Liou *et al.*[LSJ+01] a lower aspect ratio leads to stable domain configurations which are less effected by edge roughness. Experiments done by Bryan *et al.*[BAC04] showed no variation of coercivity for elements of approx. $0.2 \times 4\,\mu m^2$, but for particles with a width of $180\,nm$ and aspect ratios from 2.37 to 8.1 Smyth *et al.*[SSF+91] ascribed the increase of coercivity and remanence to the increased shape anisotropy for higher aspect ratios. So for tiny elements in the submicron regime a shape anisotropy can be expected. Contrary Van Bael *et al.*[VTMB99] investigated even for tiny elements of $360 \times 540\,nm^2$ (aspect ratio 3:2) two-domain states having two orientations, non of them favored. With respect to this result there are two reasonable options for achieving a shape anisotropy with single domains: One should use elements smaller than $360 \times 540\,nm^2$ or a shape with increased aspect ratio can be used.

Chapter 2

Machines[28]

2.1   AFM

The available *atomic force microscope* (AFM) is a Multi Mode™ Scanning Probe Microscope from Digital Instruments (DI)[Dig]. See e.g. the "Scanning Probe Microscopy Training Notebook" by DI[Dig00] for general principle of machine and measurement techniques, as well as use and functions of standard software; details of the setup can be found in [TBS+03, section 2.4]. Measurements in this thesis are done in "tapping mode", and with a magnetic tip also *magnetic force microscopy* (MFM) is possible.

2.2   CLAB and another sputter tool

The UHV magnetron *sputter* system CLAB 600 (Clustertool) from Leybold[Ley] contains an oxidation-, loading-, changing- and sputtering-chamber. The latter one has (according to [Pan05, section 2.1]) six 4 inch targets, including 1 RF for e.g. MnIr, 3 normal DC and 2 special DC for ferromagnetic materials, and one 2 inch target (Au or Ru) operated at a base pressure better than $3.5 \cdot 10^{-7}\, mbar$. As a magnetron a rod magnet is placed below the middle of the target and a ring magnet serves the corresponding magnetic pole near the border, see figure 1.21 for principle. The handler system has a load lock with 8 places for 4 inch sample holders. A sputter process can be done fully automatically. For each layer the parameters have to be chosen such as material, deposition time, Ar flow and Ar pressure, as well as energy setpoint of power supply for target. Ar pressure is set via so called "throttle position" which sets a valve before main turbo pump; lower throttle position [%] means higher pressure, normal is $21\% \approx 1.2 \pm 0.1 \cdot 10^{-3}\, mbar$[Dre06], power is normally 50–60 or $115\,W$ for testing and $115\,W$ as setpoint during sputtering, depending on the material. The parameters for the 2 inch target are $29\,W$ and $20\, sccm$[29] Ar-flow with varying throttle positions: Au

---

[28]The order is simply alphabetically, without respect to the importance for this thesis. A full list of available machines in our group can be found on www.spinelectronics.de.

[29]sccm: *standard cubic centimeters per minute* of gas at standard parameters.

Figure 2.1: CLAB 600 – main chamber and load lock. (Taken from "D2 – lab tour" at www.spinelectronics.de.)

$3\% \approx 2.4 \pm 0.05 \cdot 10^{-3}\,mbar$[Dre] and Ru 7% ($\approx 9 \cdot 10^{-3}\,mbar$; estimated from [Dre06, figure 2.1]). Thickness is given by the sputtering time and an offset for the movement of the shutter, which shields normally the sample from the targets, in combination with a calibration depending on the material and target position, as well as sputter pressure. The parameters can be viewed during the sputtering on an on-screen display.

For establishing different pinning directions one can use magnetic masks during the sputter process. These magnetic masks consist of little permanent magnets (two rods), which produce a homogenous field, aligned parallel with $15\,mm$ distance, so that maximum sample dimensions are restricted to $15\,mm$. The normally used wafers from which the samples are cutted/broken have these parameters: $100\,mm$ ($\approx 3.94\,$inch) silicon wafer from CRYSTEC[Cry], $525\,\mu m$ thick with $50\,nm$ thermal oxidized SiO_2 on top, with orientation ($1\,0\,0$), polished on front side and etched at the backside; the specific resistance is mentioned on the label to be 1-$20\,\Omega cm$.

For (plasma) oxidation the sample holder is moved without breaking the vacuum into the oxidation chamber where an *electron cyclotron resonance* (ECR) plasma oxidizes a $1.4\,nm$ Al layer to approx. $1.8\,nm$ amorphous Al_2O_3[Pan05, section 2.1]). Standard parameters are $100\,s$ with $2 \cdot 10^{-3}\,mbar$ oxygen pressure and an oxygen flow of $13\,sccm$, at $275\,W$, chosen according to THOMAS' best results, i.e. highest TMR, during his PhD thesis. Confer therefore [TBS$^+$03, sections 3.1 and 3.3] and for more details see also [Mey06, section 2.1.2].

Among other things there exist a home built sputter tool for coating Au, Ta, TaOx and SiOx from $2\,$inch targets. Reactive sputtering of Ta or Si in combination with oxygen can be used for isolating layers of TaOx and SiOx. Base pressure is below $2 \cdot 10^{-6}\,mbar$

($1\cdot10^{-6}\,mbar$ for SiOx). During sputtering of Au and Ta $2.1\cdot10^{-3}\,mbar$ argon pressure and a power of $25\,W$ are used. For SiO_2 a RF-target of silica glass is used, with the start up help of a Cu-target, with $2.3\cdot10^{-3}\,mbar$ argon and $1.1\cdot10^{-4}\,mbar$ oxygen at a power of $50\,W$[Mey06, section 2.1.1].

2.3 Cleanroom

A special room with over pressure consists of a spinner, hot-plates with digital display of temperature, a parallel lithographer and the laser lithographer (DWL 66 from Heidelberg Instruments GmbH, see [Pan05, section 2.3]), which is not used in this thesis. The spinner has the ability for two programs with speeds from $<500\,rpm$ to $>6000\,rpm$, setting for each speed the time to ramp up the motor and the spinning time itself in seconds (control unit Delta 10 from BLE[BLE]). Spinner and hot-plate can be used under an extractor hood to avoid pollution. The parallel exposer with UV-light from Thermo Oriel is available for UV-mask lithography. Therefore with the laser lithographer an inverted design is structured on a glass substrate, which are filled up via sputtering Ta, thick enough to block UV-light. After removing the fabrication of the UV-mask is finished and can be used by placing the sample under an appropriate UV-light source. The mask is placed with the design direct on top of the sample, that is the so called "contact" method. The parallel exposer contains a homogeneous UV light source with $300\,W$ for quick exposure[30] for structures $>5\,\mu m$.

2.4 MOKE

One speaks of *Magneto Optical Kerr Effect* (MOKE) when polarized light is reflected by a magnetized surface which changes ellipticity of the polarization. A main distinction can be made into "polar" for magnetization perpendicular to plain and "longitudinal" Kerr effect with magnetization in-plane. In this setup the so called "s-polarized longitudinal MOKE" is used: The magnetization is parallel to surface and optical plane, which means in-plane, whereas linear polarization of light is perpendicular to optical plane, confer [HS98, section 2.3.2, p. 27].

The setup is self made, done by Daniela Sudfeld[Sud00] in 2000 for examination and Jan Schmalhorst. A red laser ($0.5\,mW$, $\lambda = 675\,nm$) is (linear) polarized by a polarizer, going through an aperture to get rid of stray light. The sample reflects the laser light and a second polarizer acts as an analyzer, after passing an aperture because besides the normal stray light also reflections from the sample can appear. After passing a third aperture the reflected light is detected with a photodiode, measured with a Keithley Keithley "K2000" or "Model 2000 digital" multimeter[Kei]. The whole setup is covered with fabric to get rid of outer light.

---

[30]exposure time, 1–5 s, depends on the age of the UV lamp and is adjusted by the person who is in charge of the machine.
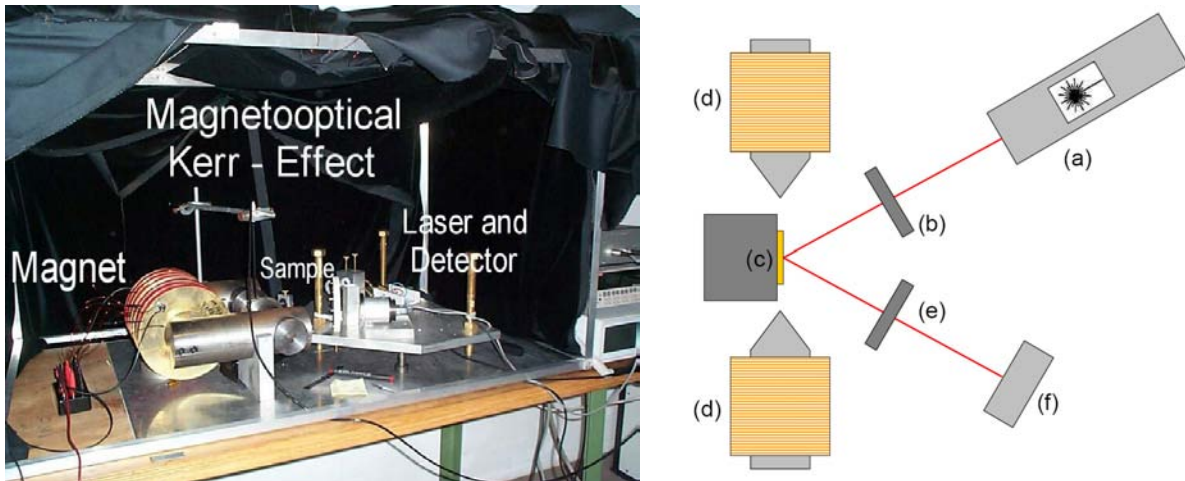
Figure 2.2: Self-made MOKE setup in chamber of fabric to protect setup from light with (a) laser, (b) polarizer, (c) sample, (d) magnets, (e) analyzer and (f) detector. (Picture taken from "D2 – lab tour" at www.spinelectronics.de, sketch from [Bor05].)

For the magnetic field the computer controls a power supply of ferrite core coils. A Bell Gauss/Tesla meter measures the field of max. about $\pm 3800\,Oe$ $(304\,kA/m)$ at an air gap of $2.5\,cm$. It exists options to adjust the measurement of field range to the abilities of the gauss meter for getting better sensitivity. With minimal intensity on detector a highest sensitivity of measurements is gained. Therefore the analyzer is adjusted at first without magnetic field so that a minimum signal is measured and then so changed that former value is doubled or differs a little bit (approx. 1° twisted).

An overview on theory and microscopy methods is given in [HS98, section 2.3]. See [Sud00] for details on Kerr effect and setup. Measurement details are given in section 3.2.1 of the exemplary preparation.

The MOKE is often used for a quick check whether a stack switches magnetically, employed after annealing before structuring: Magnetic switching and the belonging magnetic configuration is visible in figure 2.3.

Due to a spot size of about $\varnothing 100\,\mu m$ [31] it is a local technique, in opposite to AGM, and (very) surface sensitive, because intensities are related exponentially to the depth: $I = I_0 \cdot \exp\left(-t/\lambda\right)$[Enn03, section 3.3.2], with t as the optical free length and the depth of penetration λ for light, which is for metals 10–$20\,nm$ for visible light. All in all the signal originates from a depth of several nanometers.

---

[31]estimated from spot with reduced intensity due to additional polarizer on paper with mm-lines: $0.125 \pm 0.05\,mm$
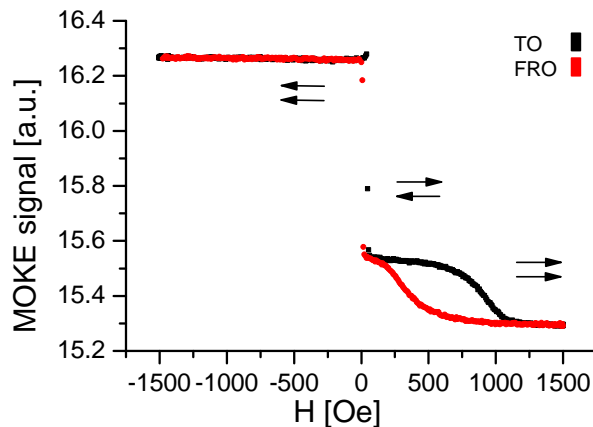
Figure 2.3: Example of a MOKE measurement with indication for parallel and antiparallel alignment of ferromagnetic layers.

2.5 SEM

The used LEO SERIES 1530 from LEO ELEKTRONENMIKROSKOPIE GMBH (Zeiss)[Zei] contains a field emission cathode whose beam is used to scan over the sample. Two detectors are available for getting information of the generated electrons: that is InLens- for backscattered electrons and SE-detector for secondary electrons (see figure 2.4). The following setpoints are used for pressure: gun chamber $<1 \cdot 10^{-9}\,mbar$, main chamber $<2 \cdot 10^{-5}\,mbar$. To avoid pollution during sample change the main chamber is vented with liquid nitrogen (LN$_2$). Several options for aperture, electron energy as well as the detector type, but also settings for contrast and brightness of picture, and of course the adjustment of stigmatism, focus and aperture alignment (the latter using a "wobble mode", i.e. varying the depth of focus to see the horizontal alignment) have big influence on viewing details and can lead to different appearance of a structure[32].

More information on general setup and principle of a *scanning electron microscope* (SEM) can be found in a short form at [HS98, section 2.5] or [Ohr02, section 10.4].

Lithography is done in combination with a RAITH ELPHY PLUS lithography system[Rai]. Designs are made with the help of "ELPHY Plus 1.4" (CAD, *computer aided design*, software from RAITH) by RAITH. The sample current is measured in a faraday cap[33] which varies with the beam current and must be given to the software before each exposure,

According to [Pan05, section 2.4] and [Mey06, section 2.2.3] the nominal resolution is $1\,nm$ at $20\,kV$; structures down to $50\,nm$ are possible in real (personal information from KARSTEN ROTT[Rot], see also [Mey06, section 2.2.3]). The normal used *working distance* (WD) is chosen as $9\,mm$, i.e. the distance between sample surface and the

---

[32]In general a SEM picture shows very sharp edges, because at the edges of structures more electrons can leave the surface than at plain areas, giving a higher signal, as depicted in figure 2.4.

[33]A simple hole on the sample stage is used as the faraday cap.
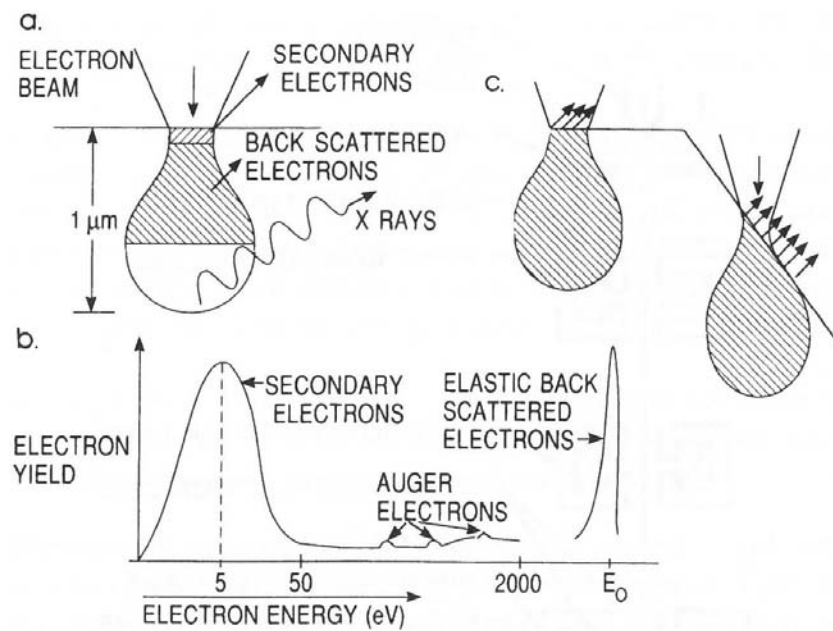
Figure 2.4: "(a) Electron and photon signals emanating from tear-shaped interaction volume during electron-beam impingement on specimen surface. (b) Energy spectrum of electrons emitted from specimen surface. (c) Effect of surface topography on electron emission." [Ohr02, p. 586, figure 10-12]

opening of the electron gun.

X-ray energy dispersive analysis (EDX) is also possible. The specifications are a depth of $1\,\mu m$ for the x-rays at $20\,kV$ beam voltage, which are detected with a Si(Li) detector, cooled with LN_2. The specific energy spectrum is compared to standard spectra with software "ISIS 2000" and should have an error of approx. $10\,\%$, confer [Enn03, section 3.2.1]. See also [Ohr02] in section 10.4.2 for origin of x-rays concerning energies and shells, as well as section 10.4.3 for equipment equal to the one here available.

2.6   SIMS

A self made apparatus (by K. Rott) is used for ion beam milling with Ar^+-ions and can also be used for sputtering Cu and Ta. A Leybold-Heraeus quadrupole mass spectrometer QMG 511 detects and counts ions with given masses, but a signal is not independent – it is correlated to nearby masses (see figure 2.5 where e.g. the XY and Au-signal (atomic mass $44\,au$ and $197\,au$, respectively) increase at approx. $500\,s$ because the Ta-signal with adjacent mass ($181\,au$) does, although XY is a fictive element[34]. Nevertheless those real-time measured and displayed signals show (more or less) at which

---

[34]Indeed Scandium Sc has an almost equal atomic mass of about $45\,au$[FD96], but this material is not used at all.
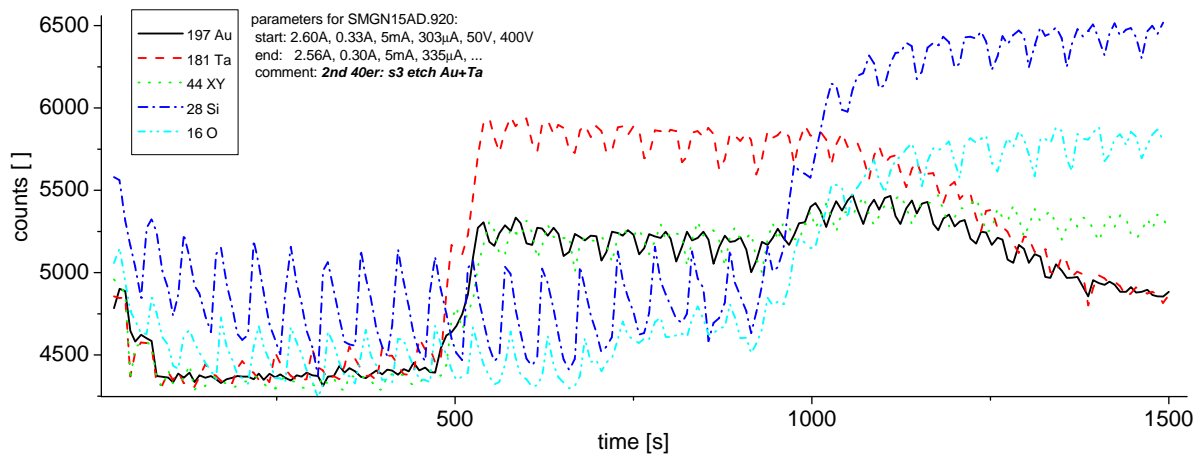
Figure 2.5: Plot of quadrupole-data of SIMS, legend shows element and its atomic mass[FD96]. This example is taken from the third process step of a sample for further research presented in section 5.5. The conductive material Au and Ta has to be etched until isolating SiOx is reached. It is visible that the gold (solid black line) gives no high signal at all, but increases at approx. $500\,s$ when the Ta layer (striped red line) is reached. The fictive element XY (dotted green line) is related to the Ta-signal in the same way as it is the case for Au.

layer of the stack the milling process acts and it is possible to stop with good accuracy in a specific layer, with respect to the etching rate and layer thickness.

The base pressure is according to [Mey06, section 2.2.4] $<8\cdot10^{-8}\,mbar$ and during etching $5.3\cdot10^{-4}\,mbar$. Different materials have different etching rates, depending also on the parameters of the beam and related ions which is normally chosen in the following way[35]: Discharge Voltage $= 50\,V$, Beam Voltage $= 400\,V$ and Accelerator Voltage $= 30\,V$ are fixed, and Cathode Filament Current is chosen so that the sample current is in the regime of 300–$400\,\mu A$. Therefore the Beam Current $[mA]$ is adjusted automatically by a control unit (ION TECH INC. MPS-3000 BPN)[Ion] where all settings except the sample current are displayed and set. Example values and resulting Discharge $[A]$ and Beam Current $[mA]$ are visible in figure 2.5.

The sample stage is rotating and tilted by $30\,°$ to avoid crafts from reflected ions and re-deposition of etched material, which could cause short-cuts by establishing a conducting wall.

More details and background information can be found in the aforementioned PhD thesis by MEYNERS[Mey06].

---

[35]An alternative concept is to chose a fixed beam current, i.e. the Filament Discharge Current is adjusted automatically which results in a more constant etching rate.

Figure 2.6: TMR measurements setup.

2.7   TMR Measurement Setup

The measurement principle is to apply a "bias voltage" and measure the current through an element to get the resistance. The current is measured in the *current perpendicular plane* (CPP) geometry with a pair of thin tips made of Au-wire.

Two collinear coils with ferrite core in C-shape create a field up to $\pm 3500\,Oe$ $(280\,kA/m)$ on the base of two power supplies driven via computer. At the air gap of the ferrite core between the coils the sample and a gauss meter tip is placed, via the tip the field is measured by a BELL 6010 GAUSS/TESLA METER[Bel][36] whose signal is read using a KEITHLEY "K2000" or "Model 2000 digital" multimeter[Kei].

Central connector is a home made measurement box which shows amplification (6 ranges of max. $100\,nA$, $1\,\mu A$, $10\,\mu A$, $100\,\mu A$, $1\,mA$ and $10\,mA$) and voltage range (max. voltage $\pm 20\,mV$, $200\,mV$ or $2\,V$), both set via computer, and has a regulator for output limitation, i.e. max. output $\pm 10\,V$, $1\,V$ or $100\,mV$. The current is measured by this electrometer amplifier, whose output is again measured by another Keithley.

The whole setup lays on a heavy stone which itself lays on rubber pads to get rid of vibrations and perturbations, see picture in figure 2.6.

More details especially on resolutions and error values are given in [TBS+03, section 2.1] by ANDY THOMAS, who built this setup.

The setup changed via measurements: Now a login-amplifier is used for readout of measurement box and sub-control of power supplies for coils, but the measurement principle is not altered.

---

[36]A long thin rod with a semiconductor using Hall-effect to get relative high voltage compared with low current in tip and magnetic field.

2.8 Vacuum Furnace

Two tasks can be done with the vacuum furnace: annealing of a stack, especially of barriers, i.e. healing of defects and reorder with the goal to increase TMR. Further "field cooling" is possible after annealing to establish an exchange bias, see section "Annealing & Field cooling" (1.3.5) (and section 1.3.4).

This home built setup has following specifications: The samples can be fixed on a Cu-block which is connected with a thermoelement[37] and consists of tubes for air (or water) cooling. The target temperature, is controlled with a "PID-Regelung" of company EUROTHERM via voltage[Sho05, section 3.1.3]. All parameters are computer controlled: target temperature, heating time, i.e. time to heat up to the target temperature and hold this temperature, base pressure for annealing (usually $1 \cdot 10^{-7}\,mbar$) and cooling time, i.e. length of time after heating time with applied cooling for the field cooling process. Therefore two permanent magnets of $1000\,Oe$ (max. $1750\,Oe$ at certain areas) and $6500\,Oe$ (max. $7500\,Oe$) are available.

The standard process for annealing in combination with field cooling of TMR is: $60\,min$ heating time with target temperature $350\,℃$ ($\approx 625\,K$) (heating up in 5.0-5.5 min, variation in target temperature about $<\pm 1\,℃$) + $30\,min$ cooling (27-30 min to reach RT) at $<1 \cdot 10^{-7}\,mbar$.

---

[37]Basic principle is the "Seebeck" effect: A *contact voltage* appears if two metals are in contact and is proportional to the temperature. A thermoelement consists of two wires of different metal, which ends are connected, i.e. soldered, on both sides. A voltmeter placed inter one wire displays a voltage which is proportional to the temperature difference of the connected ends. The advantage of such thermometer is a high sensitivity and fast reaction. From "Gerthsen Physik"[Mes04, section 6.6.1 (p. 343 et seq.)]. Here type K, i.e. NiCr-Ni(Al) is used.

Chapter 3

Exemplary Preparation and Characterization

The following detailed description of the main procedures focusses on the preparation of a sample with sensors, describing e-beam lithography with negative resist. It follows an exemplary characterization of the sensors which were used for the detection of magnetic beads in chapter 4. After the preparation this first characterization is important for later comparisons when the sensors are measured with dropped bead dilution on top. This characterization has to be repeated several times, a workflow is given below (section 3.2.3). The preparation and handling of a dilution made from beads and solvents is described at the end of this chapter.

3.1 Preparation

The main procedures during preparation are the same for all samples:
A layer-stack is sputtered on a piece of Si-wafer followed by making structures using lithography and etching. Depending on the needed structures, i.e. how many conducting lines and sensor-elements must be placed over each other, additional sputtering-, lithography- and etching steps are needed. (Finally the sample's magnetic properties are measured using the MOKE and the TMR measurement-place, presented in sections 3.2.1 and 3.2.2, respectively.)

Two processes are needed in general after sputtering the whole stack: Structuring of simple squares with varying size to see how much TMR can be expected, called "standard test", or preparing sensors in a three step process. In figure 3.1 the mask for the standard test is visible with squares of nominal $(300\,\mu m)^2$, $(200\,\mu m)^2$, $(100\,\mu m)^2$, $(22.5\,\mu m)^2$ and $(7.5\,\mu m)^2$.

Standard test

The "standard test" needs an upper layer which is conductive (the best material is Au for Au-tips), so it can be contacted directly with a tip for TMR measurements. With a
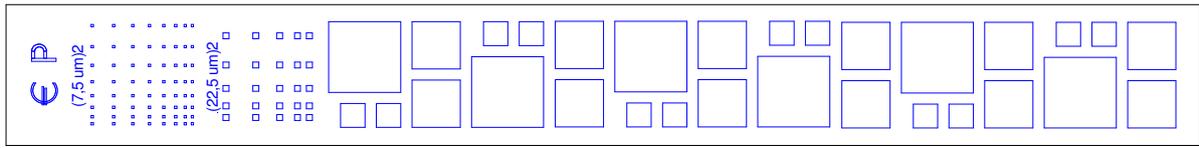
Figure 3.1: "Design of the TMR standard mask" for parallel exposition, from [Pan05, figure 2.3].

parallel mask, e.g. that in figure 3.1, positive photoresist is exposed under the parallel lithographer with UV-light in contact mode, i.e. the mask lays without a gap on the sample surface. After etching into a lower conductive layer, which lays under the sensing layers which give the magnetoresistance signal, only in the middle of the exposed area squares of different size are left and also the outer part. Here the connection to the lower part of the squares is given by pressing a tip on it, so that the thin layers are all broken and the tip has contact to the lower conducting layers. The other tip for TMR measurements must be placed on top of the squares very sensible to avoid a shortcut by breaking and going through the upper and sensing layers.

3-step structuring

(a) stack layout (b) design step 1 (c) design step 2 (on lower design) (d) design step 3
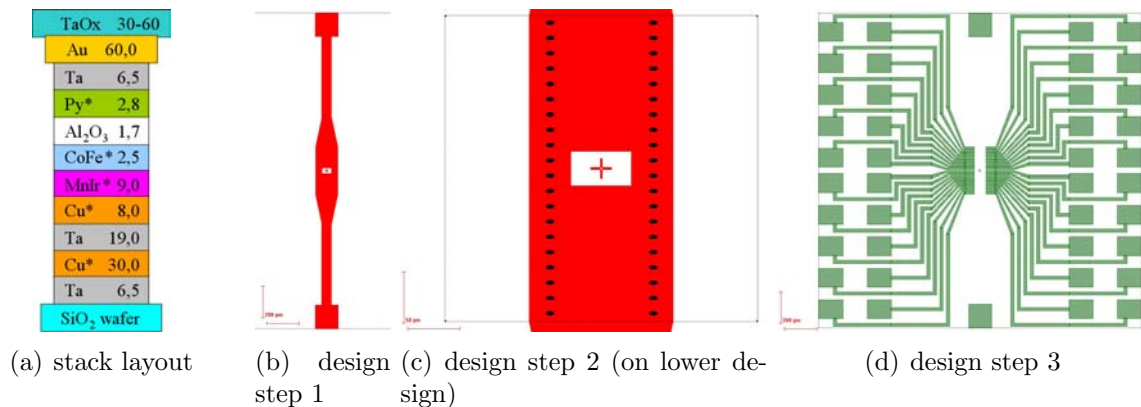
Figure 3.2: Layout of a TMR stack (a) and designs for the e-beam lithography: (b) lower conducting lines, (c) sensor-elements (on lower conducting line) and (d) upper conducting lines. (Screenshots, taken on ELPHY software.)

In figure 3.2 the designs are visible, which must be structured in 3 steps. Preparation of the sensors needs the use of e-beam lithography with the SEM, because tiny structures are needed. The lower conducting layers in the sputtered stack are utilized for the lower conducting lines by etching the surrounding material away in a first step. On top of those lines are placed in the second step the sensors by etching away the surrounding upper and sensing layers, further filled up with insulating material like SiOx or TaOx. To get

upper conducting lines two methods can be used in step 3: On the one hand conductive material can be sputtered and negative resist is exposed where the lines should be placed, so that the lines remain after etching before the "lift-off", i.e. removing of resist, see section 3.1.4. On the other hand one can make channels using positive resist, filling up those channels with the conducting material via sputtering and remove the resist. The used positive e-beam resist, see section 3.1.2, is very sensitive which increases the danger of getting an unwanted exposed area during focusing, which is the reason for using in this thesis the first method.

Before a complete sample with sensors is fabricated, an additional task should be done to test the proper doses for the sensors. This is necessary, because the dose depends not only on the kind of resist and beam-current, but also on the size and sometimes also on the environment, i.e. ground material and structures in the neighborhood[Mey06, section 2.2.3]. In a dose-test only structures near the sensors are exposed, equal to step 1 and 2 of the normal process, but several times with varying doses of the sensors.

3.1.1 Sputtering

First of all the wafer must be divided into pieces which are fixed on the sample holders after they are cleaned: To get rid of dirt (and also of dropped beads) little flasks with acetone and ethanol are placed into an ultrasonic bath and the sample is held with tweezers for approx. $10\,s$ into acetone. Less seconds are needed for ethanol, which evaporates without leaving a rest if it is blown away with a final nitrogen shower. Therefore the sample should be taken out of the ethanol flask with a closed film of ethanol on the surface, which should be blown away in one step with nitrogen. Magnetic masks limit the dimension of a sample to $1.5\,cm$ in the direction of the field, see section 2.2, so for perpendicular pinned stacks a sample is limited to $1.5 \times 1.5\,cm^2$. Furthermore the usage of clamps is prohibited due to the reduced free area by the magnetic masks. The sample is fixed with vacuum tape on the sample holder and a little drop of conducting silver is dropped at the edge of the sample to establish a conductive connection to all sputtered layers. This is necessary to avoid charging effects and destroy the tunnel barrier during oxydation. Oxydation is for example necessary to get an AlO_x-layer if only an Al-target is available. A program named "singleedit" is used to make the layout of the stack, editing for each layer the deposition time of the material. Further parameters are pressure, flow and sputter power as described in section 2.2.

If sputtering was done without magnetic masks a pinning is established via field cooling with the standard process for TMR (see section 2.8): $60\,min$ heating time with target temperature $350\,°C$ followed by $30\,min$ cooling at $<1 \cdot 10^{-7}\,mbar$.

Depending on the stack annealing can be necessary, see section 1.3.5. The usage of the vacuum furnace is simple, important is that the sample must lay flat on the Cu-block to have a homogenous heating. Furthermore it must be fixed with nonmagnetic material. Therefore molybdenum clamps and screws are used.

3.1.2 Lithography

Lithography steps are in general:

- Spin coat resist on cleaned sample where the kind of resist must be chosen to the needs of the exposure method in relation to structure size, i.e. UV-mask, laser or e-beam, here ordered by decreasing minimum structure size of $>5\,\mu m$, $>1\,\mu m$ or $<1\,\mu m$, respectively according to [Pan05, section 2.3]. (The main limit of systems are the wavelengths of the used exposing source; electrons yield the smallest structures due to the shortest wavelength compared with "normal" light.) Furthermore one can choose between positive and negative resist, which behavior can be seen in figure 3.3: Using negative resist means that the structures of the design exist as resist at the end of the lithography process, for positive resist only these areas remain uncovered.

- Bake sample to get rid of the solvent in the resist, done by placing it on a hot-plate for a specific amount of time. This hardens the resist.

- Expose sample in parallel (UV) exposer, laser exposer or in the SEM for e-beam lithography. In exposed regions of negative resist there is cross linking by induced chemical reactions. In positive resist "exposure causes scission of polymerized chains"[Ohr02, p. 236, section 5.4.1].

- Developing using adequate chemical substances. That results, if negative resist was used, that the not exposed areas are washed away, and with positive resist exposed areas are washed.

- Removing the resist, please read ahead in section 3.1.4.

E-Beam Lithography

In the lithography process several parameters must be adjusted. After focusing and setting the working distance the sample current must be measured and entered in a list of parameters in the software. Further parameters are the sensitivity of the resist and the "Area stepsize" which result in a certain speed of exposure, visible in the "Area dwelltime". The higher the sensitivity and the sample current are, the shorter an area must be exposed. This is due to a higher effectiveness of electrons or rate of electrons per time. An additional parameter is the dose chosen in the design for a structure, which is a relative factor for the exposure time. Depending on the size of a structure in general smaller structures need higher doses. The "Area stepsize" $[\mu m]$, i.e. number of "pixels" from design which are "melted" in one exposure step, is adjusted so that the "Area dwelltime" $[ms]$ should be over a threshold of about $1\,\mu s$, according to the experiences of KARSTEN ROTT [Rot].

The minimal possible sizes, the exposed area, and the shape are influenced by "forward scattering" / "scattering at small angle" and "secondary electrons" see [Mey06, section 2.2.3].
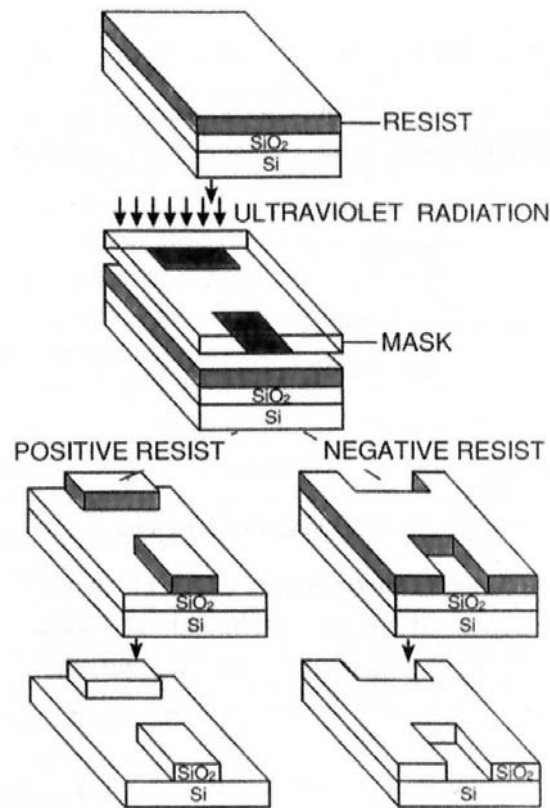
Figure 3.3: Principle of positive and negative resist in combination with etching, from [Ohr02, p. 235, figure 5-13].

Due to *proximity effects* (by backscattered electrons / large angle scattering) also nearby structures can influence the real size, i.e. with a big structure in the neighborhood little structures will become bigger themselves, and the proximity effect itself depends on the material below which hinders more or less the movement of electrons (confer [Mey06, section 2.2.3]).

One must view over and over again the gun current, because the sample current $[nA]$ depends a little bit on it and influences the Area dwelltime. The gun current always varies with respect to time of day, time in use or time without usage, and in general very much on the age of the cathode used and the cathode itself.

The sample current, measured in a faraday cap as mentioned before (see used SEM in section 2.5), is not only influenced by the beam current itself, further the aperture has an influence. So with a big aperture the beam is wider and therefore the sample current higher. If structures are very tiny, i.e. one dimension less than $1\,\mu m$ a tiny writefield of 100 or $300\,\mu m$ should be chosen to get a high resolution during exposure. This can be achieved with a small aperture resulting in low sample current and longer time for exposure. For big structures big apertures can be used.

Errors

Several sources of errors should be mentioned:

★ misalignment due to not accurate stage movement,

★ improper dose which leads to bigger/smaller structures,

★ unwanted exposition during focusing,

★ bad settings for resist sensitivity,

★ impurities in coated resist,

★ dirt like "flakes" in resist itself.

Dose tests give proper dose and resist sensitivity. Not only experience with the usage of a SEM avoids exposition due to focusing, also a good design for lithography can help, as well as for avoiding misalignments. Stage movements can be reduced with larger writefields, or can be circumvented with designs using different writefields and software options[38]. A solution for the resist is to wait till flakes sank to the bottom and avoid shaking of bottle which contains resist. Resist is taken with a pipette from top beneath the surface, where no flakes or dirt from surface should be; one can also try to filter resist.

Resists

Several resists from ALLRESIST[All] are available, in this thesis the photoresist ("AR-P 5350") as well as e-beam resists, that are positive (PMMA: "AR-P 610.03") and negative resists ("AR-N 7500.18" and "AR-N 7520.18") were used. To get thinner layers resists can be thinned with the diluter AR 600-00. Resist is filled up into a personal beaker to avoid pollution of the original flask due to permanent opening. The date of the first opening is important, because the resist is best before approx. 6–12 months afterwards.

The coating of the sample with resist is done in the cleanroom, including spinning and baking: The sample is taped on a spinner, resist is pipette spotted and the spinner turned on immediately. Baking takes place on a hot-plate (favorably under "clean air" to avoid pollution with dirt).

Resist parameters are given in table 3.1 on page 59. The positive photoresist AR-P 5350 has a special undercut profile, that helps with the lift-off process. Because of this undercut profile, the structures are always $500\,nm$ wider (see figure 3.4).

Figure 3.4: Undercut profile for resist AR-P 5350.

---

[38]See in section 5.3.2, table 5.3, the structuring of arrays containing thousands of structures.

3.1.3 Etching

Etching is done in the SIMS, presented in section 2.6, which has the benefit to see signals of materials, not quantitative but qualitative enough, to determine which layer of a stack is penetrated at the moment.

For the three step lithography process an "etching-profile" is made, i.e. etching of the whole stack into the lower SiOx of the wafer. In step 1 and 2 of lithography the etching of the whole stack is split in two steps (so that after etching in step 2 at those uncovered areas with the entire stack only the two lower Ta layers with a Cu layer in between remain as the lower contact lines). The needed time for milling the upper layers is given in the etching-profile, as well as the time for etching the complete stack. The difference of these two times is the etching time for the first lithography step.

3.1.4 Removing

The removing, or also called "lift-off", is done in an ultrasonic bath with a special remover, see table 3.1 on page 59. A temperature of 80 °C can be essential for removing, depending on the kind of resist and the height of remover liquid, wich influences the strength of vibrations.

It is good to pick up the sample out of the running ultrasonic bath, so that no dirt can stick on the surface, followed by cleaning in ethanol due to blow drying the sample with nitrogen.

The removing time depends on the structure size – little ones take much longer – and the material under the resist. Resist does not adhere on Cu, but sticks good on Ta and Ru, whereas it is harder to remove on Ta. So little structures on Ta need up to two hours till the resist is removed, but it takes only $20\,min$ for Ru (also experienced by KARSTEN ROTT[Rot]. Also the penetration in SEM is important, because the more energy the resist gets, due to longer examination in SEM and with higher beam-energy or wider apertures, the longer the removing time.

3.1.5 Examination

Observations of the samples status can be done with an optical microscope[39] (in the following named as "OM") or the SEM (see section 2.5).

For a quick check whether a material is really isolating or not a simple voltmeter can be used.

---

[39]The used ZEISS microscope has a micro precision positioning table and is equipped with a CCD-camera, see [Pan05, section 2.7] for details. The 1024×1024 pixel images possess the following resolutions towards three alternative objectives of the microscope:

- 20× ∼ $321\,nm$/pixel → $(330\,\mu m)^2$
- 50× ∼ $128\,nm$/pixel → $(131\,\mu m)^2$
- 100× ∼ $64\,nm$/pixel → $(65.7\,\mu m)^2$

(given are magnification, size of one pixel and resulting total size of one picture with 1024×1024 pixel, respectively).

The optical microscope is good for a quick check of the actual state of the structures on the sample, especially after etching and removing. The color indicates material, e.g. grey=Ta, yellow=Au etc., which could help if the SIMS-signal gives no clear indication for a specific layer. A look at borders gives indication of resist, such as border thickness and color (rainbow-effect). Elements are only visible down to $1\,\mu m$, below this limit only undefined shadows are possible, so it is not visible whether tiny elements in μm-range are removed.

Therefore the SEM is used: Areas with resist appear not sharp, white areas without kinks if resist is observed on elements. Maybe additional removing should be tried out, depending on how "healthy" the sample looks like, i.e. if damage becomes visible one has to consider carefully between the possibility and the necessity to remove the resist completely and the danger of loosing elements due to longer removing itself. An aspect is also that the longer the sample is used it can be polluted and will more oxidize.

Real Sizes of Elements

The check of real sizes of elements is also important to get proper values for dose due to comparison with nominal sizes. The real sizes are influenced by the minimum possible sizes, exposed area, shape and proximity effect, already mentioned in section 3.1.2. The question is in which state the real size should or could be measured; after developing the original dimensions of the resist are visible, which acts as the mask for etching, but due to the not-sharp appearance they cannot be measured exact. The appearance can be sharpened by using a smaller working distance, higher beam-voltages, bigger apertures or due to longer scanning, but the last three methods can make the removing harder (see section 3.1.4). Etching leaves not a vertical side at elements, but cone-shaped, where the slope depends on the applied angle in setup of etching, which should be here 30° due to the tilt of sample stage (see section 2.6). Depending on the material and its growth properties the borders can have more or less fringes, but also the design for exposure can influence the border: If the dimensions are too small rectangular edges will getting round, because in the corner an exposing dot will create a circle as described in section 3.1.2, so it is natural to get ellipses although rectangles were designed. After removing the benefit of a good contrast competes with the uncertainty of cone-shaped sides with more or less baggy borders if the structures are very little – the size can be measured again with bad accuracy.

resist	AR-P 5350 positive photoresist	AR-N 7500.18 & 7520.18 negative e-beam resist	"AR-P 610.03" – PMMA positive e-beam resist
1. spin	$200\,rpm$ $2\,s$ (ramp[a] $2\,s$), 4000 or $6000\,rpm$ $30\,s$	$200\,rpm$ $1\,s$ ($1\,s$), $4000\,rpm$ $30\,s$	$200\,rpm$ $1\,s$ (ramp $1\,s$), 4000 or $6000\,rpm$ $30\,s$ (ramp $1\,s$)
2. bake	$30\,min$ @80-90°C $\Rightarrow 1000$ or $800\,nm$	$2\,min$ @85°C $\Rightarrow 450$–$500\,nm$	$30\,min$ @190–210°C $\Rightarrow 80$ or $70\,nm$
3. exposure	UV-Lamp: 1.4–$10\,s$[b] (Dosage: 41)	electron energy $20\,keV$, sensitivity $170\,\mu C/cm^2$; dose: 0.8–1 for structures $>1\,mm$, up to 16 for structures below $100\,nm$	electron energy $20\,keV$, sensitivity 70–$80\,\mu C/cm^2$; dose: 0.8–1 for structures $>1\,mm$, up to 3 for structures below $100\,nm$
4. develop	10–$12\,s$ @18–25°C in AR 300-35 (2:1 with DI-water); rinse well with DI-water	approx. 3min @18–25°C in AR 300-47 pure; rinse well with DI-water	in cleanroom $2\,min$ AR 600-55 and $30\,min$ AR 600-60 to stop; only blow-dry with nitrogen!
5. remove	$1\,min$–$1\,h$ ultrasonic in remover AR 300-70 @RT; rinse well with ethanol	$10\,min$–$2\,h$ ultrasonic in 1-Methyl-2-pyrrolidinone (NMP)[c] @80°C; rinse well with ethanol	1–$15\,min$ ultrasonic in remover AR 300-70, up to 80°C; rinse well with ethanol

Table 3.1: Parameters of resists, taken from internal digital resources.

[a]"ramp" value is time for ramp up to nominal speed, see section 2.3.
[b]The exposure time depends on the age of the UV lamp and is adjusted by the person who is in charge of the machine.
[c]from ALDRICH[Ald]

3.2   Characterization

An existing sample was used and characterized to save the time of structuring. It was prepared in the same way that was described in section 3.1. The characterization of the sensors is done with TMR measurements, which are described below, followed by the general workflow and details on the selected sample. The first results, i.e. the individual behavior of the used sensors, can be find at the beginning of chapter 4. But at first MOKE measurements are described. These are used in general after the sputtering and annealing of a stack to see whether it is magnetic switching, generally before a structuring starts and ends with MR measurements, but MOKE measurements also can be used alone for characterization as it is done in chapter 5.

3.2.1   MOKE Measurements

Before a MOKE measurement can be done the setup must be calibrated. Therefore the gauss meter is reset and manual offset is set so that the computer for measurement gets zero signal. The polarizer which acts as an analyzer must be changed out of minimum position where the laser spot is wiped out. Sample is fixed with clamps on sample holder so that the area which should be measured is focused by the laser spot; the sample alignment depends on annealing field, i.e. orientation of pinning. The position of the sample holder must be adjusted so that the laser spot is reflected into the middle of the detector. To get rid of stray light apertures can be placed before and after the analyzer. Next the analyzers position must be tilted to minimum signal which is measured and twisted out of this position so that the minimum signal gets higher, e.g. if minimum signal is $20\,a.u.$ it is shifted to $21\,a.u.$. The shape of a measurement curve is not influenced by the degree of twist. Test measurements showed that only the total signal height increases with a higher detector signal, but not the relative change. In contrast stray light can influence the signal, so light sources have to be switched off or covered. The setup is so sensitive that e.g. the light from a computer monitor with command prompt and brown text color will at least double the signal. Therefore the whole setup can be covered with thick black fabric as seen in figure 2.2.

   Parameters of the measurement program are one outer nonsymmetric field range and two symmetric field ranges with individual step sizes for measurement, furthermore number of loops and setting sensitivity of gauss meter. After measuring several times after another with the "loops" option automatically the mean data is calculated.

3.2.2   TMR Measurements

Contact of the sample is made with one tip for the lower conducting part and with another tip the sensor pad for upper contacts are used. If the standard mask was applied the stack itself can also be used for the upper contact. This must be done carefully, because it is easy to move down the tip to fast so that it goes through the thin layers at once. A measuring tip is an Au-wire of different thicknesses, which can be made spiky due to one of three methods: Simply cut transverse and hope that end has

one small ending, or heat the end and hold it up to let the drop of melted Au go down leaving a sharp tip, and/or grind the end with sandpaper.

In general two kinds of measurements can be done: TMR curves by applying a certain bias voltage (usually $10\,mV$), vary the magnetic field and measure the current to get the resistance. Also I/V-curves can be performed by measuring the current. The magnetic field is fixed, but the bias voltage is varied from a minimum to a maximum value. The resulting (specific) current curve can be fitted after differentiation ($\rightarrow$ specific conductance curve) with the Brinkman-fit to get properties of the barrier, see the example curves in figure 3.5 and confer section 1.3.1. IV-curves are linear if the TMR element is broken, contrary the second derivative has parabolic shape if a good element is measured. The IV-curve and its derivation are more pronounced, i.e. higher slope, in parallel state, so several fields were always tried out for IV measurements to get a good parabolic curve.
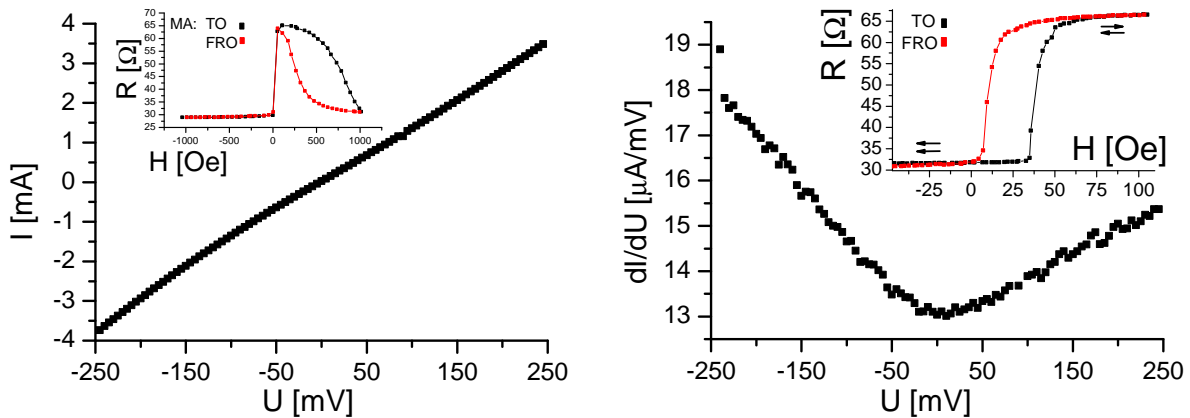
Figure 3.5: Example of measured IV-curve (left) and its derivation, measured at $100\,Oe$.

The measurement program has following options for TMR measurements: fields range a & b, so that during measurement fields values are varied as a $\rightarrow$ b $\rightarrow$ a, with a selectable increment. Further options are the bias value during measurement and after it, the number of loops, and the area, which is needed for automatic calculation of area resistance. For IV-curves the starting and ending voltage, increment and applied magnetic field can be selected.

Sensors can be very sensible and break easily so they must be treated with care: If measuring a new sample with unknown properties the smallest maximal voltage range is taken, i.e. $\pm 20\,mV$, with lowest amplification of actual $1nA/V$, and limitation is reduced to minimum. The signal should be normally out of range at the Keithley if a conductive connection is measured, so the settings, i.e. at first the limitation and further amplification, can be increased iteratively.

Especially tiny elements can be very sensible to knocks or voltage peaks, so that precautions should be taken: Switching on/off other machines, which share the same electric circuit, must be avoided. Otherwise voltage peaks could appear, although the

power circuits should be independent. Further on persons should not walk near the setup, slam doors etc.

3.2.3   Workflow of TMR Measurements

The normal TMR setup, described in section 2.7, was chosen due to its simplicity for the first tests, providing an in-plane magnetizing field for the beads by the normal measuring field.

The general measurement workflow consists of these three steps:

step 1: Characterization of sensor elements.

step 2: Measurements after beads were dropped.

step 3: Reference measurements after cleaning of the sample.

At each step the in-plane measurement field (IP) is applied, but depending on the setup also measurements are done one time with an additional applied out-of-plane field (OOP). (See the descriptions of the measurement setups in section 4.3.1, 4.4.1 and 4.5.1.)

Four different alignments of the sample according to the measuring field H_a are differing by a twist of 90°. To address those alignments following abbreviations are used:

orientation a: The measurement field H_a is parallel to the cooling field H_{FC}, i.e. the magnetization of the hard magnetic layer without a field applied.

orientation b: H_a is perpendicular to the direction of the field during cooling.

orientation c: Orientation a twisted 180°.

orientation d: Orientation b twisted 180°.

Measurements were done always for 90° twisted orientations a and b. Furthermore random chosen sensors were measured twice to see whether signals are reproducible, and sometimes also measurements in orientations a and b were added to search for somehow new aspects. To analyze further influences additional measurements were done by varying the alignment of sample towards magnetic field and tip of gauss meter (see section 4.1).

Three different loops were measured: *major loops* (MA) and *minor loops* with negative or positive saturation (MI- and MI+), respectively. Saturation means that a relative high field is applied to "saturate" the sample, so that it is in a specific state of magnetization. In the beginning saturation fields of $\pm 1000\,Oe$ were chosen. Normally the number of measured loops is in orientation a 2 MA, 10 MI- and 5 MA+, whereas in b 1 MA, 3 MI- and 3 MI+ are measured, depending on already occurred ways. Long tests showed that only 2–3 characteristic ways appeared (see figure 4.1), even after several

dozen measurements. So the given number of measurements should be enough, but it was increased just in case a second way had not appeared yet.

In general the same pads were used for the lower contact to avoid any influence of imperfections of the lower conducting lines. This should play no big role, more important are on the one hand the upper conducting lines, which are due to their smaller thickness (nominal 10–$20\,\mu m$ vs. 60–$138\,\mu m$ of lower conducting line) more sensitive to changes in resistance by bad structuring. Therefore the wires should have the same length, but as visible in figure 3.6 the length is varying (from about 501 to $1641\,\mu m$).

Data processing was done using the software Origin[40]. The following steps are applied for every measurement:

$\rightarrow$ Import of data, i.e. resistance and applied field.

$\rightarrow$ Subtraction of drift.

$\rightarrow$ Separation into way TO (increasing applied field) and FRO (H_a decreases) for each measurement to see specific ways.

$\rightarrow$ For visual comparison data of two elements are plotted over of each other.

In spite of easier handling of the data mean values of several measurements were not used in order to analyze the characteristic ways and see possible changes of them. Differences between elements with and without beads were compared, after dropping and cleaning, and further references were studied. Comparisons of double measurements were done to see whether the data is comparable at all, especially after a break during the measurements.

3.2.4 Selection of Sample

Karsten Rott made a sample available[Rot] for measurements with 4 fields, containing 40 elements each. In three field all elements were broken[41]. Only one field was available for measurements, with 40 sensor elements which have a nominal size of elliptical $2\times4\,\mu m^2$, as visible at the design in figure 3.6. Sensor elements are enumerated with 1 to 20 on left side starting on top, and going on from top on right side with 21 to 40.

The stack layout of the sample is: (substrate Si/SiO$_2$) /Ta 6.5/Cu* 30/Ta 19/Cu* 8/Mn$_{83}$Ir$_{17}$* 9/Co$_{70}$Fe$_{30}$* 2.5/AlO$_x$ 1.8/Py* (=Ni$_{80}$Fe$_{20}$) 2.8/Ta 6.5/TaOx 30–60[42] (isolation)/Au 60 (upper conducting lines); thickness given in nm (recalculated out of old sputter data with old calibrations by Karsten Rott). Layers indicated with * were

---

[40]OriginLab Corporation, http://www.OriginLab.com; version 7.0552

[41]Dots were exposed which had a such hight ratio (height:width) that in two fields all dots had been fallen down. In the third field with dots the elements were exposed as $\varnothing10\,nm$ dots resulting due to forward scattering in elements of about $\varnothing150\,nm$ which were further elongated and tilted.

Only 6 sensors were working in the beginning – too less to work with them, i.e. make comparisons between several sensors with and without beads on top, or try to use them as a gradiometer, because they are spread over the whole array. Furthermore they were expected to be very fragile and later measurements showed that there was in fact no working sensor left.

[42]15min $\sim 30\,nm$ with old calibration, but approx. $60\,nm$ with new calibration dated Jan/06, i.e. $3.9\,nm/min$ with *x-ray diffraction* (XRD) by Markus Meinert, latest value from Jul/06, $1.87\pm0.04nm/min$, fits to old calibration?!
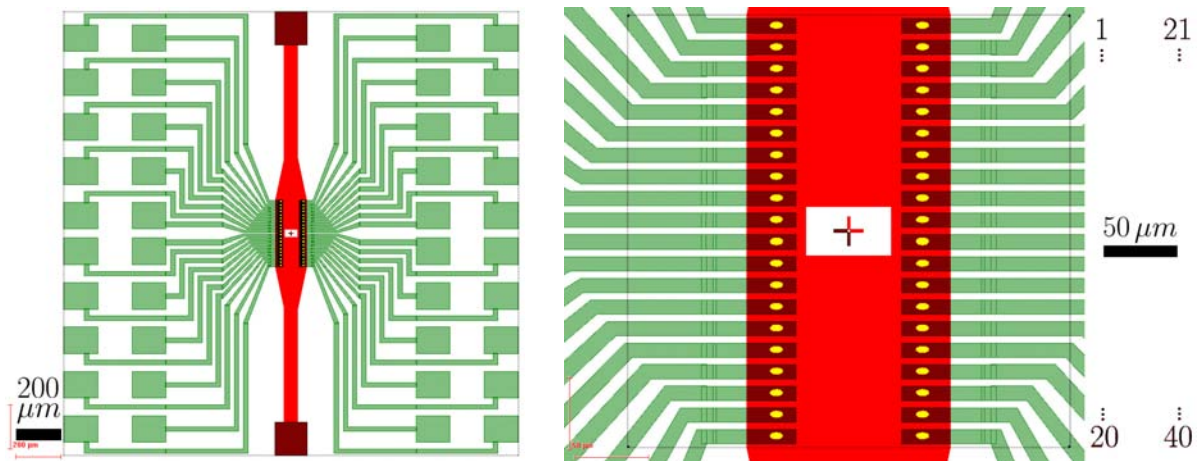
Figure 3.6: Design of sample by KARSTEN ROTT. On the left side the $2000\,\mu m$-writefield is visible which was used for the lower conducting line in red and upper conducting lines with pads in green. The elements are colored yellow, better visible in the $300\,\mu m$-writefield on the right side (incl. enumeration), which was used for their exposure, indicated by a thin gray line. (Screenshots, taken on ELPHY software, are further colored.)

sputtered with higher power of $500\,W$ than normal $115\,W$, as mentioned in section 2.2. This was done with the goal of shifting the middle of hysteresis (H_{EB})[Rot].

3.3 Bead Dilutions

Requirements for dropping of beads on the sample surface are as follows: homogenous distribution of not too many beads at an area of at least $300 \times 100 \, \mu m^2$ (see figure 3.6), so that the area with sensor elements is homogenous covered with one to five beads on top of a single sensor. A good dilution combines a proper concentration of beads in a solvent, and in the dropping process the amount of liquid and a specific temperature can be important. Furthermore the surface material can influence the behavior of the beads, i.e. whether they stick on it, that prevents agglomeration. Testing on "original" surface, i.e. the same structures and heights on equal material, would be good to avoid unwanted influences, but the original sample must be treated with care and therefore was not used. Structured samples were not tried out, because the differences in height are maximal $60 \, nm$, see sketch of stack and design on page 52, which should be not important compared to a bead radius of approx. $750 \, nm$. At first original wafers with SiOx surface were used, later replaced by wafers coated with TaOx, but the surface had only negligible influence.

Tests of concentrations started with "plain"-beads on SiOx, changed to biotinylated ones according to the personal information by MICHAEL SCHILLING, who experienced the adhesion to SiOx of these beads[Scha]. After further variation of surface material as well as concentrations and temperature a good dilution was found, see below, so it was not necessary to try out the other kinds of beads listed in section 1.2.3.

3.3.1 Selection of Solvent

The choice of the solvent is important for the distribution of the beads after dropping, because they tend to agglomerate. For measurements of a few or single beads agglomeration must be avoided.

Beads can move free until the solvent is evaporated, which implicates that a short time for evaporation is good and therefore e.g. isopropanol or hexane should be favored instead of water. Hexane should be only second choice because of the more poisonous property compared to isopropanol. With higher temperature the solvent will evaporate faster, but if the temperature is too high a drop of bead dilution can evaporate too fast, even before it touches the surface or it is not possible to drop it at all. All in all tests are helpful to get a combination of liquid which acts as a solvent for the beads and a temperature so that it will evaporate fast enough on the surface leaving beads on surface that are evenly dispersed with a specific density.

Possible solvents are for example:

DI-water should work with every bead, which is soluble in water – as seen in section 1.2.3 this fits to all MICROMOD beads. DI-water has the disadvantage of leaving dirt on the surface after evaporation.

isopropanol evaporates without residues[Schb]; comparable with ethanol which is used for washing, so this solvent will not harm the sample,

hexane (methanol, ethanol) evaporates fast; good experiences with nanoparticles[Enn].

The easiest handling has DI-water followed by isopropanol, so tests were started with these two solvents. A good dilution was found with isopropanol, see below, so it was not necessary to try out the poisonous hexane etc., which is therefore worse in handling.

3.3.2   Selection of Concentration

MICHAEL PANHORST needed "in order to position single beads at predefined places" with conducting lines a proper concentration and found out that "for the used MI-CROMOD particles, concentrations of 2–$5\,\mu g/ml$ worked very well"[Pan05, section 5.2]. Such concentrations were taken as the starting point for a lowest concentration of about $1.95\,\mu g/ml$ (1:12800) and varied up to approx. $125\,\mu g/ml$ (1:200).

Different temperatures for pipette spotting were tried out to reduce a possible agglomeration due to reduced drying time, according to the experiences in [Pan05, section 2.6]. The sample was placed on a hot-plate and 1 or $2\,\mu l$ dilution was pipette spotted. Temperature was measured with a thermoelement and a voltmeter, calibrated and given by KARSTEN ROTT, on the hot-plate surface; the real temperature on the sample surface is lower, e.g. about $75\,°C$ instead of approx. $96\,°C$.

A general behavior is the agglomeration of beads near the border of a drop, together with the dirt from dilution, that should have been already in the delivered tubes as mentioned below. Dirt of the sample surface should not play a role, because the sample surface was cleaned before dropping. When a drop evaporates from a surface it shrinks to a drop of smaller diameter, where the movement and speed depends on temperature. The disadvantage of higher temperatures is the evaporation of the drop already in the pipette tip, so that the dropping has to be done very quick. This can be dangerous to the sample, because the distance between tip and surface is so small that they can come in contact during quick movements, which can lead to the destruction of the sensors. At lower temperatures an amount of $1\,\mu l$ was enough to cover an area of about 1.5–$3\,mm$ in diameter, but with $2\,\mu l$ the handling is easier.

A combination of MICROMOD SICASTAR-M PLAIN *beads ($\varnothing 1.5\,\mu m$, OH-groups on surface), diluted 1:200 in isopropanol at approx. 50°C showed good results on flat TaOx.* With this dilution a homogenous distribution with many single beads as visible in figure 3.7 can be expected for the dropping of beads in sections 4.2 and 4.4.

Figures 3.8(a) and (b) show in later performed detailed observations via SEM of the dilution test very much dirt with only a few beads visible, recognized by their round shape as it is visible in figure 1.6(a). The diameter of the found beads lays between about 342 and $1300\,nm$. The mean value is $\varnothing 742\,nm$, but on the one hand the distinction between small beads, i.e. small round objects, and dirt is not secure. On the other hand the biggest beads were all found near the borders, as visible in figure 3.8. The possibility of beads is maybe higher at crowds (lines that were former estimated to be only dirt where the border of the drop stayed for a while), but there are always agglomerations; one has more luck with single beads in almost free areas, but most of the little points, as visible with the OM in figure 3.7, is dirt. If the dirt covers an area that is bigger than a tiny

(a)   (b)
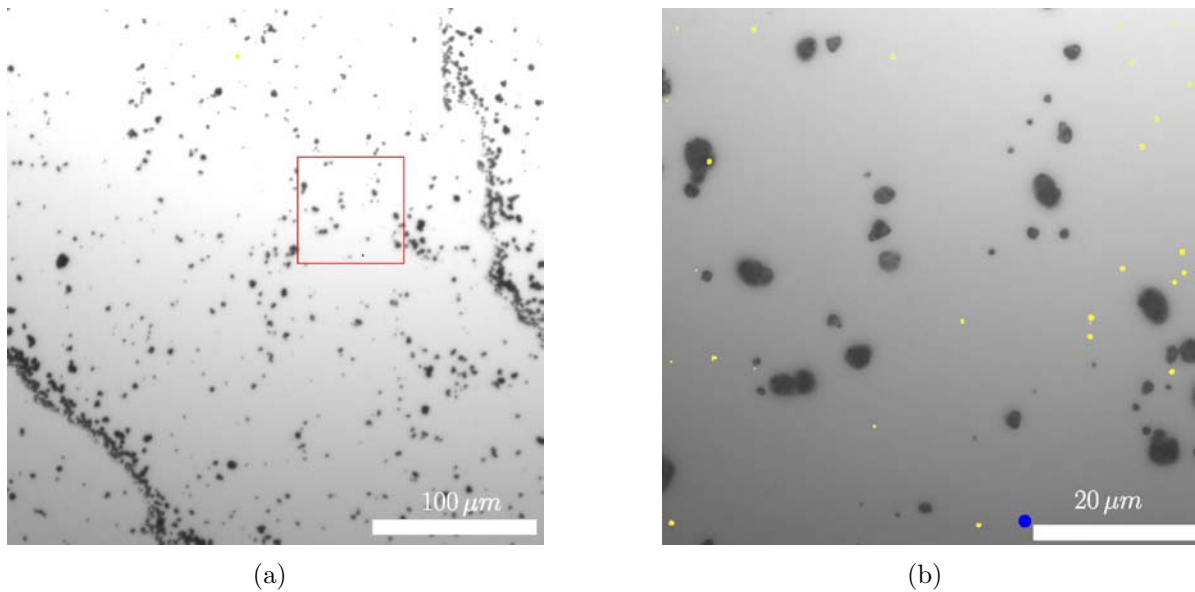
Figure 3.7: Optical microscope images of MICROMOD SICASTAR-M PLAIN $\varnothing 1.5\,\mu m$ beads, diluted 1:200 in isopropanol and dropped at about 50 ℃ on TaOx: (a) Two bands of agglomerated beads in the lower left and upper right corner are typical produced during evaporation and jerky movement of the drop borders. Dirt on objectives is colored yellow (done by hand after the brightest areas of two pictures were melted, emphasizing resulting darker structures, so that almost only dirt is left which can be selected). The red rectangle in (a) was viewed with highest magnification (100×, see section 3.1.5) visible in (b), where the blue point next to the bar has $\varnothing 1.54\,\mu m$ equal to a nominal bead.

bead it can be possible, that there are hidden beads under it. So one must keep in mind: *The analyze of dropped dilution via SEM is necessary to distinguish between beads and dirt, but in general this cannot give a certain number of beads.*

The dirt must have been already in the delivered tubes, because if the same dropping technique[Pan05, p. 18] was used for all three kinds of beads in figure 1.6, why should there be only dirt at the MICROMOD beads? Furthermore there are equal substances visible at own SEM images (see figure 3.8), so it cannot be due to the handling, e.g. dirt out of the used Eppendorf tubes.

3.3.3 Dropping of Beads

A little bit, e.g. $2\,\mu l$, of bead solution is taken with a pipette with disposable tip out of the original flask and is diluted with solvent in an Eppendorf tube[Epp]. The original flask should stay cool (e.g. in a refrigerator) and opened only for a short time to hinder any dirt going in, and so only new pipette tips are used to get the liquid out of the flask. After putting solvent to the beads the dilution has to be shaken for proper mixing, maybe with the help of an ultrasonic bath.

(a) SEM (34.2K×)   (b) SEM (8.4K×)   (c) OM (100×)
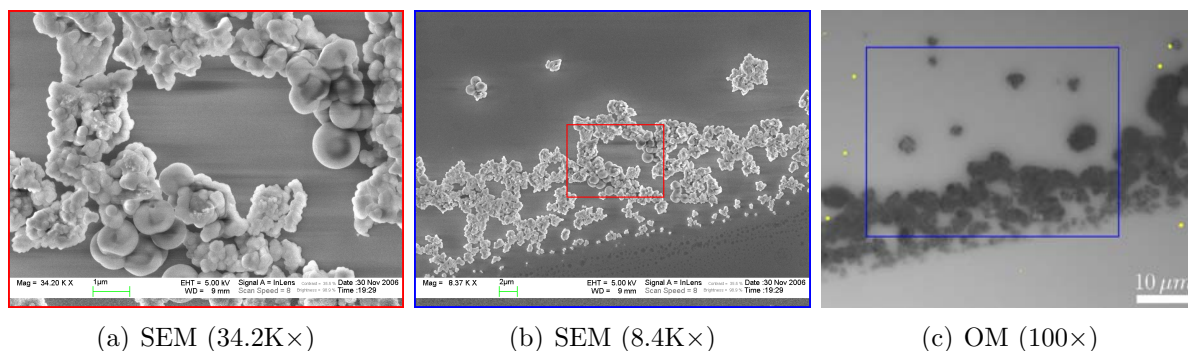
Figure 3.8: SEM and optical microscope images of the same region (This area is not representative for the size distribution, see text.): (a) A few good visible, round beads near a drop border, in the middle of (b) (red box), which cannot be distinguished from dirt in the OM (c) at its best magnification (blue box highlights area in (b); dirt of OM objective is marked yellow).

A proper amount of diluted beads, e.g. 1–$2\,\mu l$ (confer chapter 4) is dropped on top of the sensors, the sample maybe heated on a hot-plate. After a short period of time, e.g. $10\,s$, the solvent is gone by evaporation and the sample can be examined in the OM or the SEM, see section 3.1.5.

Depending on the beads total size, size distribution and the amount of dirt after dropping originated in the original dilution, the sample surface and due to treatment the SEM could be the only way to distinguish whether beads are on a sensor or not.

Chapter 4

Magnetic Particles on AlOx TMR Sensors

The first task was to measure the influence of beads on a TMR sensor. The ultimative goal is the detection of single beads without special signal enhancement. Therefore different setups were used, each approach was based on the results of the former setup. The normal TMR setup (section 4.1 and 4.2) is followed by setups with additional out-of-plane (OOP) saturation fields for the beads due to coils (section 4.3) or permanent magnets (section 4.4 and 4.5). In all setups the same sample with TMR sensors was used, which was introduced in the preparation (see section 3.1.

4.1   Results of First Sensor Characterization

First measurements without beads showed kinks in the minor loops near zero applied field, which is in the region of switching between parallel and antiparallel state in minor loops. Figure 4.1 shows exemplarily the data of one sensor. There were always two or three reproducible ways for each sensor. Sometimes the second (third) way was visible for the first time after several measurements which made it necessary to do many recurring measurements. It turned out that the occurrence of other characteristic curves took longer, if only minor loops were measured after another. Therefore, stable domains are assumed for low measurement fields. Before each minor loop measurement the sample was saturated with the same maximum field taken for major loops, usually $1\,kOe$, in negative and positive direction. Minor loops were measured with high resolution to see possible small changes in the characteristic ways with kinks. Also, several major loops were measured to get an overview of sensors behavior and to see possible changes due to the presence of beads in the outer parts, i.e. higher total values of H_a. Only a low resolution was chosen, because the effects are expected to be be at high fields stronger than at low fields. It was also checked with the major loops whether the curve is reproducible on a big scale (– otherwise it could be hard to see even relative big shifts).

In a first quick check the values of table 4.1 were measured. There are two values in orientation a, because during a pause the displacement of the sample was necessary.

(a) MA, orientation `a`

(b) MA, orientation `b`

(c) MI, orientation `a`
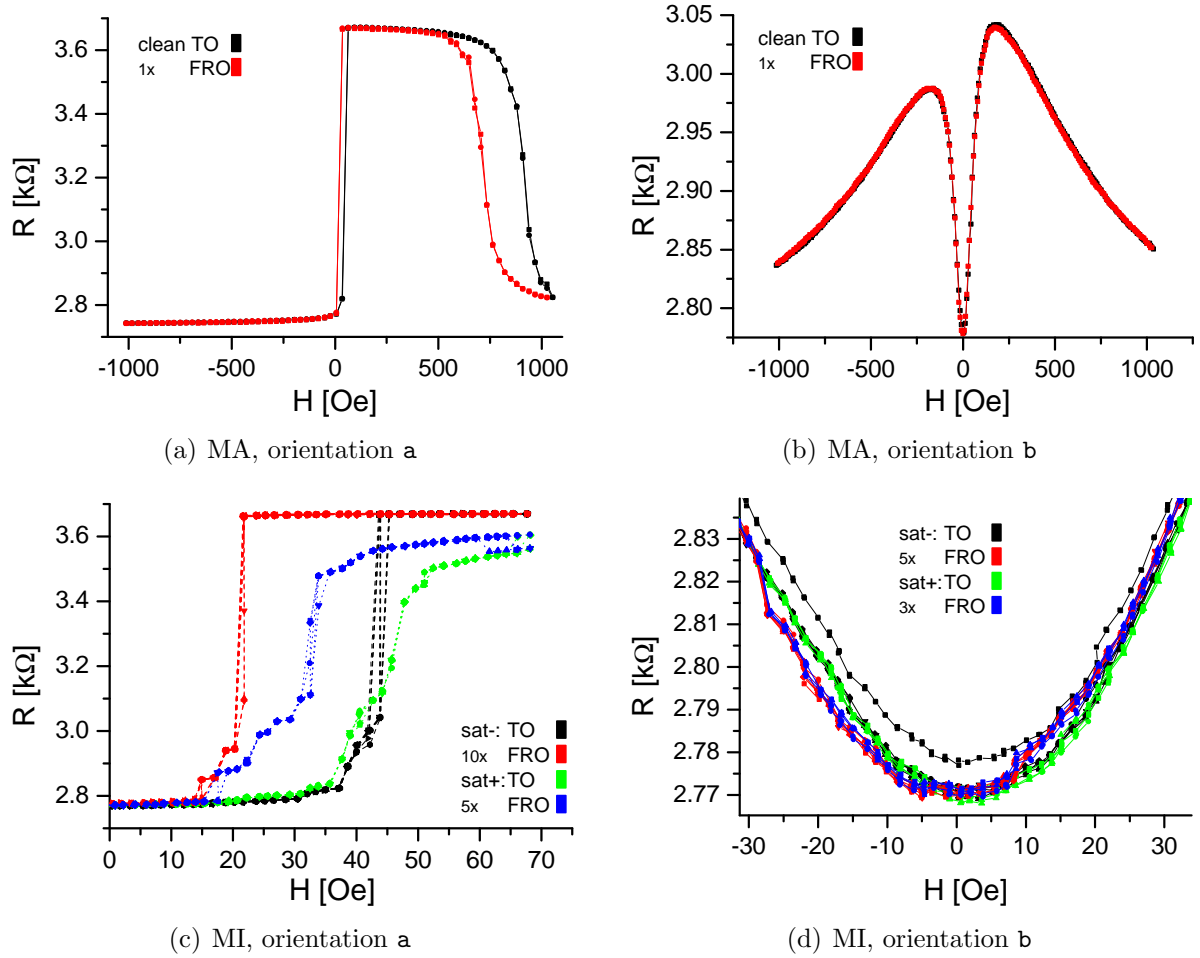
(d) MI, orientation `b`

Figure 4.1: Exemplary data of first characterization (sensor 37).

Every time when the orientation is changed, and when other measurements are done at the TMR measurement place the sample is replaced. The characterization shows that the mean values of R differ with contacting, but still are within the standard deviation. After the pause of measurements $\bar{R}$ is with $2.76\,k\Omega$ ("a after break") slightly higher than $2.73\;k\Omega$ ("a at first") or $2.74\;k\Omega$ ("b"). This cannot be due to different contact pads (see workflow in section 3.2.3), but probably due to a changing resistance of the contact. The tip is bent and moves a little bit during contact, but it does not relax always back into the old position. With the optical microscope scratches are visible on the pads and the surface is dirty after TMR measurements, so maybe surface material is collected which alters the effective surface of a tip.

A plot of the resistance of all elements is given in figure 4.2. One can see that R is characteristic for specific elements, because generally all three measured values are equal for one element. Furthermore R is not obviously related to the length of the upper conducting line, which would result in maxima near element 1, 20/21 and 40. Although R

orientation	R [$k\Omega$] (at zero field)				AR^a	**TMR** [%]			
	mean	σ	min.	max.	[$k\Omega \mu m^2$]	mean	σ	min.	max.
`a` before pause	2.73	0.04	2.61	2.80	18.2	34.11	0.41	32.80	34.70
`a` after pause	2.76	0.03	2.67	2.83	18.4	33.88	0.35	32.75	34.44
`b` before pause	2.74	0.04	2.61	2.80	18.3	9.55	0.34	8.68	10.90

[a]Area $A = \pi \cdot 4.0\,\mu m/2 \cdot 2.1\,\mu m/2$ according to a SEM image provided by KARSTEN ROTT[Rot]. Please see text for comment on dimensions.

Table 4.1: Values of first measurements for characterization.

decreases from element 1 to element 15, the maximum is around element 23, and remains on a level until the end, with respect to the normal fluctuations. These are sometimes very much, especially a low resistance at elements 9, 19 and 25, so these reproducible values characterize the elements. This result indicates, that the varying length of the upper conducting line is not important with respect to the range of individual resistance of an element.

As mentioned in section 3.1.5 the observed size of sensors can differ during lithography processes and the accuracy of the OM can be not high enough for submicron-sized elements. The different observed dimensions for the used sensor are:
- $3.904 \times 2.24\,\mu m^2$ at OM (approx. 66×35 pixel with $100\times$ magnification)
- $3.95 \times 2.14\,\mu m^2$ ($\sigma \approx 0.02\,\mu m$ each) mean values with SEM after cleaning
- $4.002 \times 2.12\,\mu m^2$ with SEM after etching of elements (by ROTT[Rot][43])
One can see that for these relative large sensors the optical images are almost as good as the SEM images. The latter differ a little bit, but that is with $<1.5\,\%$ of no concern.

The used sensors have the principle disadvantage of a hysteresis in their switching, but an influence should be visible also on such a curve in some way. Calculations of the general influence by the stray field of a bead are discussed in section 1.2.3. Therefore this field of sensors is used for measurements.

---

[43]Only one element was examined, so the removing should not be influenced (see section 3.1.5).
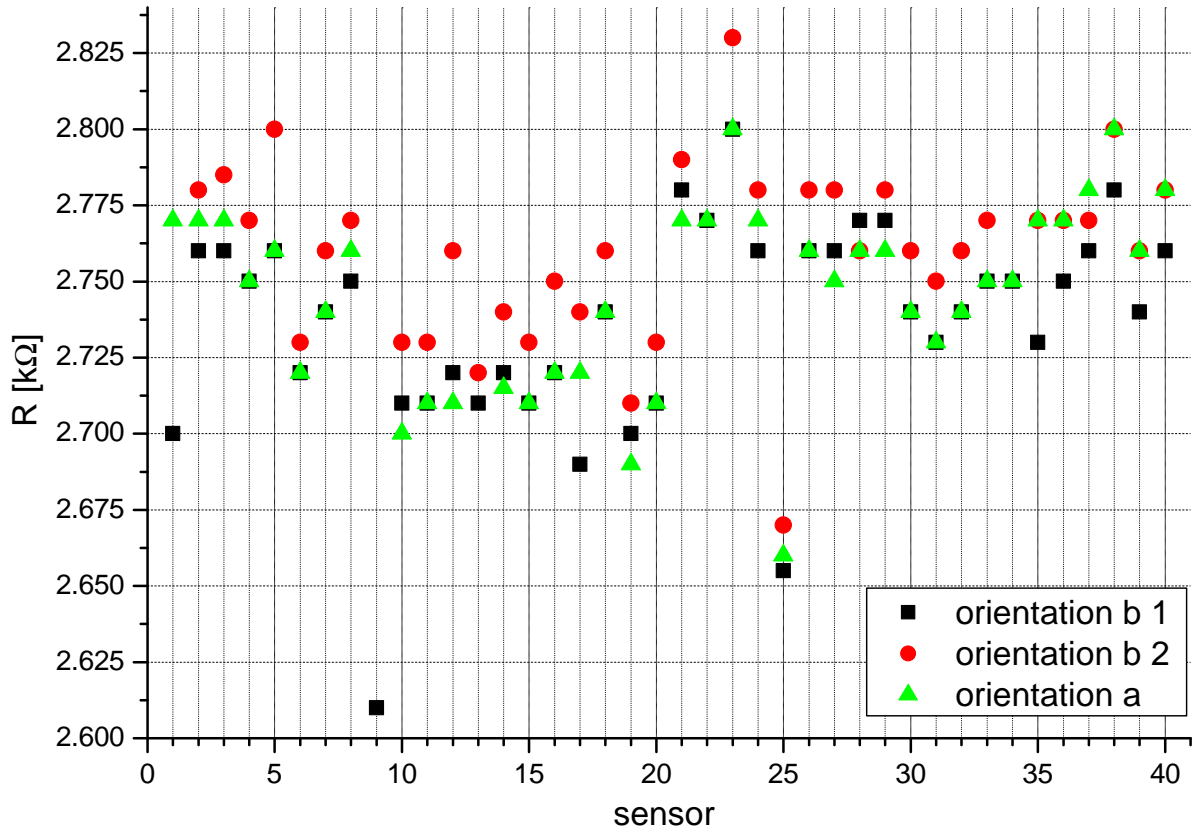
Figure 4.2: Measured resistance during first characterization.

Influence of Exact Orientation

There is no sensitive fixation possible in the original TMR setup, introduced in section 2.7, for the sample or the tip of the gauss meter related to the core magnets. A variation in the alignment results in a field variation on the tip or sample:

- Tilt of gauss meter tip caused larger/shrinked field, because if the sensitive plane of the tip is tilted out of the perpendicular position towards the magnetic field only a reduced component is measured.

- A moved tip had no influence which proved that the field is homogenous.

- Twisting the sample leads to twisted data curve, which is especially visible in orientation **b** where the curve is symmetric with the same height of current/resistance on both sides of zero applied field. If the sample is twisted at one side the signal increases, whereas it decreases on the other side. Which side is effected depends on the direction and on the strength of the twist.

The measurements show how necessary a good alignment of the sample is, in order to get reproducible curves for comparison. So as a first simple fixation the sample's position was marked with a piece of paper (sticky note) attached to the sample station.

| (a) sensor 9 | (b) sensor 17 | (c) sensor 20 | (d) sensor 27 | (e) sensor 32 | (f) sensor 37 |
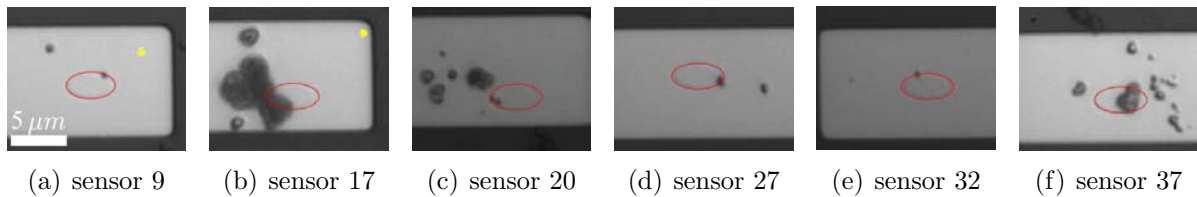
Figure 4.3: Images of working sensors which have maybe beads on top, done with the optical microscope after first dropping. (Yellow points indicate dirt at the OM, deduced by comparison with test images or a second image with a slightly shifted area.)

Easy Breaking of Sensor Elements

During measurements a lot of sensor elements broke, i.e. at the tunnel barrier appear holes which short-circuit the lower and upper conducting lines. After the measurements in the setup with double coils, see section 4.3.1, 19 of 40 elements were useless before the second dropping of beads. The main reasons can be charge effects, so that an element breaks due to a high current peak. Therefore a wooden chair, without fabric where charging of clothes can appear, was used. To avoid charge effects grounding was done with a cable that was always worn. Also the output at the measurement box can be reduced to minimum every time the sample is contacted with the measurements tips.

Summarizing it must be pointed out, that
the sensor elements had an intrinsic high affinity to break which lead to a decreasing number of working specimen.
During later measurements, sensor elements often died in between a succession of measurements, although all precautions were taken. This experience also is the reason to clean the sample only if it is really necessary and therefore it is important to find out a proper dilution of beads, which promises a good dispersion and a fair amount of markers on top of sensors.

4.2 Results of In-Plane Measurements

For the first dropping $1\,\mu l$ dilution was used leading to 6 sensors (namely 9, 17, 20, 27, 32 and 37) which are candidates of having one or two beads on top, visible in figure 4.3. In the OM all six have tiny points on top, but later observations with the SEM indicate that only on sensor 37 are at least two beads, see figure 4.4, whereas only dirt can be found on top of the other five candidates. The presence of beads under the dirt can not be neglected, but in further analyze of measurements this must kept in mind.

The strategy for measurements presented in section 3.2.3 could not be applied every time, because sometimes the sensor elements broke during measurements so that no reference (step 3) was measured and vice versa an additional measurement was sometimes rejected to save the elements. One element broke during measurements, so the results of

(a)   (b)
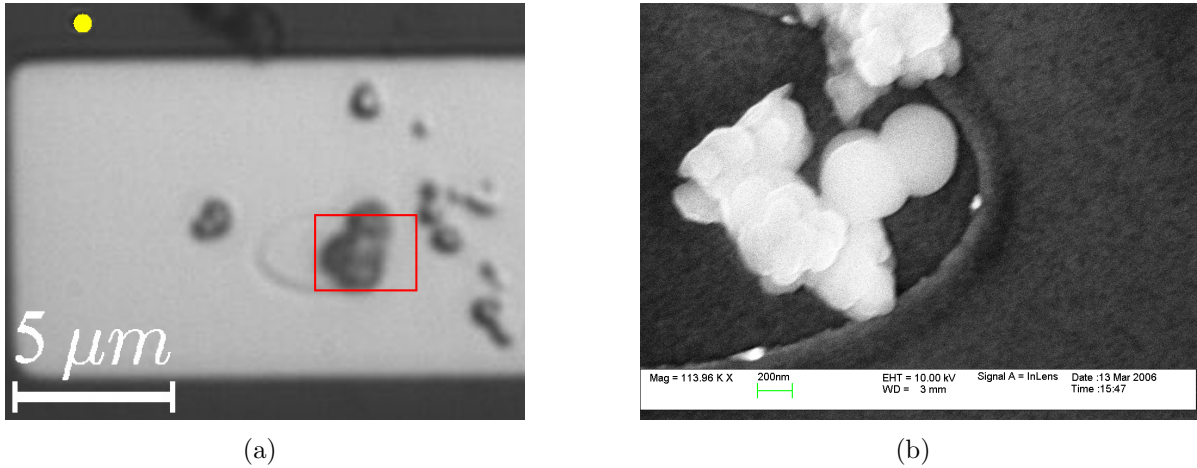
Figure 4.4: Sensor 37 with at least two beads on top: Comparison between image of optical microscope (a) at its maximal magnification and a SEM image in (b). (The $3.2 \times 2.4\,\mu m^2$ area of the SEM image is indicated in (a) by the red box, whereas the yellow point marks dirt at the OM.) With the OM one cannot distinguish between dirt and beads, but also the SEM cannot uncover possible beads under the dirt.

five sensors can be compared. With respect to the mentioned possible effects of twisted tip and sample, see section 4.1, they showed the results, which are listed in table 4.2.

	shift [Oe] in orientation **a**		shift [Oe] in orientation **b**	
sensor	of way FRO	of way TO	of way FRO	of way TO
17	-100	0		
20	0	0		no
27	0 & -45	+50 & +100		shift
32	0	+30		visible
37	(other shape)	+30		

Table 4.2: Shifts in MA of IP measurements, see text for details.

hysteresis of MA measurements, i.e. at high positive applied field, In orientation **a** the outer hysteresis, i.e. the ways TO at about $1000\,Oe$ and FRO at about $750\,Oe$, of MA were almost always shifted, but with different direction and strength as listed in table 4.2. Outstanding is the situation at element 27 where not all measurements showed a shift of way FRO, and way TO was shifted with different strength of 50 and $100\,Oe$, see figure 4.5(a). At element 37 another way FRO appeared which had a slightly other shape in the antiparallel state as visible in figure 4.5(b). Contrary in orientation **b** no difference between measurements before and after dropping was visible.

The minor loops showed in **b** only little effects, such as shifted kinks. The shift is generally around $1\,Oe$, but in different directions. In figure 4.6 are visible the MI of sensor 32, wich showed the only meaningful shift of kinks of way TO, and at sensor 37

a kink appeared at way FRO in MI. In orientation `a` the MI showed many effects, i.e. shifted (in general $<5\,Oe$) ways in different directions, but with the same shape, and new (shifted) ways with a different shape. Exemplary figure 4.7 shows element 32 with various shifts and the outstanding reduction of four ways FRO before dropping into one way. Also element 37 shows shifts of way TO, which are different for positive (MI+) and negative (MI-) saturation.

In summary no general behavior is visible, only little effects which have no clear tendency.

Discussion

There must be a specific effect of a bead to distinguish between sensors with and without bead on top. The different directions and the varying strength of the shifts, including no shift at all, are present at almost all sensors although they do not all have a bead in their neighborhood. Without this knowledge the MI measurements in orientation `b` can be suggested to be influenced by a bead: The Later switching at sensor 32 can be explained by a diminished in-plane field due to the stray-field of a bead. That element 37 has an additional kink can be the result of a diminished field, due to the stray-field of a bead, which cannot switch domains, which are "collected" and skip together, at once. But the SEM observations gives no indication for a bead on top of element 32, so that this shifted curve must be an artefact. This cannot be the influence of a twisted tip of the gauss meter, because this effect appeared only in one direction, i.e. only at an increasing measurement field. So the measurements are maybe not reliable, and also this kink at element 37 can be an artefact. On the other hand it can also be, that the appeared kink is a normal characteristic way, which appears not very often, and therefore was not measured so far. This result points out that also in orientation `a` the shifts are useless, because at both elements, 32 and 37, effects in minors, figure 4.7, as well as in major loops, table 4.2, are visible, although there should be no difference at element 32. Therefore the shiftless MA data of sensor 20 must be an astonishing coincidence and does not prove that there is no bead on top of that sensor. Summarized the result is: *This setup only shows statistical variations, but not the presence of a bead.*

One general thing can be modified: A perpendicular field (PPD) to align beads during measurement can be used. The aspects mentioned in the theory on page 17 encourage to use this kind of detection principle.
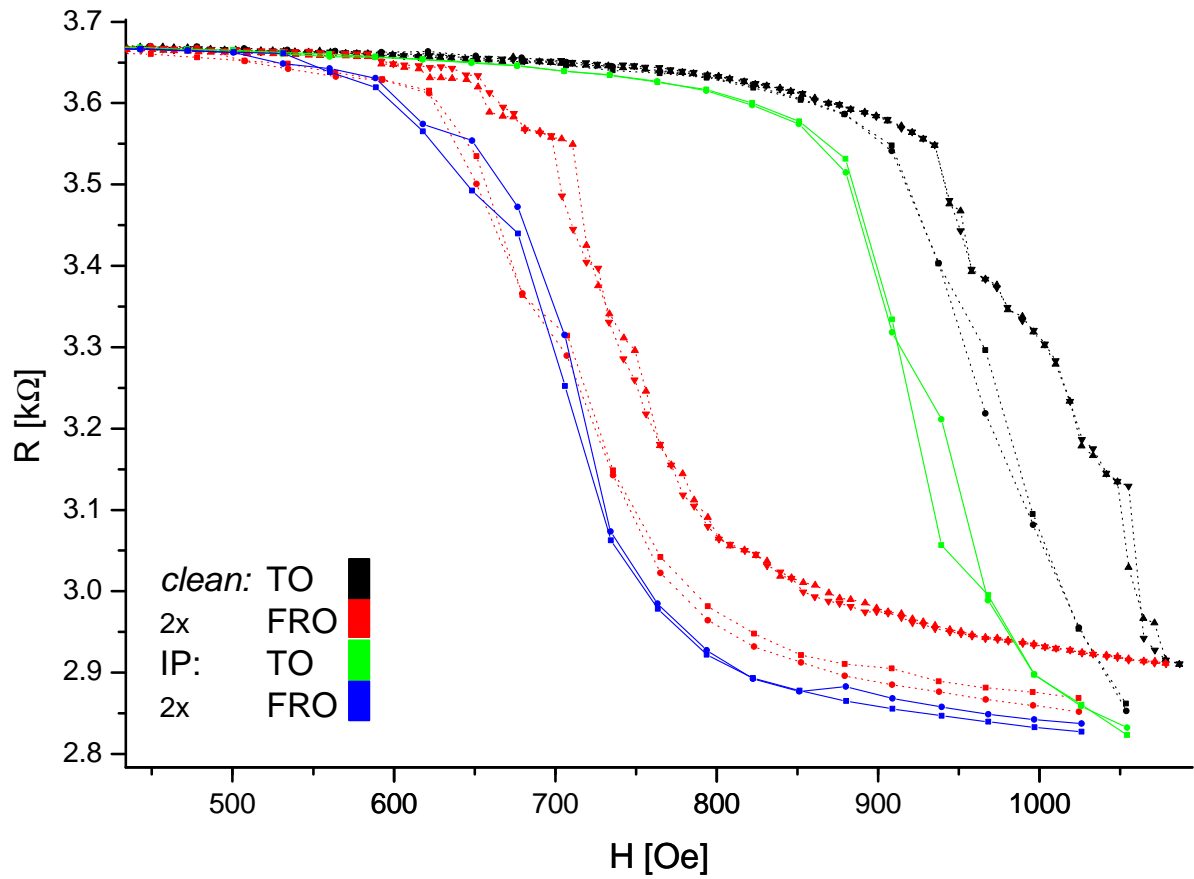
(a) sensor 27
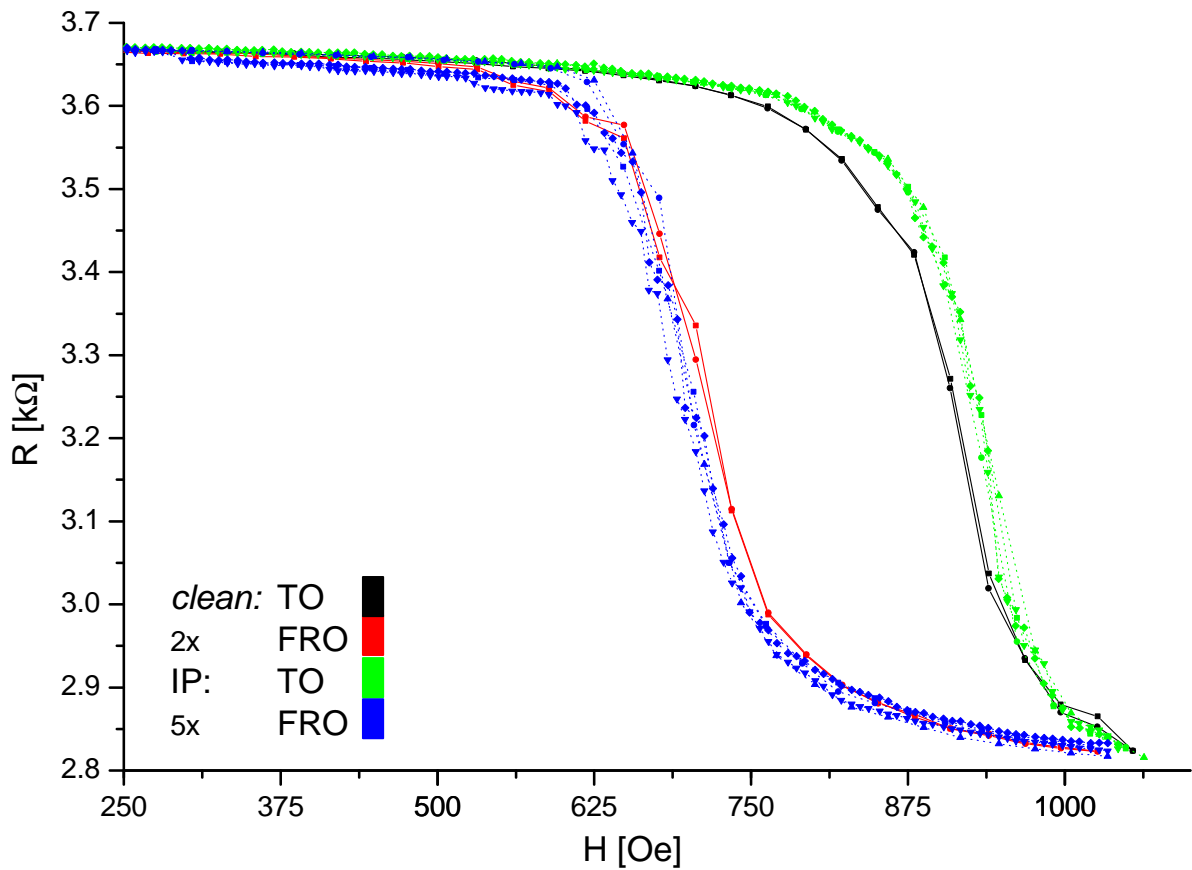
(b) sensor 37

Figure 4.5: Outstanding shifts of major loops in orientation `a` with IP magnetizing field.
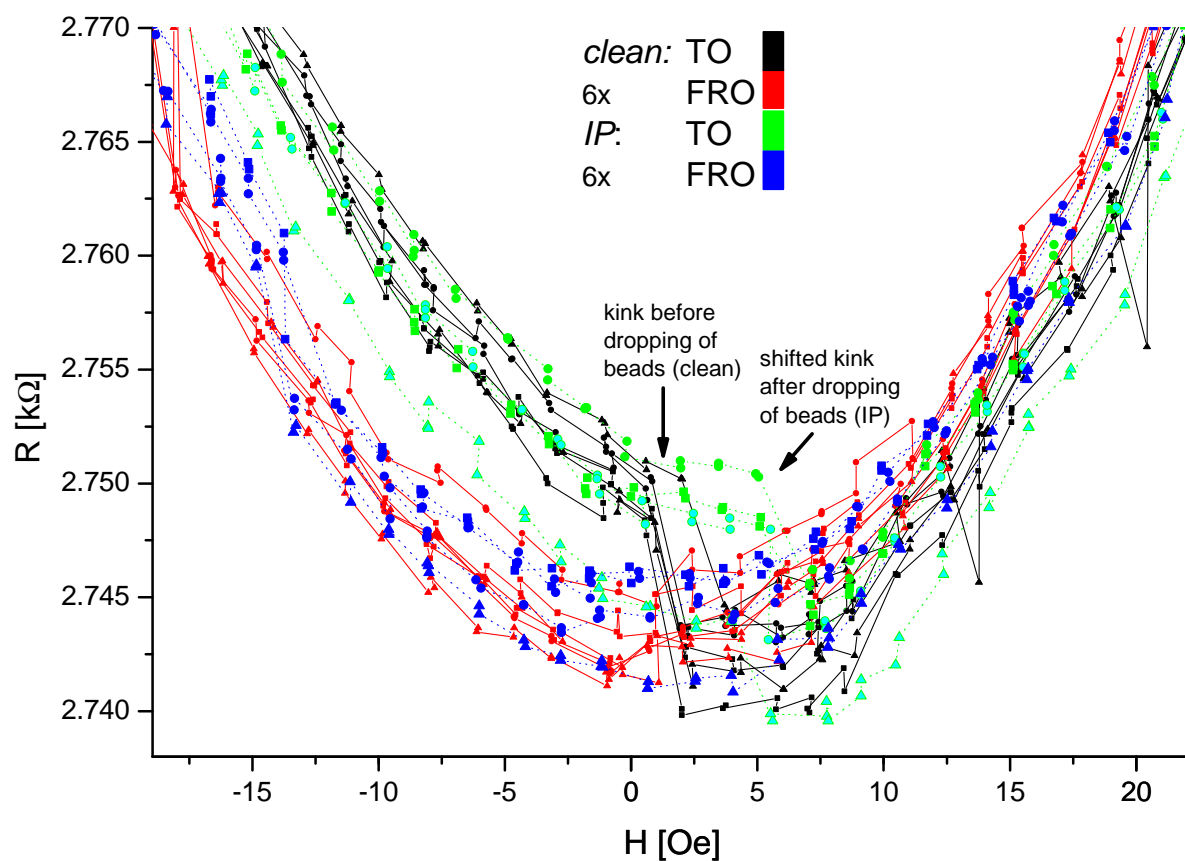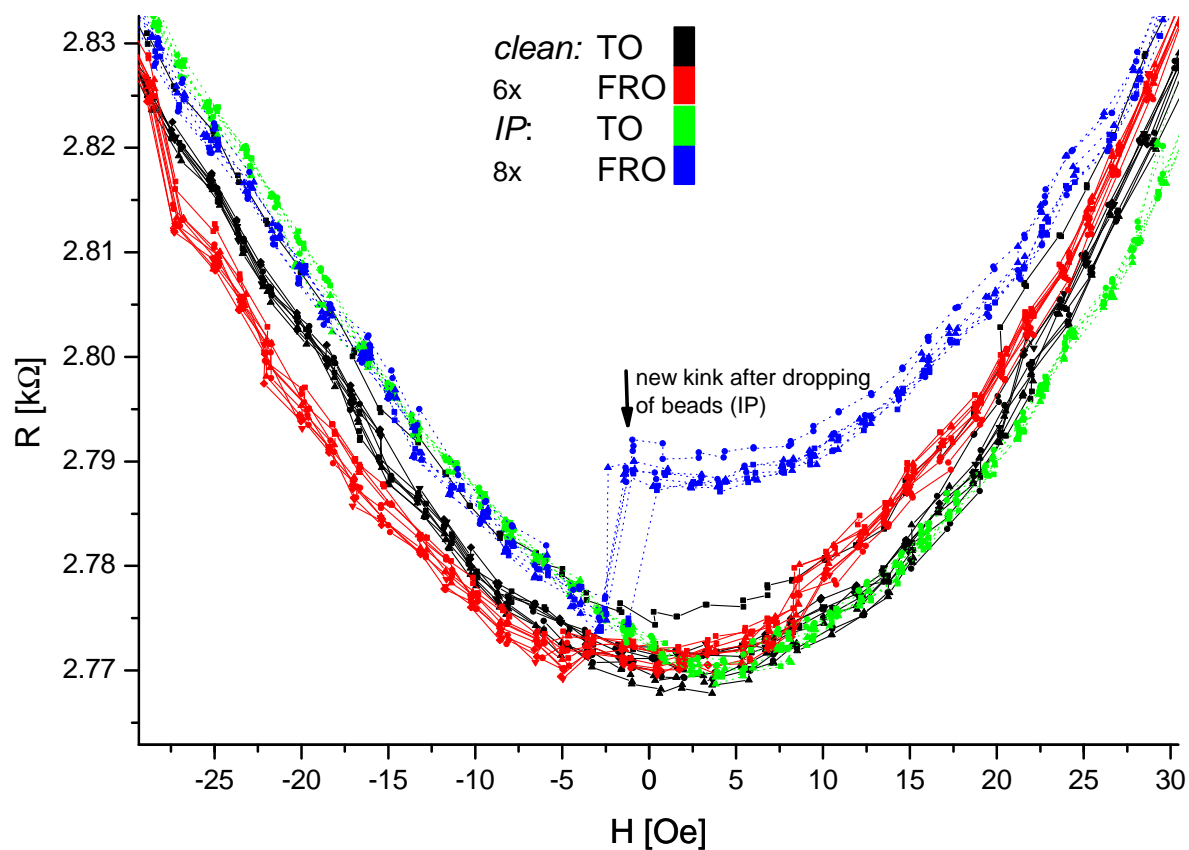
(a) sensor 32

(b) sensor 37

Figure 4.6: Visible shifts of kinks in minor loops, measured in orientation b with IP magnetizing field.
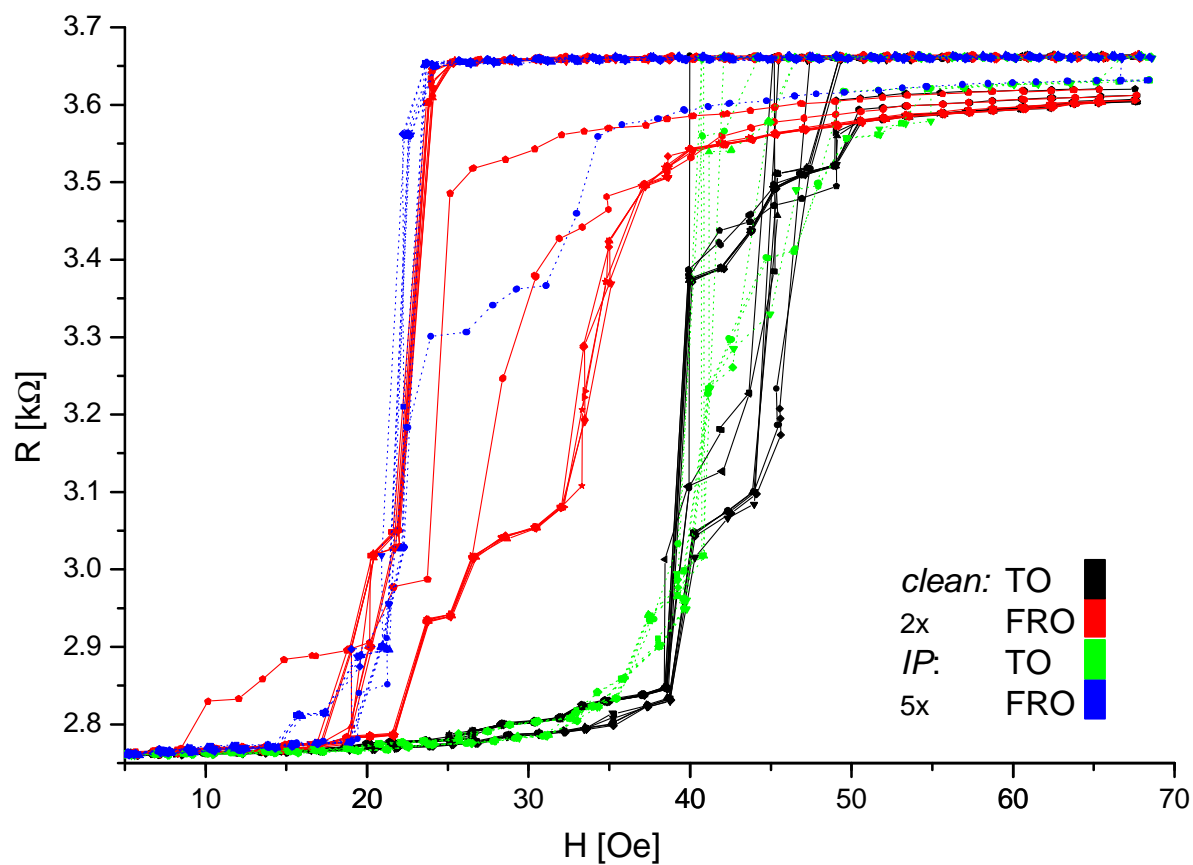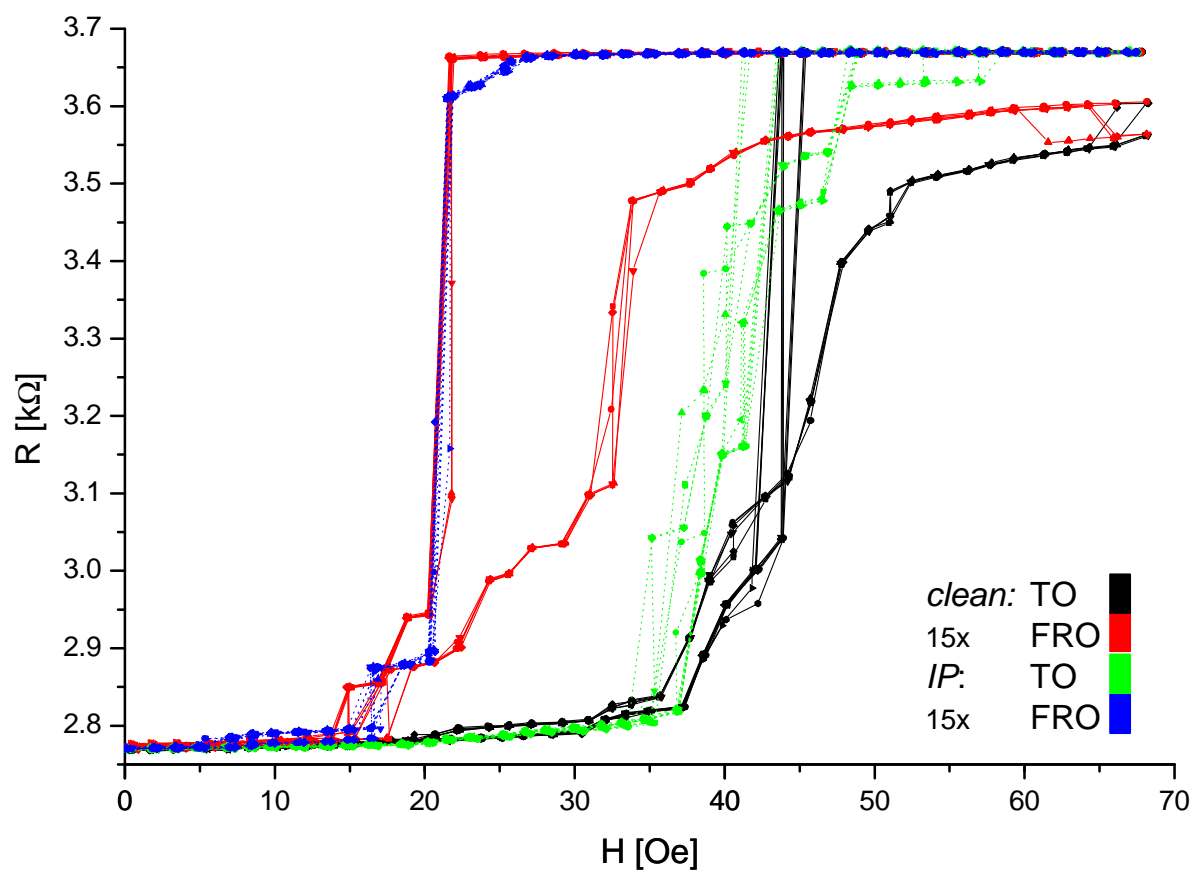
(a) sensor 32

(b) sensor 37

Figure 4.7: Outstanding characteristics of minor loops in orientation a with IP magnetizing field.

4.3 OOP Measurements with Coils

The IP setup, used in the last section, is not applicable for the detection of beads, but the discussion in the last section encouraged the application of an OOP setup: For the saturation of beads perpendicular to plane a steady field is used, e.g. based on (Helmholtz) coils or permanent magnets. (The theory of those magnetic fields was already discussed in section 1.2.1 and 1.2.2.) With respect to a later application, such as a lab-on-a-chip, coils should be used to create a variable perpendicular saturation field. If small fields are enough they can also integrated in a minimized form, to produce a local field. Solutions using permanent magnets can have the disadvantage of a not homogenous field and they cannot be switched on and off.

4.3.1 Setup
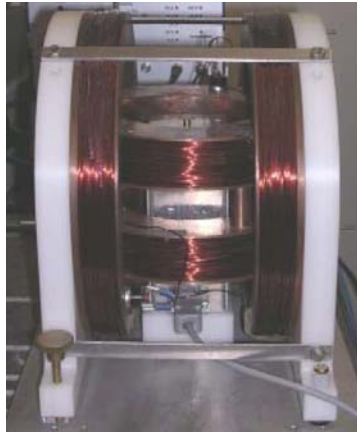
Figure 4.8: Setup with two pairs of Helmholtz-coils by JÖRG SCHOTTER. [Sch04, figure 14]

Measurements were done in a setup, visible in figure 4.8, which was used and built by JÖRG SCHOTTER[Sch04, section 2.8, p. 25]. In principle one pair of Helmholtz-coils is placed 90° twisted into a larger pair of Helmholtz-coils. One is controlled to have a steady field, the other's field is swept for being applied as a measurement field. The sample is placed at the middle of all coils, using the advantage of the Helmholtz-coils' homogenous fields. SCHOTTER wrote: "The maximum field magnitude is $40\,kA/m$ [$\approx 500\,Oe$] in one direction and $24\,kA/m$ [$\approx 300\,Oe$] in the orthogonal direction." In fact $250\,Oe$ were used for OOP field and $200\,Oe$ for IP field inclusive saturation, due to restrictions of the setup. The setup was checked with a gauss meter, which proofed the homogeneity of the PPD, but a precise alignment of the gauss meter tip towards the Helmholtz-coils and the sample was not possible. Therefore the space between the two pairs of coils hinders the measurement of angles and distances.

Further parameters and workflow are as before, including the dropped beads on the surface to save the elements and to make a direct comparison with the in-plane setup possible. After cleaning the sample reference measurements were performed.

4.3.2   Results

Full measurements of only two elements could be collected, namely bead-candidate 37 in orientations a and b, and reference element 38 in orientation a; all other bead-candidates broke during the measurement period, as well as reference element 38 after measurements in orientation a. Further measurements of elements as reference would be useless due to the changed characteristics of a new aligned sample.

data	R_p [$k\Omega$] at -150 Oe		R_p [$k\Omega$] at 0 Oe		R_{ap} [$k\Omega$] at +50 Oe	
NO & PPD	2.76	2.78	2.78	2.80	3.66	3.67
cleaned	2.83	2.81	2.85	2.83	3.74	3.72
1st charac.	2.79	2.78	2.81	2.80	3.72	3.70
sensor	*37*	*38*	*37*	*38*	*37*	*38*

	data	width [Oe]		middle [Oe]	
	NO	21	18	27	26
hysteresis:	PPD	7	10	22	29
	sensor	*37*	*38*	*37*	*38*

Table 4.3: Results of measurements with in double-coils setup in orientation a.

With PPD no hard switching on both elements is visible whereas without PPD only hard switching is observed. The resistance R is higher after cleaning, comparable to the data of the first characterization in section 4.1. General differences are visible in the hysteresis:

The characteristics of elements 37 and 38 in orientation a are listed in table 4.3. One can see that after cleaning of the sample, i.e. reference measurements, the resistance is higher, both for the parallel and antiparallel state in the range of 0.05–0.1 $k\Omega$, compared to the data without perpendicular field (NO) and with PPD applied. The shape of the curve from the cleaned sample is comparable to the data without PPD (with respect to the higher resistance level) and also to the first characterization that was done before the first dropping of beads (after a pause, see section 4.1). There are slightly other kinks and/or a shift, but the shape is all in all the same. A special detail is at element 37 one missing way FRO that appears only in NO data. At sensor 38 one way FRO (which begins at approx. 23 Oe) appears only in the old characterization, and an additional way FRO appears at a lower applied field (begin at 7 Oe) in the cleaned data curves, see figure 4.9. As an example for the slightly different shape and the shifted resistance of the measurements without field (colored black), after cleaning (red) and from the first characterization (blue; see section 4.1), the upper edges of the switching are shown in figure 4.10. Both sensors (37 and 38) show without PPD almost the same hysteresis, i.e. middle at 26–27 Oe and a width of 18–21 Oe. Equal is also that the resistance without applied PPD drops less sudden than in the other two measurements, i.e. after cleaning and the first characterization. Whereas the data from the cleaned sample shows at sensor 38 really hard switching, for sensor 37 also in the old characterization R drops abrupt.
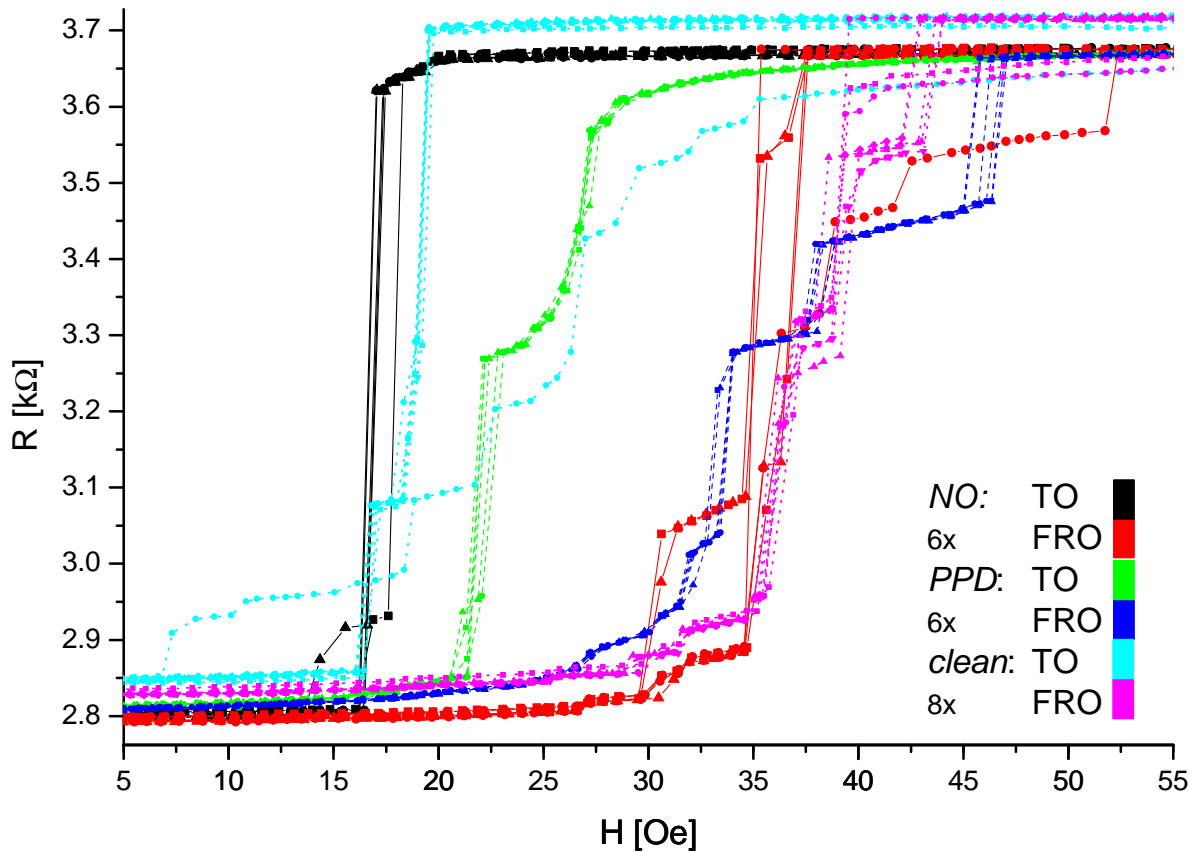
Figure 4.9: Sensor without beads: Additional ways appear in PPD measurements (orientation a with coils-setup).

These differences are negligible compared with the PPD data: As visible in figure 4.11 the curves with applied perpendicular field show a much more softer switching combined with a variation of both, the middle and the width of the hysteresis. Table 4.3 shows a much more reduced width of the hysteresis at sensor 37, i.e. $21 \rightarrow 7\,Oe$ instead of $18 \rightarrow 10\,Oe$. The middle of the hysteresis is almost equal if no PPD is applied with $27\,Oe$ and $26\,Oe$ (sensor 37 and 38, respectively), but with PPD the middle is shifted in opposite directions, i.e. $-5\,Oe$ at sensor 37 and $+3\,Oe$ at sensor 38.

In orientation b only data for element 37 is available, shown in figure 4.12, because sensor 38 broke as mentioned above. There are two kinks at $-2\,Oe$ and $37\,Oe$ at sensor 37 which are shifted to higher field values. They appear in the PPD data later at about $6\,Oe$ and $39\,Oe$, respectively. The cleaned data is comparable with the data of no PPD applied, but the resistance is shifted up at about $15\,\Omega$. The minimum of the MI is at $2.84\,k\Omega$ in the parallel state of the NO curve, and at about $3.09\,k\Omega$ in the antiparallel state. Contrary to orientation a the data of the first characterization is not equal to the NO and the cleaned data: The curves minimum is lower ($2.81\,k\Omega$) and has a slightly different shape with other kinks.

(a) sensor with bead   (b) sensor without beads
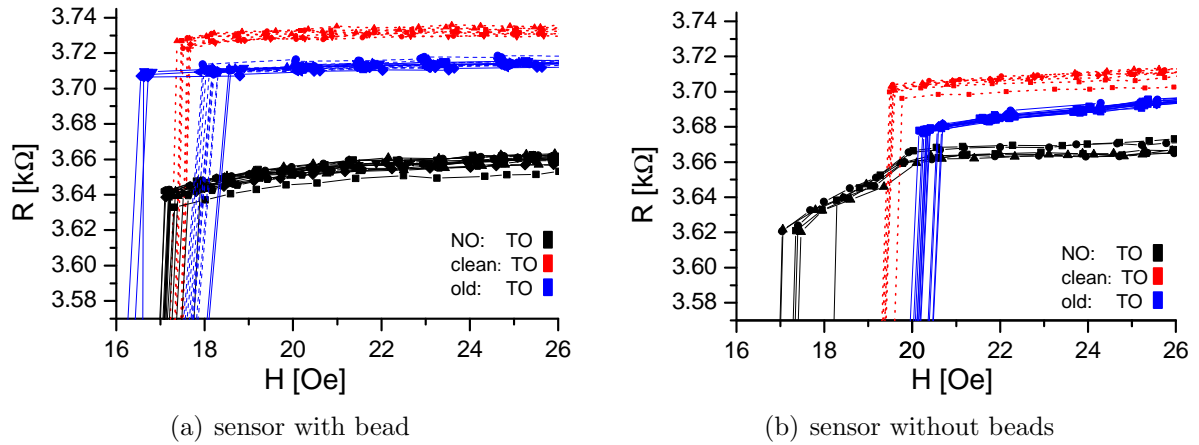
Figure 4.10: Slightly differences of switching behavior into antiparallel state (orientation **a** with coils-setup).

4.3.3   Discussion

*The possible effects by the stray field of a bead are a shifted soft switching field in orientation **a** (and maybe shifted kinks in orientation **b**).*
This result can be deduced after the discussion of the resistance, the appeared special ways and the switching behavior, i.e. soft versus hard. Due to the varied switching behavior the shape is changed very much and not at all comparable with the data of the IP setup.

As already seen at table 4.1, i.e. the results of the first characterization, the resistance can differ after a displacement of the sample, but laid still within the standard deviation. With the double coils setup the data of NO and PPD at zero field, i.e. $2.78\,k\Omega$ for sensor 37 and $2.80\,k\Omega$ for sensor 38, fit to the old mean resistance of $2.76\,k\Omega$ (measured after a pause). The value of sensor 37 is even a little bit lower than $2.81\,k\Omega$ at the old characterization, which represents almost one of the maximal measured R. These values are topped by the cleaned data, i.e. $2.85\,k\Omega$ for sensor 37 and $2.83\,k\Omega$ for sensor 38, which are not within the old standard deviation of $0.03\,k\Omega$ (at $\bar{R}$=2.76$k\Omega$). This indicates, that *the resistance is influenced by a varying contact area of the tip.*
Reasons can be dirt or a deformation of the tip itself, as mentioned on page 70.

The missing way FRO at sensor 37 (orientation **a**) would be a sign for a bead if it appears at the PPD data, or if it is missing only at the PPD data one can see also the influence of a bead. But this way is also not visible at the cleaned data and in the first characterization, so this has to be an additional way that has not appeared so far. In this case maybe the number of measurements, i.e. 2 MA, 10 MI- and 5 MI+, were not enough to get all characteristic ways. More measurements could be a solution, but as seen during the first characterization (see section "Workflow" 3.2.3) even several dozen measurements revealed not more details. If a curve appears only that seldom it

(a) sensor with beads   (b) sensor without beads
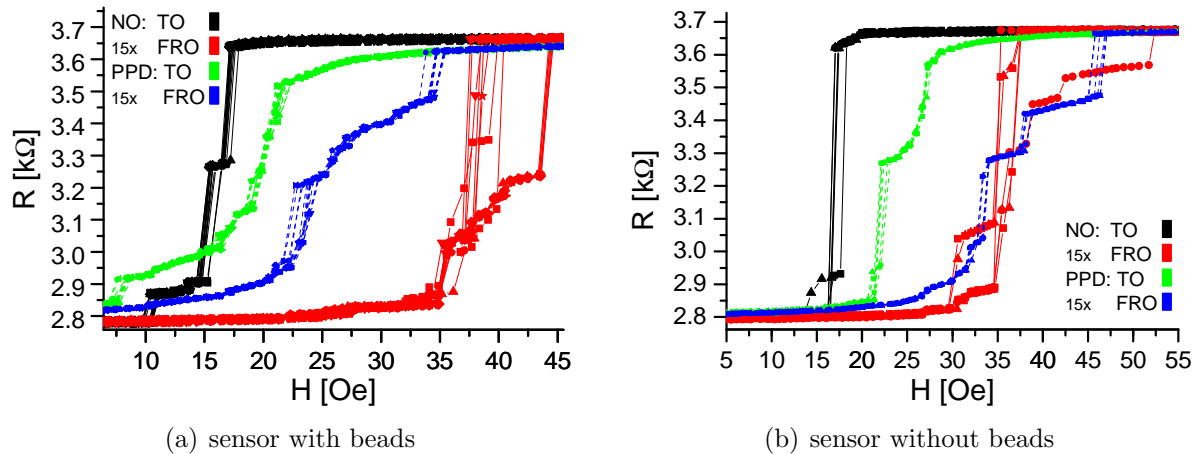
Figure 4.11: Minor loops in orientation `a` with coils-setup.

cannot be called a characteristic way, so it does not make sense to increase the number of measurements. One must keep in mind, that

there can be additional ways which are not characteristic, so it is questionable to use the special shape of a curve as an indication for beads.

With this argumentation the additional ways at sensor 38, see figure 4.9, can also be explained with two ways that simply have not appeared yet in NO and PPD.

A soft switching, combined with several kinks, can appear if the measurement field is too low. Then stable domain states are not switched at once, but via repeated movement and domains (confer section 1.5.3). This explanation does not fits to the results, i.e. no hard switching with PPD, with respect to the following reason: First of all without PPD the measuring field is high enough to produce hard switching, although it is less abrupt in NO compared with cleaned data, but both measurements were done with the same IP field of maximal $200\,Oe$ due to one pair of Helmholtz-coils. Also the stray field of an adjacent bead can reduce the applied field, if the strength of the stray field is high enough. If the presence of beads would induce the softer switching it must be less or not at all apparent at sensor 38 which has no element on top for sure. Only at a distance of 2.9 and $3.2\,\mu m$ were something visible with the OM, with about $\varnothing 3.2\,\mu m$, see figure 4.13, but whether this is dirt or there are beads cannot distinguished without an observation with the SEM (see section 3.3.2).

Much more influence can have ip-plane components of the PPD itself. With respect to the difficult adjusting of angles and distances, see above in section 4.3.1, it is reasonable, that

due to an inaccurate alignment of the Helmholtz-coils, their field is not perpendicular to the sample plane and measuring field. Therefore the PPD disturbs the applied field and is the origin of the visible soft switching.

The presence of a bead can be seen at hysteresis data in orientation `a`, see table 4.3: At both sensors the soft switching of PPD data is shifted into the hard switching field of

the curve without PPD applied, i.e. the shift is positive towards a higher measurement field. Furthermore the width of the hysteresis is reduced with PPD at both sensor as mentioned above. A difference between the sensors gives the middle of the hysteresis H_{EB}, which is with PPD at a lower applied field of about $22\,Oe$ instead of $27\,Oe$ for sensor 37 with beads on top. Contrary in the case of element 38 H_{EB} it is even enlarged with PPD applied, i.e. about $29\,Oe$ instead of $26\,Oe$. This effect cannot be explained with a in-plane component of the PPD, because that has an equal effect on both elements. The influence varies of course at different areas of the sample, but the two sensors have a distance of about $15\,\mu m$ and the PPD was proven to be homogenous in section 4.3.1. An explanation with additional ways also cannot be applied, because the majority of measured ways were all equal at PPD data (see figure 4.11). With respect to the first results (section 4.1), these ways should have appeared also at the other data curves (NO, cleaned and old characterization), so they are no characteristic ways in a setup without a perpendicular field. This is true for both directions, i.e. TO and FRO, in PPD data of element 37. At sensor 38 only the way TO is equal to way TO in the other data curves, but the ways FRO of PPD neither fits to the ways FRO in NO data nor does they fit to the first characterization. Therefore in the cleaned data the additional way appears at the same applied field where the ways FRO of PPD data appear, see figure 4.11. This can be indeed a characteristic way, as discussed above, although it did no appear in the other 36 measurements[44].

The observed shifted hysteresis is contrary to the micromagnetic calculations of SCHEPPER[SSBR04a]. As mentioned in section 1.2.3 the expected influence of beads on top of a sensor should be a shift in direction of the applied field, see figure 1.9, so only the middle of the hysteresis at sensor 38 should be shifted to higher field values. The measurements show differences to the theory in two aspects: At first sensor 38 shows also without bead a shift in the pronounced direction, and the shift at element 37 is negative. Further measurements must solve this discrepancy.

Measurements of an element without beads in orientation b were missing to decide whether later kinks are related to beads in PPD data.

Outlook

The setup yielded not very high fields, but with a (much) higher perpendicular field also the stray field of the beads is higher. If the observed little effects, i.e. a shifted soft switching field in orientation a (and maybe shifted kinks in orientation b), really belong to the PPD, they should be better visible in a higher perpendicular field. With respect to the saturation field of approx. $4400\,Oe$ for the beads, according to the AGM measurements discussed in section 1.2.3, several thousand Oerstedt should be used to get the best signal by the highest stray field from the beads.

---

[44]The following number of measurements was performed on sensor 38:

first characterization:	4 MA & 10 MI- & 5 MI+
double coils-setup without PPD:	1 MA & 3 MI- & 3 MI+
double coils-setup after cleaning:	2 MA & 5 MI- & 3 MI+

One could built up a pair of Helmholtz-coils with such field by increasing the number of turns, use higher currents with adequate wires, and by increasing the radius of the coils, leading to a bigger setup. An alternative are permanent magnets with respect to the high fields that relative small one have. An approach that uses a permanent magnet below the sample for the perpendicular field should be more easy to handle. So in a further experiment a setup with permanent magnets should be used to verify, whether the visible effect of a shifted switching field is really based on the presence of beads.
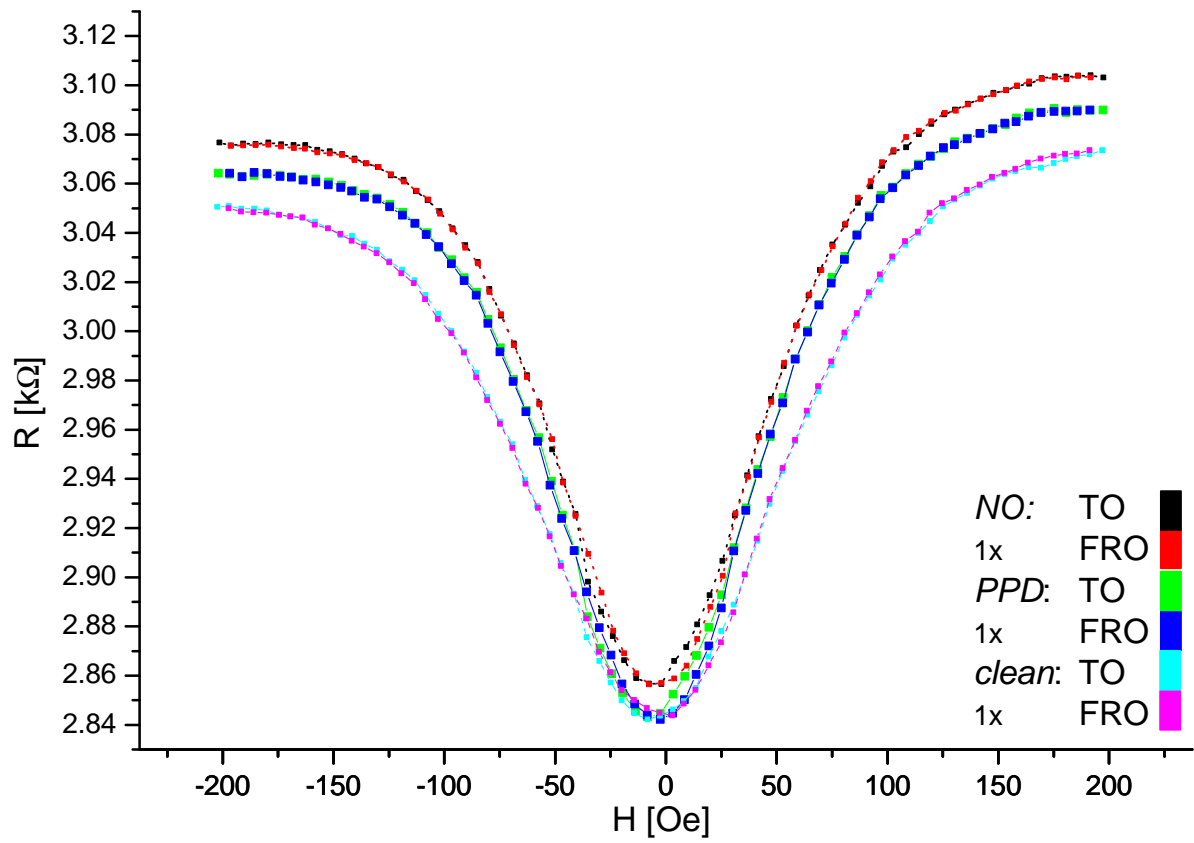
(a) MA
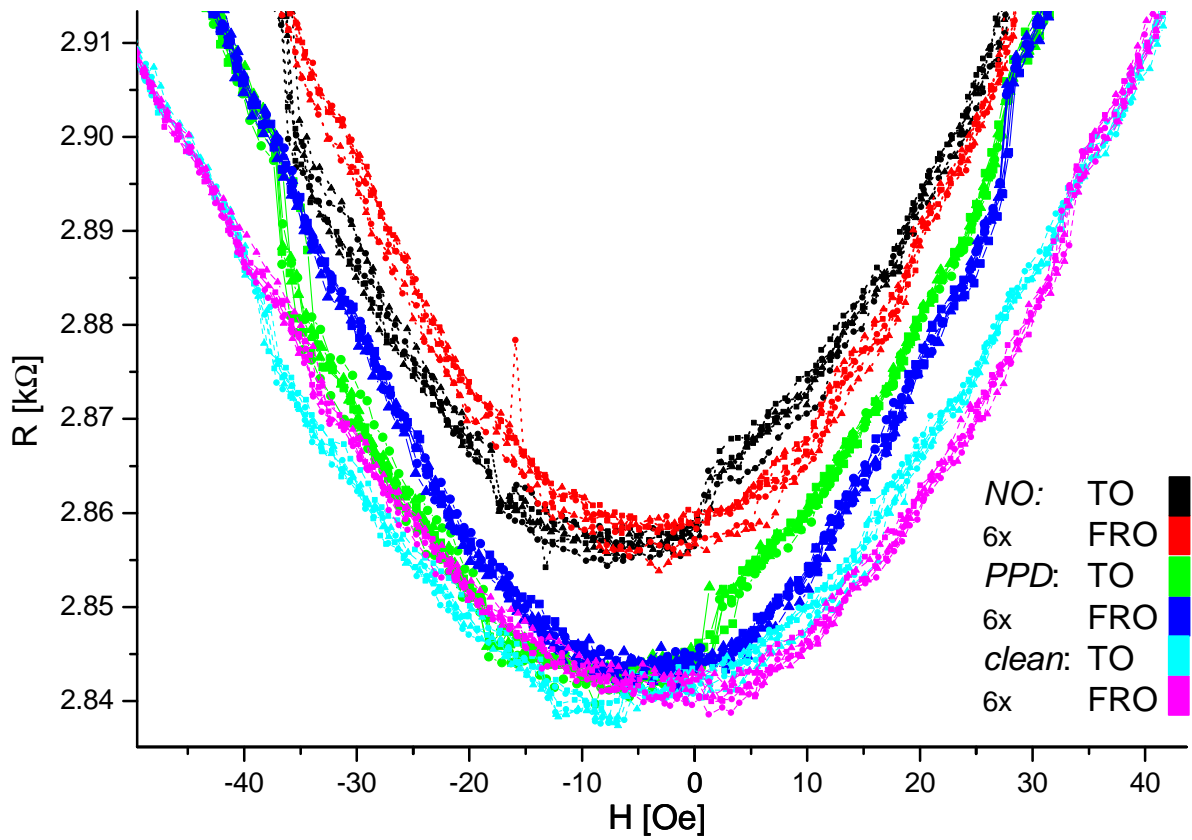
(b) MI

Figure 4.12: Sensor with beads in orientation b with coils-setup.
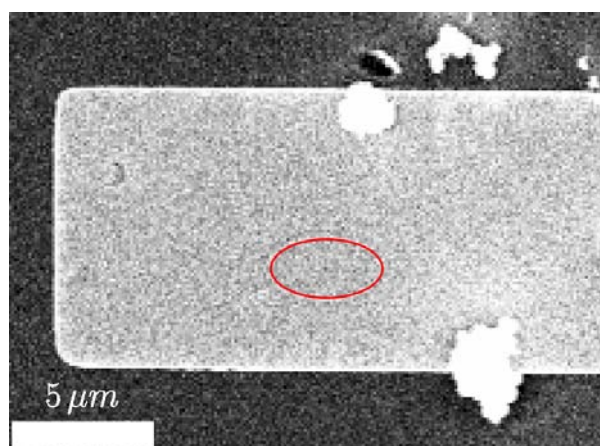
Figure 4.13: OM image (100×) of sensor 38 with adjacent objects.

4.4   OOP Measurements with a Single Permanent Magnet

For the detection of magnetic markers a setup with a permanent magnet as the source for a perpendicular field should be applicable. If the PPD field is chosen higher than that of the setup with the Helmholtz-coils, presented in the last section, the possible effects could be visible: a shifted soft switching field in orientation **a** (and maybe shifted kinks in orientation **b**) as discussed in section 4.3.3. At first the maybe most simple way for application of a permanent magnet was chosen: A special sample stage designed for the TMR measurement place by MONIKA BRZESKA was used[Brz].

4.4.1   Setup
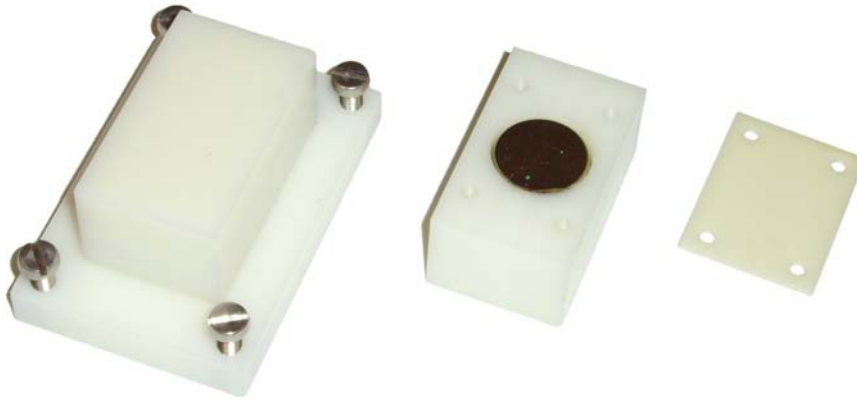
Figure 4.14: Sample stage for usage in the TMR measurement place, provided by MONIKA BRZESKA. The cubic nylon block in the middle contains one permanent magnet for PPD measurements, and is capped with the nylon sheet on the right side. Measurements without an out-of-plane field are done with the massive nylon block on the left side.

The normal sample stage in the TMR setup, which was also used for first characterizations, is replaced by an equal looking one, see figure 4.14, with a hole where a single NdFeB permanent magnet is glued. Above the magnet a $1\,mm$ thick sheet of Delrin[45] is fixed where the sample itself can be placed. The magnet dimensions are a $\varnothing 20.0\,mm$ and a height $5.0\,mm$, in the classification N35 (nominal $11.8\,kOe$[Xia06]) and offers a maximal field of approx. $2000\,Oe$ at about $\varnothing 1\,cm$ for perpendicular usage.

Saturations of $\pm 2000\,Oe$ were applied which should be better than former used $\pm 1000\,Oe$ with the goal of having a fixed state of the sample's magnetization before each MI measurement.

---

[45]"Delrin" is the trade name of the company DUPONT[DuP] for polyoxymethylene (POM), also known as e.g. acetal resin or polyformaldehyde. This engineering plastic is also sold under trade names such as "Celcon" or "Hostaform"[Wik07].

Additional measurements were also performed on sensors adjacent to a candidate with a bead on top in order to have a gradiometer. In fact there were not many possibilities for this task, because several sensors were not working, distributed over the whole array of sensors. As a "result" of former measurements only 21 of 40 elements were still working, so a final cleaning of the sample was not done in order to save the remaining elements.

4.4.2 Results

The second dropping of dilution on the sample, using $2\,\mu l$, lead to 11 candidates after first try, namely element 3, 4, 8, 11, 29, 32, 33, 35, 36, 38 and 40, visible in figure 4.15.

(a) sensor 3   (b) sensor 4   (c) sensor 8   (d) sensor 11   (e) sensor 29   (f) sensor 32

(g) sensor 33   (h) sensor 35   (i) sensor 36   (j) sensor 38   (k) sensor 40
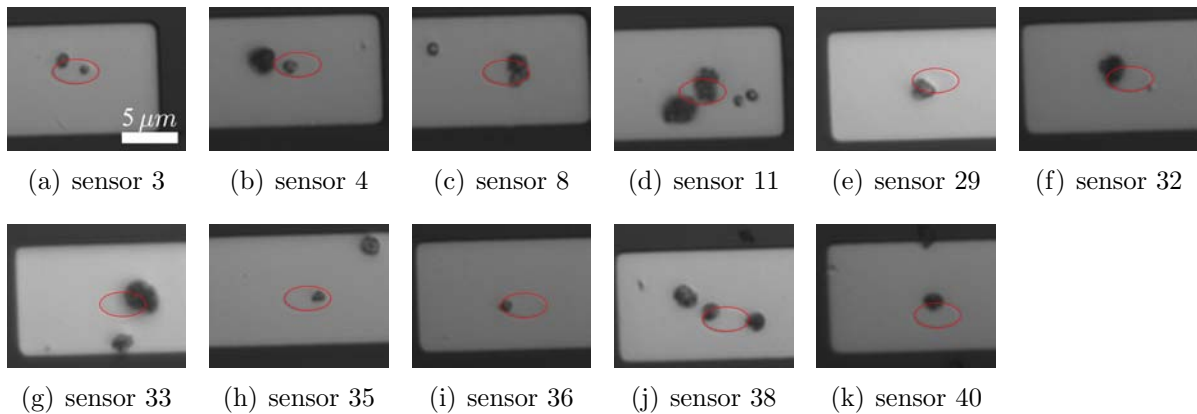
Figure 4.15: Images of working sensors which have maybe beads on top, done with the optical microscope after second dropping. (Yellow points indicate dirt, deduced by comparison with test images or a second image with a slightly shifted area.)

Comparisons of the case with an applied perpendicular field (PPD) and without a perpendicular field (NO) showed the same results. Exemplary the data with PPD is compared to data without PPD for sensor 1.

- Orientation `a` (see figure 4.16):
  The switching near zero applied field is changed very much from a hard switching at an applied field of about 5–$40\,Oe$ to a soft switching: A slope becomes visible at $<$-$200\,Oe$, which is almost linear in the range of approx. 70–$130\,Oe$. The maximum resistance is reached at $450\,Oe$, but it decreases immediately until $>$$1300\,Oe$. At this "right side" a hysteresis of about $100\,Oe$ is visible, as noted in table 4.4. This is less than without PPD where the hysteresis has a width of $190\,Oe$. The hysteresis on the left side in NO data, i.e. the switching in MI near zero applied field with a width of approx. $20\,Oe$, is not visible at all in PPD data. Generally the signal with PPD is on a lower value in the antiparallel state with about $3.5\,k\Omega$ in PPD versus a maximum of $3.66\,k\Omega$ in NO data.
  $\rightarrow$ This is characteristic for all sensors!

(a) MA

(b) MI
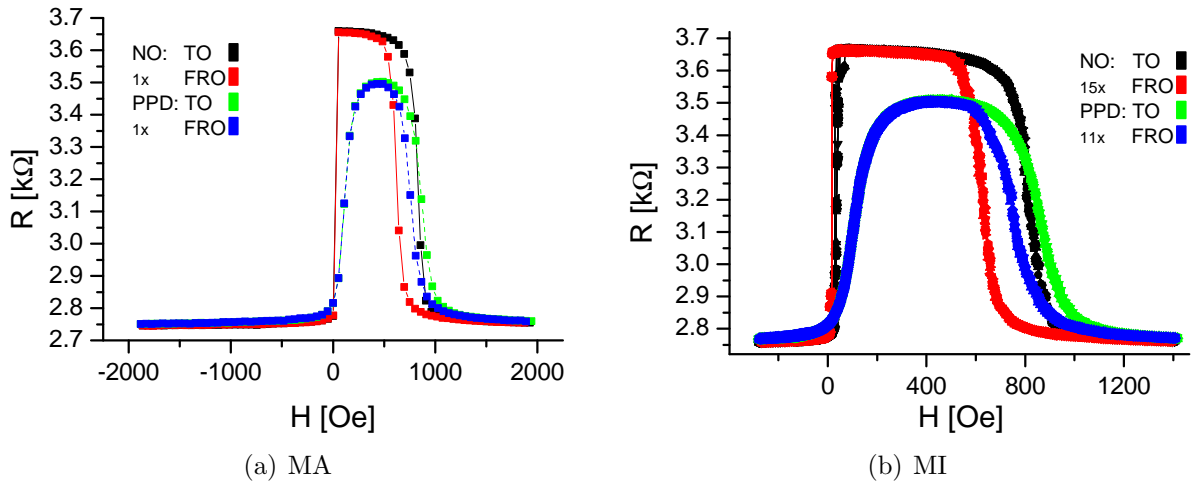
Figure 4.16: Exemplary results in orientation a with single permanent magnet.

(a) MA

(b) MI
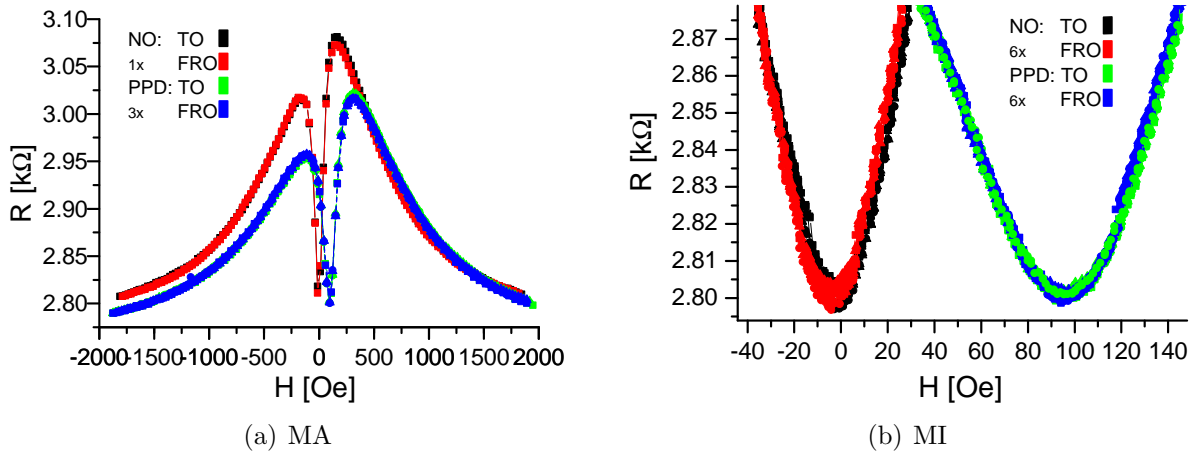
Figure 4.17: Exemplary results in orientation b with single permanent magnet.

- Orientation b (see figure 4.17):
  With PPD the whole curve is shifted to higher fields, i.e. the minimum near zero field appears $100\,Oe$ to the right (in NO data it appears at approx. $-3\,Oe$). The curve is less steep with a generally lowered maximal resistance of about $3.02\,k\Omega$ versus $3.08\,k\Omega$ at positive applied field (and approx. $2.96\,k\Omega$ instead of $3.02\,k\Omega$ at a negative field). Striking kinks near the minimum are only partly also visible in PPD, but additional kinks appear there.
  $\rightarrow$ This is characteristic for all sensors!

  For comparisons in detail the FWHM[46] of the hysteresis in orientation a was determined, as well as the shifted positions of minima in orientation b. The resulting ratio of the FWHM in NO divided by the PPD data, and the shift of minima in b are listed in

---

[46]*Full Width Half Maximum*

| element | FWHM of outer hysteresis in a | | | minima in b (positive) shift [Oe] | bead possible[a] |
	ratio	NO [Oe]	PPD [Oe]		
01	*1.73*	190	110	100	no
02	*0.90*	185	205	100	no
03	*1.60*	200	125	100	yes
04	*1.67*	200	120	≤100	yes
06	*1.87*	215	115	85	yes
11 1st	*1.75*	210	120	80	yes
11 2nd	*1.23*	190	155	75	yes
12	*1.25*	200	160	70	no
16	*1.58*	245	155	≈75	yes
26	*1.60*	200	125	90	no
29	*1.80*	225	125	75	yes
31	*1.50*	180	120	75	no
33	*1.71*	205	120	75	yes
35	*1.26*	215	170	70	yes
39	*1.35*	175	130	60	no

[a] It is not possible to give a certain number of beads, see the corresponding result in section 4.1.

Table 4.4: Comparison of data from sample stage with single permanent magnet in detail.

table 4.4.

The old characterization measurements of section 4.1 showed comparable characteristics in orientation `a` to those of NO data, but at all compared sensors (1, 3, 4 and 16) the old curves have a shift of about 5–7 Oe. Additionally not all ways are visible in both setups. In orientation `b` again all curves of the first characterization are a little bit shifted to the right of about 3–7 Oe at their minima, but due to a less high slope the curves lay over the NO data at negative applied field as visible in figure 4.18. At three elements the minimum of the old curves have a reduced resistance (-10 to -30 Ω), only at sensor 16 the resistance has a value of 2.720 $k\Omega$ instead of 2.715 $k\Omega$. Furthermore kinks are not always reproduced in the new data and vice versa.

The two measurements of sensor 11 with PPD showed these differences:
- Orientation `a` (see figure 4.19):
  A softer switching appears at the second measurement which has also a slightly lower resistance range of -30 Ω. On the right side, at a high positive measurement field, the way FRO is shifted approx. 60 Oe and the upper right edge in antiparallel state has a zigzag shape. Also the way TO differs on the right side from the first measurement with a (slightly) more negative slope.
- Orientation `b` (see figure 4.20):
  The second measurement curves are less steep at a lower resistance level of 2.72 $k\Omega$ versus 2.73 $k\Omega$ at the minima (see table 4.5 for values at zero applied field). These are

(a) MA

(b) MI
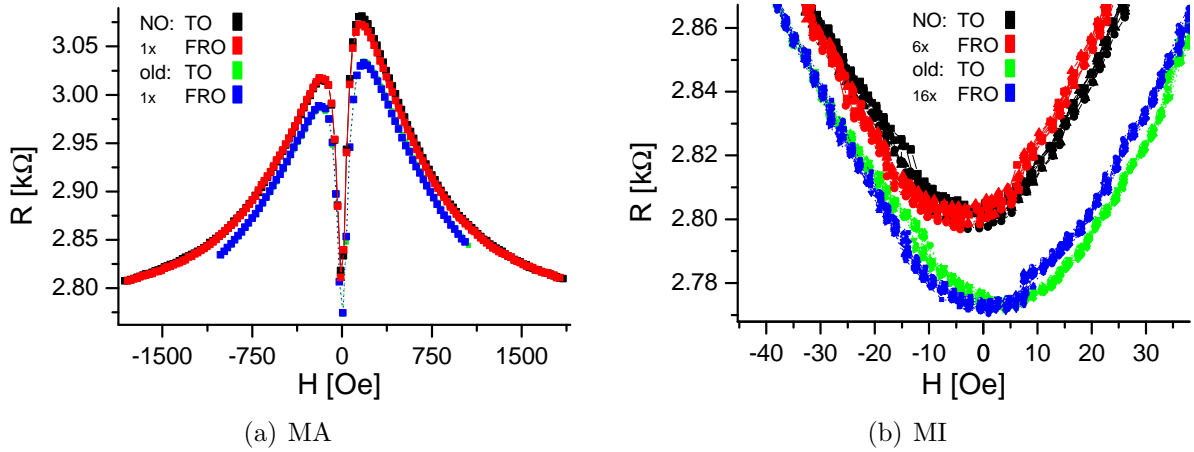
Figure 4.18: Comparison of new data without permanent magnet (NO) and first characterization (old) in orientation b.

shifted from $80\,Oe$ to approx. $75\,Oe$. A maximum resistance of $2.94\,k\Omega$ in the first measurements is reduced of $0.1\,k\Omega$ and kinks are not visible in the second measurement.

In table 4.5 the resistance at zero applied field is listed for both measurements of sensor 11, in comparison with the mean value of all sensors.

orien-	PPD			NO		
tation	mean	11 - 1st	11 - 2nd	mean	11 - 1st	11 - 2nd
a	2.77	2.75	2.8	2.75(2)	2.72	2.71
b	2.8	2.83	2.74	2.75	2.71	2.72
c	3.3					
d	3.5					

Resistance $[k\Omega]$

Table 4.5: Measured resistance with single permanent magnet as PPD: average of all elements and double measurements of sensor 11.

Variations to orientation c and d showed only marginal influence on shape (in a) compared with influence of alignment in PPD.

4.4.3   Discussion

Although the data with and without perpendicular field cannot be compared, one can summarize with respect to the resistance and due to the double measurement of sensor 11:

The alignment of the permanent magnets field towards the sample is not good enough for the detection of magnetic beads.

(a) MA

(b) MI
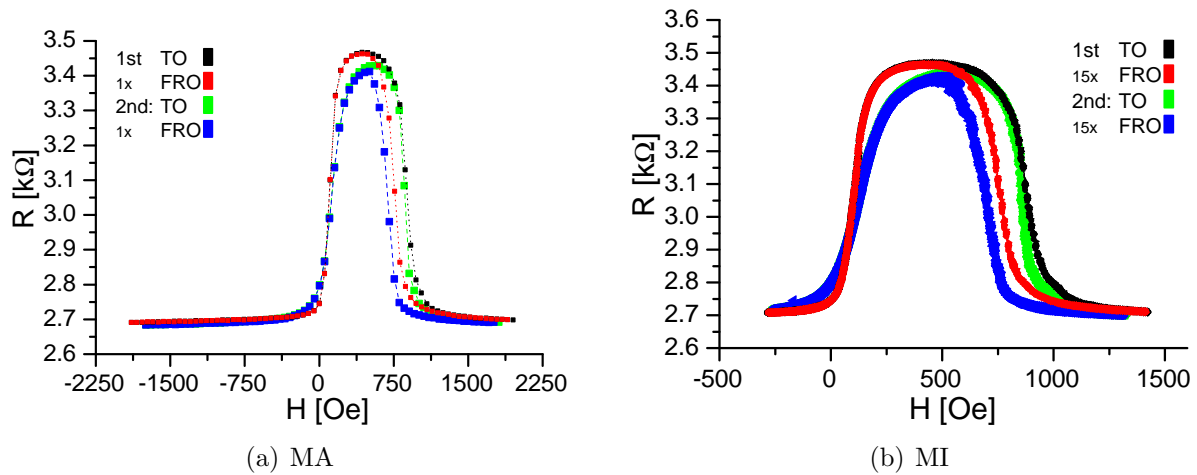
Figure 4.19: Double measurements of one sensor in orientation `a`, with single permanent magnet.

A comparison of kinks and characteristic ways of the switching near zero field cannot be performed, because at this field range the PPD data is completely different to the NO data. The latter curves are "normal" when they are compared with the old characterization, who show only small differences.

First of all one can see in table 4.5, that the resistance is in this case useless, because the values are not reproducible in PPD measurements, which is visible at the first and second measurement of sensor 11. Reasons can be a not really perpendicular alignment, so that there exist in-plane components, and inhomogeneities of the PPD. The magnet itself cannot move, because it is glued, but the position of the sample is not fixed. This result shows that

a better fixation of the sample to the permanent magnet is needed.

The resulting values in table 4.4 give no information whether beads are present or not. Neither for the ratio of FWHM-hysteresis in orientation `a` or its total values, nor for the shift of minima near zero in orientation `b`. For the sensors which have no bead on top for sure[47] the FWHM-ratios differ from 0.90 to 1.73, which includes almost all bead candidates. Although the maximum of 1.87 at sensor 6 is a little bit higher, this is trivial, because the FWHM-values for the other bead-candidates go down to 1.23 and are therefore equal to the former mentioned sensors without bead.

A striking aspect is, that the shift of the minima in orientation `b` drops down, i.e. starting with $100\,Oe$ at sensors 1–3 down to 70–$75\,Oe$ at sensors 12 and 16. Then the trend is skipped, but starts anew with $90\,Oe$ at sensor 26 and ends at sensor 39 with $60\,Oe$. At the design of the sample (figure 3.6 no such antisymmetry is visible, which

---

[47]The elements shown in figure 4.15 are the working elements with possibly at least one bead on top as the observation with the OM indicated. As mentioned for the first dropping in section 3.3.2 one cannot be sure whether there is a bead at all on top or how many are hidden under the dirt.

(a) MA

(b) MI
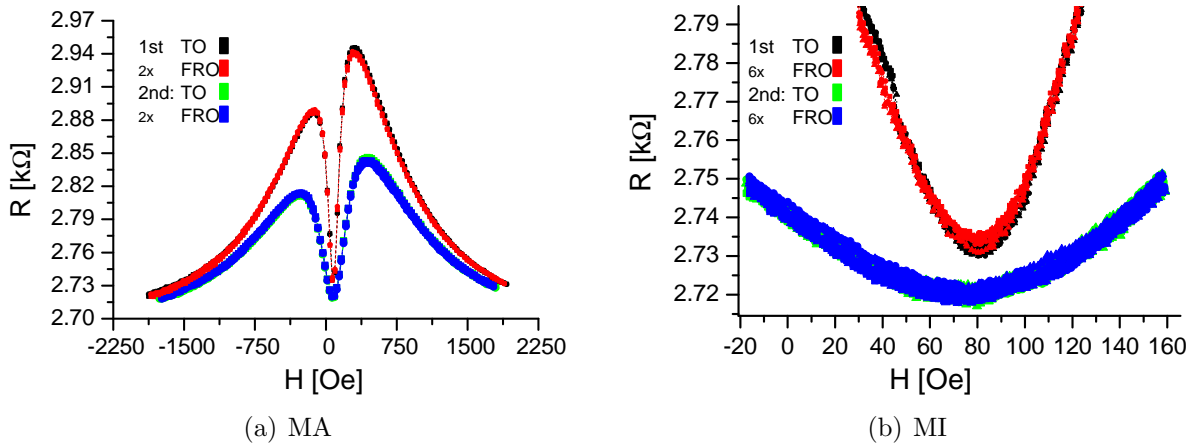
Figure 4.20: Double measurements of one sensor in orientation b, with single permanent magnet.

can be linear from top to bottom of the sensor-array. (The only difference is given by the length of the upper conducting lines, as mentioned in section 3.2.3, but this is symmetric to the middle in the direction from top to bottom.) In table 4.6 the relation between the shift and the position of the sensors on the sample is shown. The measurement sequence is added, beginning with sensor 1 (on day 1) and ending with sensor 12 as the 15. measured sensor (on day 3). Between day 1 and day 2 was a pause, i.e. a displacement of the sample after sensor 39 was measured. The displacement had not much influence on the shift, as visible at sensor 2, who has the same shift as the adjacent sensors 1 and 3. The second measurement of sensor 11 and following of sensor 12 fits also to the general tendency of a decreasing shift value with higher sensor number, although the two values of sensor 11 are not absolutely equal. This shows also no influence of the measurement sequence. Since neither the measurement process, nor the design of the sensor-array can be the reason,
the shift of minima in orientation b is caused by an varying in-plane component of the PPD.

The data of this setup with PPD applied is in general useless
as the results of the second measurement of sensor 11 show; especially the shape in orientation b differed very much, see figure 4.20, but also the soft switching in orientation a (figure 4.19) looks obviously different.

In summary the results showed that the measurements with the simple sample stage were very sensitive to the alignment towards the permanent magnet, and this alignment is very bad. These influences should forbid in principle a detection of beads with this setup, because two measurements must be compared for the detection. Therefore the measurements must be reproducible, so that they do not differ if no bead is present. But the measurements of sensor 11 show that due to the inaccurate alignment a reproducible measurement is not possible. So it does not wonder that there is no sign for the presence

measurement no.	day	sensor	orientation b shift [Oe]		sensor	measurement no.	day
1.	1	1	100		21		
13.	2	2	100		22		
2.	1	3	100		23		
3.	1	4	≤100		24		
		5			25		
4.	1	6	85	90	26	7.	1
		7			27		
		8			28		
		9		75	29	8.	1
		10			30		
5.	1	11 1st	80	75	31	9.	1
14.	3	11 2nd	75				
15.	3	12	70		32		
		13		75	33	10.	1
		14			34		
		15		70	35	11.	1
6.	1	16	75		36		
		17			37		
		18			38		
		19		60	39	12.	1
		20			40		

Table 4.6: Comparison between the position of measured sensors (black numbers), the shift of minima, and the measurement sequence, see text for details.

of a bead.

Outlook

Considerations how to establish a better fixation between sample and magnet included wax and glues as an alternative to clamps. The applicability of wax is thought to be no good opinion, because all results so far indicated, that the alignment must be really good. Ideas applying glues were tried out[48], but were not successful. In principle the application of glues is not possible in a 3-step workflow: For reference measurements the magnet has to be glued a second time which is thought to be not possible with good accuracy, or one must take a switchable (electro) magnet instead of a permanent one.

Although the maximum field strength of $2000\,Oe$ is closer to the estimated $4400\,Oe$

---

[48]Two glues were available: "UHU – schnell härtend" (working time $5\,min$, ready after $30\,min$) needs $>200\,°C$ for separation which is too high for magnetization of the used permanent magnets (NdFeB magnet "N35" is only stable up to $80\,°C$[Xia06, Con]). In another tryout with special photo glue ("Herma Klebstoff no1251 for photos") the rests of the glue could not be washed away with the normal chemicals acetone and ethanol.

saturation field of beads compared with the double coils setup, there is still place for improvement. A solution with the permanent magnets is to use a stack of them, as done in the consecutive setup with a new sample stage for a good fixation of the sample.

4.5 OOP Measurements using a Stack of Permanent Magnets

The discussion in section 4.4.3 pointed out the importance of a good alignment between a permanent magnet and the sensors. The combination of a strong PPD and a good alignment is the consequent improvement of the last setup.

4.5.1 Setup

A new sample stage was developed during this thesis and was fabricated by the mechanical workshop, based on drawings which are visible in figure 4.21 showing the four pieces named "a", "b", "c" and "d"[49]. Following features are available:

- Exact alignment in core magnet of the normal TMR measurement place, with an accuracy of 0.5° and allen screws[50] for fixation of the twistable pieces "b" or "c" in the lower piece "a".

- Easy change of orientations due to removable upper piece "d" and pins which allow only twists in steps of 90°.

- Fixed position of permanent magnets, which are placed in a hole in piece "b".

- Enough place for up to three NdFeB-magnets to get a high magnetizing field for the beads.

Again NdFeB -N35 permanent magnets were used, which are separated by piece "d" from the sample. Piece "d" has a thickness of $1\,mm$ under the sample, so the gap between magnets and beads is $1000\,\mu m$ + approx. $525\,\mu m$ wafer (+ $0.05\,\mu m$ SiOx + stack).

The saturation value was $1000\,Oe$ as a compromise between a high saturation field and less possible movement of the magnets due to a lower applied magnetic field. Additional measurements were performed with the former used saturation of $2000\,Oe$ to enable a direct comparison with the former results and to see the influence of the total value of the saturation field.

A detailed workflow shows the advantages of the new sample stage:

- The sample is fixed with clamps on piece "d".

- An alignment is defined by measuring in orientation b which gives a more or less symmetric curve. Piece "b" is twisted in piece "a" so that measurements show a balanced curve (see section 4.1 "Influence of exact orientation).

- Measurements in orientations a and b are done by a simple twist of piece "d"; maybe also orientations c and d are used to see an influence on the curve. This is done always with and without perpendicular field by changing piece "b" and "c".

---

[49]Non-magnetic materials brass and aluminum were used; dimensions were chosen according to the gap in the TMR setup and for cleaning in an ultrasonic bath.
[50]German: "Inbus®-Schraube"

(a) piece "a"   (b) piece "b"   (c) piece "c"   (d) piece "d"
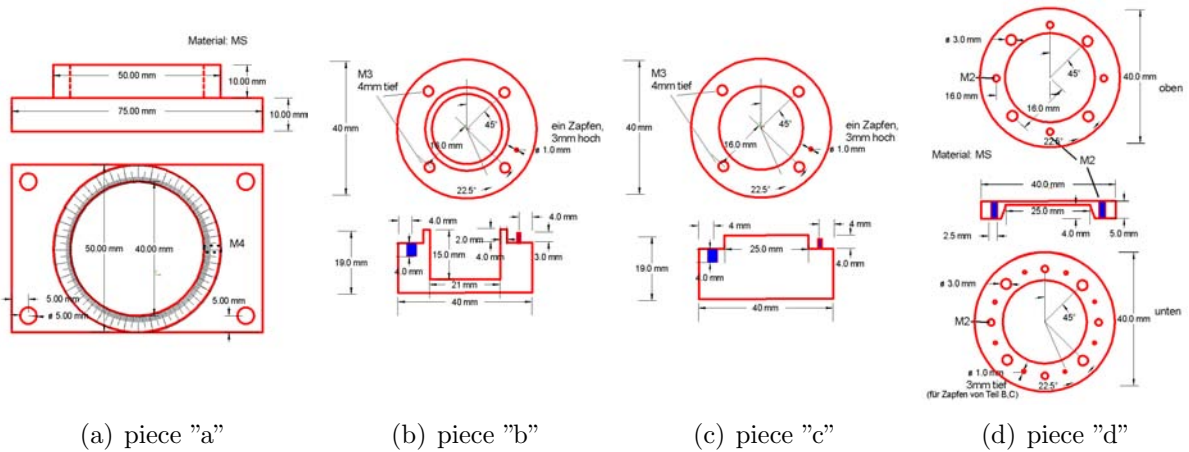
Figure 4.21: Drawings of the new sample stage for the mechanical workshop. From left to right are visible the bottom piece "a" which has a hole where pieces "b" with permanent magnets or piece "c" for measurements without a perpendicular field can be placed. The sample is fixed with clamps on piece "d" which can be placed itself on piece "b" or "c". See text for details on the usage.

- For cleaning, piece "d" is placed within a beaker into an ultrasonic bath.

- Measurements in varying orientations with and without perpendicular field are done as a reference.

Characterization of the Magnetic Field

The magnetic field of the stack of permanent magnets was measured in a quick check with a gauss meter. Therefore piece "b" was placed in the lower piece "a", without piece "d" on top (confer figure 4.22). The middle of the gauss meter tip is placed with a vertical distance of $1.5 \pm 0.1\,mm$ on top over the magnets, i.e. the position of the sample. Its horizontal position is varied in steps of $1\,mm$ or $2\,mm$, where the origin lays at the center of the upper permanent magnet. The out-of-plain component, i.e. tip angle of 90°, was measured twice and one measurement was performed with varying angles of 83° and 75°. Furthermore the in-plane component was measured at a tip angle of 0° and 7°.

The IP component of the stack of permanent magnets was deduced from the measurements at 0° and 7° to approx. $< \pm 500\,Oe$.

In figure 4.23 the measurement of the PPD at 90° is illustrated. The variation for a step of $1\,mm$ is between $10\,Oe$ near the origin, and max. $200\,Oe$ (in diagonal direction) more distant to the center. Generally the PPD variation differs in different directions and increases very much with at a larger distance to the middle. The values are not very symmetric to the origin (x=y=0 mm), and the maximal values lay near x=-1 mm. This behavior is in principle also visible at the second measurement with 90°, and at those with an angle of 83° and 75°.

Figure 4.22: Picture of new sample stage with piece "c" between piece "a" and on top piece "d". Besides is visible piece "b" with the permanent magnets inside.

At an area of $2000{\times}2000\,\mu m$ (centered to the origin) the total difference is about $200\,Oe$. For an area of $300{\times}300\,\mu m$, i.e. the maximal dimension of the sensor-array which is placed in the middle on top of the stack, the field difference is calculated to $30\,Oe$. Therefore a linear decrease was assumed between the values at the origin and the at the adjacent positions with a distance of $1\,mm$ or $2\,mm$, see table 4.7. The relative difference is not very much, because the middle has a mean level of about $3535\,Oe$ (3420–$3685\,Oe$), so it is $1\,\%$ at the sensor-array.

Furthermore the stability of the PPD during the measurements was analyzed. Therefore the variation of the PPD was measured with an applied IP measurement field of $H_{meas} = \pm2\,kOe$. The permanent magnets' (stack) field has a value of $3.43\,kOe$ at $H_{meas} = 0\,Oe$, which changes to $3.45\,kOe$ at negative saturation ($H_{meas} = -2\,kOe$) and decreases to $3.35\,kOe$ at positive saturation ($H_{meas} = 2\,kOe$. The difference of $100\,Oe$ is not as much as the influence due to the movement of the magnets. As mentioned above a strong measurement field leads to a tiny movement of the permanent magnets, so that the PPD varies between $3.30\,kOe$ at positive saturation and $3.48\,kOe$ at negative saturation.
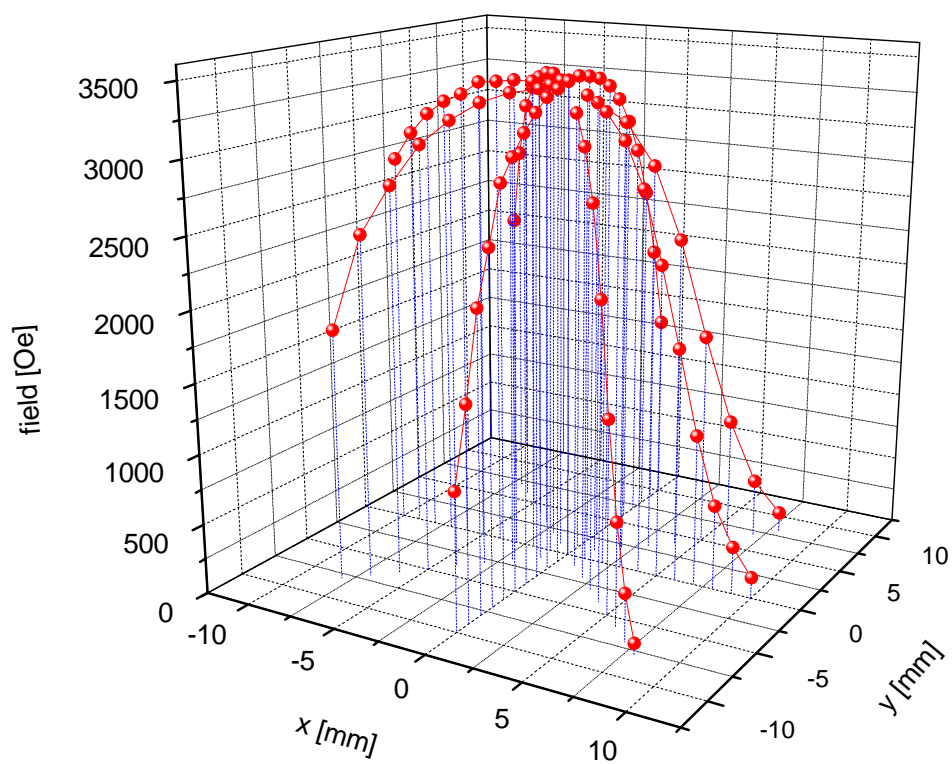
Figure 4.23: Perpendicular field of permanent magnets stack: measurement with gauss meter tip at 90°.

90° 1st		-2.00	-1.00	-0.15	0.00	0.15	1.00	2.00	x [mm]
	2.00	3410			3410			3120	
	1.00		3390		3430		3260		
	0.15			*3416*	*3422*	*3396*			
	0.00	3390	3420	*3420*	3420	*3407*	3330	3230	
	-0.15			*3414*	*3414*	*3392*			
	-1.00		3380		3380		3230		
	-2.00	3350			3340			3040	

90° 2nd		-2.00	-1.00	-0.15	0.00	0.15	1.00	2.00	x [mm]
	2.00	3560			3300			3280	
	1.00		*3530*		*3400*		*3390*		
	0.15			*3505*	*3485*	*3484*			
	0.00	3450	*3475*	*3496*	3500	*3498*	*3485*	3470	
	-0.15			*3502*	*3504*	*3480*			
	-1.00		*3515*		*3525*		*3365*		
	-2.00	3530			3550			3230	

83°		-2.00	-1.00	-0.15	0.00	0.15	1.00	2.00	x [mm]
	2.00	3800			3530			3590	
	1.00		*3743*		*3608*		*3638*		
	0.15			*3694*	*3673*	*3678*			
	0.00	3610	*3648*	*3679*	3685	*3689*	*3713*	3740	
	-0.15			*3683*	*3690*	*3666*			
	-1.00		*3673*		*3718*		*3560*		
	-2.00	3660			3750			3435	

y [mm]

Table 4.7: Measured and calculated (italic) field values [Oe] of the stack of permanent magnets for different angles of the gauss meter tip.

4.5.2 Results

Only 3–4 sensors were compared, caused by the often mentioned high affinity to break of the sensors. (At the end of these measurements only 11 out of 40 elements were still working.)

There are no big differences in shape, i.e. soft or hard switching visible, or changing number of characteristic ways or kinks, that indicated the presence of a bead. As it was done at the last approach, using a single permanent magnet, the focus was laid on detailed comparisons of the FWHM of the hysteresis in orientation `a` and maybe shifted positions of minima in orientation `b`. The results are visible in tables 4.8 and 4.9, exemplarily are the graphs of element 25 (without bead) and 35 (maybe with bead on top) shown in figure 4.24.

(a) sensor 25, MA, orientation `a`

(b) sensor 35, MA, orientation `a`

(c) sensor 25, MI, orientation `b`

(d) sensor 35, MI, orientation `b`
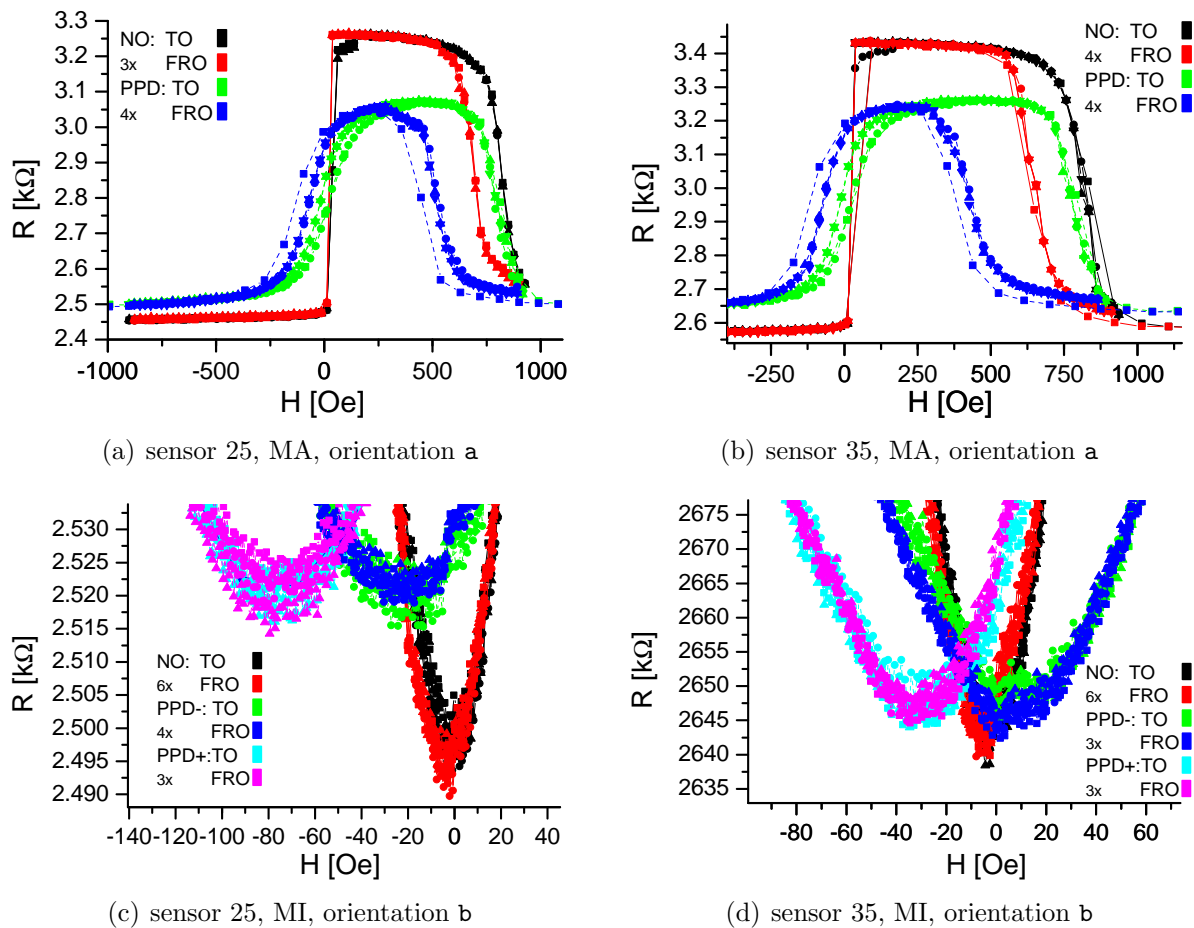
Figure 4.24: Exemplary results of two sensors with PPD, based on a stack of permanent magnets.

Comparison between NO and PPD field in orientation `a` showed no effect of possible beads which was expected to be possibly visible at the ratios. The total values of FWHM

FWHM in orientation `a`

ele-	before cleaning		*ratio*	after cleaning		*ratio*	bead
ment	PPD	NO	*PPD*	PPD	NO	*PPD*	possi-
no.	[Oe]	[Oe]	*/NO*	[Oe]	[Oe]	*/NO*	ble[a]
25	280	130	*2.15*	280	135	*2.07*	no
26	310	160	*1.94*	element broken			no
28	225	175	*1.29*	245	170	*1.44*	yes
35	340	170	*2*	330	175	*1.89*	yes

[a]At least one bead can be on top of the element as the image of the OM shows, see figure 4.15.

Table 4.8: Comparison of data from stack of permanent magnets in orientation `a` - looking at FWHM of hysteresis.

Shift of minima in orientation `b`

ele-	before cleaning				after cleaning				bead
ment	PPD			NO	PPD			NO	possi-
no.	MI+	MI-	*difference*	MI	MI+	MI-	*difference*	MI	ble[a]
	[Oe]	[Oe]	[Oe]	[Oe]	[Oe]	[Oe]	[Oe]	[Oe]	
25	-75	-20	*55*	-2	-104	-26	*78*	-3	no
28	-50	-9	*41*	-2	-88	-13	*75*	-2	yes
35	-29	+11	*40*	-4	-64	+2	*66*	0	yes

[a]At least one bead can be on top of the element as the image of the OM shows, see figure 4.15.

Table 4.9: Comparison of data from stack of permanent magnets in orientation `b` - looking at shift of minima.

of hysteresis are varying also at all sensors without a tendency if values before and after cleaning are compared.

A striking thing, visible at measurements in orientation `b`, is that the minima of minors with positive and negative saturation (MI+ and MI-, respectively) split under the influence of the perpendicular field[51]. Without this field there is only one minimum as it has been always before, and it is almost centered at zero field, see columns titled with "NO" in table 4.9. This separation appears independently of the cleaning and further measurements reveal, that this effect increases with higher saturation of $2000\,Oe$ instead of $1000\,Oe$. The total values MI+ and MI- lead to the question whether there could be more shift without beads. Prior data from measurements done with the simple sample stage containing one permanent magnet showed at element 7 without bead a shift of about $115\,Oe$ in PPD, whereas at element 35, which was maybe with bead on top, a lower shift of approx. $45\,Oe$ was measured. If this is true the difference between

---

[51]Detailed comparison showed that way TO of MA fits to MI- and the way FRO of MA fits to MI+, so the hysteresis in major loop could have its origin in the high fields applied for a MA which had the same effect as the saturation before measuring minor loops.

minima with PPD applied should give an even better indication, because the shift is taken into account twice due to the split of the minimum. One can see indeed in the table a difference of $40\,Oe$ at the elements with bead on top instead of $50\,Oe$, but the relative range of $10\,Oe$ is far less than the difference of shift in the former setup with (115-45=) $70\,Oe$. The measurements after cleaning should give a smaller relative range if the difference in minima is really influenced by a bead.

After cleaning there were still higher differences in the range of about 65–$80\,Oe$, along with larger total values of separated minima of MI+ and of MI-.

4.5.3   Discussion

There has been no indication for an influence due to a bead, neither by the FWHM of hysteresis in a nor by the shifted minima in orientation b.
With respect to the individual characteristics of each sensor one can see that the relations are always the same: The relative range of shifted minima of $15\,Oe$ is even higher than it was before cleaning ($10\,Oe$), so the variations of differences are inconclusive. Only the general signal was varied, e.g. after cleaning the differences of minors were larger in general. This could be maybe due to different measurement conditions.

A comparison between the position of the sensors and the differences of the minima in table 4.9 shows a similar result as found in the last section (4.4.3): With a higher sensor number, which is equal to a lower position according to the design (see figure 3.6), the value drops from sensor 25 to sensor 35. With this point of view sensor 28 shows a special behavior, i.e. before cleaning its value is equal to that of sensor 35 with a difference of about $40\,Oe$. But after cleaning the difference of $75\,Oe$ is more equal to the value of sensor 25 with $78\,Oe$. So the difference of minima in orientation b could be originated from a varying PPD field, as it happened at the last setup with one permanent magnet. This leads to a possible effect of the stray field:
The lowered relative difference value, i.e. the shifted minima in orientation b, of sensor 28, compared with adjacent sensors before cleaning, can be the influence of a bead, if special assumptions are made.
This can be true if sensor 35 has no bead on top. Such a assumption can be done, because it is only statistics whether there is first of all something after dropping on top of a sensor. Furthermore even an observation with the SEM cannot answer the question whether in the OM images is only dirt visible, without a bead under it (see section 3.3.2 "Selection of concentration").

There are several variations in the in-plane and out-of-plane fields, which makes a comparison of the measurements questionable:
The characterization of the magnetic field from the stack of permanent magnets showed a difference of $30\,Oe$ at an area which is as large as the sensor-array. If the sample is placed besides the middle of the magnets with the lowest variation of the PPD, this difference increases more ($200\,Oe$ at $2000{\times}2000\,\mu m$) and, as seen in figure 4.23, not only linear. Furthermore it was mentioned in section 4.5.1 that if the magnets are moving in an applied field which is relative strong ($\pm2\,kOe$) there is even more variation of

about $180 \, Oe$. On the other hand also an in-plane component of up to $\pm 500 \, Oe$ acts on the sensors which is high value compared to the measurement field. All in all the total applied field is different for the sensors, so that a comparison is not reasonable, especially for sensors with larger distances to each other.

In this setup the hysteresis at high applied fields gets larger with PPD applied. Contrary the hysteresis (FWHM) width of the former setup with one single permanent magnet, see table 4.4, generally is reduced. This could be also caused by strong variations in the in-plane and out-of-plane fields, but this cannot be analyzed without simulations.

In summarization it is impossible to detect a bead with this setup, because the field of the used stack of permanent magnets is too inhomogeneous, so that its influence is much bigger than all signal from a bead.

4.6 Conclusion

The influence of a bead was seen at the setup with the double coils: In orientation `a` the hysteresis was less shifted at the sensor with bead on top than for the sensor without bead, see (section 4.3.3). In general the sensors have a hysteresis and the first measurements showed different characteristic ways for each sensor. The measurements and data processing of the characteristic ways, which were measured in the first characterization (section 4.1), took a long time. But a result of those detailed measurements with the double-coils setup is, that there are additional ways which are not characteristic. This makes it questionable to use the special shape of a curve as an indication for beads.

Measurements were more difficult due to a high affinity to break which led to a decreasing number. Furthermore the strategy for measurements presented in section 3.2.3, i.e. referecne measurements before the dropping of beads and again after cleaning, could not be applied every time.

Furthermore are two effects, but they are not secure. There could be shifted kinks in orientation `b`, also seen with the double-coils, but it is not sure whether this effect only appears at a sensor with beads due to a missing reference (see section 4.3.2). An other effect was maybe visible at the measurements in orientation `b` with a stack of permanent magnets for PPD field: The separation of the minima, which appears if a high PPD field is applied, is larger due to the influence of a bead. Therefore in section 4.5.3 the assumption has to be done, that on another sensor only dirt instead of beads are present.

This leads at once to the important aspect of the uncertainty whether beads are on a sensor or not. The dilution with MICROMOD SICASTAR-M PLAIN beads consists of too much dirt, so that a count of beads is impossible (confer section 3.3.2). Also a tendency for agglomeration was seen which can be based on the ferromagnetic behavior of certain beads (section 1.2.3), although the beads should be superparamagnetic. Furthermore the beads have a broad size distribution and all beads are not as large as expected, i.e. instead of nominal $\varnothing 1.5 \, \mu m$ SEM images show only a diameter of about 0.34 to and $1.30 \, mum$

Looking back the approach with double coils is the most prominent candidate of the used setups, although due to an inaccurate alignment of the Helmholtz-coils the PPD influenced the applied field with its in-plane components, and led to a soft switching. . The first setup without PPD fields only showed statistical variations, but not the presence of a bead.

The alternative of permanent magnets for the perpendicular field turned out to be not as easy to handle as estimated. In the simple setup the alignment of the permanent magnet was not good enough for the detection of magnetic beads, because measurements were not reproducible. Visible was a shift of minima in orientation b that was produced due to the in-plane components of PPD. This led to a better fixation of the sample towards the permanent magnet in the last setup, but there were again several variations in the in-plane and out-of-plane fields, which makes a comparison of the measurements questionable.

It was seen by field measurements (section 4.5.1) that generally the high perpendicular fields of the used permanent magnets were not enough homogenous. Furthermore an influence on the resistance by a varying contact area of the measurement tip was visible in section 4.3.3.

In principle a setup with a perpendicular field for the magnetization of the beads is working, as the results with the double Helmholtz-coils shows.

A successful application of coils (or magnets) for the applied fields is not obvious as an article from FERREIRA et al.[FFGF05] in 2005 indicates: For SV sensors the role of sense current and magnetostatic current was simulated. Its influence on the beads field should not be neglected and furthermore they come to the conclusion, that the best operating conditions are to use no external fields at all and therefore apply as much current as possible.

In section 1.4.3 the necessity of a hysteresis-free and smooth signal was pointed out. The behavior of the used sensors is the opposite to these characteristics of a good biosensor. One cannot get rid of the multi-domains which are responsible for the many kinks. Therefore the used sensors of about $4 \times 2 \, \mu m^2$ are too big as it is given in the theory of domains (confer section 1.5.3). With respect to this disadvantage it is astonishing to measure the influence of a bead at all.

Outlook

Further measurements are necessary in orientation a to reproduce a hysteresis, which has a shift that depends on the presence of a bead, and to solve the discrepancy with theory. Therefore a setup with two Helmholtz-coils can be applied, but one must pay much attention on an accurate alignment, so that the PPD field has no in-plane components.

For a new dropping beads have to be used, that are really superparamagnetic to avoid agglomeration. Also no dirt has to be in a dilution, which is of course possible, as the images of other kinds of beads in figure 1.6 show, and they should show a small variation in size. Therefore other beads must be tried out.

Good sensors are needed, so an other task is the fabrication of sensors with such good characteristics as mentioned above, such as a signal without hysteresis near zero field. Furthermore the sensors should have only single domains to get rid of kinks in the switching curve, which means they must be in the submicron-regime according to section 1.5.3.

For higher TMR ratios a prominent choice would be MgO as barrier material. Therefore also a higher sensitivity could be expected, with respect to possible problems that are mentioned in section1.4.3.

Chapter 5

Measuring the shape anisotropy in TMR elements with MOKE

This chapter describes the fabrication of submicron MgO TMR sensors and their characterization using MOKE. Miniaturization is a common task as the necessity for integration in chips and the application in sensor arrays, for measurements as a gradiometer or the tracking of motion. Furthermore the miniaturization of sensors is thought to be good and necessary for achieving a smooth TMR curve without kinks. KUBOTA *et al.*[KAM$^+$03] examined very small MTJs of $1\,\mu m$ down to $50\,nm$ with aspect ratios of 1:1 to 1:7, see figure 5.1. They found out that elements of $300{\times}600\,nm^2$ can show very smooth behavior. In this case the pinning, indicated by the shift of the curve, changes its sign from positive (due to Néel coupling) to negative (magnetostatic coupling dominates). In general the shifted field is larger with higher aspect ratios. Although the stack layout used
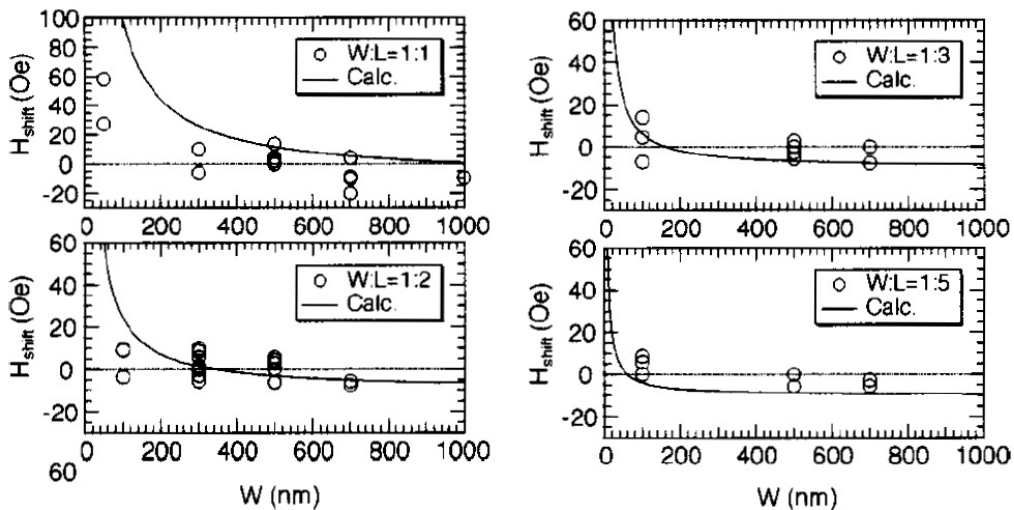

Figure 5.1: Strength of pinning H_{shift} for several sizes and aspect ratios varying from 1:1 on top to 1:5 at bottom, analyzed by KUBOTA *et al.* [KAM$^+$03].

(Si/SiO$_2$ /Ta 5/Cu 30/CoFe 1.5/Ru 0.9/CoFe 2.2/Al 1.5(plasma oxidized)/NiFe 6/Ta 5/Au 30; thickness in nm) is different to the one tried out in this thesis, the results point out the importance of miniaturization. Also the results shown in chapter 4 encourage the use of smaller elements.

MgO will be used as the barrier material, with respect to its advantages over AlO$_x$ as barrier material, mentioned in section 1.4.3. The higher TMR ratios should lead to a higher sensitivity.

The last ingredient for a good biosensor is, besides a smooth and steep curve, a hysteresis-free signal (see section 1.4.3). Therefore a perpendicular pinning will be used, encouraged by the articles of JANG[JNK$^+$06] and VAN DIJKEN[vDC05], as well as conclusions by SCHOTTER[Sch04, section 6.6] (see section 1.4.3).

5.1   Perpendicular Pinning of MgO-Stack using Shape Anisotropy

5.1.1   Application of Perpendicular Pinning on MgO

Perpendicular pinning should be applied also on MgO sensors, but that is not easy to achieve. The exchange bias is normally established due to the field cooling, so only one pinning direction is possible, confer section 1.3.5, but MgO has only such superior ratios after annealing, as seen in figure 1.15. In-situ pinning via sputtering with magnetic masks, see sections 1.3.4 and 2.2, was already tried out, but was not successful: Although the MOKE measurements showed magnetic switching, in the standard test, mentioned in section 3.1, no TMR is available. Also an annealing ($60\,min$ @350 ℃) does not help.

One solution is to induce a pinning based on shape anisotropy, i.e. to use small, thin elements with a single domain (confer e.g. [Wie06, p. 72]). They offer a field with determined direction so that perpendicular pinning of a traditionally annealed stack can be achieved if the elements long axis is perpendicular to the cooling field.

As already mentioned on page 109 KUBOTA *et al.*[KAM$^+$03] got for tiny elements stronger pinning with higher aspect ratios. In the diploma thesis of ASTRIT SHOSHI[Sho05, section 5.4.2.2] the structuring of thin lines ($2\times1000\,\mu m$ with a distance of $7\,\mu m$) of a GMR stack lead to a hysteresis-free curve, visible in figure 5.2. Also ANDY THOMAS got a signal without mentionable hysteresis for a GMR stack with thin lines as structures[Tho], as well as DIRK MEYNERS, who got no hysteresis for some $100\times200\,nm^2$ TMR elements[Mey], so the prospect to apply a perpendicular pinning via shape anisotropy at submicron elements to get a hysteresis-free sensor is really good.

A structuring can have also negative influence for other characteristics than the hysteresis, such as the sensitivity. The aforementioned thin long lines by SHOSHI reduced the sensitivity by a factor of 20 compared to an unstructured sample[Sho05, p. 100]. But in this thesis the setup is different, i.e. tiny submicron elements and a TMR stack, so one has to see in which way the sensitivity will change.

(a) structured   (b) unstructured
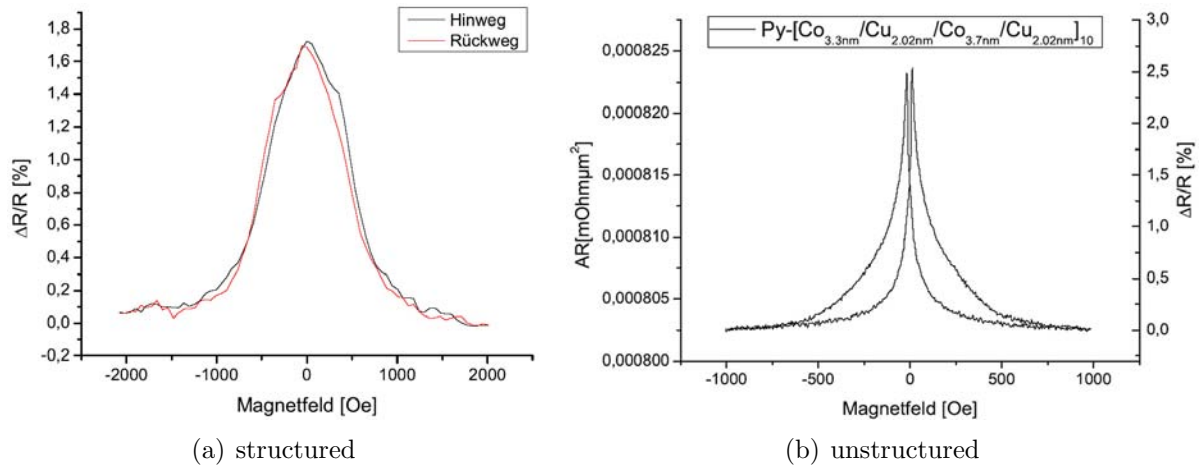
Figure 5.2: Thin lines, see text for details, can lead to a hysteresis-free signal (a) of a GMR stack (b) [Sho05, p. 99, figure 5.11].

Furthermore one could try out very thin CoFeB layers according to JANG *et al.*[JNK$^+$06]. They got an intrinsic perpendicular pinning for $20 \times 10 \, \mu m^2$ sensors with CoFeB / MgO / CoFeB, which contain a thin ($\leq 1 \, nm$) upper $Co_{60}Fe_{20}B_{20}$ layer, after annealing and field cooling with $300 \, °C$ in $1 \, kOe$. It is not known, whether this approach can also be used for sub-micron sensors, which are planned to be structured in this thesis. Therefore the solution of applying shape anisotropy with thin elements, which worked for sure as the examples above show, is chosen.

At first a stack composition which yields high TMR values should be applied. Therefore a sample provided by VOLKER DREWELLO was chosen, which has a TMR curve of quite normal shape, with little hysteresis of about $25 \, Oe$ (9–$34 \, Oe$) and a TMR effect of $120 \, \%$. This is a relative high ratio and a relative small hysteresis, so a good starting point for the application as a sensor. The stack layout is: Ta 7.2/Cu 30/Ta 7/Cu 5/MnIr 10/CoFeB^{52} 3/MgO 1.5/CoFeB 4/Ta 7/Cu 40.7 (values are the nominal thickness in nm), sputtered at $21 \, \%$ throttle position ($\approx 1.2 \pm 0.05 \cdot 10^{-3} \, mbar$ @20 $sccm$ Ar-flow) except MgO which was done with $3 \, \%$ ($\approx 2.4 \pm 0.1 \cdot 10^{-2} \, mbar$)^{53}.

For further experiments own samples with MgO were sputtered in the CLAB with the following stack layout: Ta 7.2/Cu 30/Ta 7/Cu 5/MnIr 10/*CoFeB 2.5*^{54}/MgO 1.5/*CoFeB*

---

[52]Target composition is $40 \, \%$ cobalt, $40 \, \%$ iron and $20 \, \%$ boron.

[53]In former standard MgO stacks a thin Mg layer was sputtered before MgO, such as $0.5 \, nm$ / MgO $1.5 \, nm$. Mg could collect oxygen out of MgO during annealing[Dre06, p. 41], so no closed layer is needed. The special throttle position of $3 \, \%$ was tried out by VOLKER DREWELLO during his diploma thesis[Dre06, p. 41 et seqq.]. He made the experience, that there is at such relative high pressure not only no need for Mg below MgO, but furthermore Mg even limits the TMR.

[54]Old calibration was $0.17 \, nm/s$, used calibration by DREWELLO $0.27 \, nm/s$, but a new calibration showed $0.16 \, nm/s$[Dre]. This encouraged the assumption that maybe the used calibration was wrong

2.37[54]/Ta 7/Cu 40.7, sputtered at 21 % throttle position except MgO which was done with 3 %. The new sputtered MgO samples exhibit 75 %, max. 95 %, TMR which is not as good as the original ratio from VOLKER DREWELLO, but good enough to work with it.

5.1.2   Analyze in MOKE

Before applying shape anisotropy on sensor elements a test was done to answer whether the approach in general works and which combination of size and aspect ratio is the best. It was thought to be a quick check before going on with structuring which can take a lot of time. The switching behavior can be analyzed with the MOKE or the AGM. The latter has the disadvantage of only one type of structure is possible on one sample, so the MOKE was chosen to save consumption of time and material.

The measured loops in MOKE measurements are an average of all loops from the elements that are in the laser spot. Therefore the measured loops are based on the data of about 4500 to 18000 elements, if all elements contribute to the signal. Each individual loop could be slightly different, due to varying element sizes and ratios within one array. Further variation in the material is possible due to not fully homogenous etching and resist coating, as well as possible differences in the sputtered stack. The average of all signals will result in a smoother loop.

A possible dipole interaction has to be considered when elements are arranged in an array. A simple picture is as following, mentioned e.g. by ABRAHAM and LU[AL05]: If the spacing in direction of the elements *easy axis* (EA), i.e. the longer dimension, is tight enough dipole interaction results in a chain oriented in EA direction. A field applied parallel to EA will switch the element with the lowest switching field first and due to the chain character also the other elements of the corresponding chain are switched at once. If the spacing in *hard axis* (HA) direction, i.e. elements short axis, is tight enough a field applied in direction of EA has to be higher to switch all elements. The antiferromagnetic coupling scheme of adjacent elements prevents every second element from parallel alignment to the applied field. This results in a wider hysteresis, opposite to a sharpen transition in the former case with the chain characteristic.

As done for the last chapter (section 3.2.3), abbreviations are used to name the alignment of the sample towards the measuring field: In orientation `a` is the measurement field parallel towards cooling field, so that it is parallel to the short axis of the elements (HA). Therefore in orientation `b` the measurement field is perpendicular towards cooling field, which means that it is parallel to elements long axis (EA). Again orientation `c/d` is orientation `a/b` twisted 180°, respectively.

---

so that instead of nominal $3\,nm$ (=$10.56\,s$ with $0.27\,nm/s$) only $1.8\,nm$ (=$10.56\,s$ with $0.16\,nm/s$) was sputtered, which is near the threshold of a closed layer. As a compromise $2.5\,nm$ (=$15.07\,s$ with $0.16\,nm/s$) or $2.37\,nm$ (=$14.26\,s$ with $0.16\,nm/s$) were sputtered, using a $Co_{40}Fe_{40}B_{20}$ (at. %) alloy target.

5.2   Preparation

On two samples were arrays of (sub-)micron elements structured with e-beam lithography and ion beam milling. Different stacks as well as different sizes and aspect ratios were used for the elements. The sample from VOLKER DREWELLO was chosen as the "first sample", and one piece of the sputtered MgO-stack was used for the "second sample". The resist 7520.18, 1:1 diluted with thinner, was spined $1\,s$ @$200\,rpm$ and $30\,s$ @$6000\,rpm$, baked $2\,min$ @$85\,°C$, to get an approx. $150\,nm$ thick layer. The elements long axis was aligned perpendicular to the direction of the annealing field to get a perpendicular pinning, because the field originated in shape anisotropy is parallel to the long axis of the elements.

A compromise has to be found between enough area for a good MOKE signal and preparation handling, because the need of time increases with the preparation of several samples. The placement of all arrays on one sample is necessary to have the same conditions which can influence the TMR ratio, such as the stack characteristic and the treatment of the sample. The sputtering and etching is most homogenously in the middle of the sample surface, which limits the maximum area that should be used. Several fields of the same elements are necessary so that the laser spot with a diameter of about $100\,\mu m$, see section 2.4, can be focussed on a specific array. In general up to six arrays of $10{\times}10$ fields for each size and ratio were exposed on one sample. The fields are structured using a $(100\,\mu m)^2$ writefield for better resolution. This reduces the number of elements in one writefield, so limits of soft-/hardware are of no concern. Each field has a $10\,\mu m$ border to avoid overlaps during exposition. This precaution was taken because the SEM can produce shifts up to several microns when driving to a new position. Due to the small dimensions of the elements also small writefields must be used to get the shape as good as possible. Then the size and aspect ratio of the written elements are fine, confer the description of e-beam lithography in section 3.1.2. Nominal rectangles were used but one gets always ellipses for tiny structures as mentioned in section 3.1.5.

5.2.1   Provided MgO-Sample   (1st Sample)

Pre-experiments lead to the parameters that are used in the following:

Tested sizes and aspect ratios are: $100{\times}400$, $115{\times}345$ and $90{\times}450\,nm^2$, all with spacing $3{\times}$, keeping area constant at different aspect ratios of 1:4, 1:3 and 1:5 respectively. These variations in aspect ratio were chosen to see whether there is a high sensitivity to size/ratio at this length scales. Even an aspect ratio of 1:2 could be enough if sizes are small enough, as seen in figure 5.1 and mentioned in section 1.5.5. Therefore a lower limit of 1:3 should work for sure. Furthermore, with a spacing of $2{\times}$ dimensions, bigger elements of $200{\times}800\,nm^2$ and $200{\times}1000\,nm^2$, as well as $100{\times}400\,nm^2$ for comparison with the larger gap, were chosen. The gaps of $2{\times}$ and $3{\times}$ are chosen to get a measurable signal, which depends on the surface coverage. The dose for exposure was with respect to the pre-experiment chosen to 2.3 for the bigger elements, and 2.6 for the smaller elements (confer section 3.1.2 for doses). Each array consists of $10{\times}10$ fields of $(100\,\mu m)^2$ writefields, including a border of $10\,\mu m$.

The sample was post annealed in the standard way for TMR, etched through Cu into Ta about $3.5\,nm$[55] and measured in the MOKE as reference. After exposure of the elements it was removed $138\,min$ ($= 43 + 33 + 31 + 31\,min$)[56] and measured again.

5.2.2   Sputtered MgO-Stack   (2nd Sample)

As further improvements, necessary from the results of the first sample which will be discussed in section 5.3.1, following parameters were used for new arrays: $10{\times}10$ fields of effective $80{\times}80\,\mu m^2$ with elements of $100{\times}400\,nm^2$, $90{\times}450\,nm^2$, $115{\times}345\,nm^2$ (all with gap 2×, dose 2.8), $200{\times}800\,nm^2$ (gap 2×, dose 2.4), $100{\times}800\,nm^2$ (gap 3×, dose 2.8) and $100{\times}400\,nm^2$ (gap 4×, dose 3.2).

After post annealing, using the standard parameters for TMR, milling of the upper Cu into half of Ta layer was done. Additionally $5\,nm$ Ta ($25\,s$) was sputtered to have a closed Ta layer on top, before reference data was measured. The cleaned sample was exposed with the arrays mentioned above and removed $161\,min$ ($= 32 + 18 + 24 + 21 + 15 + 25 + 26\,min$)[57] for the first MOKE measurements. MOKE measurements were done including reference data of the etched surface. Additional reference data of an unstructured surface was collected from an extra sample, which was prepared via etching through Cu into Ta and extra Ta sputtering.

5.3   Results and Discussion

5.3.1   Provided MgO-Sample   (1st Sample)

The reference sample, i.e. the same sample before lithography, has a mean SNR of 57:1[58] and hysteresis of $25\,Oe$, beginning at $10\,Oe$ unto $35\,Oe$ (orientation `a`, see table 5.1 and figure 5.3(a/c)). These characteristics of the hysteresis are equal to those of the TMR measurements. The hub of the hysteresis is 0.75 a.u., by using the MOKE signal difference. Total values are useless due to inexact/varying tilt of the analyzer (confer

---

[55]Two ways to get the etched depth were compared: Comparison of time, beginning from signal rise to end of signal fall after a plateau, showed that Ta was etched for approx. $170\,s$. In an older data set etching of $7\,nm$ Ta took about $700\,s$. This gives a deduced etched thickness of approx. $1.7\,nm$ Ta. Comparing the shape of the curve, with the same area as before, indicates that about half of the Ta was etched, i.e. approx. $3.5\,nm$. The latter method is the better one, because in the data sets the cathode filament current varies very much, from $2.9\,A$ to $2\,A$ in the actual data set in between 12 days. As mentioned in section 2.6 the etching rate depends also on this filament current, so naturally the etching time varies.

[56]Please see below for a comment on the split of removing time.

[57]After $32\,min$ no change of the surface was visible with the OM, so removing was carried on for $18\,min$. The sample was viewed with the SEM, because again no change was visible with the OM. Observations in the SEM showed resist on top of elements and made further removing necessary: $+ 24\,min + 21\,min + 15\,min + 25\,min$ and after anew observation $+ 26\,min$. An interval of about $20\,min$ was chosen, between recurring observation with the OM, in order to stop at once when a big change occurs.

[58]SNR of all measurements: 65, 75, 48, 58, 41, 87, 16 and 64:1

(a) MA orientation `a`

(b) MA orientation `b`

(c) MI orientation `a`

(d) MI orientation `b`
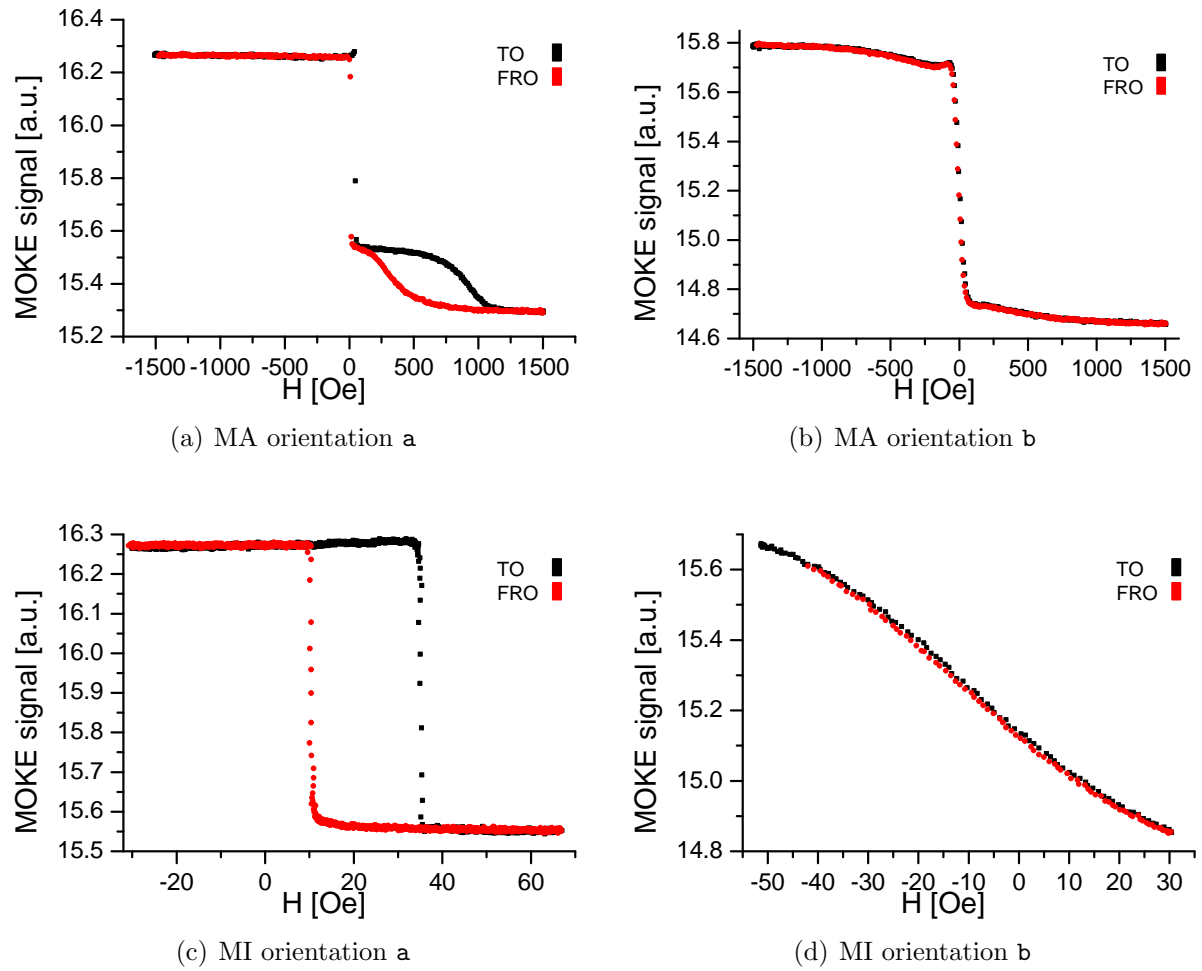
Figure 5.3: MOKE measurements of reference for first sample.

setup of MOKE in 2.4 and measurement process in 3.2.1), but the total change in signal value is independent, as test measurements with strong varying analyzer positions showed. In orientation `b` there is almost no hysteresis visible as seen in figure 5.3(d); the values in table 5.1 are given by a slightly difference of about $0.5\,Oe$.

A linear part of the MOKE curve can be estimated per eye e.g. at the hard switching of way FRO in orientation `a` from about $34\,Oe$ to $36\,Oe$. With the corresponding hub of $0.67\,$a.u. the slope in that region is $0.34\,$a.u./Oe. In orientation `b` the slope is only $0.012\,$a.u./Oe in between $-30\,Oe$ and $10\,Oe$. These values will be compared later to the characteristics of the sensors.

The SNR is related to the thickness of the stack above the sensing MgO layer, i.e. approx. $8\,nm$ after etching of Cu into Ta with remaining CoFeB $4\,nm$ / Ta $3.5\,nm$. In pre-experiments a SNR of only 5:1 was achieved with a approx. $50\,nm$ thick upper layer, which shows the high surface sensitivity of the Kerr-effect in MOKE measurements. A SNR of 57:1 means, that the signal difference caused by the elements must be better than

orien-		field		hysteresis					linear range			
tation		min	max	hub*	begin	end	width	middle	hub*	begin	end	slope 10^{-3}
& array		[Oe]	[Oe]	[a.u.]	[Oe]	[Oe]	[Oe]	[Oe]	[a.u.]	[Oe]	[Oe]	[a.u./Oe]
a	100	-330	310	0.029	-50	200	30–40	75	*0.021*	*5*	*100*	**0.22**
a	ref	-31	67	0.75	10	35	25	22.5	*0.671*	*34*	*36*	*335.50*
b	100	-180	145	0.01	-80	80	90	**0**	0.007	-70	-10	0.11
b	ref	-51	30	*0.62*	*-30*	*25*	*0.5*	*-2.5*	0.485	-30	10	12.13

*Please see comment in text on total values.

Table 5.1: Characteristics from MOKE measurements of first sample.

2 % noise. This makes a minimal surface cover of also >2 % necessary, which is reached with the chosen gaps: The surface cover is approx. 3.8 % with gaps of 3× dimensions. This is not much than than the minimal value and therefore the 2× spacing was chosen, which leads to about 6.8 % surface coverage.

One can find e.g. following working values of surface cover for MOKE measurements: In the aforementioned diploma thesis of ASTRIT SHOSHI at least 22 % of the surface are covered (with maybe only approx. $3\,nm$ material on top of magnetic active layers)[Sho05, p. 79 et seqq.]. Arrays for Moke by NILS WIESE had a surface cover of 16 % (with maybe $5\,nm$ on top)[Wie02, p. 34] or 12.5 % (with 8–15 nm Ta on top)[Wie06, p. 35 et seq.].

With respect to the simple model of interacting elements, presented in section 5.1.2, a possible drawback of these tiny gaps is a influence between the magnetizations of the sensors, which have dipole character at these dimensions. Therefore e.g. ASTRIT SHOSHI[Sho05] used a gap of $7\,\mu m$ for $2000\,\mu m$ long lines with 2–20 μm thickness, which successfully eliminated crosstalk. In the publication of ABRAHAM and LU[AL05] the influence of an array of $300{\times}600\,nm^2$ elliptic elements with varying distances in between was analyzed. For gaps of 1.7, 2.9, 4.6× length (longer side of element, i.e. the easy axis) and (2.2,) 4.1, 7× width (hard axis) almost always the same influence was investigated. This was suggested to be based on the normal influence of an array of noninteracting elements. A gap of 1.1× width showed an interaction, which almost becomes visible at a gap of 2.2× width.

The conclusion with respect to these literature values is that the surface cover of 3.8 or 6.8 % is relative low and the gaps can be near the threshold of interacting elements. The good SNR makes it reasonable to keep these gap values and do not decrease them for a higher surface coverage.

Five arrays showed nothing in the MOKE, i.e. only noise, only one showed a signal. It were the elements with $100{\times}400\,nm^2$ at a distance of 2× dimensions, so the surface coverage was 6.86 %. The magnetic switching in orientation a, visible in figure 5.4(a/c), is not as sharp as in the reference with a hysteresis of approx. 30–40 Oe in between -50 and $200\,Oe$ in orientation a. A striking thing is the second hysteresis at a lower applied field around -800 Oe, visible in figure 5.4(a). A less pronounced second hysteresis is visible at the measurement with a lower applied field (figure 5.4(c)) of max. $<\pm330\,Oe$, where

(a) MA orientation a

(b) MA orientation b

(c) MI orientation a
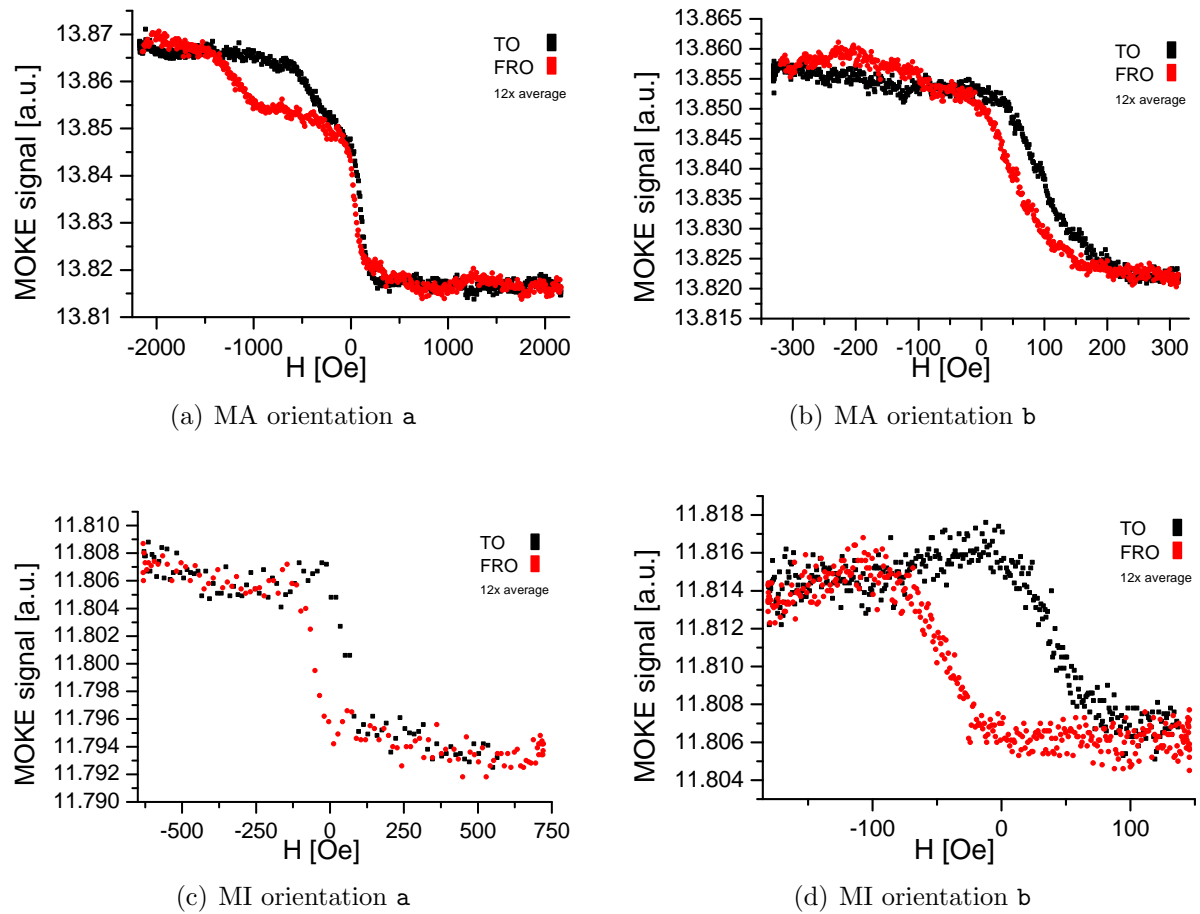
(d) MI orientation b

Figure 5.4: MOKE measurements of the $100 \times 400 \, nm^2$ at the first sample.

it appears around -200 Oe. Further measurements in orientation b showed a hysteresis of about 90 Oe in between $\pm 80 \, Oe$, see figure 5.4(b/d). The wider hysteresis can be explained due to the different characteristics of the elements, confer the simple model mentioned on page 5.1.2. This aspect favors measurements in orientation a, where the hysteresis is only 5–15 Oe wider than the reference value. Furthermore the slope is twice of the value $0.11 \cdot 10^{-3}$ a.u./Oe in orientation b. The drawback can be the position of the hysteresis, with a middle at about 75 Oe. This forbids measurements with smaller fields. A centered hysteresis around zero field is the only advantage that the measurement in orientation b shows, but the hysteresis width of 90 Oe is bad. Although this value is wider than that of a single sensor, it still shows, that
the sensors exhibit less hysteresis if they are measured in orientation a.

The removing of the first sample was stopped after a total time of 138 min to save the sample, with a mixture of not-removed, already removed and destroyed elements. The caps of overlapping elements (due to an error in the lithography software) were all removed which could be due to the fact that bigger areas can be removed more easily.

An iterative use of a short removing time and a following SEM observation is necessary, but one must find a compromise to save the elements.

There is not much time of removing between a state of elements with resist and destroyed elements. After $50\,min$ the elements were still standing, but after additional $20\,min$ all elements where gone. So it is necessary to have a look with the SEM on the elements after a relative short time in the ultrasonic bath. This is the reason for the split of removing time mentioned in the preparation section 5.2. Contrary the penetration with an e-beam leads to a longer removing time or even makes the removing impossible, so it is undesirable to look often at the sample.

	optical	SEM
with cap	dark	pale white
removed	white	darker
assumptions	darker color of the resist	larger side-area $\rightarrow$ more signal

Table 5.2: Different appearance of resist in optical microscope and SEM, with possible reasons (see text for details).

Problems were encountered to determine a proper removing time because it was hard to see a difference between removed and other elements, including non-removed and already destroyed ones. Comparison of optical microscopy and SEM showed that the appearance of resist is exchanged in OM and SEM, most probably caused by the origin of signals as mentioned in table 5.2. In OM the resist has a darker color than the surrounding area. This appearance can be inverted in the SEM due to a high signal from the borders. Resist on top of an element enlarges the side area, and the sides five more signal in the SEM due to more SE electrons, as visible in figure 2.4(c). Contrary to this effect is the generally darker appearance of material with a low mass: The used resists generally consist of H, O and C, i.e. maximal $16\,au$, but the surrounding material is Ta, i.e. $180\,au$. Therefore the resist should be darker, but this effect is covered by the higher signal from the borders. One must remember, that the appearance in SEM images depend on the chosen parameters, as mentioned in section 2.5. Visible is this different appearance in figure 5.5 where a SEM picture is compared with an image from the OM, both are showing the same elements. The added AFM data reveals the real heights. In the SEM pictures the resist borders were only visible at high magnifications using the InLens detector. If the contrast at the SEM is adjusted one can see the inverted, i.e. negative, image of the OM. The AFM measurements, done by DIRK MEYNERS, showed pillars of different height:

- approx. $3\,nm \leftarrow$ removed pillars

- approx. $65\,nm \leftarrow$ only stack remained

- approx. $148\,nm \leftarrow$ resist still on top

SEM and also AFM measurements revealed too big dimensions of elements, e.g. $390{\times}1100\,nm^2$ instead of nominal $200{\times}1000\,nm^2$ or $270{\times}600\,nm^2$ vs. nominal $100{\times}400\,nm^2$. SEM images show a large range of dimensions for tiny elements at different fields in the exposed array, such as $112{\times}319$ up to $193{\times}419$. (Although it is

possible that the AFM images show indeed even larger elements, these values depend on the parameters during scanning. If the speed is e.g. to high, the dimensions can be enlarged, so maybe this could be the reason for the larger dimensions of the elements in the AFM.)

These results confirmed that removing was too long and the used doses too high. This is the reason for a new dose test, including tests on removing, before a sample with the new MgO-stack was structured.

(a) Optical microscope

(b) AFM

(c) SEM

(d) SEM

(e) SEM detail

(f) SEM detail
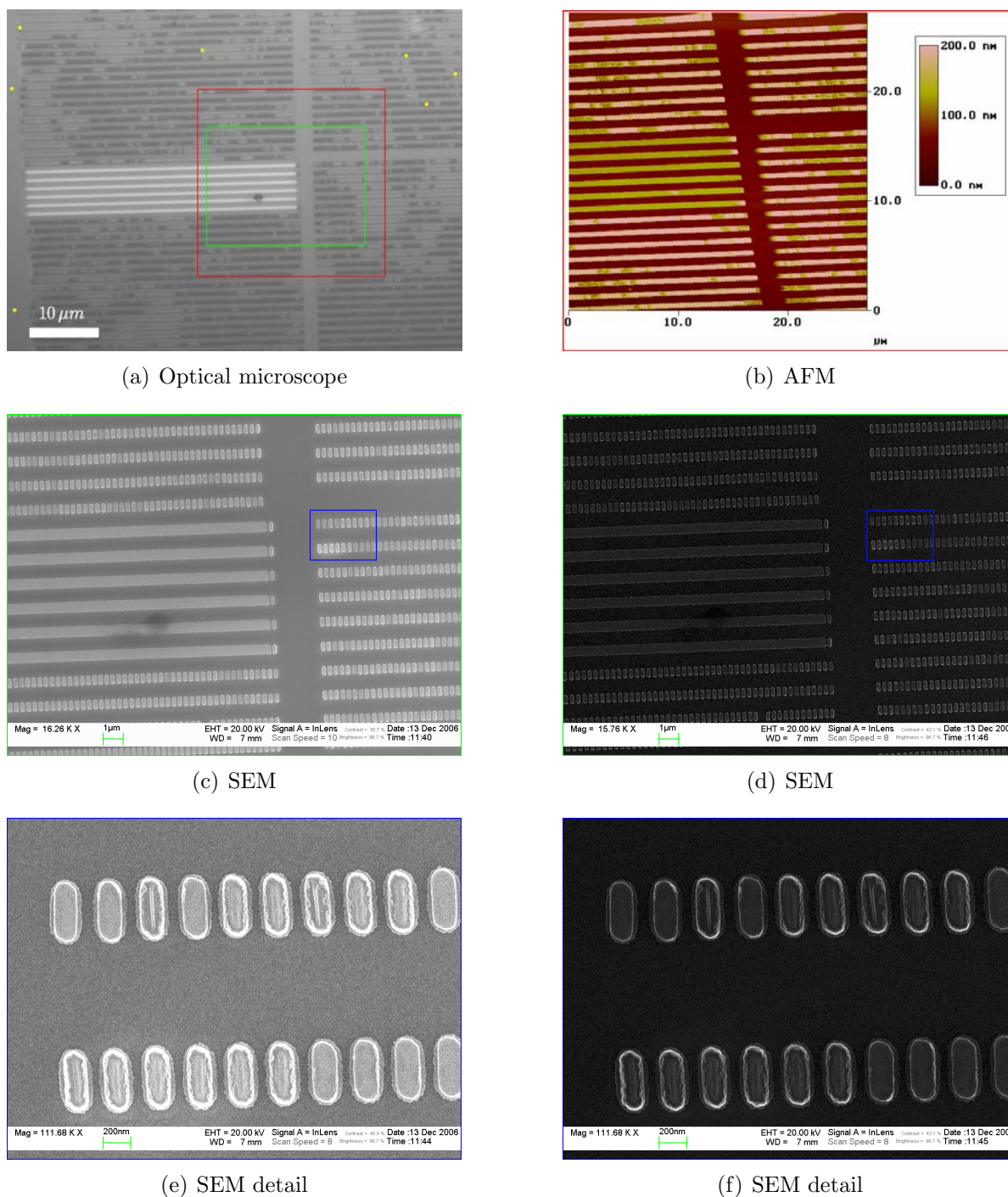
Figure 5.5: Comparison of elements with and without resist on pictures done with the OM (a), AFM (b), and SEM (c–f). The AFM area of about $(27\,\mu m)^2$ is indicated in (a) with the red box, and the SEM area of about $22.8\times17.1\,\mu m^2$ (c,d) is indicated with the bigger green box. The detailed view of elements in (e,f) of about $3.3\times2.5\,\mu m^2$ is indicated in (c) and (d) with the blue box. Comparison of left (c,e) and right (d,f) SEM images shows the influence of contrast settings. At (f) it becomes visible, that the white appearance of elements in the SEM is related to the element borders. See text for details. (At (a) the contrast and brightness was enhanced.)

nominal		
size	$90{\times}450\,nm^2$	$200{\times}800\,nm^2$
area	$40500\,nm^2$	$160000\,nm^2$
surface cover	$7.22\,\%$	$7.29\,\%$
in real / removing		
size after $50\,min$	$161{\times}378\,nm^2$	$266{\times}492\,nm^2$
	$(142{\times}265\,nm^2)$	$249{\times}433\,nm^2$
		$254{\times}446\,nm^2$
mean^a area	$39196\,nm^2$	$134176\,nm^2$
after $135/161\,min$		$(73761\,nm^2)$
difference to nominal	$-3.2\,\%$	$-16.1\,\%$
surface cover	$6.98\,\%$	$6.11\,\%$
number of elements	$297{\times}60$	$134{\times}34$
distance [dimensions]	$2\times$	$2\times$
dose	2.8	2.4
	with "hierarchy"^{b}	no separation needed

^{a}Real areas were deduced from the number of pixels in the SEM images. See text for details on image processing.
^{b}With this option of the lithography software the writefield was split into four parts. This has the advantage that no gap is needed, because the stage is not moved.

Table 5.3: Analyzed arrays of the second sample.

5.3.2 Sputtered MgO-Stack   (2nd Sample)

Four of the six arrays were not proper exposed, maybe due to very strong varying sample current, but elements of $90{\times}450$ and $200{\times}800\,nm^2$ could be analyzed, see table 5.3. These elements will be cited as "90er" ($90{\times}450\,nm^2$) and "200er" ($200{\times}800\,nm^2$) in the following, and in the same way the $100{\times}400\,nm^2$ elements from the first sample are called "100er".

Observation with the SEM after $135\,min$ removing showed that the resist was removed only partly, but after additional $26\,min$ some elements were OK and some elements were already destroyed. The sample was measured although the resist was only partly removed, because further penetration in ultrasonic bath could have led to a loss of too many elements.

Nominal surface coverage is 7.2 or $7.3\,\%$ but the real area of an element is below the nominal one due to reduced length[59], which is not fully compensated by the larger width[60]. The real size of the elements was determined with the help of commercial image editing software: On the original SEM image contrast was enlarged and brightness reduced so that the area of an element remained white on black background. This image was shrinken into a grey scale image of one pixel. Out of the grey value of this

[59]Factor 0.84–0.59 for $90{\times}450\,nm^2$ elements and 0.62–0.54 for the other ones.
[60]Factor 1.58–1.79 for tiny elements and 1.25–1.33 for bigger ones with $200{\times}800\,nm^2$.

pixel the amount of white pixel can be calculated which gives in combination with the magnification, which is saved in the SEM image, the area of the element. The uncertainty of this method depends on the resolution of the SEM image and should be $\leq 10\,\%$. As visible in table 5.3 the real area of $90\times450\,nm^2$ is only about $3\,\%$ reduced, so with respect to the uncertainty the nominal surface cover of $7.2\,\%$ is not changed. For $200\times800\,nm^2$ elements an area reduction of $16\,\%$ means that at least $6\,\%$ surface cover was achieved.

Diffraction patterns were always visible if an array is in the focus of the laser spot. The origin lays in the periodic pattern, so the laser spot was clearly on an array. Minor loops were measured before and after the major loops to see wether there is an effect of the high fields applied for major loops on the minor loops. The latter MI were generally equal to the former measured ones, which is reasonable: Only the very first measurement represents really a "virgin" MI, because both arrays are placed on the same sample. The corresponding measurement was performed on the array with 90er elements and was not differing from later measurements – no hysteresis was visible. Noise in the data signal made it necessary that (almost) always 12 loops were used to see something (at all) at the MOKE measurements.

orien-tation & array		field		hysteresis					linear range			
		min [Oe]	max [Oe]	hub* [a.u.]	begin [Oe]	end [Oe]	width [Oe]	middle [Oe]	hub* [a.u.]	begin [Oe]	end [Oe]	slope 10^{-3} [a.u./Oe]
c	200	-345	325	0.016	-220	-20	50	-120	0.012	-150	-50	0.12
c	**90**	**-145**	**115**	-	-	-	**0**	**0**	**0.023**	**-50**	**50**	**0.23**
c	90	-1480	1400	*0.2*	*-600*	*100*	*70*	*-250*	-	-	-	-
a	ref 2	-5	135	0.542	45	60	15	52.5	*0.409*	*58*	*61*	*136.33*
a	100	-330	310	0.029	-50	200	30–40	75	*0.021*	*5*	*100*	***0.22***
a	ref 1	-31	67	0.75	10	35	25	22.5	*0.671*	*34*	*36*	*335.50*
d	200	-340	280	0.025	-150	100	20–25	-25	0.018	-100	100	0.09
d	200	-2780	2630	*0.04*	*-400*	*800*	*50–100*	*200*	-	-	-	-
d	90	-340	280	0.014	-150	200	120	25	-	-	-	-
d	90	-2770	2640	*0.02*	*-400*	*600*	*200*	*100*	*0.011*	*-100*	*100*	*0.06*
b	ref 2	-245	210	-	-	-	**0**	**0**	0.388	-100	100	1.94
b	100	-180	145	0.01	-80	80	90	0	0.007	-70	-10	0.11
b	ref 1	-51	30	*0.62*	*-30*	*25*	***0.5***	*-2.5*	0.485	-30	10	12.13

*Please see comment in text on total values.

Table 5.4: Characteristics from MOKE measurements of second sample (columns "200", "90" and "2nd ref") as well as for the first sample (columns "100" and "1st ref", data taken from table 5.1).

The parameters of the measured curves, such as applied field, hysteresis and values of a linear range, are listed in table 5.4. Additional the data from the first sample is given for comparison. For the linear range an almost linear part of the curve was determined per eye. Uncertain values are marked (*gray italic text*), as well as outstanding

characteristics (**bold text**). If two rows exist for one kind of element the data was taken from measurements with differing applied fields as mentioned in the third and fourth column. Measurements were done also in orientation `c` and `d` for which the measured curves are equal to those of orientation `a` and `b`, respectively, as test measurements showed. (This was necessary for the fixation of the sample in the MOKE setup.)

Results in orientation `a` (/`c`), see figure 5.6:
- The reference has a hard step with hysteresis of $15\,Oe$ from approx. 45 to $60\,Oe$. If a high measurement field is applied both arrays show a wider hysteresis of $50\,Oe$ (200er) or $70\,Oe$ (90er), with a shift of the middle of about -170 and $-300\,Oe$, respectively. Therefore the reference curve gets wider and softened at the arrays. The bigger 200er elements show this hysteresis also at lower measurement fields, but at the 90er the hysteresis vanishes at a measurement field between approx. $-145\,Oe$ and $115\,Oe$. less influence of $200 \times 800\,nm^2$ elements is visible.
- The slope of the hysteresis-free 90er is with $0.23 \cdot 10^{-3}$ a.u./Oe almost the double of the 200er value and symmetric to zero field with $\pm 50\,Oe$. Also the 200er elements show a linear behavior of $100\,Oe$, but this range begins at $-150\,Oe$. The slope is much less than the reference value of $136 \cdot 10^{-3}$ a.u./Oe, which corresponds to the hard switching.

Results in orientation `b` (/`d`), see figure 5.7:
- Contrary to the hysteresis-free reference curve at the arrays hysteresis appears. As it was already seen in orientation `a` it is larger with high measurement fields of $> \pm 2.5\,kOe$, i.e. $200\,Oe$ for 90er and 50–$100\,Oe$ for 200er elements, and round about halve of these values with an applied field of $-340\,Oe$ to $280\,Oe$. The middle of the hysteresis also varies from $\geq 100\,Oe$ to $\pm 25\,Oe$ for the lower measurement fields. The values for the higher applied fields are for both arrays not precise due to many fluctuations.
- At the arrays the curve is much more flat compared to the soft slope of the reference, which has a value of $1.94 \cdot 10^{-3}$ a.u./Oe, contrary to $0.09 \cdot 10^{-3}$ a.u./Oe for the 200er elements. Both arrays show a linear behavior between -100 and $100\,Oe$, but accuracy of the 90er value is bad due to a not smooth curve. That is also the reason for missing values of 200er at high fields, and 90er at low fields.

The behavior in orientation `a` of all three arrays of the first and second sample fit together: A sharp transition is softened and widened. This softer curve corresponds to the general influence of an array of elements which have slightly different characteristics, as mentioned in section 5.1. In orientation `b` the normally soft slope without hysteresis gets wider and hysteresis becomes visible along with a higher slope. This behavior was extreme at the array of the first sample, where the gap between the elements in HA-direction is below $2\times$ dimensions. If shape anisotropy is still working at such small elements, it gives rise to antiferromagnetic interaction of adjacent elements. This means that the magnetization of adjacent elements is parallel to EA but in opposite directions, in accordance with the simple view mentioned on page 112. At first this interaction would hinder about half of the elements from proper alignment. Those antiparallel oriented elements will be switched at an applied field if it is high enough. The specific

point of switching depends at least on the individual size and shape, so that the average switching is smeared. Contrary to this the visible switching in MOKE is relative sharp for the measured array on the first sample. With respect to the aforementioned simple view this can be explained due to elements which are connected via dipolar coupling in direction of easy axis. This results in a sharp switching behavior due to a chain-reaction if one element changes its magnetic orientation.

The MOKE results show, that one should use a low measurement field in general, in order to get a hysteresis-free signal.
A good assumption for the application of elements as sensors is no hysteresis, in order to have one measuring point with specific current at an applied field. The collected data in table 5.4 show for higher applied fields larger hysteresis, which can even vanish if the measuring field is reduced, as the 90er data in orientation $\mathtt{a}$ shows. These elements have also the highest slope of $0.23 \cdot 10^{-3}$ a.u./Oe, compared with he other arrays. The 100er have indeed a similar slope of $0.22 \cdot 10^{-3}$ a.u./Oe, but a hysteresis of 30–40 Oe, which is not centered at zero field. Also at this aspect the 90er show a good symmetry with a linear range of -50 Oe to 50 Oe. The 200er in orientation $\mathtt{b}$ have the largest range of 200 Oe, which is also symmetric, and have the smallest hysteresis of 20–25 Oe of all elements in orientation $\mathtt{b}$. It is reasonable that single elements will have less hysteresis, because the measured value is the mean value of all elements of the 200er array, i.e. a maximum number of about 4500 elements[61].

In orientation $\mathtt{b}$ the 100er show the best symmetry of the hysteresis, but the width is 90 Oe and the linear range of the way FRO is besides zero field from -70 to -10 Oe. The way TO is not as linear as the way FRO and a linear range can be only from about 65 Oe unto about zero field, so these characteristics cannot be applied for a sensor. For the structuring of sensors the real sizes are important, i.e. approx. $145 \times 270 \, nm^2$ for the 90er, $270 \times 500 \, nm^2$ for the 200er, according to table 5.3[62] (the real size of the 100er elements is uncertain as mentioned on page 5.3.1, but according to SEM and AFM images round about between 110–270×320–$600 \, nm^2$).

Summarizing the following elements are promising candidates for the application as biosensors:
If the measuring field is applied perpendicular to the sensors easy axis, i.e. orientation $\mathtt{a}$, elements with approx. $145 \times 270 nm^2$ show a hysteresis-free signal with the best slope at a linear range of $100 Oe$, which is symmetric to zero field.
For H_a parallel to the long axis, i.e. orientation $\mathtt{b}$, approx. $270 \times 500 nm^2$ sized sensors should have $<25 Oe$ hysteresis width, in combination with a linear signal in between -100 and $100 Oe$.

The results show a decrease of sensitivity due to the structuring.

---

[61]The laser spot in the MOKE setup (section 2.4) has a diameter which is equal to the (write-)field size. Each field contains nominal 134×34 elements (see table 5.3), but some can be destroyed due to the removing.

[62]The values are calculated with respect to the given example dimensions and the mean area:
90er: example $142 \times 265 \, nm^2$, mean area $39196 \, nm^2 \rightarrow 145 \times 270 \, nm^2 = 39150 \, nm^2$
200er: example $266 \times 492 \, nm^2$, mean area $134176 \, nm^2 \rightarrow 270 \times 500 \, nm^2 = 135000 \, nm^2$

Between the uncertain slope of the second reference in orientation `a` ($136 \cdot 10^{-3}$ a.u./Oe) and the 90er value ($0.23 \cdot 10^{-3}$ a.u./Oe) is a factor of approx. 580. That is very much, compared with SHOSHI[Sho05, p. 100]: Structured GMR multilayer showed a sensitivity that is reduced with a factor of 20 ($1.7 \cdot 10^{-3}$ %/Oe instead of $35 \cdot 10^{-3}$ %/Oe). In orientation `b` the minimal factor of reduction is only 22, for a comparison between the reference of the second sample and 200er elements, which have both the same linear range.

Discussion

The main problems during the preparation were the difficult removing and also the varying sizes of the elements. These aspects are also important if one uses e.g. an AGM, whose disadvantages were mentioned in section 5.1.2, as an alternative to the MOKE measurements. The problem of changed dimensions was caused by unstable parameters of the SEM during exposure, i.e. sample current. So also dose tests cannot help, if e.g. a new cathode with changing parameters is in use, but an uncertain shape is in general a problem if tiny elements are structured. Another resist can be helpful to reduce edge roughness, but also its thickness can be varied, to get a determinable size which is near to the nominal dimensions. Therefore in the design one should use ellipses instead of rectangles, or one can try to write "lines" in order to get a structure as small as possible, i.e. a width of $50\,nm$[Rot] for the used SEM as KARSTEN ROTT tried out.

More important is the long removing of the elements which causes a loss or damage, and prevented the removing of all resist. So the signal of good removed elements could be disturbed by those, which are in an undefined state. A solution is to use a material, whose removing time is much shorter than that of Ta. Therefore Ru is a good choice for a faster and reliable removing, e.g. CAMELIA ALBON[Alb] needed only $30\,min$ for removing of approx. $140 \times 260\,nm^2$ elements.

Based on the TMR effect amplitudes of already existing sensors a simple assumption for the sensitivity of a sensor will be done. Values of TMR stacks are e.g. approx. 13 % for AlO_x in [Pan05, figure 6.2], round about 30 % for own sputtered AlO_x (during prework before this thesis) and 75 % or max. 95 % for the sputtered MgO stack, which were used for the second MOKE sample (please look on page 111). The latter MOKE sample shows a maximal hub of 1.04 a.u. in orientation `a` and 0.59 a.u. in `b`. Taking the lowest TMR and the larger hub one gets a pessimistic factor of 12.5 %(TMR)/a.u.(MOKE). (An optimistic factor of 161 %(TMR)/a.u.(MOKE) is given by the maximal TMR and lower hub value.) Therefore a possible sensitivity can be calculated to 0.0029 %(TMR)/Oe for sensors, based on the 90er sensitivity of $0.23 \cdot 10^{-3}$ a.u./Oe (optimistic value: 0.0377 %(TMR)/Oe). A comparison with the results of SHOSHI[Sho05, p. 100] shows that the sputtered TMR stack with MgO can show better characteristics than GMR multilayer: The structured GMR stack had a sensitivity of 0.0017 %(GMR)/Oe, so the assumed sensitivity in this theses is better with a factor of 1.7 (and the optimistic value even with factor 22). The TMR ratios are high enough to compensate the drop of sensitivity mentioned in the last section, because the structured GMR stack had 1.7 % MR (unstructured 2.4 %).

The assumed value of $0.0029\,\%(\text{TMR})/Oe$ $(0.0377\,\%(\text{TMR})/Oe)$ is not as good as the sensitivity SHEN[SLMX05] was able to use, i.e. $0.4\,\%(\text{TMR})/Oe$, for the detection of single magnetic beads. Also the values of JANG[JNK+06] or SCHOTTER[Sch04] are missed with a factor of about 100 (optimistic value: factor 10), confer section 1.4.3. Although this comparison shows, that one cannot expect a detection of (single) magnetic markers at once, one must wait for the concrete application and improvement of the elements as sensors.

5.4   Conclusion

A signal from the arrays was measurable and the shape anisotropy works well. For relative small fields the wanted perpendicular pinning results in fact into (almost) hysteresis-free switching behavior, so that those elements should be applied as sensors in further research (please read ahead in section 5.5 "Characterization of MgO TMR Elements").

Although the perpendicular pinning works, it would be interesting whether dipolar coupling plays a role or not. This could be due to the reduced distances of the elements at the first and second sample. The real gap at the arrays of the second sample, averaged over the detailed data from SEM observation, is 1.4×3 for $200\times800\,nm^2$ elements and 1.4×2.4 for $90\times450\,nm^2$ elements. The decreased gap of the hard direction and conversely enlarged gap in direction of easy axis originates in a too low dose. This shrinks the elements nominal dimensions, in competition with the broadening of thin structures due to de-focus and forward scattering, confer section 3.1.2. Nine elements of nominal $200\times800\,nm^2$ at the second sample showed dimensions of approx. 253–268×582–$637\,nm^2$. These shall be compared with the results of ABRAHAM and LU[AL05], to see wether there might be an interaction between the elements. ABRAHAM and LU tested 16 combinations of gaps for the width and height of elliptic elements with nominal $300\times600\,nm^2$; 1.1, 2.2, 4.1, 7 for the width and 0.9, 1.7, 2.9, 4.6 for the height. A comparison of these elements with the own 200er is possible, because the difference in size is not very much and due to the natural deformation the self-made elements also have an elliptic shape. The gap of 1.4×3 which is found with the SEM is compared with 1.1×2.9 from the article. Therefore a dipole coupling was observed, resulting in "a broadening of transition [...] and a slight increase in switching field"[AL05] due to a relative tight placement in the direction of the elements hard axis. This comparison cannot give quantitative values, but it points out that there should be in fact some dipole interaction. Widened transition, due to dipolar interaction, means a less steep switching signal, and a higher coercitive field means a switching more distant to zero field. These influences of the suggested dipole coupling are in general contrary to the needs of a sensor. Consequently the vanishing dipolar interaction could lead to an even better sensor characteristic of such analyzed elements.
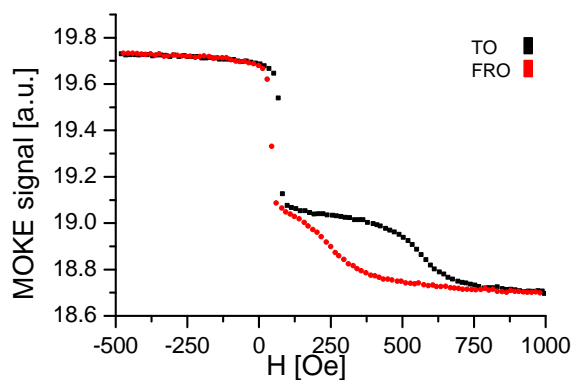
(a) reference, MA orientation `a`
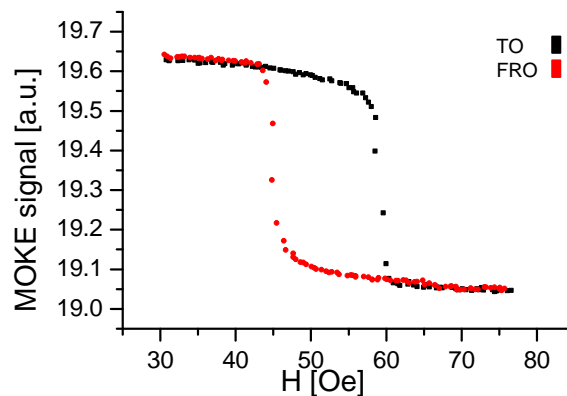
(b) reference, MI orientation `a`
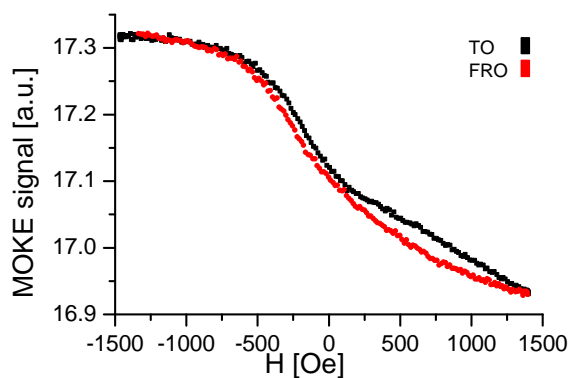
(c) $90{\times}450\,nm^2$ elements, MA orientation `c`
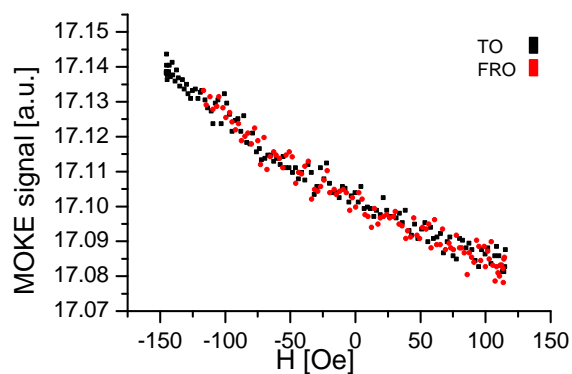
(d) $90{\times}450\,nm^2$ elements, MI orientation `c`
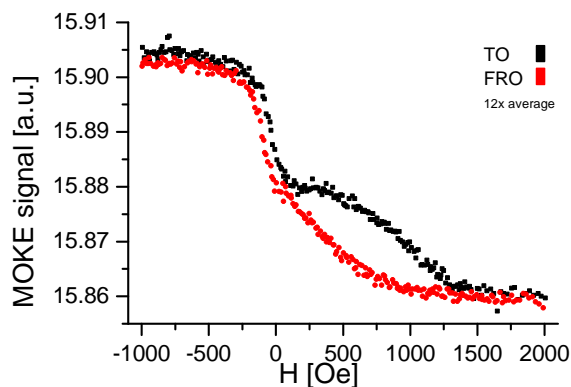
(e) $200{\times}800\,nm^2$ elements, MA orientation `c`
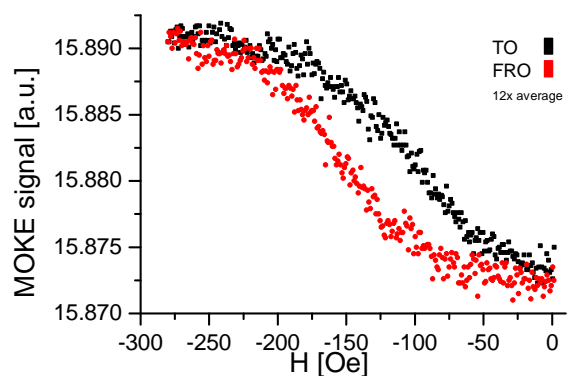
(f) $200{\times}800\,nm^2$ elements, MI orientation `c`

Figure 5.6: MOKE measurements of the second sample in orientation `a` or, equal to, `c`.

(a) reference, MA orientation `b`

(b) reference, MI orientation `b`

(c) $90 \times 450\,nm^2$ elements, MA orientation `d`

(d) $90 \times 450\,nm^2$ elements, MI orientation `d`

(e) $200 \times 800\,nm^2$ elements, MA orientation `d`

(f) $200 \times 800\,nm^2$ elements, MI orientation `d`
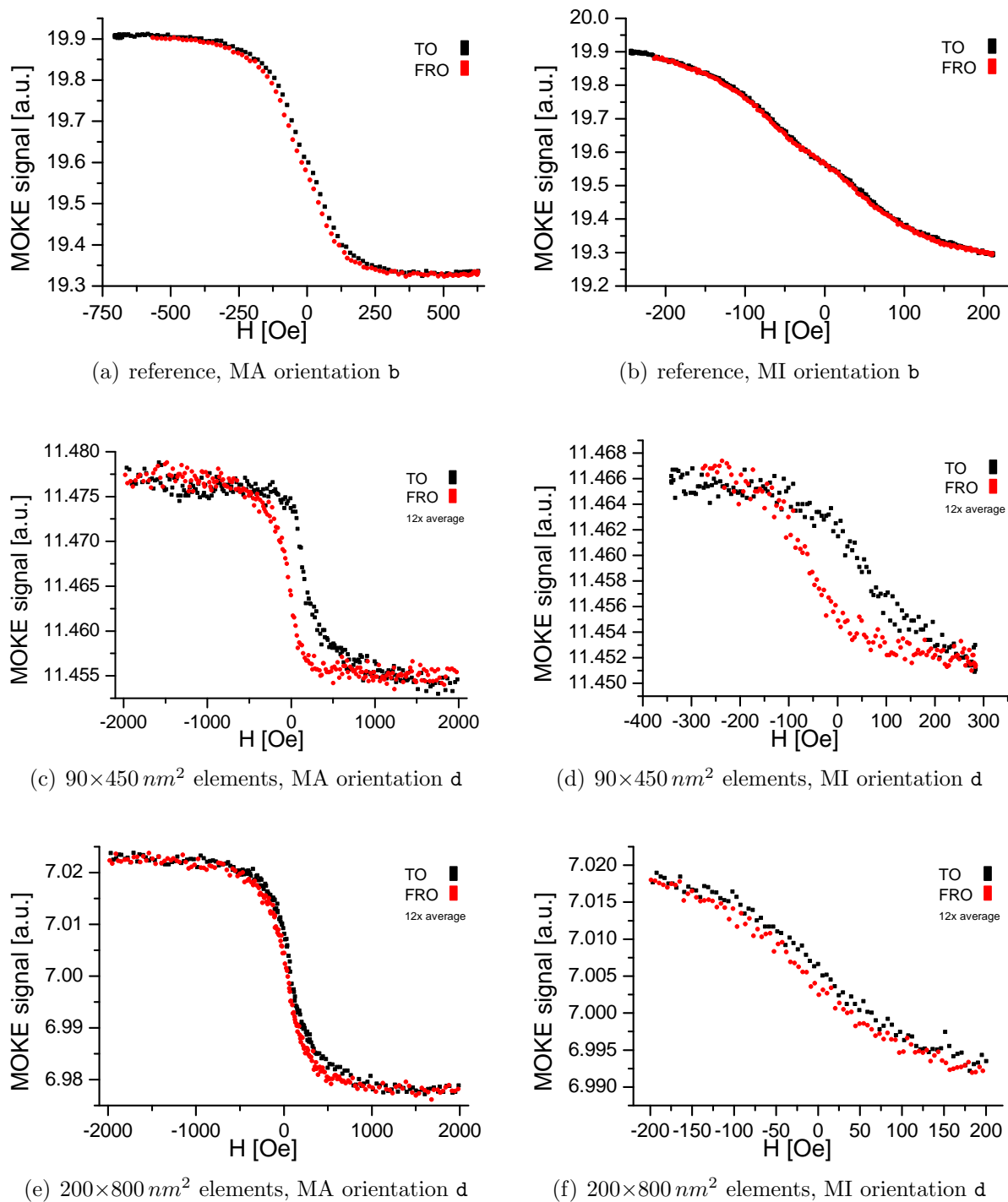
Figure 5.7: MOKE measurements of the second sample in orientation `b` or, equal to, `d`.

5.5 Characterization of MgO TMR Elements

5.5.1 Preparation

For the implementation of the tiny elements, which were found in MOKE measurements, as sensors a design for 40 sensors is used, further related to as "sensor-array". The design was made by KARSTEN ROTT and has been already used in a simple variant for the sample which was used in chapter 4. The improved version has the benefit that all sensors are exposed in a $100\,\mu m$-writefield. This gives the best resolution for sensors and is equal to those writefields used for MOKE-arrays, so that the experienced doses should be easily adapted. Nevertheless it is important to do dose tests on the original ground. Therefore an area of the lower conducting line, about $138 \times 180\,\mu m^2$ which is adjacent to the sensors, is exposed.

Lithography consists of three steps, which are all done with negative e-beam resist, for the lower conducting lines (figure 5.8a), sensor-elements itself (figure 5.8b) and upper conducting lines with concluding contact pads (figure 5.8c), see the description below. All sensors which are exposed in the second step are connected via one lower conducting line. The upper contact is made by the upper conducting lines, whereas the big contact pads are necessary to place a tip for TMR measurements. Additional contact pads are of course exposed in step 2 and 3 for the lower conducting line, placed on the top and bottom in the design. For the conducting lines and pads a large $2000\,\mu m$-writefield is used, because the lines are relative large. This writefield is big enough so that everything is structured in one step which avoids overlapping problems, and a smaller writefield is not necessary for big structures.

The original design was a little bit modified to make the alignment easier, which is especially useful if more than one design is structured on the same sample. In fact four designs are placed on one sample because different sensors varying in size and aspect ratio are tried out, so that all are treated in the same way. After finishing the structuring one must drop bead dilution only one time for all four sensor arrays, which enlarges the possibility to have a bead on a working sensor.

The different lithography steps and other preparation parts are listed below with the parameters of the structured sample.

Basic preparation A sample of the new sputtered MgO-stack from section 5.1, page 111, was annealed for $60\,min$ at $350\,°C$ heating and $30\,min$ cooling in big magnet $(6500\,Oe)$ for field cooling, see section 1.3.5. Etching through top Cu layer, into Ta was followed by sputtering about $6\,nm$ Ta to get a closed layer of pure Ta on top.
(A MOKE test verifies, that the stack shows magnetic switching.)

Step 1 Coating with resist AR-N 7520.18 @$4000\,rpm$, and after exposure developing $3\,min$ in AR300-47 was done. The etching into upper Ta layer was followed by removing $50\,min$ in heated ultrasonic bath ($80\,°C$).

Step 2 Cleaning in ultrasonic bath and SIMS, i.e. etching only several seconds to get
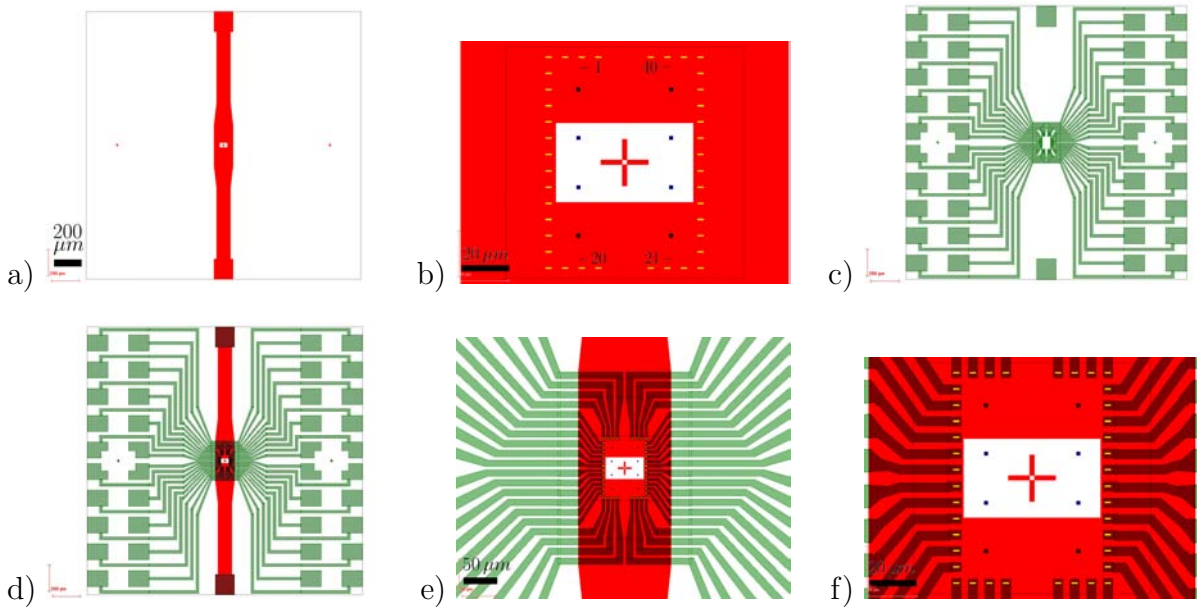
Figure 5.8: Designs for the three steps to structure 40 sensors at one field. In the upper line the single designs for step 1 (a) and step 3 (c) with a $2000\,\mu m$-writefield are visible. In (b) on the red lower conducting line the sensors are colored yellow, the $100\,\mu m$-writefield for exposure is indicated by the thin gray line. In the lower line all designs at once are visible with higher magnifications from left (d) to the right side (f). (Screenshots, taken on ELPHY software, are further colored.)

rid of maybe oxidized surface, was necessary after a break in the process. AR-N 7520.18 was diluted 1:1 with thinner and spined @$6000\,rpm$ for a thin resist-layer which was developed after exposure for $3\,min\,30\,s$. After etching in the SIMS into SiOx or upper Ta, $75\,nm$ SiOx was sputtered as protection layer. Iterative removing and observation in OM or SEM took $235\,min$ (= $92\,min$ + $73\,min$ + $70\,min$, see comments on resist in text and table 5.5).

Step 3 After cleaning as in step 2 the conductive material for upper conducting lines was sputtered: Ta $8.7\,nm$ as glue layer and Au $59.57\,nm$. For exposure AR-N 7520.18 @$4000\,rpm$ spined, exposed and later $3\,min$ developed. Etching of Au and Ta left the upper conducting lines on top after a final removing of $30\,min$.

A quick check of surface conductivity is performed with a voltmeter to see whether the isolating material is good. If e.g. the oxygen flow is not sufficient, it can happen, that conductive Ta is sputtered instead of TaOx.

Elements were exposed with nominal rectangular shape of 100×400 (dose 3.2 and 3.3), 100×1200 (dose 3.1) and $500\times2500\,nm^2$ (dose 2.3), one kind of sensor per field. The big ones are chosen, because removing is easier, i.e. faster, for bigger structures and their shape should not be changed into an ellipse. Most interesting are the tiny $100\times400\,nm^2$ sensors, so two fields were prepared in order to have more tiny sensors for

measurements. To make sure one kind of sensors offers shape anisotropy, a third kind of sensors with $100{\times}1200\,nm^2$ were structured.

5.5.2 Results and Discussion

The properties of the four fields of the last sample are written in table 5.5 and discussed in detail afterwards:

nominal size $[nm^2]$	dose $\rightarrow$ real size $[nm^2]$ & shape	comment on removing
$100{\times}400$	3.2 $\rightarrow 150{\times}400$ elliptic...	three without resist
$100{\times}400$	3.3 $\rightarrow$ ...with aspect ratio 1:2.7	maybe two without resist
$100{\times}1200$	3.1 $\rightarrow 90{-}150{\times}730{-}840$	grainy, rough structure
$500{\times}2500$	2.3 $\rightarrow 520{\times}2480$ rectangular	only two with resist

Table 5.5: Elements of the four fields on last sensor approach, nominal rectangular, see text for details.


(a) MA

(b) MI
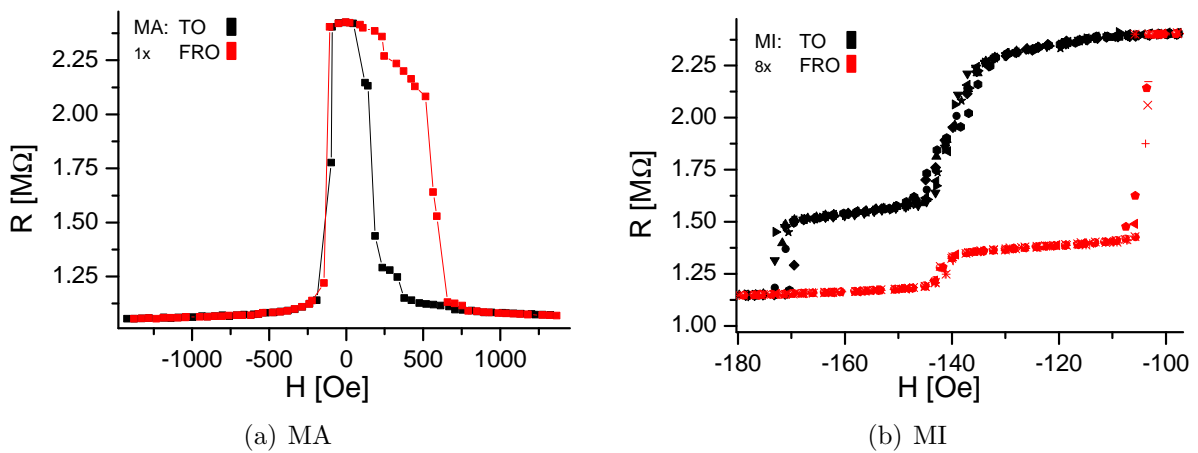
Figure 5.9: Working $150{\times}400\,nm^2$ sensor with $130\,\%$ TMR (orientation `a`).

$100{\times}400\,nm^2$:
Only three sensors with dose 3.2 had no resist and showed a signal: One is OK with $130\,\%$ (at MA), showing switching in two steps which could be a sign for two domains (figure 5.9). Although the small dimensions should prefer a single-domain state a split can be induced by kinks in the rough shape, as is visible in figure 5.10(a). A hysteresis of approx. $40{-}70\,Oe$ ranges from -170 to $-100\,Oe$. Furthermore one sensor has an even better TMR ratio of $138\,\%$ (figure 5.11, SEM image in figure 5.10(b)) but a "strange" curve which is not smooth, showing hysteresis of about $340\,Oe$ from -320 to $20\,Oe$. The third working sensor-element showed only $5\,\%$ (figure 5.12), but switching in one smooth

(a) sensor with 130 % TMR, switching in two steps

(b) sensor with 138 % TMR but a strange TMR switching curve
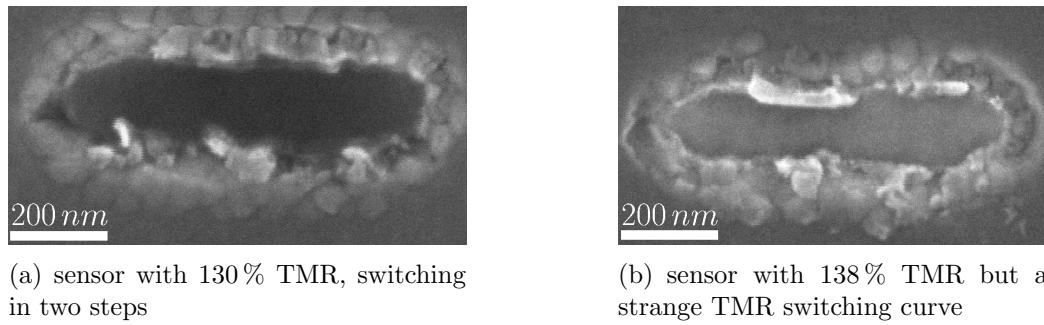
Figure 5.10: SEM images, showing the rough shape of sensors (nominal rectangular $100{\times}400\,nm^2$).


(a) MA

(b) MI
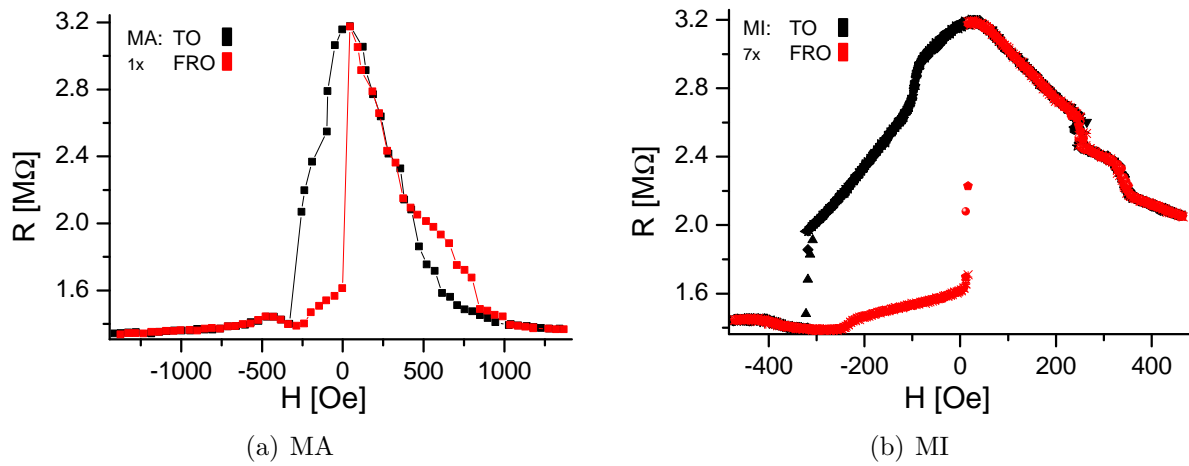
Figure 5.11: Working $150{\times}400\,nm^2$ sensor with 138 % TMR (orientation a).

step with maximal $45\,Oe$ hysteresis from 0 to $110\,Oe$. The resistance, which is lowered by a factor of 10^4 compared to the other two sensors, indicates that a shortcut was measured.

$100{\times}1200\,nm^2$:
SEM pictures and measurements show that no element is left.

$500{\times}2500\,nm^2$:
Almost all sensor-elements were looking freed from resist. During a quick check only two sensors gave no signal, most probably due to resist on top, and one had 5 % TMR. At most sensors the TMR ratio is 100–135 %, but a few show less down to 80 % (and sensor 1 has only about 32 % TMR). The curves show in general kinks, often two or even three reproducible ways and a relative hard switching. Exemplary in figure 5.14 the data of sensor 23 and 24 are shown. The cases with only one way coincident with an almost rectangular switching which is often around zero field. In repeated detailed measurements of sensor-elements (1–10, 21–30 and 39–40) are different ways apparent
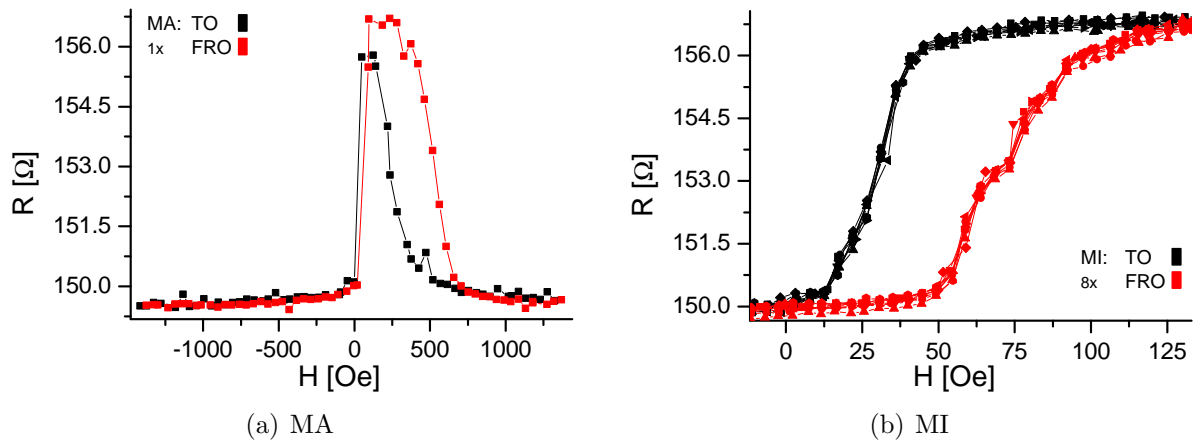
Figure 5.12: $150{\times}400\,nm^2$ sensor with $5\,\%$ TMR (orientation a).

at six sensors (5, 21, 23, 27, 29 and 30), four showed only little differences (24, 25, 39 and 40), and one way is visible at three sensors (1, 22 and 28). Additional measurements were done in orientation c (H_a parallel to H_{FC}) the same two "normal" specific ways were visible. They were comparable to measured data in orientation a (180° twisted compared with c), after inverting field values and the current values are also on the same level. Maybe an additional third way is induced by saturation – such effect was visible not often, in fact only at first and further measurements of sensor 5, see figure 5.13.
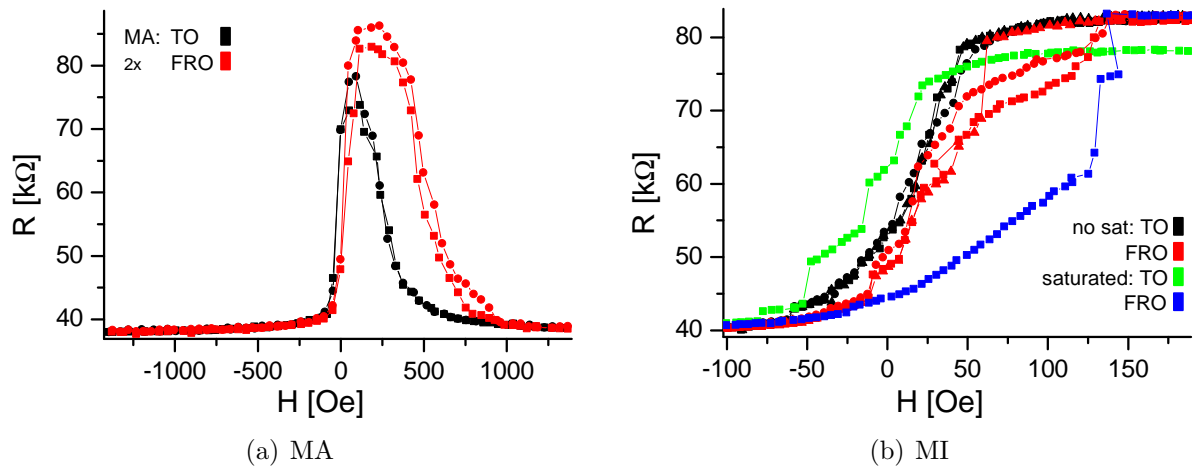
Figure 5.13: At one sensor ($500{\times}2500\,nm^2$) a third way only appeared after saturation (orientation a).

In general the sensors are too big, which results in the existence of domains, visible in the mentioned kinks. Therefore it will be useless to use those sensors, because the expected result is not better than that of the already tried out sample in chapter 4. Contrary to those larger sensors of approx. $4 \times 2\,\mu m^2$, the characterized sensors show a large variety in behavior. In fact two sensors, namely 24 and 40, showed very little hysteresis, see figure 5.14, so this size of elements can be near the threshold to elements applicable as sensors.
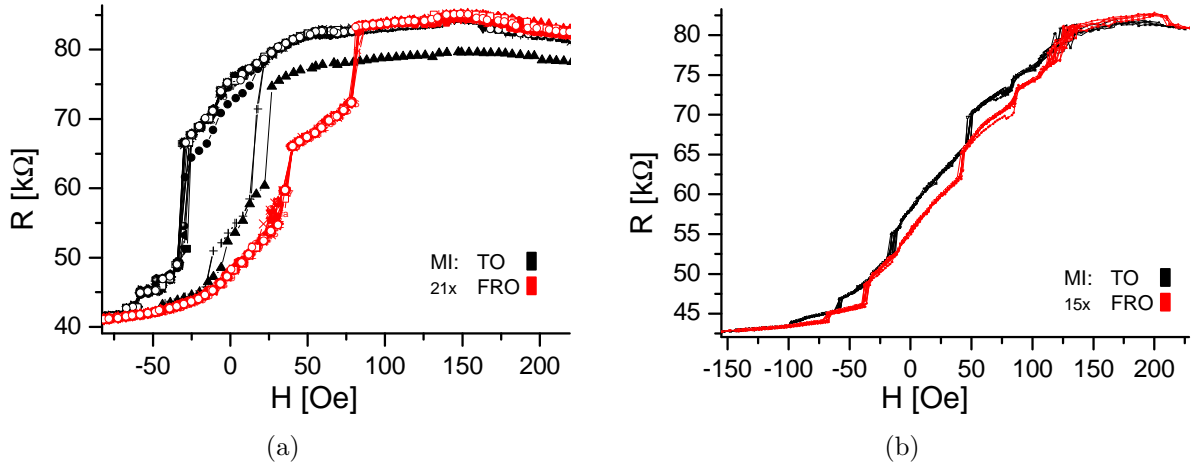
Figure 5.14: Almost all sensors $(500 \times 2500\,nm^2)$ showed (at least) two characteristic ways, exemplary in (a) those of sensor 23 with big differences to each other and relative big hysteresis. Two sensors, namely 24 (b) and 40, showed only little hysteresis (with little differences of the two characteristic ways; all measured in orientation a).

Although a few big sensors of $500 \times 2500\,nm^2$ show no hysteresis, all measurable tiny sensors of $100 \times 400\,nm^2$ still have hysteresis in spite of the smaller dimensions. This might be explained due to a loss of perpendicular pinning, but this is not reasonable with respect to the shape visible in figure 5.10. The SEM image shows not a sharp border for the tiny elements, but one can deduce two dimensions. The dimensions of the inner structure are about $76 \times 344\,nm^2$ and $89 \times 366\,nm^2$, giving an aspect ratio of 1:4.5 and 1:4.1, respectively. One can also look at the maximum dimensions of visible structure whose dimensions are about $165 \times 429\,nm^2$ and $201 \times 464\,nm^2$, with aspect ratios of 1:2.6 and 1:2.3, respectively. The area between minimum and maximum value are most probably the slope side caused by etching, so the height difference should be similar to the etching depth in step 1 and step 2. This is calculated to $74\,nm$ from the stack layout[63], and the MgO barrier is located approx. $12.6\,nm$ below the top. With a linear slope at the sides of the elements, which is reasonable due to the constant milling angle, the area of the barrier can be calculated to $91 \times 358\,nm^2$ and $108 \times 383\,nm^2$. So the

---

[63]Ta 7.2/Cu 30/Ta 7/Cu 5/MnIr 10/CoFeB 2.5/MgO 1.5/CoFeB 2.37/Ta 3.5/Ta 6 in *nm*, see page 111, after etching into about half of the upper Ta in step 0 and sputter additional $6\,nm$. In steps 1 and 2 approx. $1\,nm$ of the lower Ta layer was left, based on the etching plots.

relevant aspect ratio of the elements is 1:3.9 and 1:3.5, which is enough for establishing shape anisotropy, confer section 1.5.5.

These considerations do not mean that such tiny sensors will have in general the drawback of hysteresis, because it was only possible to measure three sensors. Nevertheless it cannot be expected any longer to have only hysteresis-free sensors.

Further tasks are the characterization of outstanding $500{\times}2500\,nm^2$ sensor-elements in orientation c to see, whether more hysteresis-free sensors can be found (and maybe are also additional ways only in combination with saturation visible). The application as biosensors is not recommend with respect to the results of chapter 4, which showed, that showed the difficulties of sensors with hysteresis and kinks in the TMR curve.

Summary and Outlook

On the way to a sensor for the detection of (single) magnetic beads with TMR sensors, at first AlO_x MTJs were used to see an influence due to beads. Various setups with in-plane and out-of-plane magnetizing fields were analyzed. Furthermore arrays of submicron sized elements with MgO barrier were structured. Shape anisotropy was successfully applied for a future application as hysteresis-free sensors.

For measurements, the following characteristics played an important role:

⋆ An upper stack-material, such as Ru, has to be used, so that the removing of the resist can be done fast and reliable.

⋆ The sensor-elements must have a smooth border. Due to a single domain state kinks during magnetic switching are avoided.

⋆ The stack above the sensing layer should be as thin as possible to have a minimal distance towards a magnetic marker.

⋆ A homogenous perpendicular field is chosen for the saturation of the magnetic marker; most recommend are Helmholtz-coils.

⋆ An alignment of the sensors/sample towards the magnetic fields is needed with extended accuracy.

In a measurement process the measurement's field strength should be only as high as needed for a minor loop during measurement, whereas a high saturating field of several $100\,Oe$ produces a specific starting point. At first, the clean sensors are characterized with and without OOP field (step 1), which is repeated after dropping of the beads (step 2). After the sensors have been cleaned further measurements are done for comparison (step 3) of the cleaned state. At each process step additional measurements of a few sensors should be done, to see wether the measurements are reproducible.

In the first experimental part of this thesis, the hysteresis of $2\times4\,\mu m^2$ sensors with an AlO_x tunnel barrier was shifted in different ways, which depends on the presence of a bead. This was done with a setup of two pairs of Helmholtz-coils, one for the in-plane measurement field and the other one for a magnetization of the beads out-to-plane.

Also permanent magnets were tried out, with the result, that the used ones cannot be applied for the out-of-plane field. Contrary to the field of Helmholtz-coils, the field of the permanent magnets is not homogenous enough and has too strong in-plane components.

The large size of the sensors led to kinks in the curves, and furthermore a hysteresis was visible, which is impractical for a sensor and showed the importance of a

single-domain state. Therefore, in the second experimental part of this thesis, submicron elements were structured with the goal of reducing the hysteresis and to get a smooth signal. MOKE measurements were performed on arrays of submicron elements, which are based on a TMR stack with MgO barrier. With the application of shape anisotropy on elements of $145{\times}270\,nm^2$, it was possible to get a hysteresis-free signal due to perpendicular pinning.

Outlook

The question is now, what will happen for a single element, as it should be normally used as a sensor: Will there be enough perpendicular pinning without dipole interaction left so that one gets a hysteresis-free TMR curve? Latest results of unfinished experiments show a hysteresis at $100{\times}370\,nm^2$ sensors with working shape anisotropy. Therefore, measurements are outstanding, as well as for the reproduction of the mentioned effect, which can be produced by beads.

Several possible improvements and alternatives exist for further research:

- Stack composition:
  In MgO-stacks Ru should be used instead of Cu to avoid Cu-diffusion[Dre]. Furthermore Ru in an artificial ferromagnet[64] can be used, if a stronger pinning is necessary.

- Hysteresis-free signal:
  After sputtering MgO with masks, one could try out only annealing, without field during cooling, with only 100–150 ℃ applied, so that stack can anneal.

  Recently, publications by JANG *et al.*[JNK+06] showed an intrinsic perpendicular pinning of thin ($\leq 1\,nm$) CoFeB sensing layers. This is for relative large sensors of $20{\times}10\,\mu m^2$, so the question is, whether this will work with tiny sensors.

  According to [Wan05] a two-step annealing can work to get perpendicular pinning, the first one for establishing the pinning field, and the second one for resetting the free layer orthogonal to the pinning layer.

- OOP field:
  Helmholtz-coils should be used to create a variable perpendicular saturation field. They have the benefit of a relative high resolution when using only a low field range. An alternative to coils could be "integrated on-chip wires for excitation" of the beads, an approach DE BOER *et al.*[dBKJ+06] are searching at PHILIPS to build a compact GMR based biosensor platform.

- Magnetic marker:
  Other beads with varying sizes and material as well as coating could be tried out, which has an influence on the agglomeration in generally and on a special surface material. Also available are rods of different dimensions, such as $10\,\mu m{\times}2\,\mu m$ or $250\,nm$ long nickel tubes.

---

[64]The use of an artificial ferromagnet with Ru, i.e. antiferromagnetic coupled CoFe and CoFeB with Ru as interlayer, showed a stronger pinning of approx. $600\,Oe$ instead of about $300\,Oe$[Dre].

- Positioning of beads:
  Approaches with conducting lines work to position single beads on top of a sensor[Pan05], or sinks in resist can maybe do the same, but this does not collects only magnetic material[GP06].

- Characterization:
  The characterization of a few or single sensor-elements can be done e.g. with a SQUID ("Superconducting Quantum Interference Device", see e.g. [HS98, p. 367], or a "nanoMOKE", which is a MOKE with a typical laser spot diameter of $4\,\mu m$[W$^+$05, p. 70].

- Measurement of magnetic domains:
  Via *Lorentz microscopy* or *magnetic force microscopy* (MFM) (see [HS98, section 2.6.1]), the magnetization of sensors can be imaged. Tests with toroidal magnets could be used to see, whether Stoner-Wohlfarth-asteroids indicate single domains[LTA$^+$99].

All together we conclude that a lot of options are available to reach the goal of the detection of single magnetic beads without a signal enhancement.

References

[AL05]   David W. Abraham and Y. Lu. Observation of switching of magnetic particle arrays with weak dipole interaction field effects. *Journal of Applied Physics*, **98**:023902– 1–5, Jul 2005.

[Alb]   Camelia Albon. Personal information.

[Ald]   Sigma-Aldrich Chemie Gmbh, Munich, Germany; www.sigmaaldrich.com.

[All]   ALLRESIST GmbH, Am Biotop 14, D-15344 Strausberg; http://www.allresist.de.

[Ash76]   Ashcroft. *Solid State Physics*. Saunders College Publishing, 1976. QE700 A823.

[BAC04]   M. T. Bryan, D. Atkinson, and R. P. Cowburn. Experimental study of the influence of edge roughness on magnetization switching in Permalloy nanostructures. *Applied Physics Letters*, **85**(16):3510–3512, Oct 2004.

[Ban]   Bangs Laboratories, Inc., 9025 Technology Drive, Fishers, IN 46038-2886; http://www.bangslabs.com.

[BBB+04]   Hubert Brückl, Monika Brzeska, Dirk Brinkmann, Jörg Schotter, Günter Reiss, Willi Schepper, Paul-Bertram Kamp, and Anke Becker. Magnetoresistive logic and biochip. *Journal of Magnetism and Magnetic Materials*, **282**:219–224, 2004.

[BBD+02]   Pierre-A. Besse, Giovanni Boero, Michel Demierre, Vincent Pott, and Radivoje Popovic. Detection of a single magnetic microbead using a miniaturized silicon Hall sensor. *Applied Physics Letters*, **80**(22):4199–4201, Jun 2002.

[BBF+88]   M. N. Baibich, J. M. Broto, A. Fert, F. Nguyen Van Dau, F. Petroff, P. Eitenne, G. Creuzet, A. Friederich, and J. Chazelas. Giant Magnetoresistance of (001)Fe/(001)Cr Magnetic Superlattices. *Phys. Rev. Lett.*, **61**(21):2472–2475, Nov 1988.

[Bel]   Lucent Technologies: Bell Labs Innovations; http://www.bell-labs.com/.

[BG03]   Daniel E. Bürgler and Peter A. Grünberg. *Nanoelectronics and Information Technology: advanced electronic materials and novel devices*, chapter Magnetoelectronics – Magnetism and Magnetotransport in Layered Structures, pages 110–128. Wiley-VCH, 2003.

[BGSZ89]   G. Binasch, P. Grünberg, F. Saurenbach, and W. Zinn. Enhanced magnetoresistance in layered magnetic structures with antiferromagnetic interlayer exchange. *Phys. Rev. B*, **39**(7):4828–4830, Mar 1989.

[BJS$^+$04]   M. Brzeska, M. Justus, J. Schotter, K. Rott, G. Reiss, and H. Brückl. Development of magnetoresistive sensors for the detection of single molecules by magnetic markers. *Molecular Physics Reports*, **39**:32–38, 2004.

[BL59]   C. P. Bean and J. D. Livingston. Superparamagnetism. *Journal of Applied Physics*, **30**(4):S120–S129, Apr 1959.

[BLE]   B.L.E. Laboratory-Equipment GmbH, Lugwaldstr. 17-19, 75417 Mühlacker, Baden-Württemberg (B.L.E. Laboratory Equipment, 1600 Dell Ave., Suite S, San Jose , California 95113, UNITED STATES, phone: 408-866-3465).

[Bor05]   Jan Bornemeier. *Magnetoresistive elements in combination with Schottky-barriers on GaAs*. PhD thesis, Bielefeld University, Feb 2005.

[Bra97]   A. M. Bratkovsky. Tunneling of electrons in conventional and half-metallic systems: Towards very large magnetoresistance. *Phys. Rev. B*, **56**(5):2344–2347, Aug 1997.

[Bri]   Dirk Brinkmann. Personal information.

[Brz]   Monika Brzeska. Personal information.

[BT99]   A. E. Berkowitz and Kentaro Takano. Exchange anisotropy – a review. *Journal of Magnetism and Magnetic Materials*, **200**:552–570, 1999.

[Car00]   Francois Cardarelli. *Materials handbook: a concise desktop reference*. Springer-Verlag London, 2000.

[Cha74]   B. N. Chapman. Thin-film adhesion. *Journal of Vacuum Science and Technology*, **11**(1):106–113, Jan 1974.

[Che]   chemagen Biopolymer-Technologie AG, Arnold-Sommerfeld-Ring 2, D-52499 Baesweiler, Germany; http://www.chemagen.com/.

[Coe99]   R. Coehoorn. *Magnetic multilayers and giant magnetoresistance; Giant Magnetoresistance in Exchange-Biased Spin-Valve Layered Structures and its Application in Read Heads*, chapter 4, pages 65–128. Springer, 1999.

[Con]   PERMANENTMAGNET PIC-M0805. Internet. Conrad Electronic SE, Klaus-Conrad-Str. 1, 92240 Hirschau.

[COT⁺02]   Jin-Woo Choi, Kwang W. Oh, Jennifer H. Thomas, William R. Heineman, H. Brian Halsall, Joseph H. Nevin, Arthur J. Helmicki, H. Thurman Henderson, and Chong H. Ahn. An integrated microfluidic biochemical detection system for protein analysis with magnetic bead-based sampling capabilities. *Lab Chip*, **2**:27–30, 2002.

[Cry]   CrysTec GmbH, Köpenicker Str. 325, D-12555 Berlin,Germany; http://www.crystec.de.

[CTMH05]   Horia Chiriac, Mihai Tibu, Anca-Eugenia Moga, and Dumitru D. Herea. Magnetic GMI sensor for detection of biomolecules. *Journal of Magnetism and Magnetic Materials*, **293**:671–676, 2005.

[DBB⁺02]   C. L. Dennis, R. P. Borges, L. D. Buda, U. Ebels, J. F. Gregg, M. Hehn, E. Jouguelet, K. Ounadjela, I. Petej, I. L. Prejbeanu, and M. J. Thornton. The defining length scales of mesomagnetism: a review. *J. Phys.: Condens. Matter*, **14**:R1175–R1262, 2002.

[dBKJ⁺06]   B. de Boer, J. Kahlman, Th. Jansen, H. Duric, and J. Veen. An integrated and sensitive detection platform for magneto-resistive biosensors. oral talk, May 2006. [O8] at Biosensors 2006, Toronto.

[DGW⁺04]   T. Dimopoulos, G. Gieres, J. Wecker, N. Wiese, and M. D. Sacher. Thermal annealing of junctions with amorphous and polycrystalline ferromagnetic electrodes. *Journal of Applied Physics*, **96**(11):6382–6386, Dec 2004.

[Dig]   Digital Instruments, Inc., 797 Sheridan Drive, Buffalo, NY 14150; http://www.digitalinstruments.com.

[Dig00]   Digital Instruments Veeco Metrology Group, 112 Robin Hill Rd., Santa Barbara, CA 93117, (805)967-1400. *Scanning Probe Microscopy Training Notebook*, 3rd edition, 1999/2000. p in FP.

[DJM⁺04]   J. Dolinšek, P. Jeglič, P. McGuiness, Z. Jagličić, A. Smontara, E. Tabachnikova, and V. Bengus. Magnetic and electrical investigations of $Fe_{85-x}Co_xB_{15}$ metallic glasses. *Applied Physics A*, **79**(8):1947–1953, Dez 2004.

[Dre]   Volker Drewello. Personal information.

[Dre06]   Volker Drewello. Untersuchung der Spinpolarisation von 3d-Ferromagneten in MgO Tunnelsystemen. Diplomarbeit, Universität Bielefeld, Dec 2006.

[DTN⁺05]   David D. Djayaprawira, Koji Tsunekawa, Motonobu Nagai, Hiroki Mae-
            hara, Shinji Yamagata, Naoki Watanabe, Shinji Yuasa, Yoshishige Suzuki,
            and Koji Ando. 230CoFeB/MgO/CoFeB magnetic tunnel junctions. *Ap-
            plied Physics Letters*, **86**:092502– 1–3, 2005.

[DuP]   Du Pont de Nemours (Deutschland) GmbH, Bad Homburg, phone:
            +49(0)6172 - 87 0; http://www.dupont.com.

[Dyn]   Dynal A. S., Oslo, Norway; www.dynal.no ← Invitrogen Corpora-
            tion, 1600 Faraday Avenue, PO Box 6482, Carlsbad, California 92008;
            http://www.invitrogen.com.

[Enn]   Inga Ennen. Personal information.

[Enn03]   Inga Ennen. Charakterisierung von Cobalt-Nanopartikeln und Unter-
            suchungen zur Herstellung granularer Strukturen. Diplomarabeit, Univer-
            sität Bielefeld, 2003.

[Epp]   Eppendorf AG, Barkhausenweg 1, 22339 Hamburg, Germany, phone: ++
            49 40 53 8010; www.eppendorf.de.

[ETS⁺00]   R.L. Edelstein, C.R. Tamanaha, P.E. Sheehan, M.M. Miller, D.R. Baselt,
            L.J. Whitman, and R.J. Colton. The BARC biosensor applied to the detec-
            tion of biological warfare agents. *Biosensors & Bioelectronics*, **14**:805–813,
            2000.

[FD96]   Tilo Fischer and Hans-Jerg Dorn. *Physikalische Formeln und Daten*. Ernst
            Klett Schulbuchverlag GmbH, Stuttgart, 1996.

[FFGF05]   H. A. Ferreira, N. Feliciano, D. L. Graham, and P. P. Freitas. Effect of
            spin-valve sensor magnetostatic fields on nanobead detection for biochip
            applications. *Journal of Applied Physics*, **97**:10Q904– 1–3, 2005.

[FGFC03]   H. A. Ferreira, D. L. Graham, P. P. Freitas, and J. M. S. Cabral. Biode-
            tection using magnetically labeled biomolecules and arrays of spin valve
            sensors (invited). *Journal of Applied Physics*, **93**(10):7281–7286, May 2003.

[FSK⁺97]   Hiromi Niu Fuke, Kazuhiro Saito, Yuzo Kamiguchi, Hitoshi Iwasaki, and
            Masashi Sahashi. Spin-valve giant magnetoresistive films with antiferro-
            magnetic Ir-Mn layers. *Journal of Applied Physics*, **81**(8):4004–4006, Apr
            1997.

[GFB⁺02]   D. L. Graham, H. Ferreira, J. Bernardo, P. P. Freitas, and J. M. S. Cabral.
            Single magnetic microsphere placement and detection on-chip using current
            line designs with integrated spin valve sensors: Biotechnological aplications.
            Journal of Applied Physics, **91**(10):7786–7788, May 2002.

[GLZC91]   Wei Gong, Hua Li, Zhongren Zhao, and Jinchang Chen. Ultrafine parti-
cles of fe, co, and ni ferromagnetic metals. *Journal of Applied Physics*,
69(8):5119–5121, Apr 1991.

[GM01]   M. Gadella and J. Mateo. Quantum irreversibility and gamov states. In
I.V. Filimonova and N.V. Orlova, editors, *Fundamental Problems of High
Energy Physics and Field Theory*, pages 191–202, 2001. Proceedings of the
XXIV workshop on high energy physics and field theory; Protvino, June
27–29, 2001.

[GnQ$^+$01] N. García, M. Mu noz, G. G. Qian, H. Rohrer, I. G. Saveliev, and Y.-W.
Zhao. Ballistic magnetoresistance in a magnetic nanometer sized contact:
An effective gate for spintronics. *Applied Physics Letters*, **79**(27):4550–
4552, Dec 2001.

[GP06]   Michael J. Gordon and David Peyrade. Separation of colloidal nanoparticles
using capillary immersion forces. *Applied Physics Letters*, **89**:053112– 1–3,
2006.

[GSP$^+$86] P. Grünberg, R. Schreiber, Y. Pang, M. B. Brodsky, and H. Sowers. Lay-
ered Magnetic Structures: Evidence for Antiferromagnetic Coupling of Fe
Layers across Cr Interlayers. *Physical ReviewLetters*, **57**(19):2442–2445,
Nov 1986.

[Gut00]   O. Gutfleisch. Controlling the properties of high energy density permanent
magnetic materials by different processing routes. *J. Phys. D: Appl. Phys.*,
33:R157–R172, 2000.

[Har61]   Walter A. Harrison. Tunneling from an Independent-Particle Point of View.
Phys. Rev., **123**(1):85–89, Jul 1961.

[HS98]   Alex Hubert and Rudolf Schäfer. *Magnetic Domains The Analysis of Mag-
netic Microstructures*. Springer, 1998. QE700 H878.

[HSE$^+$04] Andreas Hütten, Daniela Sudfeld, Inga Ennen, Günter Reiss, Wiebke
Hachmann, Ulrich Heinzmann, Klaus Wojczykowski, Peter Jutzi, Wahib
Saikaly, and Gareth Thomas. New Magnetic Nanoparticles for Biotechnol-
ogy. *Journal of Biotechnology*, **112**(1–2):47–63, Aug 2004.

[IHL$^+$05] Shoji Ikeda, Jun Hayakawa, Young Min Lee, Ryutaro Sasaki, Toshiyasu
Meguro, Fumihiro Matsukura, and Hideo Ohno. Dependence of tunnel
magnetoresistance in MgO based magnetic tunnel junctions on Ar pressure
during MgO sputtering. *Japanese Journal of Applied Physics*, **44**:L 1442–L
1445, 2005.

[Ion]   Ion-Tech GmbH, Gewerbering 10, D-09337 Hohenstein-Ernstthal, phone:
++49 (0) 3723 4988 93; www.ion-tech.de.

[Jac75]   John David Jackson. *Classical Electrodynamics*. John Wiley & Sons, Inc., 2nd edition, 1975. 17 QD080.5 J13; 178/654671+12.

[JKS+97]   M. Jimbo, K. Komiyama, Y. Shirota, Y. Fujiwara, S. Tsunashima, and M. Matsuura. Thermal stability of spin valves using amorphous CoFeB. *Journal of Magnetism and Magnetic Materials*, **165**(1–3):308–311, Jan 1997.

[JLMB06]   Z. Jiang, J. Llandro, T. Mitrelias, and J. A. C. Bland. An integrated microfluidic cell for detection , manipulation, and sorting of single micron-sized magnetic beads. *Journal of Applied Physics*, **99**:08S105– 1–3, 2006.

[JNK+06]   Youngman Jang, Chunghee Nam, J. Y. Kim, B. K. Cho, Y. J. Cho, and T. W. Kim. Magnetic field sensing scheme using CoFeB/MgO/CoFeB tunneling junction with superparamagnetic CoFeB layer. *Applied Physics Letters*, **89**:163119– 1–3, 2006.

[Jul75]   M. Julliere. Tunneling between ferromagnetic films. *Physics Letters A*, **54**(3):225–226, Sep 1975.

[KAM+03]   H. Kubota, Y. Ando, T. Miyazaki, G. Reiss, H. Brückl, W. Schepper, J. Wecker, and G. Gieres. Size dependence of switching field of magnetic tunnel junctions down to 50 nm scale. *Journal of Applied Physics*, **94**(3):2028–2032, Aug 2003.

[Kas56]   Tadao Kasuya. A Theory of Metallic Ferro- and Antiferromagnetism on Zener's Model. *Progress of Theoretical Physics*, **16**(1):45–57, Jul 1956.

[Kei]   Keithley Instruments, Inc., 28775 Aurora Road, Cleveland, Ohio 44139; http://www.keithley.com.

[Kit86]   Kittel. *Introduction to solid state physics*. John Wiley & SOns, Inc., New York, Chichester, Brisbane, Toronto, Singapore, 1986. QE700 K62.

[KJO+04]   H. J. Kim, S. H. Jang, K. H. Oh, T. S. Kim, and K. Y. Kim. The fabrication of high sensitive spin-valve sensor for magnetic bead detection. *Physica Status Solidi Applied Research*, **201**:1961–1964, June 2004.

[KPF+02]   B. Kalska, J. J. Paggel, P. Fumagalli, M. Hilgendorff, and M. Giersig. Magneto-optics of thin magnetic films composed of Co nanoparticles. *Journal of Applied Physics*, **92**(12):7481–7485, Dec 2002.

[Krä04]   Michael Krämer. *Nanostrukturierung von TMR-Bauelementen*. Dissertation, Ruhr-Universität-Bochum, Jun 2004.

[LeC02]   Patrick Rouyce LeClair. *Fundamental aspects of spin polarized tunneling*. PhD thesis, Technische Universiteit Eindhoven, 2002.

[Ley]   Oerlikon Leybold Vacuum Dresden GmbH; http://www.oerlikon.com/; Switzerland: Oerlikon Corporate Pfäffikon (Headquarter), Churerstrasse 120, Pfäffikon 8808.

[LHI+06]   Y. M. Lee, J. Hayakawa, S. Ikeda, F. Matsukura, and H. Ohno. Giant tunnel magnetoresistance and high annealing stability in CoFeB/MgO/CoFeB magnetic tunnel junctions with synthetic pinned layer. *Applied Physics Letters*, **89**:042506– 1–3, Jul 2006.

[LJW+03]   G. Li, V. Joshi, R. L. White, S. X. Wang, J. T. Kemp, C. Webb, R. W. Davis, and S. Sun. Detection of single micron-sized magnetic bead and magnetic nanoparticles using spin valve sensors for biological applications. *Journal of Applied Physics*, **93**(10):7557–7559, May 2003.

[LPLK06]   Diandra L. Leslie-Pelecky, V. Labhasetwar, and R.H. Kraus, Jr. *Advanced Magnetic Nanostructures; Nanobiomagnetics*, chapter 15, pages 461–490. Springer, 2006.

[LSJ+01]   S. H. Liou, R. F. Sabiryanov, S. S. Jaswal, J. C. Wu, and Y. D. Yao. Magnetic domain patterns of rectangular and elliptic arrays of small permalloy elements. *Journal of Magnetism and Magnetic Materials*, **226–230**(2):1270–1272, May 2001.

[LTA+99]   Yu. Lu, P. L. Trouilloud, D. W. Abraham, R. Koch, J. Slonczewski, S. Brown, J. Bucchignano, E. OŚullivan, R. A. Wanner, W. J. Gallagher, and S. S. P. Parkin. Observation of magnetic switching in submicron magnetic-tunnel junctions at low frequency. *Journal of Applied Physics*, **85**(8):5267–5269, Apr 1999.

[LWSL+05]   L. Lagae, R. Wirix-Speetjens, C.-X. Liu, W. Laureyn, G. Borghs, S. Harvey, P. Galvin, H.A. Ferreira, D.L. Graham, P.P. Freitas, L.A. Clarke, and M.D. Amaral. Magnetic biosensors for genetic screening of cystic fibrosis. *IEE Proc.-Circuits Devices Syst.*, **152**(4):393–400, August 2005.

[MB56]   W. H. Meiklejohn and C. P. Bean. New Magnetic Anisotropy. *Phys. Rev.*, **102**(5):1413–1414, Jun 1956.

[MB57]   W. H. Meiklejohn and C. P. Bean. New Magnetic Anisotropy. *Phys. Rev.*, **105**(3):904–913, Feb 1957.

[MBR03]   D. Meyners, H. Brückl, and G. Reiss. Influence of boundary roughness on the magnetization reversal in submicron sized magnetic tunnel junctions. *Journal of Applied Physics*, **93**(5):2676–2680, Mar 2003.

[Mes04]   Dieter Meschede. *Gerthsen Physik*. Springer, 2004.

[Mey]   Dirk Meyners. Personal information.

[Mey01]   Dirk Meyners. Domänenuntersuchungen an nanostrukturierten magnetis-
            chen Tunnelelementen. Diplomarabeit, University of Bielefeld, 2001.

[Mey06]   Dirk Meyners. *Herstellung und Charakterisierung von Logikarrays mit
            ultrakleinen magnetischen Tunnelelementen.* Dissertation, University of
            Bielefeld, 2006.

[Mic]   micromod Partikeltechnologie GmbH, Friedrich-Barnewitz-Str.4, 18119
            Rostock-Warnemuende, Germany; http://www.micromod.de/.

[MP05]   Mischa Megens and Menno Prins. Magnetic biochips: a new option for sen-
            sitive diagnostics. *Journal of Magnetism and Magnetic Materials*, **293**:702–
            708, 2005.

[MRMRS03]   J. Moussa, L. R. Ram-Mohan, A. C. H. Rowe, and S. A. Solin. Response of
            an extraordinary magnetoresistance read head to a magnetic bit. *Journal
            of Applied Physics*, **94**(2):1110–1114, Jul 2003.

[MXvM⁺05]   Goran Mihajlović, Peng Xiong, Stephan von Molnár, Keita Ohtani, Hideo
            Ohno, Mark Field, and Gerard J. Sullivan. Detection of single magnetic
            bead for biological applications using an InAs quantum-well micro-Hall
            sensor. *Applied Physics Letters*, **87**:112502– 1–3, 2005.

[Nüb04]   Elmar Nübold, June 2004. Information prospect laying out in church for
            visitors.

[NHT⁺05]   T. Nozaki, A. Hirohata, N. Tezuka, S. Sugimoto, and K. Inomata. Bias
            voltage effect on tunnel magnetoresistance in fully epitaxial MgO double-
            barrier magnetic tunnel junctions. *Applied Physics Letters*, **86**:082501–
            1–3, 2005.

[NIS04]   The NIST Reference on Constants, Units, and Uncertainty, Last update:
            June 2004. http://physics.nist.gov/cuu/Reference/contents.html.

[NS99]   J. Nogués and Ivan K. Schuller. Exchange bias. *Journal of Magnetism and
            Magnetic Materials*, **192**(2):203–232, Feb 1999.

[Ohr02]   Milton Ohring. *Materials Science of Thin Films.* Academic Press, 2nd
            edition, 2002. QD080.5 O38.

[Pan05]   Michael Panhorst. *On-chip manipulation and positioning of biomolecules
            with magnetic beads.* PhD thesis, University of Bielefeld, 2005.

[PKP⁺04]   Stuart S. P. Parkin, Christian Kaiser, Alex Panchula, Philip M. Rice, Brian
            Hughes, Mahesh Samant, and See-Hun Yang. Giant tunnelling magnetore-
            sistance at room temperature with MgO (100) tunnel barriers. *nature
            materials*, **3**:862–867, Dec 2004.

[PPL90]   X. Portier and A. K. Petford-Long. The formation of 360° domain walls in magnetic tunnel junction elements. *Physical ReviewLetters*, **64**(19):2304–2308, May 1990.

[Rai]   RAITH GmbH, Hauert 18, D-44227 Dortmund, Germany; www.raith.com.

[Ram97]   A. P. Ramirez. REVIEW ARTICLE: Colossal magnetoresistance. *Journal of Physics: Condensed Matter*, **9**(39):8171–8199, Sep 1997.

[Ree04]   Standard Magnets – For Reed Switches and Sensors, Dec 2004. Reed Relays and Electronics India Limited; info@reed-sensor.com; Fax 91-44-2496-0098.

[RK54]   M. A. Ruderman and C. Kittel. Indirect Exchange Coupling of Nuclear Magnetic Moments by Conduction Electrons. *Physical Review*, **96**(1):99–102, Oct 1954.

[Rot]   Karsten Rott. Personal information.

[Scha]   Michael Schilling. Personal information.

[Schb]   Jan Schmalhorst. Personal information.

[Sch01]   Jan M. Schmalhorst. *Magnetische, thermische und dielektrische Stabilität von magnetischen Tunnelelementen.* Dissertation, Universität Bielefeld, May 2001.

[Sch04]   Jörg Schotter. *Development of a magnetoresistive biosensor for the detection of biomolecules.* PhD thesis, University of Bielefeld, Oct 2004.

[Ser]   Seradyn Inc., 7998 Georgetown Road, Suite 1000, Indianapolis, IN 46268; http://www.seradyn.com/.

[Sho05]   Astrit Shoshi. Suche nach magnetischen Führsystemen und GMR-Sensoren zur on-chip Manipulation und Detektion von magnetischen Teilchen. Diplomarbeit, Universität Bielefeld, 2005.

[SHR$^+$03]   J. Schmalhorst, V. Höink, G. Reiss, D. Engel, D. Junk, A. Schindler, A. Ehresmann, and H. Schmoranzer. Influence of ion bombardment on transport properties and exchange bias in magnetic tunnel junctions. *Journal of Applied Physics*, **94**(9):5556–5558, Nov 2003.

[Sim63]   John G. Simmons. Generalized Formula for the Electric Tunnel Effect between Similar Electrodes Separated by a Thin Insulating Film. *Journal of Applied Physics*, **34**(6):1793–1803, Jun 1963.

[SLMX05]   Weifeng Shen, Xiaoyong Liu, Dipanjan Mazumdar, and Gang Xiao. In situ detection of single micron-sized magnetic beads using magnetic in situ detection of single micron-sized magnetic beads using magnetic tunnel junction sensors. *Applied Physics Letters*, **86**(Jun):253901– 1–3, 2005.

[Slo89]   J. C. Slonczewski. Conductance and exchange coupling of two ferromagnets separated by a tunneling barrier. *Physical Review B*, **39**(10):6995–7002, Apr 1989.

[SMZ$^+$06] Weifeng Shen, Dipanjan Mazumdar, Xiaojing Zou, Xiaoyong Liu, B. D. Schrag, and Gang Xiao. Effect of film roughness in MgO-based magnetic tunnel junctions. *Applied Physics Letters*, **88**:182508– 1–3, May 2006.

[SSBR04a]   W. Schepper, J. Schotter, H. Brückl, and G. Reiss. Analysing a magnetic molecule detection system – computer simulation. *Journal of Biotechnology*, **112**:35–46, 2004.

[SSBR04b]   W. Schepper, J. Schotter, H. Brückl, and G. Reiss. Single molecule detection with magnetic beads – computer simulation. *J. Magn. Magn. Mater.*, **272–276**:el695–el696, 2004.

[SSBR06]   W. Schepper, J. Schotter, H. Brückl, and G. Reiss. A magnetic molecule detection system – A comparison of different setups by computer simulation. *Physica B Condensed Matter*, **372**:337–340, feb 2006.

[SSF$^+$91] J. F. Smyth, S. Schultz, D. R. Fredkin, D. P. Kern, S. A. Rishton, H. Schmid, M. Cali, and T. R. Koehler. Hysteresis in lithographic arrays of permalloy particles: Experiment and theory (invited). *Journal of Applied Physics*, **69**(8):5262–5266, Apr 1991.

[Ste77]   Mary Beth Stearns. Simple explanation of tunneling spin-polarization of Fe, Co, Ni and its alloys. *Journal of Magnetism and Magnetic Materials*, **5**(5):167–171, April–May 1977.

[Sud00]   Daniela Sudfeld. Examensarbeit, Universität Bielefeld, 2000.

[Sud05]   Daniela Sudfeld. *Hochauflösende Mikrostrukturanalyse von magnetischen $(Fe_{1-x}Co_x)_{1-y}Pt_y$-Nanopartikeln*. Dissertation, Uiversität Bielefeld, May 2005.

[SWN99]   Manish Sharma, Shan X. Wang, and Janice H. Nickel. Inversion of Spin Polarization and Tunneling Magnetoresistance in Spin-Dependent Tunneling Junctions. *Phys. Rev. Lett.*, **82**(3):616–619, Jan 1999.

[TBF$^+$99] Jose Maria De Teresa, Agnes Barthelemy, Albert Fert, Jean Pierre Contour, Francois Montaigne, and Pierre Seneor. Role of Metal-Oxide Interface in Determining the Spin Polarization of Magnetic Tunnel Junctions. *SCIENCE*, **286**:507–509, 1999.

[TBS$^+$03] A. Thomas, H. Brückl, M. D. Sacher, J. Schmalhorst, and G. Reiss. Aluminum oxidation by a remote electron cyclotron resonance plasma in magnetic tunnel junctions. *J. Vac. Sci. Technol. B*, **21(5)**:2120–2122, 2003.

[Tel06]   Joachim Teller. Email to NILS MELLECH: "'Informationsmaterial zu Sicas-tarpartikeln", 09 2006. Email to Nils Mellech: "Informationsmaterial zu Sicastarpartikeln".

[Tho]   Andy Thomas. Personal information.

[Tip99]   Tipler. *Physics for Scientists and Engineers*. W.H.Freeman and Company, 4th edition, 1999. at Günter.

[TM71]   P. M. Tedrow and R. Meservey. Spin-Dependent Tunneling into Ferromag-netic Nickel. *Phys. Rev. Lett.*, **26**(4):192–195, Jan 1971.

[TPJ⁺05]   Mark Tondra, Anthony Popple, Albrecht Jander, Rachel L. Millen, Nikola Pekas, and Marc D. Porter. Microfabricated tools for manipulation and analysis of magnetic microcarriers. *Journal of Magnetism and Magnetic Materials*, **293**(1):725–730, May 2005.

[TPL00]   Mark Tondra, Marc Porter, and Robert J. Lipert. Model for detection of immobilized superparamagnetic nanosphere assay labels using giant magnetoresistive sensors. *Journal of Vacuum Science and Technology*, **18**(4):1125–1129, Jul 2000.

[Uni]   Magnetic Materials. Internet. The University of Birming-ham, Edgbaston, Birmingham, B15 2TT, United Kingdom; http://www.aacg.bham.ac.uk/magnetic_materials/.

[vDC05]   Sebastiaan van Dijken and J. M. D. Coey. Magnetoresistance sensor with an out-of-plane magnetized sensing layer. *Applied Physics Letters*, **87**:022504–1–3, Jul 2005.

[Vog97]   H. Vogel. *Gerthsen Physik*. Springer, 1997.

[vONP06]   K. van Ommering, J. Nieuwenhuis, and M. Prins. Characterization of sub-micrometer superparamagnetic beads for biosensors by brownian motion analysis. poster session, May 2006. [P155] at Biosensors 2006, Toronto.

[VTMB99]   M. J. Van Bael, K. Temst, V. V. Moshchalkov, and Y. Bruynseraede. Mag-netic properties of submicron Co islands and their use as artificial pinning centers. *Physical Review B*, **59**(22):14674–14679, Jun 1999.

[W⁺05]   Wiese et al. Switching of submicron-sized, antiferromagnetically coupled CoFeB/Ru/CoFeB trilayers. *Journal of Applied Physics*, **98**:103904– 1–5, 2005.

[Wan05]   Shan X. Wang. Towards a magnetic microarray for sensitive diagnostics. *Journal of Magnetism and Magnetic Materials*, **293**:731–736, 2005.

[Wie02]   Nils Wiese. Nanostrukturierte Schichtsysteme zur Messung elektronischer Transportlängen. Diplomarbeit, Universität Bielefeld, Jul 2002.

[Wie06]   Nils Wiese. *Coupling phenomena and scalability of CoFeB/Ru/CoFeB sandwiches*. Dissertation, Bielefeld University, Feb 2006.

[Wik07]   Dupont. Internet, Jan 2007. From Wikipedia, the free encyclopedia.

[WSP+06] Bingqing Wei, Mutsuhiro Shima, Ranjit Pati, Saroj K. Nayak, David J. Singh, Renzhi Ma, Yubao Li, Yoshio Bando, Saburo Nasu, and Pulickel M. Ajayan. Room-temperature ferromagnetism in doped face-centered cubic fe nanoparticles. *small*, **2**(6):804–809, 2006.

[WTN+88] D. A. Wharam, T. J. Thornton, R. Newbury, M. Pepper, H. Ahmed, J. E. F. Frost, D. G. Hasko, D. C. Peacock, D. A. Ritchie, and G. A. C. Jones. One-dimensional transport and the quantisation of the ballistic resistance. *J. Phys. C: Solid State Phys.*, **21**:L209–L214, 1988.

[Xia06]   NdFeB Magnet XIANGYING. Internet, Apr 2006. NdFeB Magnet ©2006 Xiangying Magnetic Materials Co., Ltd.; magnets@public.xm.fj.cn.

[YFK+06] Shinji Yuasa, Akio Fukushima, Hitoshi Kubota, Yoshishige Suzuki, and Koji Ando. Giant tunneling magnetoresistance up to 410fully epitaxial Co/MgO/Co magnetic tunnel junctions with bcc Co(001) electrodes. *Applied Physics Letters*, **89**:042505– 1–3, Jul 2006.

[YNF+04] Shinji Yuasa, Taro Nagahama, Akio Fukushima, Yoshishige Suzuki, and Koji Ando. Giant room-temperature magnetoresistance in single-crystal Fe/MgO/Fe magnetic tunnel junctions. *nature materials*, **3**:868–871, Dec 2004.

[Yos57]   Kei Yosida. Magnetic Properties of Cu-Mn Alloys. *Phys. Rev.*, **106**(5):893–898, Jun 1957.

[Zei]   Carl Zeiss AG, Carl-Zeiss-Str. 22, 73447 Oberkochen, Germany; http://www.zeiss.de.

[ZYYJ05] Zongzhi Zhang, Liu Yaowen, Y. P. Yang, and Q. Y. Jin. Micromagnetic Simulation for nanobeads detection using planar Hall senors. *IEEE Transactions on Magnetics*, **41**, 2005.

Acknowledgements

First of all I want to thank my supervisors *Prof. Dr. Andreas Hütten* and *Prof. Dr. Günter Reiss* for being the "big" bosses of our group and reviewers of this thesis. You kept the general ideas and gave important recommendations.

Furthermore I want to thank our "little" bosses, especially
Dr. Michael Schilling concerning introduction to topic and machines, supervising and care in general as well as the reading of this thesis,
Dr. Simone Herth for supply with papers and tips as well as reading of this thesis — you outlined many important aspects for a good "diploma thesis recipe" (and those for yummy food as well),
Dr. Jan Schmalhorst for help with MOKE and general tips on measurement of TMR data,
Dr. Andy Thomas for tips and company in coffee breaks.

Many thanks go to
Dr. Karsten Rott for supply with samples and know-how on several machines, especially the SIMS, SEM and "coati", as well as all the lithography stuff,
Dirk Brinkmann for many tips and interesting conversations, as well as for the music,
Dr. Dirk Meyners for AFM measurement, many tips ...,
Volker Drewello for data on sputtering and Mgo-stacks, further for the use of one of his samples,
Volker Höink for tips,
Camelia Albon for latest data of sensors in a skipped section...,
Markus Meinert for XRD measurement,
Monika Brzeska for making available the setup with single permanent magnet and giving additional information,
Andrea Niemeyer for mental support during bonding (which was luckily not used for the tasks of this thesis)
Nils Mellech for email and company,
Inga Ennen for helping with a former try out with nanoparticles,
Daniel Meißner from the department of chemistry for hand over of nanoparticles and further solvents, not used in this thesis,
Dr. Paul-Bertram Kamp from the faculty of biology for hand over of disposable tips and short presentation of their equipment,
Gerhard Ahlers for help with computer hardware problems,